CONTRACTOR REPORT

Parabolic Dish Module Experiment Final Test Report

Defense and Information Systems Division
Sanders Associates, Inc.
95 Canal Street
Nashua, NH 03061

Printed March 1986

Parabolic Dish Module Experiment Final Test Report

Defense and Information Systems Division
Sanders Associates, Inc.
95 Canal Street
Nashua, NH 03061

Abstract

A development test model of the 8-meter Solar Brayton Parabolic Dish Module has been designed, fabricated, and tested. The test model consists of five major subsystems: Sanders ceramic honeycomb solar receiver; LaJet LEC460 solar concentrator; AiRsearch SABC MKIIIA engine, Abacus 8 kW ac inverter; and a Sanders designed and built system controller. Goals of the tests were to integrate subsystem components into a working module, demonstrate the concept, and generate 5 kWe (hybrid) and 4.7 kWe (solar only) input. All subsystem integration goals were successfully achieved, but system performance efficiency was lower than expected. Contributing causes of the lower performance efficiencies have been identified. Modifications needed to restore performance to the required levels and improve the system life cycle cost have been addressed and are the subject of this final report.

SOLAR THERMAL TECHNOLOGY
FOREWORD

The research and development described in this document was conducted within the U.S. Department of Energy's (DOE) Solar Thermal Technology Program. The goal of the Solar Thermal Technology Program is to advance the engineering and scientific understanding of solar thermal technology, and to establish the technology base from which private industry can develop solar thermal power production options for introduction into the competitive energy market.

Solar thermal technology concentrates solar radiation by means of tracking mirrors or lenses onto a receiver where the solar energy is absorbed as heat and converted into electricity or incorporated into products as process heat. The two primary solar thermal technologies, central receivers and distributed receivers, employ various point and line-focus optics to concentrate sunlight. Current central receiver systems use fields of heliostats (two-axis tracking mirrors) to focus the sun's radiant energy onto a single tower-mounted receiver. Parabolic dishes up to 17 meters in diameter track the sun in two axes and use mirrors or Fresnel lenses to focus radiant energy onto a receiver. Troughs and bowls are line-focus tracking reflectors that concentrate sunlight onto receiver tubes along their focal lines. Concentrating collector modules can be used alone or in a multi-module system. The concentrated radiant energy absorbed by the solar thermal receiver is transported to the conversion process by a circulating working fluid. Receiver temperatures range from 100°C in low-temperature troughs to over 1500°C in dish and central receiver systems.

The Solar Thermal Technology Program is directing efforts to advance and improve promising system concepts through the research and development of solar thermal materials, components, and subsystems, and the testing and performance evaluation of subsystems and systems. These efforts are carried out through the technical direction of DOE and its network of national laboratories who work with private industry. Together they have established a comprehensive, goal directed program to improve performance and provide technically proven options for eventual incorporation into the Nation's energy supply.

To be successful in contributing to an adequate national energy supply at reasonable cost, solar thermal energy must eventually be economically competitive with a variety of other energy sources. Components and system-level performance targets have been developed as quantitative program goals. The performance targets are used in planning research and development activities, measuring progress, assessing alternative technology options, and making optimal component developments. These targets will be pursued vigorously to insure a successful program.

The objective of this Parabolic Dish Module (PDM) was to perform studies leading to the selection of components, design, construction and test of an integrated system. Tests were conducted to show the viability of the Brayton cycle engine as an economic converter of solar to electric energy.

Goals of the test program were to integrate subsystem components into a working module, then test it to demonstrate concept feasibility, and identify areas for performance improvement. These goals were achieved, and the first solar Brayton Parabolic Dish Module was operated successfully in the hybrid mode on June 8, 1984, and with a solar-only power input on July 10, 1984.

LIST OF SYMBOLS

GREEK

A	Area
AC	Alternating Current
An	Incremental Area Element
Cp	Specific Heat at Constant Pressure
DC	Direct Current
Dw	Window Diameter
FS	Full Scale
FVa	View Factor of Absorber
FVc	View Factor of Cavity Walls to Window
Gr	Grash of Number
h	Heat Transfer Coefficient
I	Insolation
InWC	Inches of Water Column
IR	Infrared
K	Thermal conductivity
KRPM	Thousand RPM
L	Length
M	Mass Flow Rate
P	Pressure
Pr	Prandtl Number
Q	Heat Flow Rate (Power)
R	Gas Constant
R	Reflectivity
Re	Reynolds Number
RET	Receiver Exhaust Temperature
RIT	Receiver Inlet Temperature
RPM	Revolutions Per Minute
SABC	Subatmospheric Brayton Cycle
T	Temperature
TC	Thermocouple
X	Axial direction
Y	Perpendicular Axis

α	Absorbtivity
δ	Half Wall Thickness
Δ	Difference
ϵ	Emissivity
∞	Ambient condition
λ	Wavelength
μ	Viscosity
σ	Stefen-Boltzman Constant
Σ	Summation
θ	Temperature Ratio
τ	Transmissivity

SUBSCRIPTS

a	Absorber
aw	Absorber to Window
acw	Absorber to Cavity to Window
c	Cavity
cw	Cavity to Window
F	
n	Element Segment
Q	Quartz
r	radius
RI	Receiver Inlet
WI	Outside Window Surface
0	Total (Stagnation) Condition
1	Compressor Inlet
2	Compressor Exhaust
3a	Recuperator High Pressure Exit
3b	Receiver Inlet
4a	Receiver Exhaust
5	Turbine Inlet
6a	Turbine Exhaust
6b	Recuperator Low Pressure Inlet
7a	Recuperator Low Pressure Outlet
7b	Heat Sink Inlet

vii

TABLE OF CONTENTS

TABLE OF CONTENTS (CONT.)

APPENDICES

LIST OF TABLES

LIST OF ILLUSTRATIONS

SECTION 1

INTRODUCTION TO TEST PROGRAM

The objective of the Parabolic Dish Module Experiment (PDME) program was to design and demonstrate a Brayton engine-based solar thermal electric generating system for distributed parabolic dish collector fields.

Late in 1982, the sub-atmospheric Brayton cycle (SABC) being developed by Garrett AiResearch (Torrence CA.) for a 10-ton commercial heat pump application was identified as a reasonable engine selection in spite of its smaller size. The (then)-anticipated commercial heat pump market would provide a production base for the engine that would hold its unit cost below $5K. Predicted engine performance made the engine a good match with the 34 kWt LaJet Energy Corporation stretched membrane solar dish concentrator. This concentrator was entering production for a 4.3 MW solar plant and was the only low-production cost concentrator available. It appeared that this combination could be the basis for a viable 8 kWe production module for the near and mid-term market.

Accordingly, Sanders recommended (and JPL concurred) that worthwhile technology development toward an interim renewable energy source could be achieved with the SABC engine and LaJet concentrator. The PDME program then proceeded on a two-phase plan.

Phase I concentrated on the development and test of a Development Test Module (DTM) shown in Figure 1. The DTM system (Figure 1) used an existing heat pump-configured SABC MK IIIA engine modified to accept solar input. The dynamometer that AiResearch had developed for testing the SABC engine was used as a shaft speed alternator to convert shaft power to electrical power. The engine, shown in Figure 2, was expected to produce 4.5 kW electric output and operate at 17% thermal-to-electric efficiency.

Phase II of the program was to include an upgrade of the DTM design, fabrication of a second power conversion assembly (PCA) with an improved SABC MK IIIB engine, and integration and test of an 8 kW-electric parabolic dish module (PDM) at the Sandia-Albuquerque Distributed Receiver Test Facility (DRTF). The configurations of the DTM and PDM were to be nominally similar, with the exception that the PDM would incorporate an improved engine and packaging refinements.

As a result of sharply inflated production cost estimates for the SABC engine, and poor performance efficiency of the DTM during testing, Sanders recommended to Sandia National Laboratories, Albuquerque (SNLA) at the June 1984 Critical Design Review (CDR) that the remaining PDM effort (Phase II) be redirected. At this time, two
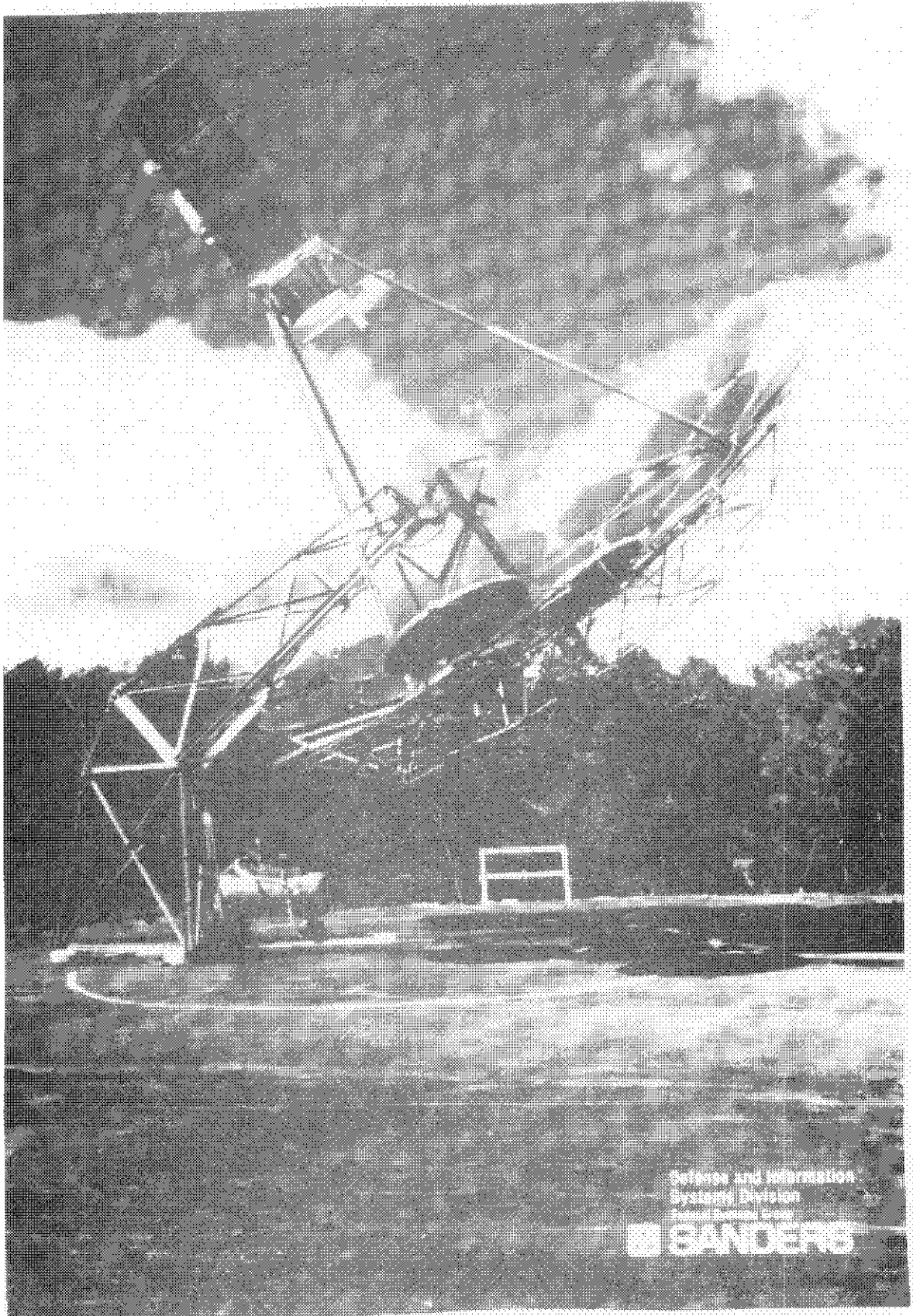
Figure 1. Brayton Parabolic Dish Module DTM
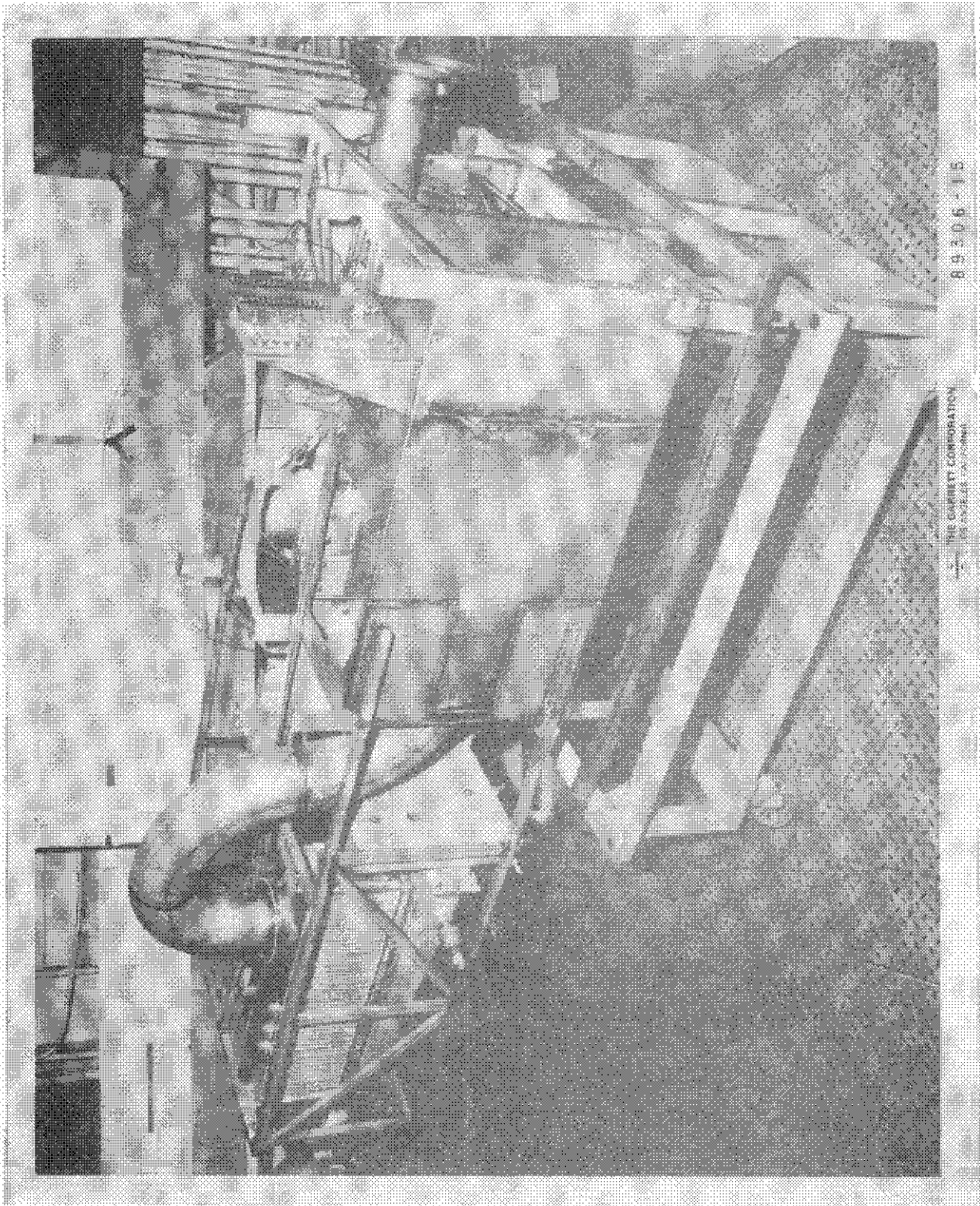
Figure 2. SABC Mark IIIA Engine

new subsystems had been identified which could be used as the basis for a more efficient and cost-effective 20 kWe module. One was a recently advanced and more cost-effective engine, the Williams WTS-34, and one was the low cost Innovative Concentrators which were scheduled for demonstration in two years. A careful production cost estimate of this 20 kWe system yielded a very competitive production cost estimate of $2.70/W installed.

SNLA, in consensus with JPL and the DOE-ALO representative, concurred with Sanders recommendation that this combination become the basis for the PDM. However, subsequent DOE funding cutbacks permitted only the initial design definition of the 20kW-e Brayton PDM to be completed on this contract. This work will be in the program final report. Hence the system description which follows relates specifically to the Phase I DTM, as tested.

SECTION 2
DTM SYSTEM DESCRIPTION

The Brayton parabolic dish module development test model (DTM) consists of five major subsystems:

- o Receiver
- o Solar Concentrator
- o Engine
- o Inverter
- o Controller

The system is based on a solar dish-mounted inverted (sub-atmospheric) Brayton cycle turbo-generator. The turbo generator is driven by heat from a concentrated solar energy thermal receiver, or by heat from a (methane) gas-fired combustor, or by a combination of solar energy and gas combustion heat. The engine-generated shaft power is converted to double shaft frequency ac electric power by a two-pole permanent magnet alternator, and is full-wave rectified to dc power. The dc power is conducted to an inverter, where it is converted to grid-compatible single-phase 240 Vac power.

An Intel model 8086 microprocessor-based controller monitors engine performance, controls the engine and inverter, commands the subordinate solar dish tracking controller, and provides operator interface via video terminal.

2.1 DTM RECEIVER DESIGN AND EVOLUTION

The solar thermal receiver used in the DTM represents a design that incorporates features developed by Sanders over the last ten years, and that meets the new design requirements of the SABC engine and its low-cost concentrator.

Figure 3 is a cutaway view of the DTM receiver as used in the test program. System efficiency and reliability is enhanced and low product cost is achieved by several features:

1. The high temperature capability quartz window contains the receiver air flow and sharply reduces the convection losses present in all open cavity receivers. The spectral characteristics of the window greatly reduce cavity reradiation while absorbing less than 2% of the solar terrestrial spectrum.

2. The central air inlet duct provides effective window cooling, as well as recovery of cavity reradiation that is absorbed on the inner face of the window. The central duct intrinsically provides circumferentially uniform airflow in the receiver.

5

GRAPHITE SHIELD RINGS   QUARTZ WINDOW   INLET DEFLECTOR   CERAMIC HONEYCOMB ABSORBER

FRONT COVER

HOUSING

FIBEROUS CERAMIC INSULATION

RIGID CERAMIC INSUATION   BACK COVER   INLET   OUTLET   EXHAUST FILTER
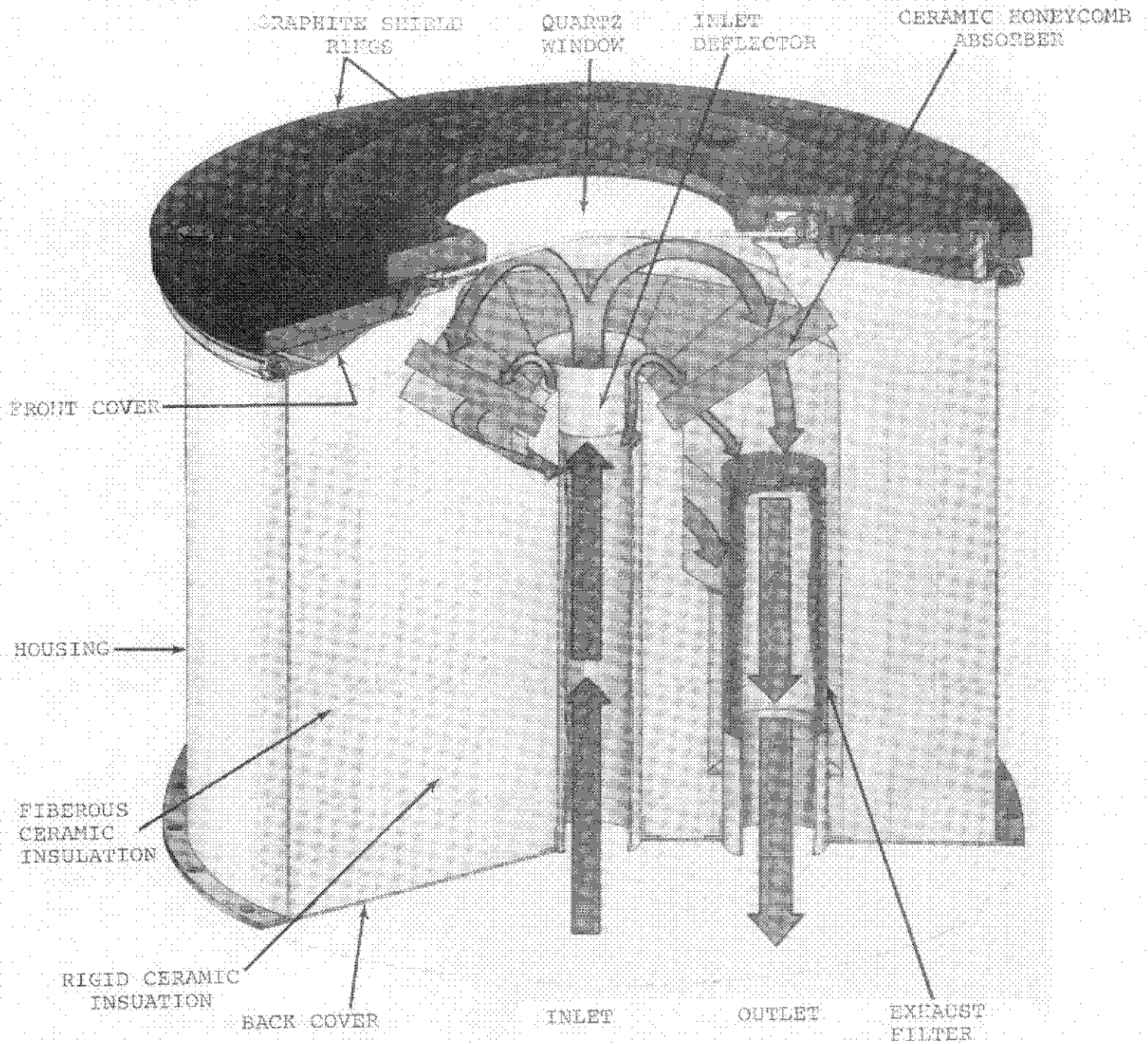
Figure 3. DTM Solar Receiver

6

3. The ceramic honeycomb provides highly efficient conversion of solar radiation to sensible heat and effective convection to the working fluid. The segmented conical design provides excellent tolerance to thermal shock while also assuring good volumetric distribution of radiation absorption.

4. Semi-rigid cavity insulation provides effective thermal impedance and reliable internal structural integrity to temperatures above 2000°F. It also allows for relatively simple receiver assembly.

New receiver features that improve its efficiency with the low-cost, light-weight concentrator, while taking advantage of unique concentrator and engine characteristics, include:

1. A lightweight, rolled sheet steel receiver housing and spun sheet steel endcaps to reduce weight at the concentrator focal point. This is made possible by the low pressure characteristic of the inverted Brayton cycle.

2. An increased receiver window (aperture) diameter to maximize net energy capture from the dish by accommodating its relatively low average concentration ratio (550 suns).

3. A passive receiver face shield for protection during solar walk-off, in the event of tracker drive failure or power loss. This feature eliminates the parasitic power requirements and the ancillary hardware of actively cooled shields. It is made possible by low peak fluxes (1,500 suns) in the concentrated spot.

4. Metal duct liners and a low impedance receiver exhaust filter to protect the engine from airborne particle erosion damage. This is made possible by relatively low (1600-1700°F) receiver operating output temperatures.

While the basic reentrant cone configuration of the receiver cavity provides good radiative efficiency, the optimum configuration was somewhat compromised on PDME to allow the use of the ceramic absorber panels used in the high-temperature receiver that was so successfully tested on the 11-meter test bed concentrator (TBC-1) at the Edwards Parabolic Dish Test Site (PDTS) in 1980-1981.

The active absorber area-to-window area ratio, Aa/Aw, of the earlier receiver was higher than expected due to the significantly lower concentration ratio of the low cost LaJet 460 concentrator. A new size absorber panel for PDM could not be obtained without

7

expensive and long-lead retooling of the absorber panel extrusion dies.

Analysis of test results has identified some receiver configuration modifications that would improve its performance. These are discussed in Appendix H, (Conclusions).

2.2 DESIGN AND EVOLUTION OF CONCENTRATOR

The selection of the LaJet LEC460 Concentrator (Figure 4) was based on its unique status as the only concentrator of truly low cost production design. This assessment of the design was supported by the negotiations, on-going at the time, for the installation of a 4.3 MW power plant at Warner Springs, CA. This installation would utilize hundreds of these concentrators and thus assure a competitive production cost.

The most unique feature of this concentrator design is its reflectors. There are 24 five-foot diameter mirrors, each consisting of a four-inch-deep aluminum rim covered on each face with a mylar membrane. The front membrane consists of 3M company's ECP 91 aluminized mylar solar reflective film. The interior volume between the films is evacuated to a pressure of several inches of water via an orifice located in the center of the disk's backside. The reflective face is thus drawn down to form a hemispherical mirror surface. Its focal length is determined by the point at which the film contacts the orifice and shuts off the vacuum to maintain the shape.

The mirror support structure and the cantilever that supports it are constructed of galvanized structural steel. The dish is counterbalanced by the engine assembly so that two very small electric motors can power the tracking system. A microprocessor-based controller provides fully automatic or manually controlled electrically driven dish operation.

2.3 ENGINE CYCLE DESCRIPTION

The Sub-Atmospheric Brayton Cycle (Inverted Brayton) differs from the normal or standard Brayton open cycle in the following way: the high pressure side of the inverted cycle remains at or near ambient atmospheric pressure, and the low pressure side is at partial vacuum. Whereas in the standard Atmospheric Brayton Cycle (ABC), the low pressure side is at or near atmospheric pressure and the high pressure side is pressurized above atmosphere. Figures 5 and 6 are block diagrams of these cycle variations. As a result of these differences, the inverted Brayton cycle engine must use a waste heat sink exchanger to precool compressor inlet air to reduce compressor power requirements. Without this heat sink exchanger, the inverted Brayton cycle cannot deliver net power.

8
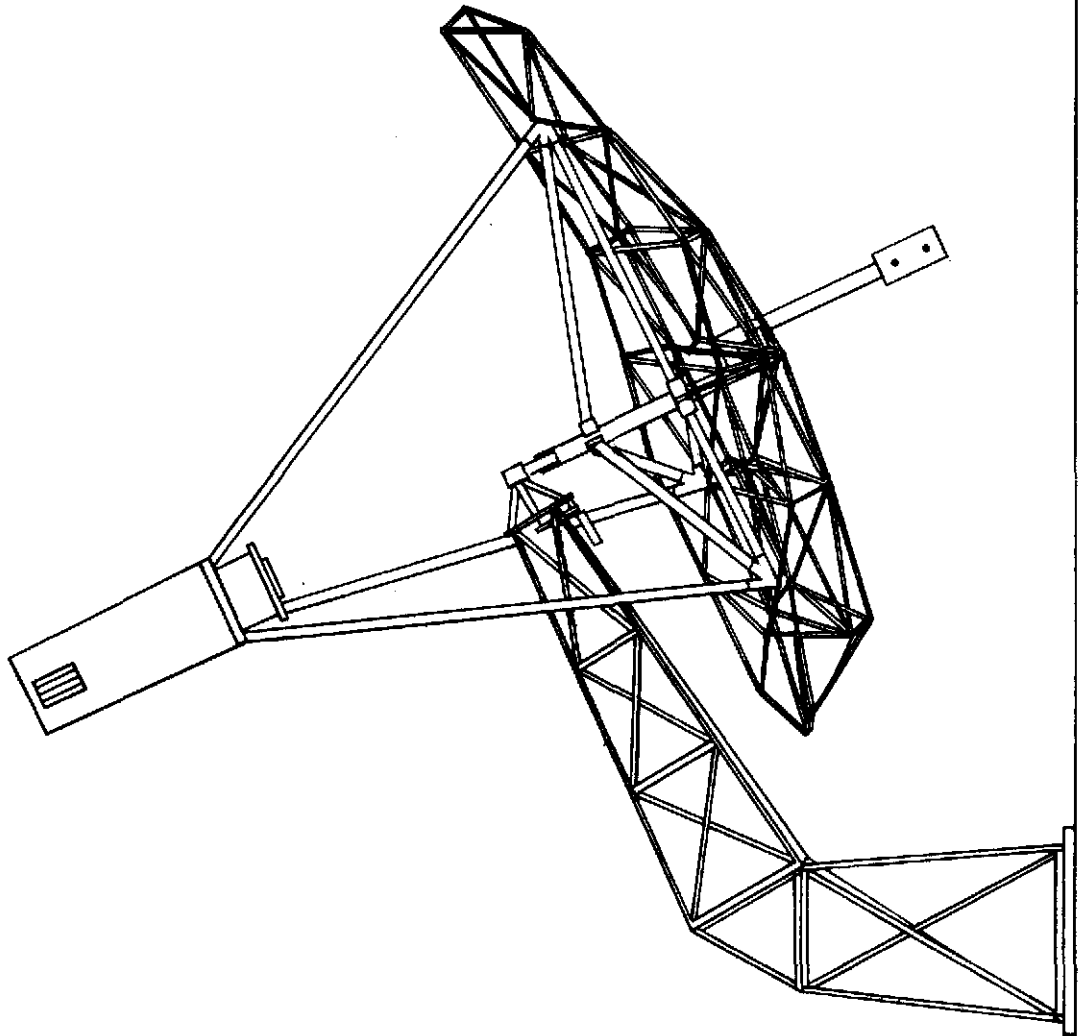
Figure 4.   LEC 460 Solar Concentrator

06114-66

9

SIMPLIFIED SYSTEM SCHEMATIC
FOR FEASIBILITY DEMONSTRATION SYSTEM
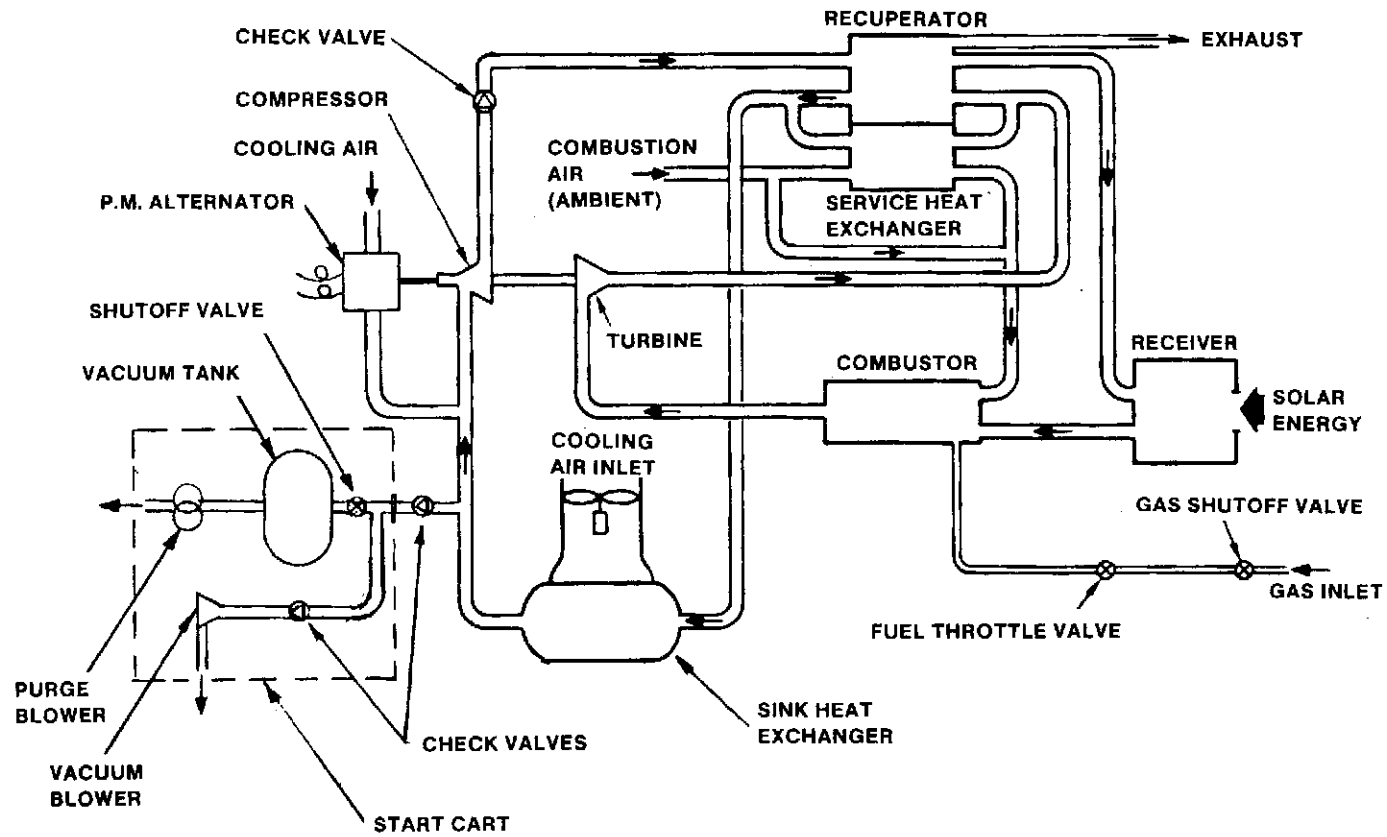
FIGURE 5. SUB-ATMOSPHERIC BRAYTON CYCLE (SABC)

GAS
INLET

GAS
COMPRESSOR

MAIN GAS
SHUTOFF
VALVE

GAS
MODULATING
VALVE

TURBO-
COMPRESSOR

COMBUSTOR

RECUPERATOR

GENERATOR/
STARTER

FILTER

FRESH AIR
INLET

EXHAUST
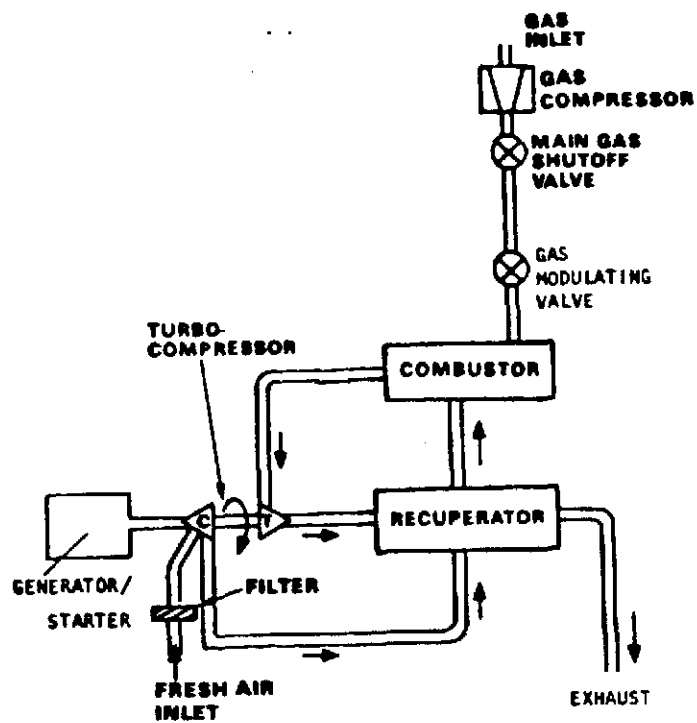
POSITIVE PRESSURE BRAYTON-CYCLE ENGINE
SIMPLIFIED SYSTEM SCHEMATIC

Figure 6. Positive Pressure Brayton-Cycle Engine

In this sense, the inverted Brayton cycle is very similar to a closed cycle Brayton. In the SABC MKIII engine, 85% of the engine mass flow is recirculating (by design) while combustion air and exhaust accounts for 15% of design mass flow.

The engine uses a vacuum "start cart"[1] to bring the engine up to idle speed. The executive processor controller commands the solar dish tracker to acquire and track the sun to direct concentrated solar flux into the solar receiver. Thermal energy from the solar receiver augments combustion heat and the engine accelerates to rated speed and power. The control system automatically reduces combustor fuel flow to limit maximum engine thermal input. Once the solar energy input satisfies engine power requirements, the combustor flame is extinguished and the module is 100% solar fired. As the insolation level decreases due to clouds or time of day, the combustor is restarted and gradually assumes a larger share of the load until, when solar input drops to zero, the module is 100% fossil fuel fired.

2.4 CONTROLS

The DTM control system functions in multiple capacities to satisfy three principal requirements:

1. Command and control,
2. interactive operator interface; and
3. signal output for data logging (see Figure 7).

In the command function, the executive processor monitors the subsystem controllers and issues appropriate commands. The subsystem controllers then autonomously controll their respective subsystems until the executive processor issues another command (e.g., start, stop, change mode).

In the control function, the executive processor acts as an active controller of engine speed and of engine load. Speed control is accomplished by comparing alternator speed with set point speed. The software algorithm provides proportional, derivative, and integral correction to fuel flow to achieve rapid, but stable, speed control with minimum droop.

----

1. The "start cart" is a portable vacuum tank assembly (see Figure 5) which is connected by a solonoid valve to the compressor. When the system is properly preheated the valve is opened and the flow of air through the compressor into the vaccuum tank spin the engine up to idle speed.
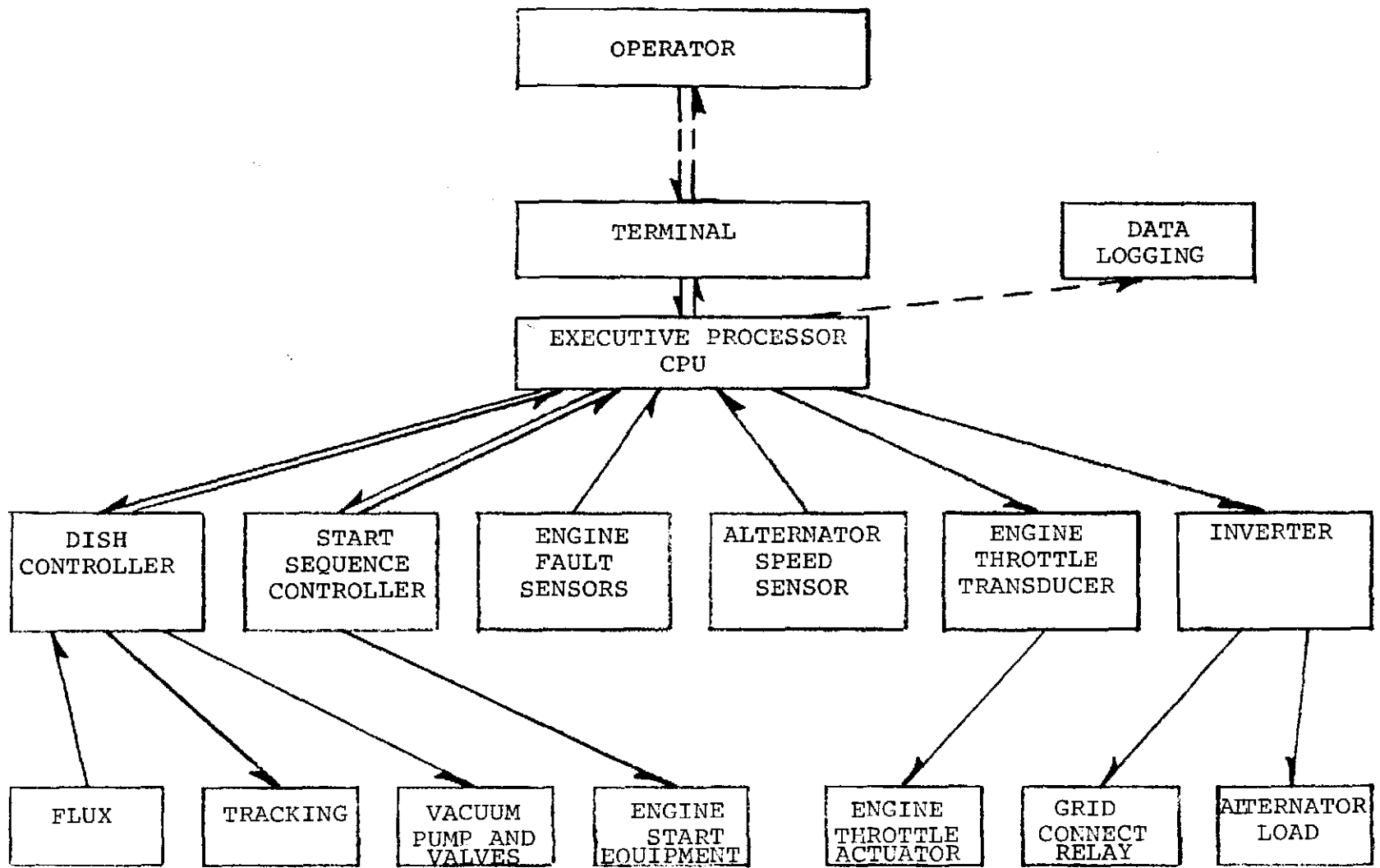
Figure 7. DTM Control System

13

Engine load control was used to help the engine stay near its best power vs speed schedule. The controller monitors engine speed, and then calculates the appropriate inverter load (as a function of speed and ambient temperature) to place a near optimum torque load on the engine.

The operator interface capacity provides (via video terminal and keyboard) a menu-driven set of control modes and operating parameter displays. The operator is presented a continuously updated alphanumeric display of system set points and operating conditions and mode-of-operation flags.

Capability to adjust engine proportional, derivative, integral (PDI) control gain, damping, and reset factors, and the ability to update the engine load temperature factor is available in real time. This facility is particularly useful in tests to optimize engine stability and transient response.

Engine speed and inverter power signals are provided as an input to the data logging equipment.

SECTION 3
TEST PROGRAM DESCRIPTION AND RESULTS

The DTM represents the first integrated assembly of small Brayton PCA subsystems. Because the DTM was built around an early MK IIIA engine, and because it used a 5kW rated dynamometer that was driven through a magnetic coupling rather than the shaft-mounted alternator proposed for the improved MK IIIB engine, performance efficiency and output power were not of primary interest. The major goals of the test and the results are shown in Table 1.

This table shows significant success in meeting the system integration goals. While the performance of the MK IIIA engine was less than predicted, the test program as a whole was notably successful for a prototype system. The subsystems and components generally performed well for developmental hardware. In-depth analysis of the test data (presented later in this report) and careful post-test inspection of the PCA has revealed a number of engine and receiver design deficiencies with cumulative effects which undermine the performance of the subatmospheric engine cycle. Our analysis indicates that the compressor and turbine aerodynamics are reasonably good, but the system (low pressure side) leaks and air bearing cooling air requirements result in compressor choking and a significant mismatch between compressor and turbine flow. This is discussed in Section 3.2.

This section describes the demonstration of module controls and the test and analysis of the DTM subsystems. Also addressed are design-to-cost issues as well as experiences gained in operating and maintaining the system in the field. In addition, post-test inspections and results are described.

3.1 DEMONSTRATION OF MODULE CONTROLS

The automatic controller (executive processor) provided seven modes of operation:

o   Start
o   Idle
o   Fossil
o   Hybrid
o   Solar
o   Shutdown
o   Emergency

The normal sequence is START, with an automatic shift to IDLE for warm up.

15

TABLE 1. DTM GOALS AND ACCOMPLISHMENTS

GOALS	ACCOMPLISHMENTS	TECHNICAL ISSUES
Integrate subsystems into operating Development Test Model (DTM)	1) Ran world's first/only solar Brayton 2) Ran world's first/only hybrid module	No major issues. Need $2 Meg to develop mature components
Adapt high temperature receiver to lightweight low pressure design	1) Reduced weight to 450 lb 2) Operated at 1600°F with low cost concentrator	Sealing around window and flanges needs improvement to eliminate leaks
Adapt (LaJet) concentrator to operate with SABC engine	1) Structural mods for extra weight 2) Added counterbalance to reduce driven loads	Concentrator optical quality needs to be improved. Facet fabrication is key
Modify GRI SABC engine to operate on solar energy on dish	1) Added receiver ducting interfaces 2) Modified heat sink mounting 3) Provided new condensate drains	Closed loop vulnerable to leaks & inefficiencies. Open loop needed for terrestrial application. Need .25 efficiency & low cost.
Develop executive processor controller to control and monitor DTM system	1) Fully successful control of fuel and inverter 2) Stable engine control 3) Reliable logic interface with system 4) Developed concentrator control interface	Simplify for commercial product
Provide production cost estimates	1) $2,700/kw cost driven to $3,815 by engine cost escalation to $13,900	Need to reduce engine cost from $1,750/KW to $400/KW. Can be done with open cycle
Assess economic viability of Brayton, ORC, and Stirling systems	1) Performed economic analysis. Brayton offers best potential to meet with DOE cost goals at 4.4¢/kw-hr energy cost over 20 year life	Cost of improved concentrator is major open issue
Recommend future Brayton development	1) Recommended shift to 20 KW size module to reach $2,200/KW production cost goal 2) Prepared preliminary design of 20 kW module	Solar specific 20 KW engine and low cost Innovative Concentrator are needed.

16

FOSSIL mode, in which all energy is supplied to the engine from fossil fuel combustion, or HYBRID mode, in which solar energy supplements the fuel input, can be entered from idle.

SOLAR mode, in which all thermal energy input comes from the sun and the combustor flame is extinguished, is also available.

SHUTDOWN (and EMERGENCY) can be entered from any of the running modes. Normal shutdown is manually keyed by the operator. Emergency is activated by any of the following temperature limit switches or alarm flags:

o   Recuperator inlet temperature
o   Heat sink exchanger temperature
o   Turbine bearing temperature
o   Alternator bearing temperature
o   Inverter internal fault
o   Utility disconnect

Both the shutdown and emergency modes trigger the same sequence of valve closures, concentrator offset and grid disconnect.

The system was successfully run and shut down in each of the five modes. There were no true emergencies where personnel or equipment were in imminent danger, though several "emergency" automatic shutdowns were triggered by bearing temperature limits or inverter faults.

The system and its controls operated successfully and stably in each mode.

3.2   TEST AND ANALYSIS OF DTM SUBSYSTEMS

The major goal of the test program was to demonstrate the technology and operate the system at the specified levels. Twelve major issues were addressed during the test and analysis of the DTM subsystems:

o   Concentrator characterization
o   Controls checkout
o   Engine leak tests
o   Receiver leak tests
o   Combustion Air throttle
o   Mirror focusing
o   Receiver analysis
o   Engine analysis
o   PMA/Rectifier losses
o   Transmission losses
o   Inverter performance
o   Parasitic power requirements

Each of these issues is described in this subsection.

3.2.1 CONCENTATOR CHARACTERIZATION

To evaluate the performance of the DTM system, it was necessary to measure the power entering the solar receiver. One method of doing this is with a low temperature calorimeter. LaJet had constructed and used a calorimeter modeled after the JPL design, using a constant flow of water to cool the cavity while recording the temperature rise in the water across the cavity. With the use of water cooled aperture plates of varying diameter, they obtained reasonably good data on the flux distribution and intercept factor for their prototype concentrator.

Sanders considered the construction of a similar calorimetry set-up for DTM use but chose instead to design and construct a scanning heat flux calorimeter, or flux rake, for the following reasons:

1. We had successfully designed and used the Georgia Tech flux rake and were therefore familiar with its design, operation and performance.

2. The flux rake permits the measurement of flux distribution at many planes across the optical axis, which can provide volumetric distribution data as well as the flux distribution at the aperture and at the surface of the absorber.

3. It permits the measurement of flux distribution on the absorber.

4. It can be positioned to profile the flux just ahead of the aperture during actual operation of the system to provide real time correlation of energy versus power out.

5. It was less expensive to construct than a cold water calorimetry set-up.

6. The second LaJet concentrator to be installed at Sandia was to be extensively characterized with a cold water calorimeter by Sandia.

Thus, with JPL approval we designed the flux rake shown in Figures 8 and 9. It consists of 1 1/4 inch wide by a 1 1/4-inch thick water cooled flux sensor bar with 29 flux sensor locations at one inch spacings along its length. A remotely controlled motor driven worm screw can sweep the sensor bar laterally across the receiver aperture with a stroke of + 17 inches from the optical axis (see Figure 10). The 4 sensor bar sweep speed can be remotely adjusted over the range

18
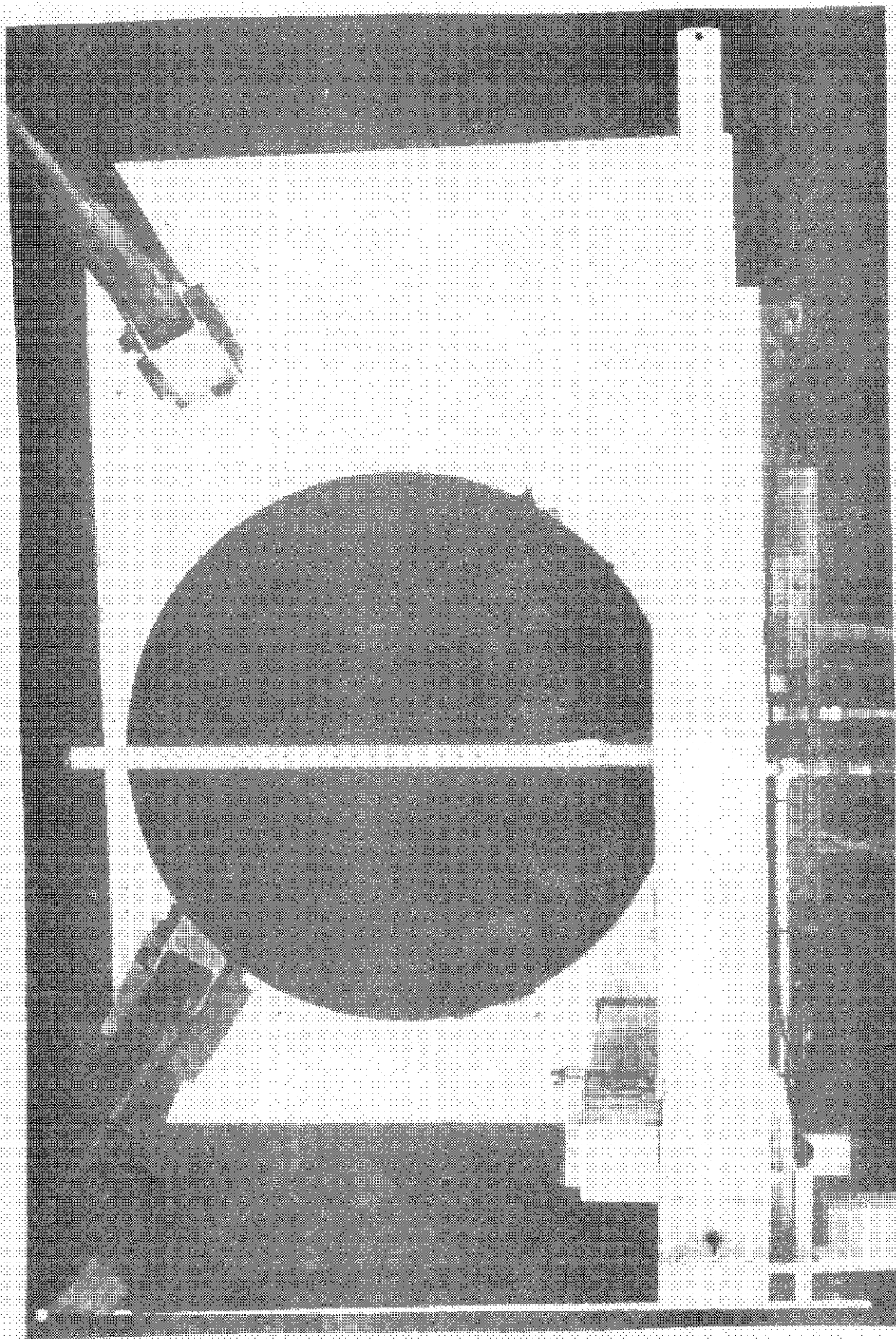
Figure 8.   Flux Rake in Front of Receiver
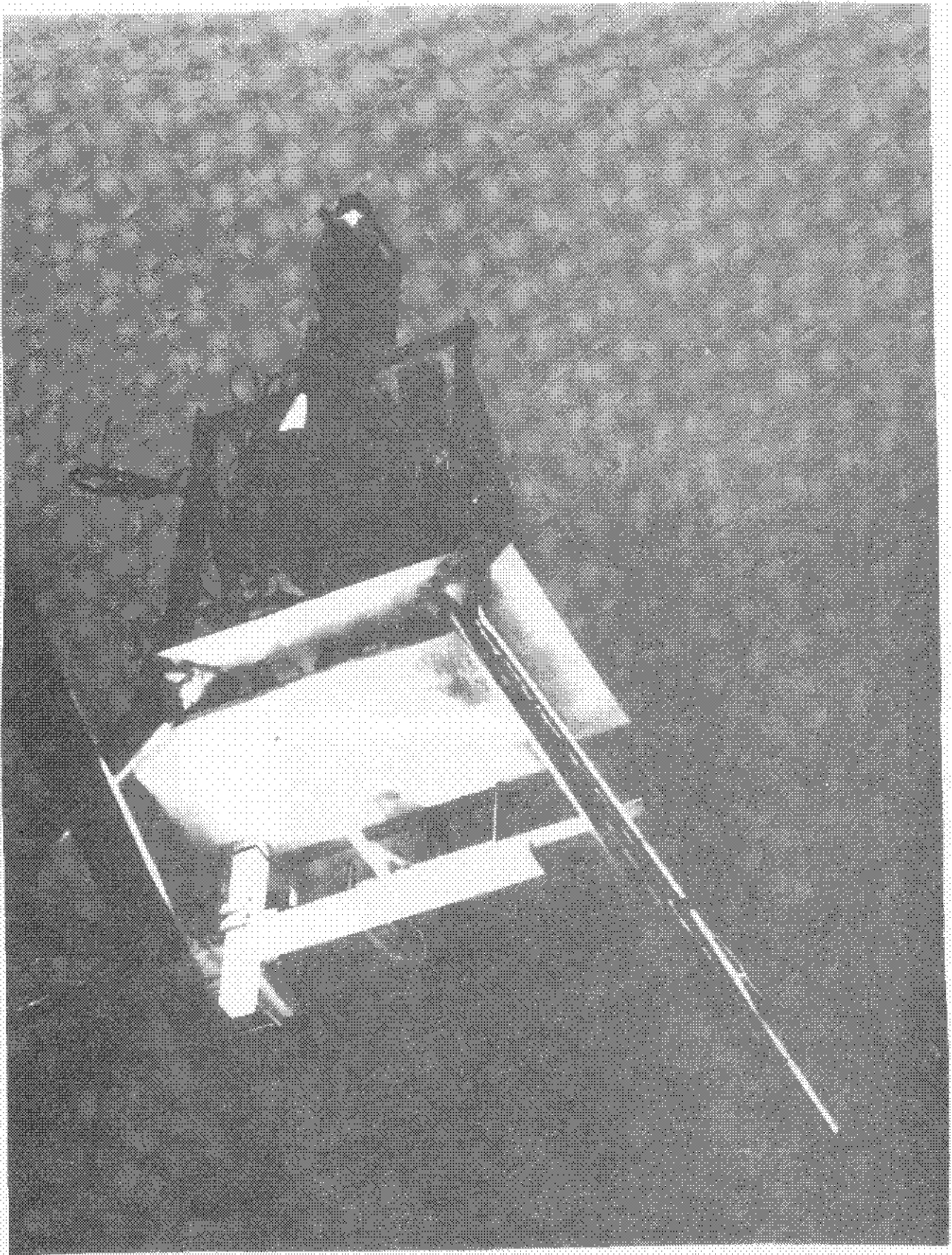
Figure 9. Flux Rake Sweeping Across Focal Plane

FIGURE 10. FLUX RAKE OPERATING RANGE X = 34" Y = 28"

BAR POSITION SIGNAL (VOLTS)

BAR POSITION (INCHES)

SENSOR BAR

11" DIA RECEIVER APERTURE

29 FLUX SENSOR LOCATIONS AT 1.00 INCH SPACING

16 FLUX SENSOR DATA CHANNELS AVAILABLE

21
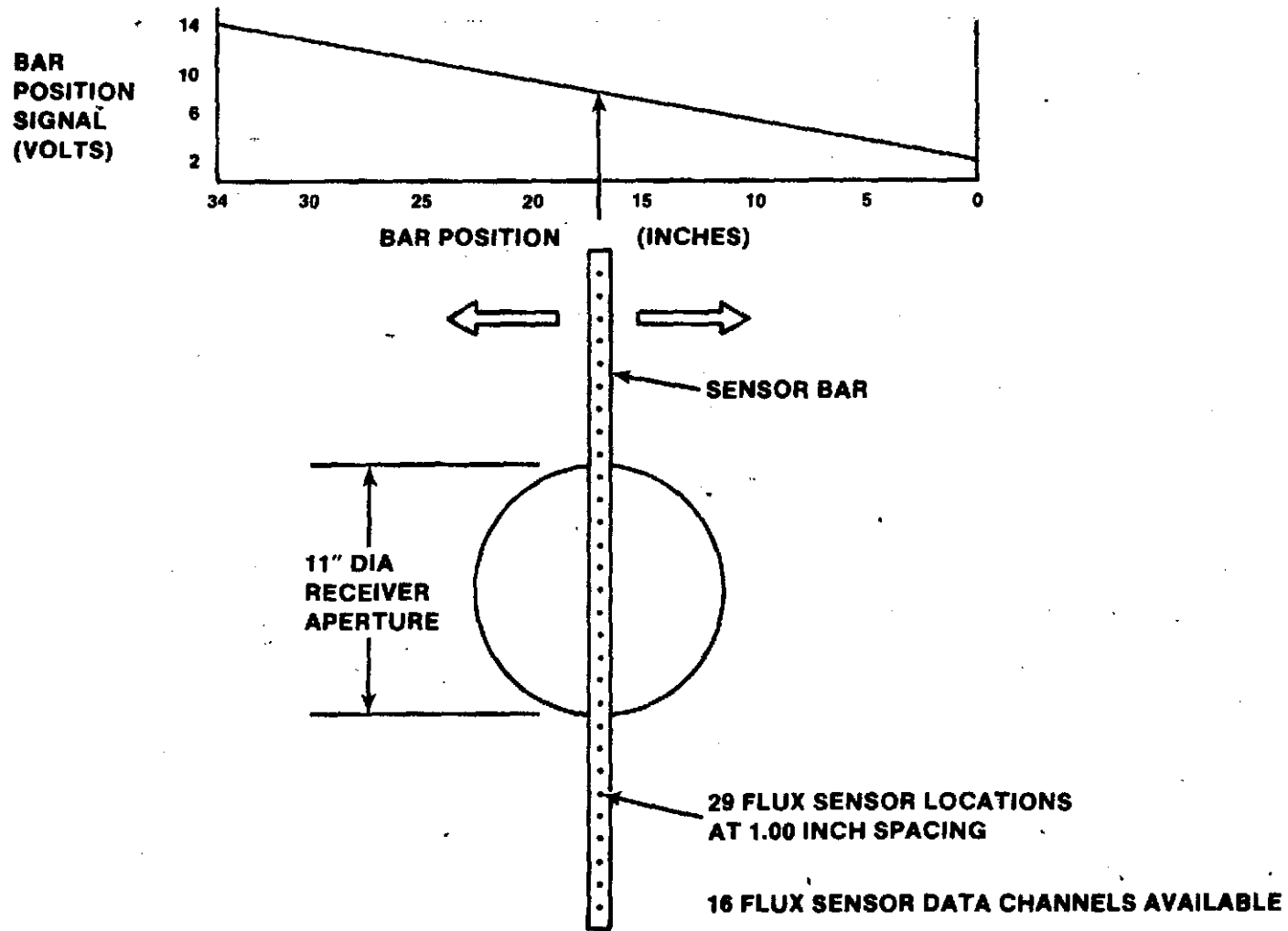
of .06 to 0.6 inches per second. The bar position is indicated by a linear voltage output from a precision potentiometer coupled to the drive actuator.

Output signals from the flux rake are as follows:

o   Sixteen flux sensor data channels.

o   Bar traverse position

o   Cooling water temperature in the sensor bar.

The entire flux rake assembly is clamped to a 40-inch long by 4-inch square aluminum tube, which is mounted on the interface frame parallel to the optical axis. This permits the plane swept by the flux rake to be adjusted from 12 inches ahead of the focal plane of the concentrator to 2 inches behind the focal plane, as shown in Figure 11. It as intended that the flux rake should be operable 6 inches behind the focal plane but interference with one of the concentrator tripod legs prevented this.

The entire flux rake, including the flux sensor bar, is painted with a high temperature silicon base paint with a 90% solar reflectance. However, to permit the flux rake to be traversed very slowly across the aperature, or stopped in the flux without overheating, it was necessary to provide water cooling. This was accomplished with a small circulating pump, a long, narrow water storage tank which also serves to shield the drive assembly from accidental exposure to the focused energy, and a small radiator and cooling fan. The pump and fan are controlled from the ground.

Figure 12 shows the flux rake control and data logger set up in the instrumentation trailer. The control panel contains the switches for powering up the system, turning on the circulating pump and fan, and reversing the bar sweep direction, along with the speed control potentimeter. A meter indicating bar position is located above the panel.

The 16 flux sensor outputs, plus the bar temperature and bar position sensor outputs, were hard wired to a Fluke data logger where they were digitized, multiplexed, and recorded on one channel of a Columbia Data Products instrumentation tape recorder.

Flux Measurement Error Analysis

The flux rake measurement of the concentrator intercept factor, distribution and integrated power are subject to the following three classes of error:

22

FIGURE 11. FLUX RAKE SENSOR BAR POSITIONING LIMITS

UP TO 12" AHEAD OF FOCAL PLANE

3" MIN AHEAD OF FOCAL PLANE WITH RECEIVER IN PLACE

AT FOCAL PLANE WITHOUT RECEIVER

2" MAX BEHIND FOCAL PLANE WITHOUT RECEIVER

RIM ANGLE (~ 90°)

APERTURE

23

101/08074-30
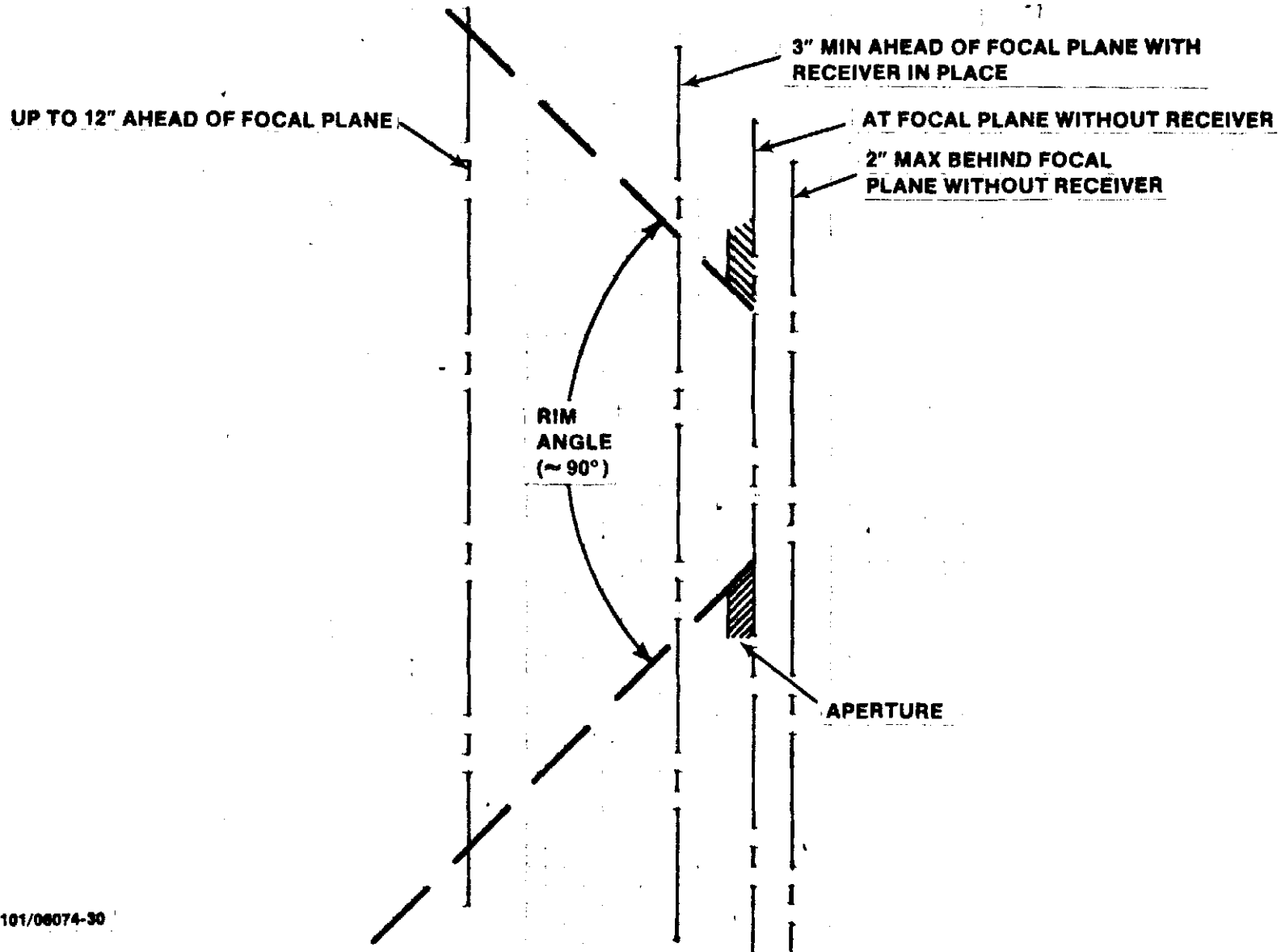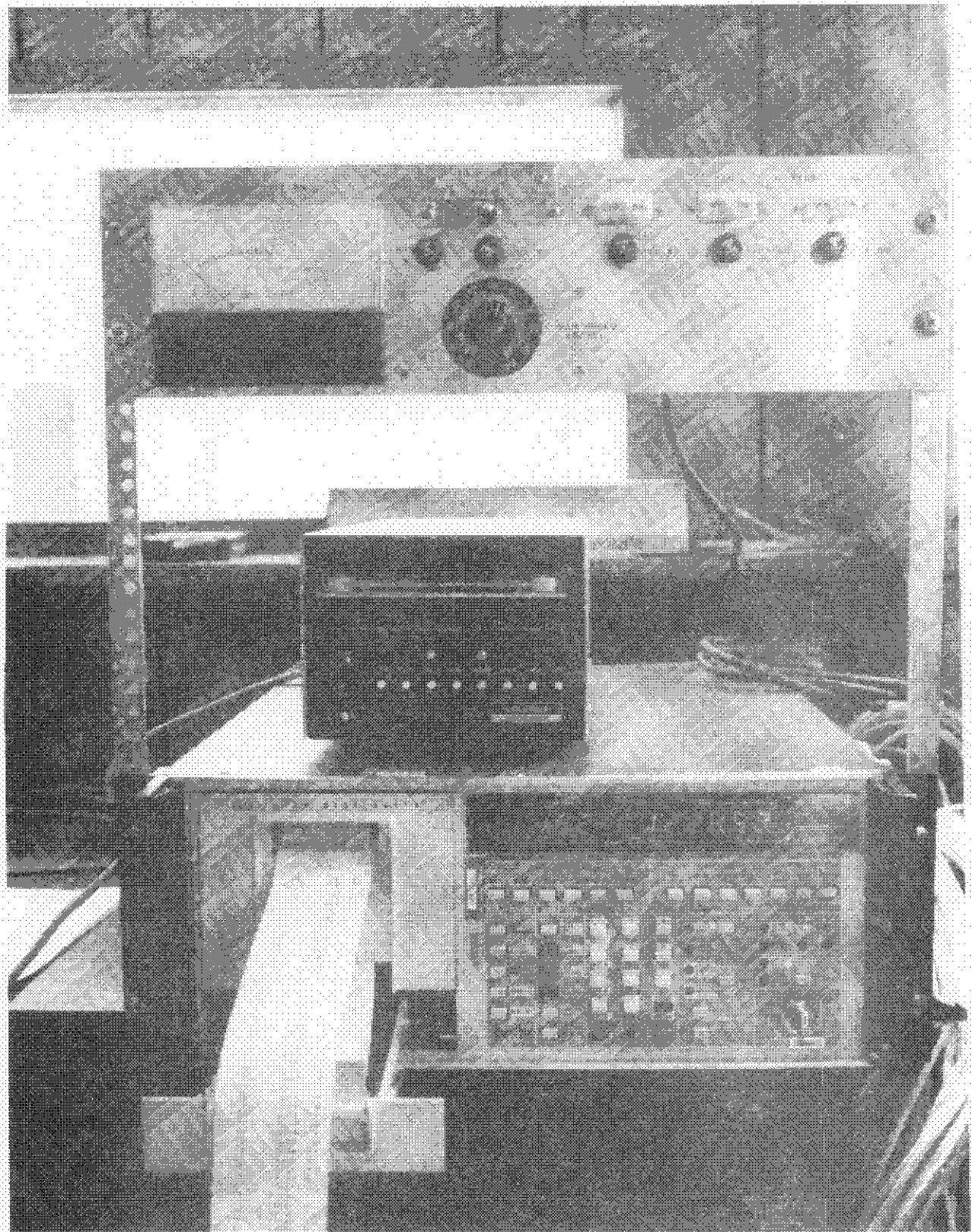
Figure 12. Flux Rake Control and Data Logging Setup

a. Measurement system accuracy errors
b. Dynamic response induced errors
c. Data point density induced errors

a. <u>Measurement System Accuracy</u> includes the calibration and operating errors of the flux sensors and the data transmission logging, recording and processing system. Figure 13 is a block diagram of this system. Effectively all of the system errors are in the analog portion of the system and these are dominated by the flux sensor calibration error, as shown in the following table:

ERROR SOURCE	ERROR AS A PERCENT OF SIGNAL	FIXED ERROR AS A PERCENT OF FULL SCALE
FLUX SENSOR CALIBRATION	2.5%	0
FLUX SENSOR REPEATABILITY	0	0.5
TRANSMISSION LINE LOSS	0	0
TRANSMISSION LINE NOISE	0	0
DATA LOGGING SYSTEM	0.03%	.04

TOTAL MEASUREMENT SYSTEM = 2.53% OF SIGNAL PLUS 0.54% OF FULL SCALE

The calibration error of the Hy Cal flux sensor is primarily the cumulation of calibration errors in the traceability of their instrumentation to the National Bureau of Standards (NBS). The 0.5% of full scale sensor repeatability error is added to the 2.5% calibration error.

Transmission lines from the flux sensors to the data logger are #22 twisted shielded pairs with grounded shields. The transmission line loss is two orders of magnitude less than the signal and hence a negligible error source. Some very high frequency noise was present on the signal lines, but this was effectively removed by the low pass filters on the data logger.

The data logger system errors listed above are for within one, year of calibration and an operating temperature range of 15 to 35 degrees. Our unit was factory calibrated within six months of our testing and was operated within the indicated temperature range.

b. <u>Dynamic Response Induced Errors</u> can result when the rate of change in flux approaches 10X the time constant of the flux sensor. To minimize this effect, the sensor bar sweep rate was kept low, which results in a reduced rate of change of signal as the bar traverses the flux gradients. Figure 14a qualitatively indicates that dynamic response induced errors were negligible, as there is essentially no

Figure 13. Block Diagram of Flux Measurement System
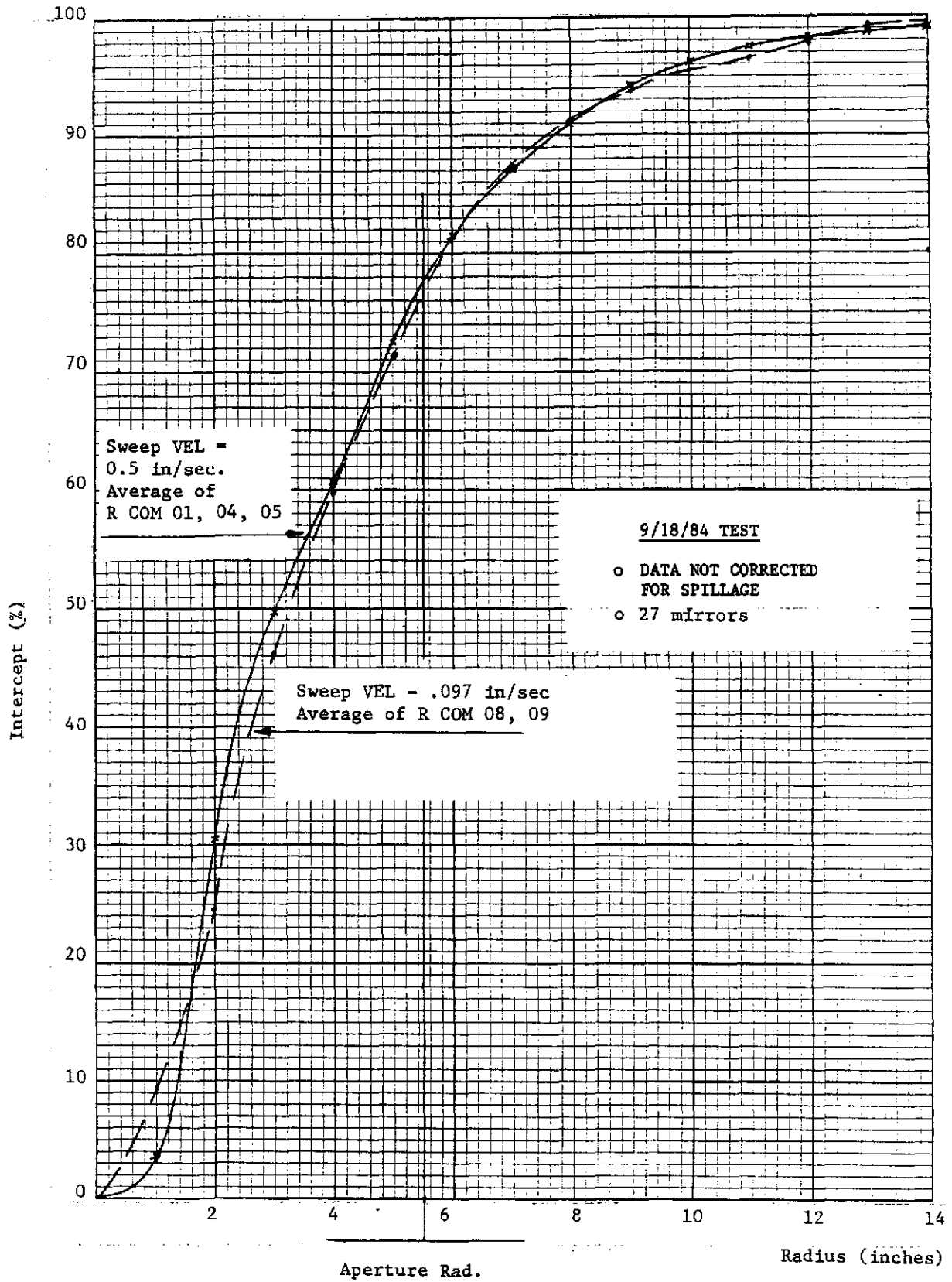
Figure 14a. Flux Sweep Rate Did Not Affect Data Accuracy

The following text appears within the figure:

Y-axis: Intercept (%)

Sweep VEL =
0.5 in/sec.
Average of
R COM 01, 04, 05

Sweep VEL - .097 in/sec
Average of R COM 08, 09

9/18/84 TEST

o DATA NOT CORRECTED
FOR SPILLAGE

o 27 mirrors

Aperture Rad.

Radius (inches)
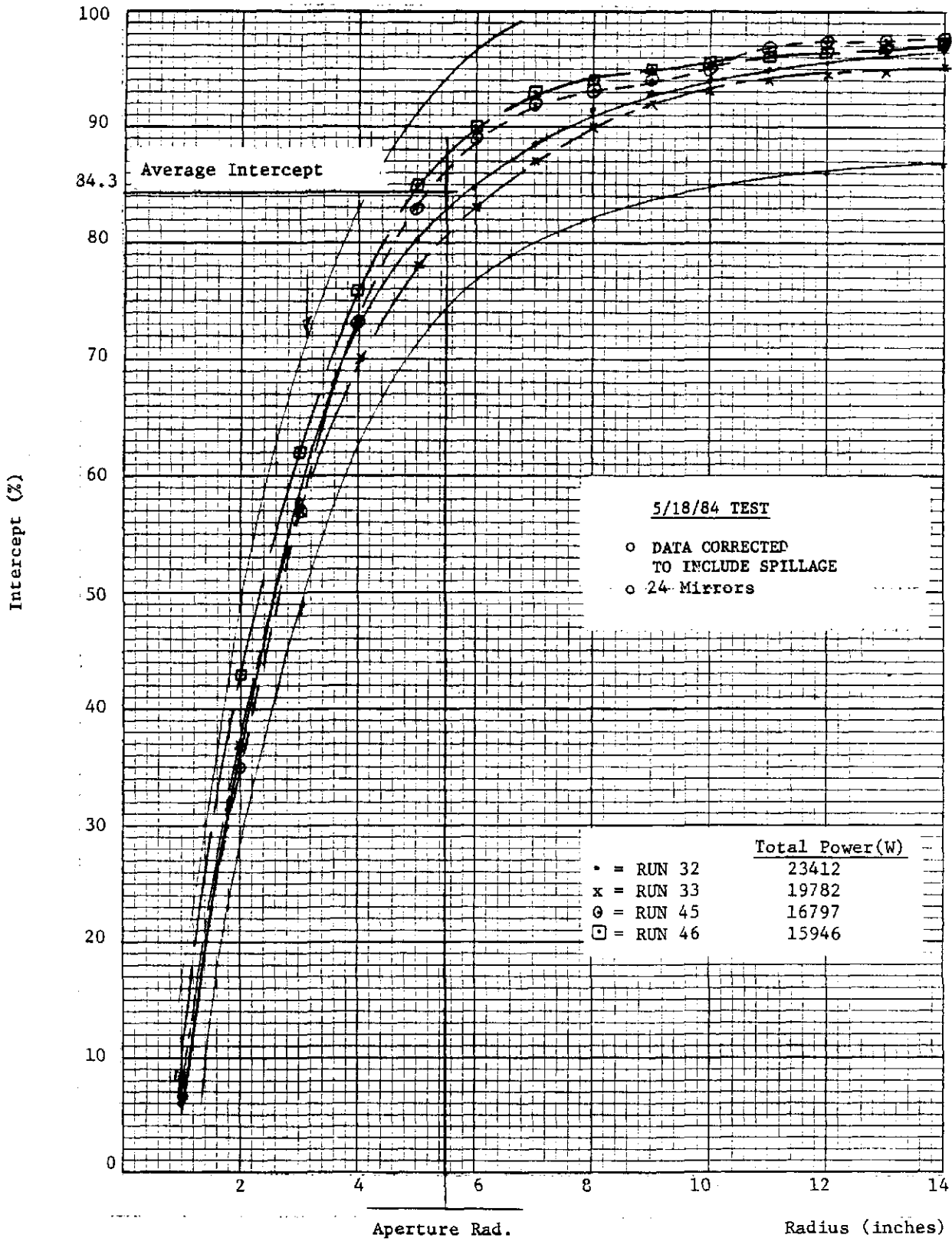
Figure 14b. Intercept Vs. Radius for LEC 460 Concentrator

The figure shows a plot of Intercept (%) versus Radius (inches). The vertical axis is labeled "Intercept (%)" ranging from 0 to 100, with a marked value at 84.3 labeled "Average Intercept". The horizontal axis is labeled "Radius (inches)" ranging from 2 to 14, with "Aperture Rad." marked near 5.5.

Legend box:
5/18/84 TEST
o DATA CORRECTED TO INCLUDE SPILLAGE
o 24 Mirrors

		Total Power(W)
• =	RUN 32	23412
x =	RUN 33	19782
⊕ =	RUN 45	16797
⊡ =	RUN 46	15946

Figure 14c. Intercept Vs. Radius for LEC 460 Concentrator

difference between the averaged data at the normal sweep speed of 0.15 in/sec and that taken 35% slower at 0.097 in/sec.

To look at this quantitatively, we determined the lag error that would result from the maximum observed increase in flux (1600 kW/M²) in a single data sampling interval (7.14 sec), assuming a linear increase in flux. Figure 15 illustrates this case and shows how the sensor output will lag the actual flux level due to the sensor time constant. A calculation of the worst case sensor lag error, E, is also presented:

The flux sensor responds as a low pass, first order system. Its response to a linear increase (or decrease) in flux is given by the following relationship.

$$f = F \left[1 - \frac{\tau}{T} (1 - e^{-T/\tau})\right]$$

Where T = Time between data samples (sec)
       F = Linear increase in flux over time T (kW/m^2)
       f = Increase in sensor output over time T (kW/m^2)
      τ = Flux sensor time constant = .05 sec
      E = Sensor lag error = (F - f) kW/m^2

For T = 7.14 sec
and F = 1600 kW/m^2.

f = 1589 kW/m^2

and the sensor lag error, E, is F-f = 1600 - 1589 = 11 kW/m^2 or 0.7% of the change in flux level for that data point.
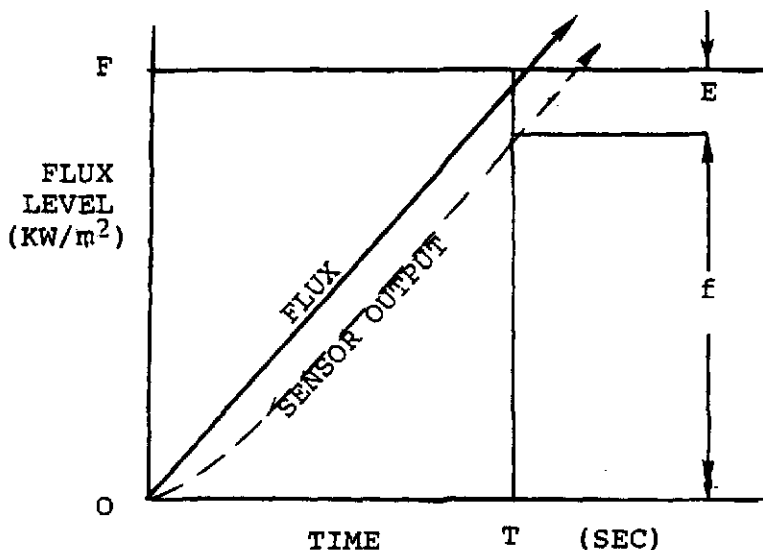
Figure 15. Flux Rake Dynamic Response

30

It can be seen that the magnitude of a dynamic response induced error is proportional to the rate of change in flux at the time a sensor is being sampled. The effect is to cause that data point to be higher (or lower) than the actual flux level by the amount of lag. Selecting a very high rate of change example of flux distribution test data we determined that:

o   Less than 3% of the data points in any run showed a change in flux of more than 400 kW/m^2, or 0.175% error.

o   The steeper flux peaks are relatively symmetrical so that minus error on increasing signals will be nominally offset by plus error on decreasing signals.

We thus conclude that sensor lag error has a negligible effect on the data be it affects only a very small part of the data to an insignificant degree.

C.   Insufficient Data Point Density appears to be a significant error source in the flux rake data. The effect is for each sensor to record apparent variations in flux level from run to run due to it being sampling at different points along its traversing path on each run and due to shifts in the position of the flux pattern due to flexibility in the concentrator structure. This effect is more noticeable in the regions of sharp flux gradients, where a small change in flux sampling location can register a significant change in flux level.

This condition could be improved by increased or continuous data sampling for each sensor and more sensors along the bar. Both options are feasible but were too costly to implement on this program.

The data from most runs indicated that there was a small amount of flux (called spillage) outside the swept area of the flux rake and therefore not included in the total power computed for the run. The data for Figure 14b and 14c were corrected for this effect by extrapolating the missing energy on each run and including it with the measured data.

CONCLUSIONS

The great reduction in full scale error in the second data set results from the use of lower range flux sensors operating at closer to full scale. This proportionally reduces the effect of the dominant .54% of full scale error factor. The relatively wide range of total power in each data set could be further reduced by increasing the data point density.

For the second data set, (9/18/84 tests) three mirrors were added to the periphery of the original 24 mirror set to increase the solar input. These mirrors were thus furthest from the optical axis, causing a larger percentage of spillage at the aperture. The result was slightly increased total power but reduced intercept factor.

3.2.2   CONTROLS CHECKOUT PROCEDURES

The controller provides seven modes of engine operation: start, idle, fossil, hybrid, solar, shutdown, and emergency. The mode menu and internal flags prevent illegal mode transfers. For example, the system (at rest) must sequence through at least start and idle before it can go to solar. Alternatively it can enter solar from hybrid. The system will not accept a solar command while in the shutdown or start mode. Several such disallowed transfers are defined to assure safe and conservative engine operation. The key characteristics of the seven modes are shown in the Table 2.

Integration of the software went exceptionally well. A very major subset of the package and water was the User Interface Module. A large volume of software was required to provide user-friendly menus and interactive response along with continuously updated data displays.

A second module of the software was the heart of the controller. Described as creating a finite state machine, the control module software monitored many internal state flags, allowed only legal mode transitions, kept an ever watchful alert for operator input from the keyboard and for fault signals from the engine, and provided active control to the throttle and inverter when appropriate. Integration of this module went smoothly and engine control was always safe and predictable.

The third software module, the concentrator communications module, eventually worked properly, but its integration was vexsome. The difficulty arose from the very fluid and poorly supported concentrator software package. This difficult situation was a consequence of the concentrator vendor's own intense effort to make their first field installation of 700 concentrators work within a very tight schedule. The concentrator control hardware itself was developmental and numerous minor hardware faults necessitated software changes. The changes were implemented to meet new hardware requirements or to bypass problems. After frequent management level communications between Sanders and LaJet necessitated which new and uncharted limits of forbearance were explored), an adequate level of software support was provided by LaJet and the module was completed and successfully tested.

32

TABLE 2. CONTROLLER REQUIREMENTS AND MODE FUNCTIONS

	ENTER FROM:	ACTUATE TIME SEQUENCER	SHUTDOWN VALVES	COMBUSTOR ON	ACTIVE SPEED CONTROL	ACTIVE LOAD CONTROL	THERMAL CONTROL BY FACETS	DISH TRACKING	REMARKS
START	ONLY WHEN STOPPED	YES	NO	YES	YES	NO INVERTER OFF	NO	NO	SHIFTS TO IDLE AFTER SPEED REACHED
IDLE	START FOSSIL	NO	NO	YES	YES	NO, INVERTER OFF	NO	NO	AFTER ENTRY NO SHIFTS FOR 2 MINS. EXCEPT TO SHUTDOWN OR EMERGENCY
FOSSIL	IDLE HYBRID	NO	NO	YES	YES RAMPS TO SET POINT	YES	NO	EITHER	NO SHIFT DURING RAMP EXCEPT TO SHUTDOWN OR EMERGENCY
HYBRID	IDLE FOSSIL	NO	NO	CYCLES AS REQUIRED	YES	YES	YES-IF COMBUSTOR OFF	YES	
SOLAR	IDLE HYBRID	NO	NO	OFF	NO	YES	YES	YES	
SHUTDOWN	ANY MODE ANYTIME	NO	YES	OFF	NO	NO	NO	OFFSET	
EMERGENCY	ANY MODE ANYTIME	NO	YES	OFF	NO	NO	NO	OFFSET	<ESC> FOR SINGLE KEY_ENTRY AUTOMATICALLY W/HAULT SIGNAL

3.2.3 ENGINE LEAK TESTS

The engine test was performed separately on the following four engine components:

1. Turbine exhaust cone piston ring
2. Heat sink
3. Compressor
4. Recuperator

All leak tests on the PCA were performed by maintaining a vacuum of 7.1 PSIA in the components being tested while measuring the flow rate required to maintain this pressure. To locate the leaks, the units were pressurized at 2-3 PSI above atmosphere and sprayed with a soap and water solution. Leaks were indicated by bubbles. To determine the leak rate for individual leaks, a 7.1 PSIA vacuum was again applied to the unit and the flow rate measured. An individual leak area was then sealed using "mastic" and tape, and the reduced flow rate was measured. The individual leak rate was then determined was by subtraction. The results of these leak tests are as follows:

ENGINE LEAK TEST RESULTS

COMPONENT	LEAK RATE
1. Piston Ring (Figure 16)	0.06 lb/min
2. Compressor (Figure 16)	0.08 + lb/min
3. Heat Sink (Figure 17)	0.23 + lb/min
4. Recuperator	0 + lb/min

1. Piston Ring - The 0.06 lb/min leak was located around the piston ring which allowed for axial expansion of the engine relative to recuperator.

2. Compressor - The 0.08 lb/min leak was located around the compressor mounting flange.

3. Heat sink - The heat sink leaked at many areas, the wosrst of which was a counter located on the fiberglass outlet duct which had apparently broken through the wall of the duct. This leaked at a rate of about 0.094 lbs/min. Other locations on the heat sink which leaked were the vacuum start hose connector pipe flanges and cap, bolt heads on fiberglass plenum, fiberglass to heat exchanger core gasket, 1 1/4" aluminum pipe fitting to fiberglass, etc.

4. Recuperator - The leak rate of the recuperator was too low to be measured the Meriam 50MW20-1. A vacuum of 7.1 PSI was sealed into the unit and only a slight increase in pressure

Piston Ring Leak

Receiver

35

Bellows

Compressor Leak
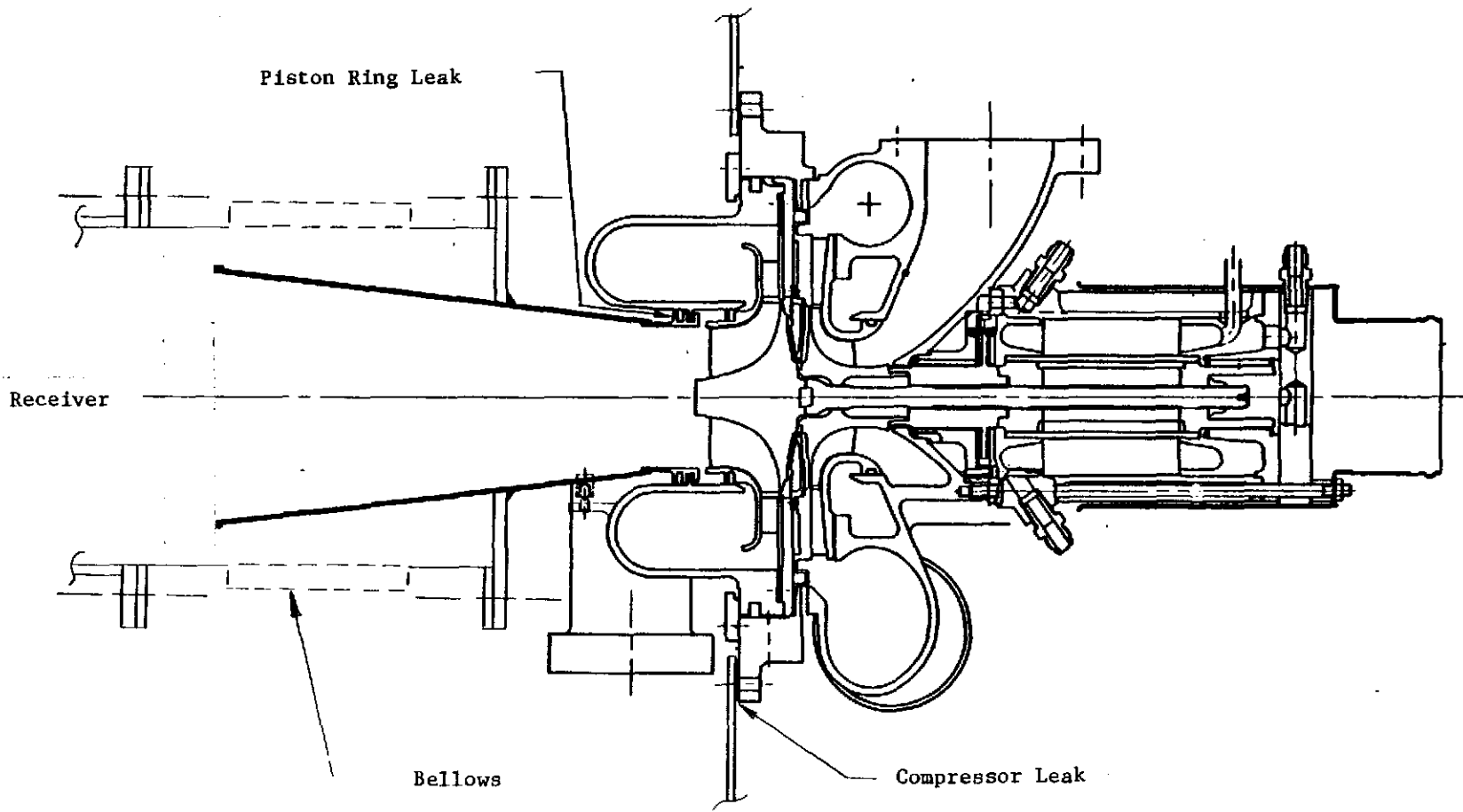
Figure 16. Engine Leak Locations

SINK HEAT EXCHANGER

31 IN.
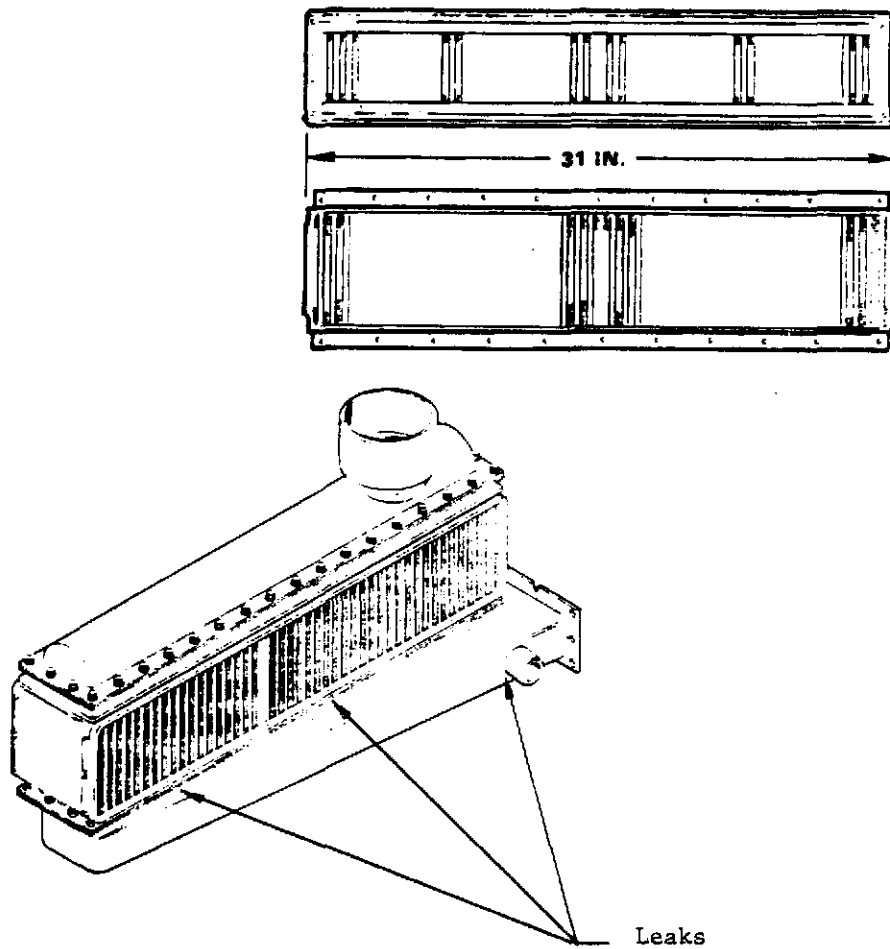
Leaks

Figure 17. Heat Sink Exchanger

36

was observed over a five minute period. A Schematic of the engine leak test set-up is presented in Figure 18.

3.2.4   RECEIVER LEAK TEST

A series of tests was performed on the Sanders receiver to locate any leaks and to determine their leak rate. We then evaluated the impact of the leaks on receiver efficiency.

The receiver was operated for a total of 68 hours preceding the tests. This operating time consisted of about eight hours using the Sanders preheater, eight hours in a hybrid mode using both the Sanders preheater and solar energy, 16 hours using the Garrett engine, and 36 hours in a hybrid mode using the Garrett engine and solar energy.

The first group of tests were performed at vacuums of 1, 2 and 3 inches of water below atmospheric pressure. These are tests #1-5, 7, and 10 in Table 3. Figure 19a illustrates the vacuum test setup. Three inches of water is the lowest normal operating vacuum seen by the receiver, and it produced the greatest leak rate (0.63 lbs air/min) of the subatmospheric pressure tests performed, as shown in test #1 in Table 3. After blocking the leak paths indicated by - numbers 2, 3, 4 and 5 in Table 3 and illustrated in Figure 19c, the leak rate was reduced to 0.21 lbs/min. as shown in test 5 in Table 3.

The second group of tests were run at pressures of 2, 3 and 4 inches of water above atmosphere. (Refer to tests 6, 8 and 9 in Table 3 and the pressure test setup illustration in Figure 19b). The maximum leak rate was 0.71 lbs air/min. as shown by test #9 at 4" of water, which is the highest normal operating pressure reached by the receiver. After blocking the leak paths as previously described, the leak rate was reduced to 0.27 lbs/min. (test #8). A further reduction in leakage was not pursued at this time.

Only minor design changes appear to be necessary to permanently correct the leaks discovered and temporarily sealed during these tests. More assembly fasteners in the flange areas, more hold downs for the quartz window, and improved gasketing techniques will reduce the leakage to below the levels attained during this test.

3.2.5   COMBUSTION AIR THROTTLE

Late in the DTM testing, Sanders discovered a second unrestricted flow path into the combustor. A throttling butterfly valve was fabricated and installed to control this air inlet. The purpose of this modification was to limit the ingestion of ambient air while in the "solar-only" mode of operation. The valve remained open while in the fuel mode since the combustion air requirements had to be satisfied.

37

Compressor Exhaust
Sealed

7.1 PSIA
For All Tests

Recuperator

Turbine Inlet
Sealed

Heat Sink

System Pressure

Meriam ΔP

INCLINED MANOMETERS

Vacuum

Meriam
50 MW 20-1
Flow Meter

Control
Valve
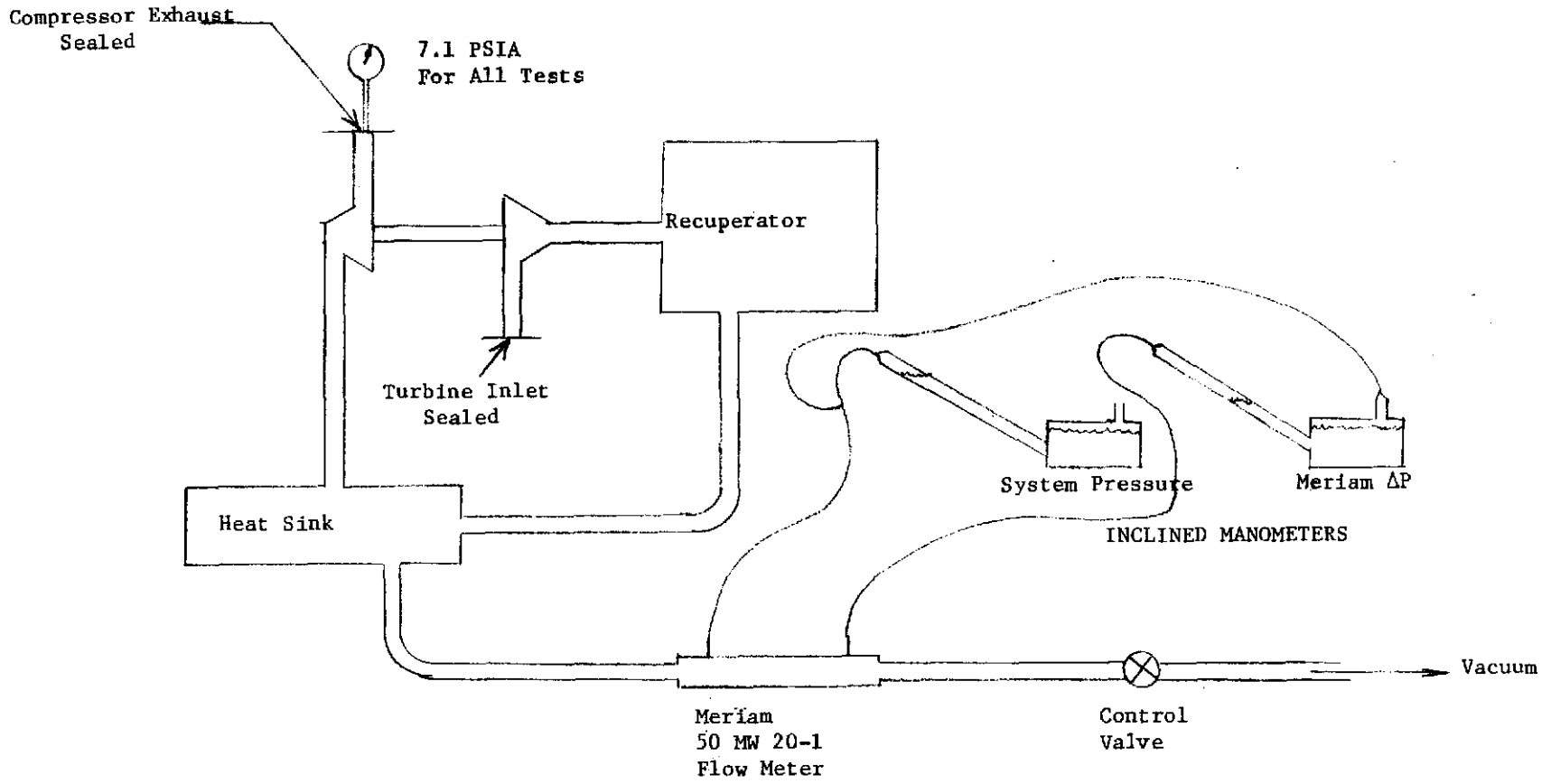
Figure 18. Engine Vacuum Leak Test Setup

MERIAM
INLET
PRESSURE

MER ΔP

RCVR P

PDME SOLAR RECEIVER

TO VACUUM TANK

MERIAM Model 50MW 20-1
Flow Meter

1" ID x 20" L

39
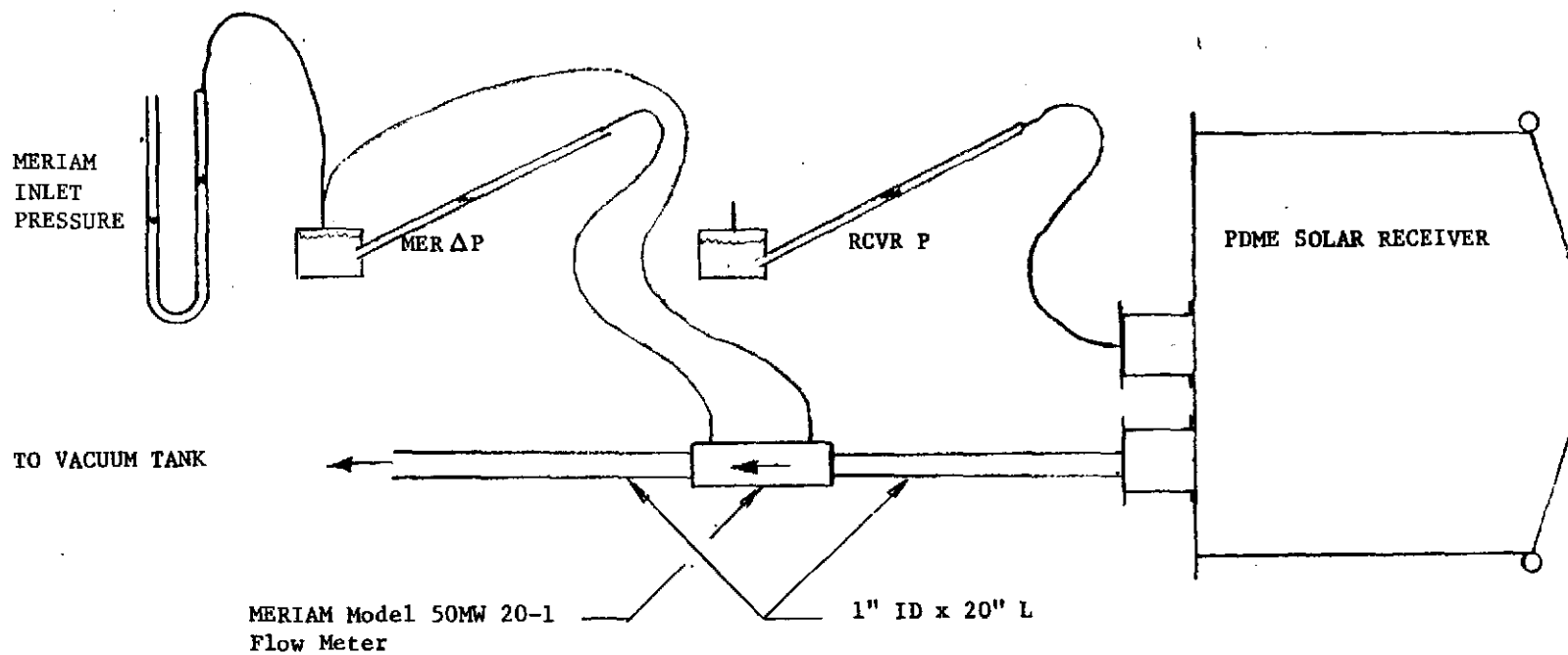
Figure 19a. Solar Receiver Vacuum Leak Test Setup for Tests 1 to 5, 7
+ 10 Conducted 9/84

MERIAM
INLET
PRESSURE

MERIAM
ΔP

RECEIVER
PRESSURE

DTM SOLAR RECEIVER

40

FROM PRESSURE TANK

MERIAM MODEL
50 MW20-1
FLOW METER

1" ID x 20" L
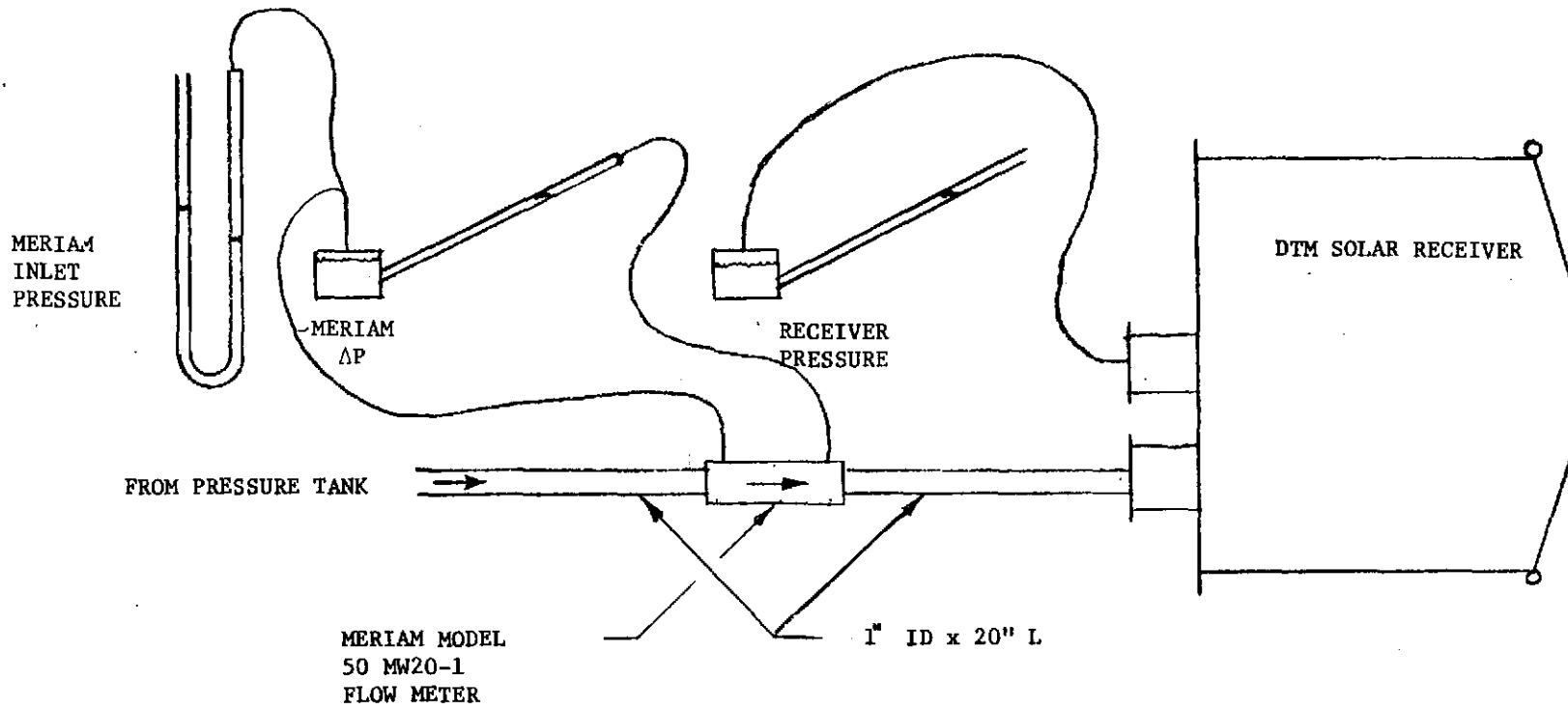
Figure 19b.   Solar Receiver Pressure Leak Test Setup for Tests 6, 8 +
9, Conducted 9/84
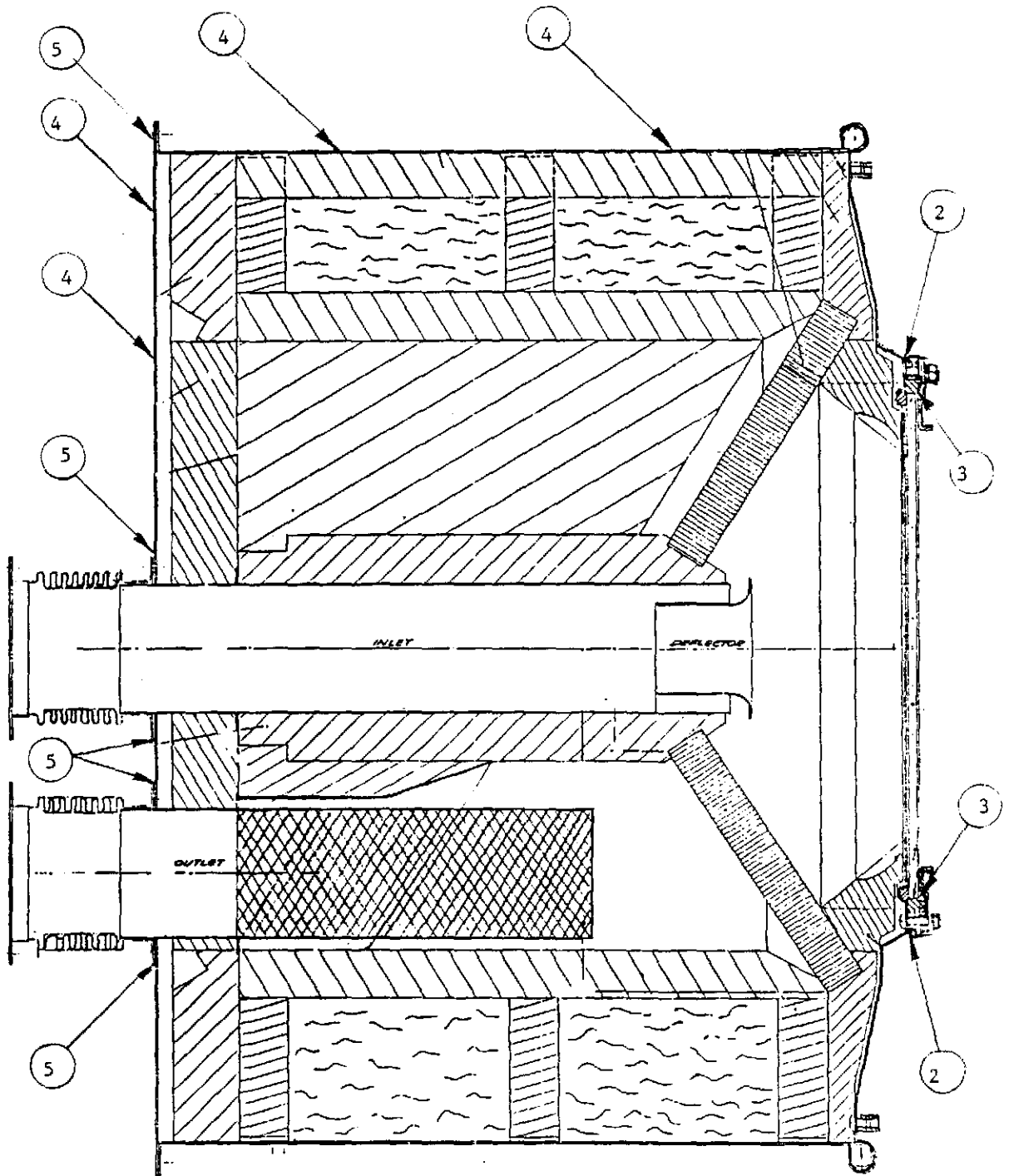
N = Leak sealed for test number indicated

Note: Unless otherwise indicated in Table 4 the sealing material was left in place for the succeeding test

Figure 19c.   Location of Receiver Leaks.   Leak Tests
                2,3,4 and 5

TABLE 3.
RECEIVER LEAK TEST DATA

Tests performed from 9/24/84 to 9/27/84

TEST #	MODE	DESCRIPTION	RCVR P	AIR °F	MERIAM ΔP	MER. INLET PRESS.	MERIAM CFM	MASS FLOW	
1	VACUUM	As removed from conc. concentrator mtg. bolts not in place	-1.00	66.00	3.95	-0.50	4.00	0.30	
			-2.00	67.00	6.65	-1.10	6.55	0.49	
			-3.00	68.00	8.85	-1.70	8.45	0.63	← V
2	VACUUM	Seal Item 6 to 7 of 4029102 Receiver (Drumhead to Ring)	-1.00	70.00	3.90	-0.50	3.95	0.30	
			-2.00	70.00	6.43	-1.05	6.35	0.47	
			-3.00	70.00	8.68	-1.65	8.32	0.62	
3	VACUUM	Full window seal to Drumhead Item 7 to 11	-1.00	75.00	3.55	-0.50	3.60	0.27	
			-2.00	76.00	5.80	-1.05	5.75	0.42	
			-3.00	77.00	7.65	-1.65	7.40	0.55	
4	VACUUM	Plugged 2 .1 Dia. holes in drum & 2 .1 Dia. holes in rear cover	-1.00	81.00	3.20	-0.50	3.25	0.24	
			-2.00	81.00	5.12	-1.00	5.12	0.37	
			-3.00	81.00	6.76	-1.60	6.63	0.48	
5	VACUUM	Sealed inlet & exhaust flanges, TC feed thru, rear cover to drumbolts, RCVR - conc. mtg. bolts	-1.00	93.00	1.28	-0.45	1.32	0.09	
			-2.00	93.00	2.20	-1.00	2.28	0.16	
			-3.00	93.00	2.90	-1.50	2.97	0.21	← V
6	PRESS	Preliminary + P test	2.00	102.00	2.05	1.95	2.12	0.15	
7	VACUUM	Duplicate #5 except remove seal from RCVR inlet flange	-1.00	86.00	1.40	-0.45	1.46	0.11	
			-2.00	86.00	2.30	-1.00	2.37	0.17	
			-3.00	86.00	3.06	-1.50	3.12	0.23	
8	PRESS.	Duplicate #7 except + pressure	2.00	86.00	2.20	2.00	2.07	0.15	
			3.00	85.00	3.00	3.00	3.06	0.22	
			4.00	84.00	3.60	3.80	3.65	0.27	← P
9	PRESS.	Remove all ductseal and tape, Duplicates as mtd. on concentrator	2.00	85.00	4.83	3.40	4.85	0.36	
			3.00	84.00	6.80	4.80	6.66	0.49	
			4.00	82.00	9.60	7.00	9.18	0.71	← P
10	VACUUM	Same configuration as #9	-1.00	60.00	2.74	-0.48	2.80	0.21	
			-2.00	60.00	4.78	-1.05	4.78	0.36	
			-3.00	60.00	6.45	-1.58	6.35	0.48	

TABLE 3. THESE TESTS WERE CONDUCTED AT ROOM TEMPERATURE UNDER QUASI STATIC CONDITIONS. THE FLOW WAS MEASURED WITH A CALIBRATED PRESSURE DROP FLOW METER (ΔP MER), ALL PRESSURE (P) IN INWC (INCHES WATER COLUMN), MASS FLOW IN LBm/min.

42

Our post-test inspection of the hardware revealed that the partitioning of the recuperator for preheating makeup air for combustion had apparently been based on the assumption that the engine performance would meet its original high efficiency goals of about 30% (fuel to shaft). When the hardware was originally designed and fabricated, AiResearch expected a fuel flow that was a factor of two or three below what was ultimately needed to deliver the rated shaft power. This error lead to an inadequate allocation of makeup air flow. Thus the portion of te recuperator partitioned for preheating makeup air was only capable of intaking less than half the volume required by the combustor to deliver rated shaft power.

The preferred solution would have been to move the partition in the recuperator to provide more flow area for preheating the make up air. The simpler option was to decrease the resistance of the make up air flow path to the combustor without changing the original recuperator design. AiResearch chose the latter alternative. Over the course of their testing, a relatively large hole was put through the plenum wall to allow fresh air to directly enter the combustor without preheating. It was this air supply which was regulated by the add-on combustion makeup air throttle valve.

The combustion makeup air throttle valve consisted of a butterfly disk closely fitted to the ID of the 5" diameter air inlet pipe, and a unidirectional motor actuator. An external pointer indicated the position of the flapper. To close the valve, power was applied to the actuator until the valve reached the desired position. At the conclusion of testing, the valve was manually reset to the open position for the next test.

3.2.6   DESCRIPTION OF MIRROR FOCUSING PROCEDURE

Initially, all facets were roughly focused by setting the vacuum orifice to protrude through the aluminum facet hub by about 3/4". Next, a target was mounted in the aperture plane of the receiver. The target was one-inch thick ceraform rigid insulation with a cross of one-inch wide woven ceramic tapes marking its center. This target worked very well and proved capable of withstanding the concentrated flux of the entire concentrator for short periods.

Then the facets were installed on the concentrator and the final focusing adjustment of the vacuum orifice was made to produce the smallest possible spot diameter on the target. The mirror was then aligned to center the spot on the target. Vacuum was applied to only one mirror at a time to eliminate confusion as to which mirror was being focused or aligned.

The first facet to be focused and aligned was used as a reference mirror during the final adjustment of the other mirrors. The

43

reference mirror was focused frequently (vacuum applied) to confirm that the concentrator was properly tracking the sun and to ensure that all mirrors were being aligned to the same point on the target.

3.2.7 RECEIVER ANALYSIS

3.2.7.1 Receiver Thermal Analysis

The objective of this analysis is to advance the receiver technology to the point where receiver design optimization can be accomplished. The DTM receiver is the fifth hot air receiver built and tested by Sanders. Each of the previous receivers was designed for a very different set of concentrator and fling characteristics. Data gathered over this broad set of conditions has demonstrated the survivability of the hardware and the feasibility of the ceramic honeycomb concept. Optimization of the cavity configuration, the window size, and the vessel insulation techniques can only be undertaken after developing and qualifying the analytical tools with which to examine the heat loss mechanisms. This DTM receiver test program has contributed valuable performance data and tested analytical techniques which will be used to develop future receiver designs.

The approach for the thermal analysis of the receiver is outlined in the following five steps:

1. Characterize the heat loss through the insulated vessel over a receiver inlet ai temperature range of $1100^\circ F$ to $1600^\circ F$ by:

   a. Measuring the surface temperature of the vessel at 38 locations.
   b. Applying convection coefficients derived from previous receiver test programs.
   c. Correlating the losses from various surface zones with the internal gas temperature.

2. Analyze the radiative characteristics of the receiver cavity during solar and non solar tests of two internal configurations.

   a. Obtain temperature measurements of the solar absorber and the cavity walls at 26 locations.
   b. Input data into a model which considers the specific geometric and material characteristics of the cavity and derive the transmitted losses.

3. Conduct an energy balance of the quartz window and determine the heat loss associated with the window.

44

a. Measure interior and exterior surface temperatures of the quartz.
b. Analyze thermocouple readings and apply corrections where possible.
c. Implictly predict window temperatures through an energy bale

4. Conduct a total energy balance of the receiver for both solar and non solar test points.

   a. Combine empirical results from steps 1, 2, and 3 to develop a composite heat loss model by summing:

      o Step 1, vessel conduction.
      o Step 2, cavity transmission radiation losses.
      o Step 3, window exterior surface losses.

   b. Calculate the enthalpy drop or rise experienced by the working fluid as it flows through the receiver based on thermocouple and mass flow measurements.

   c. Check the composite heat loss results against the enthalpy rise measurements with the energy input of the concentrator during solar tests.

5. Develop a theoretical model of the solar absorber which considers the thermodynamic, fluid and radiative characteristics of the cavity environment.

   a. Perform similitude measurements of the flow field on the surface on the absorber matrix.
   b. Assume a flux distribution based on Step 4 results.
   c. Correlate theoretical model with thermocouple measurements across the matrix surface.

3.2.7.2 Analysis of Receiver Vessel conduction Losses

The evaluation of heat lost by conduction through the insulated receiver walls was a prime objective of tests conducted on 1/3/84. In these tests, the auxiliary burner and blower assembly was used to preheat the inlet air to temperatures of $1200^{\circ}F$ to $1600^{\circ}F$. The blower supplied air to the preheater at approximately the design mass flow rate.

The methodology developed in this analysis is based upon the testing conducted on the SAGT-1A receiver. In that program, the heavily instrumented receiver included a vast array of thermocouples imbedded at various depths throughout the insulation and on the exterior vessel surface. Special attention was directed towards

45

precisely locating of over 80 thermocouples inside and out. In those areas where applicable, one dimensional (in cylindrical coordinates) conduction analysis between imbedded thermocouple readings allowed the determination of an exterior heat transfer coefficient. At 12 locations around the vessel, natural convection coefficients were calculated. No appreciable difference between the horizontal and vertical surface coefficients was detected when the receiver was mounted horizontally. The investigation was conducted on a range of similar temperatures for wind speeds below 10 ft/S. Results indicate that an average heat transfer coefficient of 2.3 BTU/hr/ft/R is appropriate for the test condition. These previous tests and results are discussed in more detail in an earlier report.[1]

Handbook[2] approximations for the free convection on a horizontal cylinder may yield coefficients of only about half the magnitude of those determined here. The reason for the discrepancy is that radiation, intermittent forced convection effects, and the forced coefficient phenonmen are superimposed in this single value of 2.3 BTU/hr/ft^2/^{o}R. Some dependence on temperature should be considered, but has been omitted in this study because of the limited temperature range under investigation.

Forty-four thermocouples, representing 38 designated areas on the receiver shell, were considered in the DTM receiver heat loss analysis. These area elements encompass the total surface of the rear cover, the cylindrical walls and the front header surface surrounding the window. Thermocouple stations are shown in Figures 20a and 20b. Each type K junction was bonded to the vessel with a very small spot of aluminum filled epoxy to assure good thermal contact. In each of five tests, steady state conditions were verified by when stable temperatures were reached on the outside vessel wall thermocouples. For a burner exhaust temperature of nominally 1200°F, the initial warm-up period was 90 minutes before the rising wall temperature stabilized. Consecutive increments of increasing burner exhaust temperature up to 1600°F were given a stabilizing period of about 40 minutes.

The results of the heat loss analysis were found to correlate with the internal air flow temperatures. Since all enthalpy drop (or rise during solar addition) of the internal flow occurs at the silicon carbide absorber, the receiver can be divided into two isothermal zones. Plotting the calculated heat loss from the front header (excluding window) against the receiver inlet air temperature displays a predictable, nearly linear trend. Similarly, correlation of the
****

1./Thermal Test Report for the SAGT-1A Receiver, Sanders Assoc., 8/11/82.

2./Rohsenow, W, Harnett, J., Handbook of Heat Transfer McGraw-Hill Book Co., 1973.
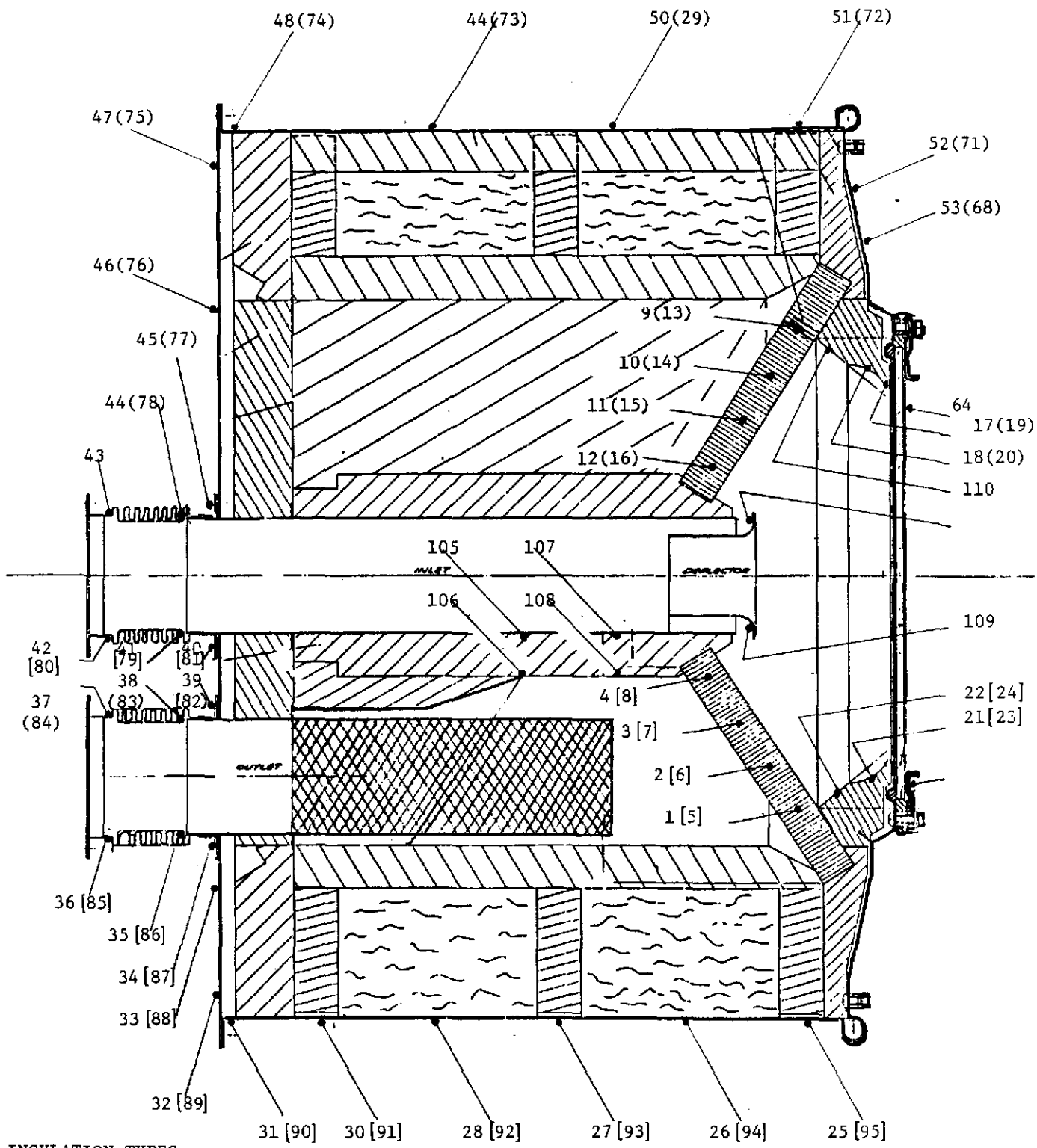
INSULATION TYPES

≋ = Cera Blanket
/// = Cera Form

(xx) rotated 90° toward viewer
[xx] rotated 90° toward viewer

Figure 20a.   Thermocouple Locations on DTM Solar Receiver
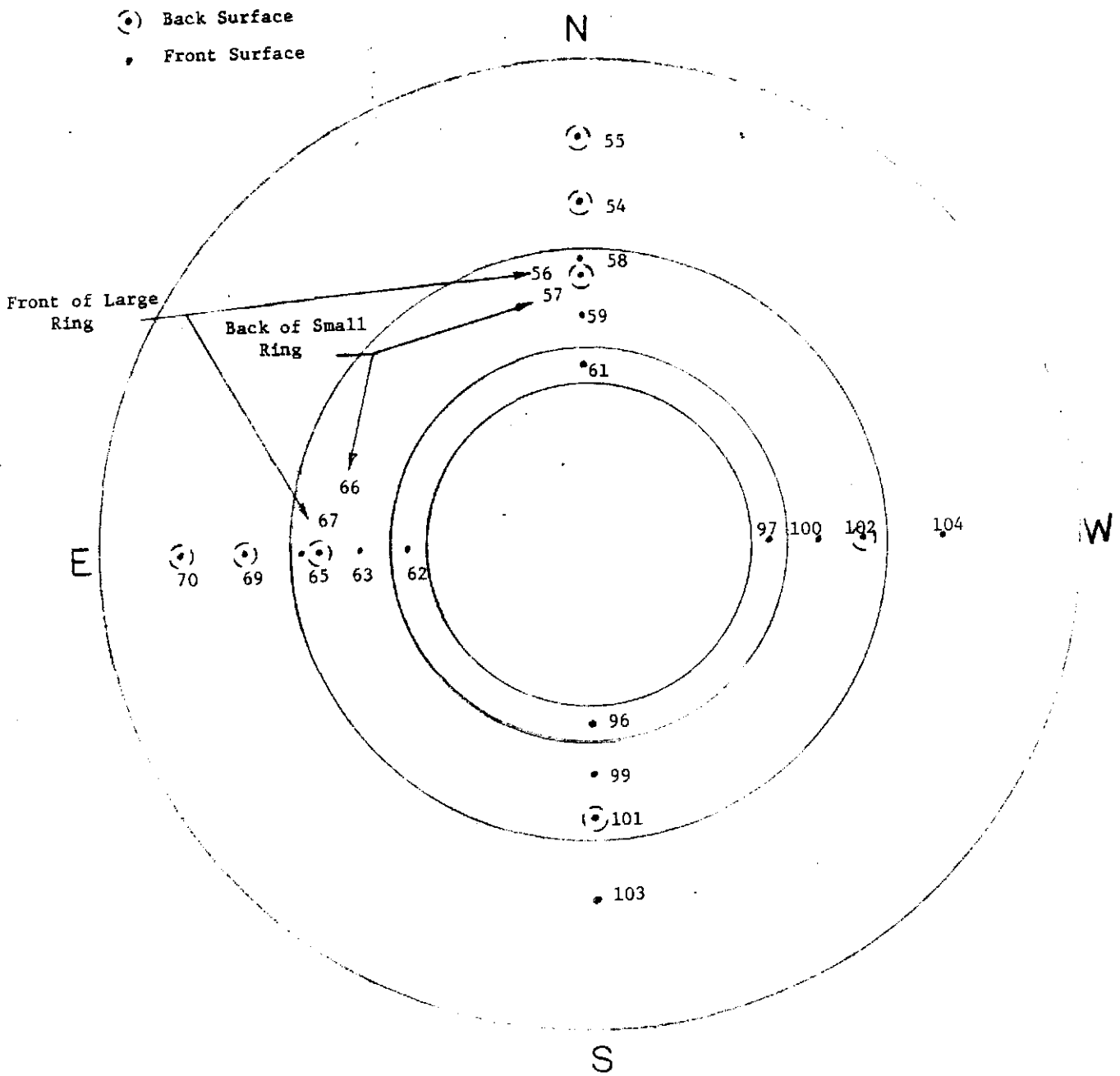
Figure 20b. Thermocouple Locations on Graphite Shield Rings

cylindrical vessel walls and top, behind the absorber plane, with the exhaust temperature is shown in Figure 21. The total convection heat loss is therefore derived by summing the values for the two zones at the appropriate inlet and exhaust temperatures. A temperature linear scaling factor is also applied to adjust the values for the actual ambient temperature.

The principal reason for developing empirical relations relating the vessel heat losses to inlet and exhaust gas temperature is to shift the data acquisition load for subsequent tests. To stay within the limits of the 50 channel data logger utilized throughout this program, the 44 shell-mounted thermocouples had to be given up in favor of instrumentation necessary for the characterization of the rest of the system. The empirical relations incorporated into the composite based receiver loss model are included in Appendix A.

Several important observations have been made as a result of these tests. Heat loss through the receiver walls is excessive, especially in the vicinity of the window and the rear cover. Approximately five times more heat loss is associated with the vessel insulation in this receiver than in the earlier SAGT-1A receiver.[3]

Widely varying hot and cool spots were monitored on the front and rear surfaces of this DTM receiver with a hand-held thermocouple probe. This situation could certainly distort the fixed thermocouple test data intended to represent uniform surface temperatures. While these tests were conducted at an inlet gauge pressure of about 5 inwc, several external leak points were discovered. After this preliminary test (1/3/84), many of the leaks were partially connected by stiffening the bolt circle on the rear cover, tightening down on the window retainer and adjusting gaskets. However, many leaks went undetected and were not located until more thorough measurements were conducted in the lab at the conclusion of all testing. Results and discussions of the post test inspection are presented in Section 3.4.

Since external leak points did not appear in close proximity to wall temperature monitors, thermocouples were not likely to have been subjected to forced heating. However, the presence of internal leak paths may have contributed to the high overall heat loss as well as to the local hot spots. In contrast to earlier (30 PSIG) receiver designs, some blanket type insulation was utilized in this DTM receiver. A combination of both rigid Cera Form*[4] and Cera Blanket*
****

3./In 1980 Sanders designed and built a receiver for the Solarized Autmotive Gas Turbine (SAGT). This was a pressurized receiver with a heavy, carefully sealed pressure shell.

4./*Trademark products of Johns Manville

Figure 21. Results of Composite Heat Loss on Receiver Vessels

The figure shows a plot with the following labels:

- Y-axis: THERMAL LOSS—KW(θ)
- X-axis: DEGREES—F
- Curve labels: EXTERIOR WALLS AND TOP, FRONT HEADER

INLET TEMP FOR FRONT HEADER LOSS

EXHAUST TEMP FOR REST OF RECEIVER
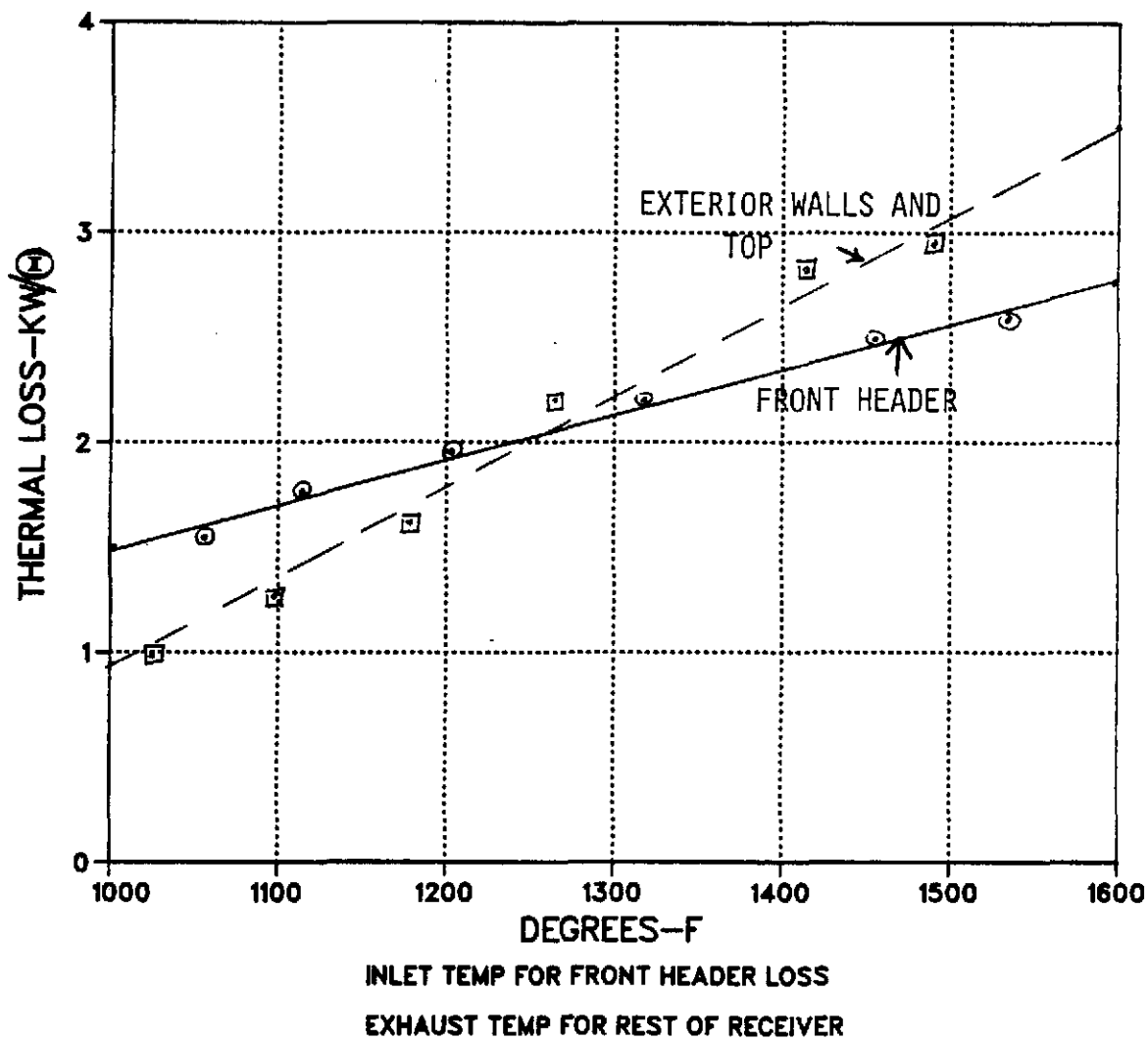
Heat loss by conduction through the insulated vessel has been obtained by dividing the exterior surface of the receiver into 38 sections. Losses from the front of the vessel (excluding the window) are plotted against the receiver inlet temperature (RIT). The cylindrical walls and the back of the receiver are correlated with the exhaust temperature (RET)

$\theta = T_\infty(^\circ R)/502^\circ R$

was incorporated into this design (Figure 20a). The problem of maintaining a tight fit between insulation and the interior vessel walls has always been difficult and has received special technical attention. The difference between this receiver and the SAGT receiver is that small external leaks provided the pressure differential required to cause hot gas to migrate. Unlike the SAGT receiver design which had to satisfy ASME pressure vessel codes, the DTM receiver was specified for operation at low pressure differentials, so less emphasis was given to sealing and more attention was directed toward quick lightweight and low cost production design.

An additional factor not previously encountered was the condensation of water vapor within this receiver. Throughout these initial tests (1/3/84), water was observed to be trickling from the low points on the rear cover V-clamp connection. Between 20 to 35 lbm/hr of water was generated during combustion of propane in these tests. Most of this moisture is at a temperature well in excess of the dewpoint. Air leaking to relatively cool external metal surfaces can liberate condensate. Saturation of a portion of the insulation would significantly increase the effective thermal conductivity and hence the heat loss. However, the subsequent tests using the engine, where the receiver operated at a slightly subatmospheric pressure (-1 to -3 inches of water) probably did not experience this degradation. Upon disassembly and inspection of the receiver mid-way through the program (4/20/84), no visible damage to the insulation was observed.

The preceding arguments relating to the pressurized receiver tests led to a conservative manner of estimating. The heat losses in the receiver for the actual DTM tests with the subatmospheric engine. In the subatmospheric configuration, where air infiltrates through leaks, the hot spots, saturation of insulation and energy lost to the heat of vaporization would not occur. Heat losses resulting from these conditions have been correlated with the internal gas temperature and are allocated to each of the subsequent tests, both pressurized and subatmospheric. However, infiltration may have an even more severe effect on the efficiency of the receiver. This situation is discussed later with respect to the DTM receiver performance. Also, an estimation of the potential magnitude of this infiltration effect is calculated in Appendix B.

3.2.7.3 Analysis of Receiver Cavity Radiation Losses

Infrared radiation emitted from the receiver cavity represents a substantial portion of the overall heat loss at temperatures characteristic of Brayton cycles. Extensive characterization data at a broad range of cavity temperatures up to 1600°F has been obtained on this test program. To expand the scope of the characterization of cavity related losses, two cavity configurations have been evaluated. The DTM test bed receiver was designed to allow the absorber to be

moved fore and aft relative to the fixed aperture position (see Figure 22). Thermocouple measurements within the cavity provided the basis for the radiative heat loss calculations.

Cavity instrumentation consisted of 16 thermocouples located on the absorber, 8 stations just below the surface of the cavity insulation and two points on the stainless steel air deflector. Nichrome wire clips supported the 1/16-inch diameter shielded thermocouples at the mid depth of the honeycomb passages. The sensors were, therefore, 6 diameters in from the flow entrance of the 1.1-inch thick silicon carbide matrix. A geometrical analysis of an individual matrix cell indicates that less than 0.3% of the incident solar radiation will penetrate to this depth. For this reason, measurement corrections due to direct solar impingement on the thermocouple sheath are considered negligible. Each probe was bent slightly prior to insertion to cause the probe to fit snugly into the 0.084 inch square cell. No corrections were attempted to adjust the thermocouple reading for the true wall temperature for the case in which the flow through the cell was not impeded by the presence of the probe. These effects are also considered to be very small since the thermal conductivity is relatively high while wall thickness is very small.

Although no solar flux is incident on the cavity walls, the elimination of absorber radiation influence on the cavity wall thermocouples was a design consideration. The thermocouples were depressed into the surface of the semi rigid cast Cera Form insulation. Then several coats of Johns-Manville's Cerakote refractory slurry were applied over the cavity surface and the thermocouples. This produced the situation in which the 8 thermocouples were flush mounted in the cavity insulation with only a thin (.08 inch) separation from the receiver working fluid. Therefore, a very good representation of the actual wall temperature was obtained.

Thermocouple locations are shown in Figure 2oa. Absorber and cavity wall temperature data for the 24 locations is presented in Table 5 for the 11 solar test conditions. Solar tests conducted with the preheater and blower assembly extend through 5/3/84. Testing thereafter was with the SABC power conversion assembly. Each data point presented in this table reflects a time averaging of 10 steady state readings over a two minute period. Also listed in this table is the arithmetic mean absorber temperature (TAVG), the standard deviation of the 16 readings and the average radiation temperature for this same period. Since radiation is governed by a fourth power relation, the average radiating temperature is represented by the fourth root of the sum of the 16 local temperatures to the fourth power ($\sqrt[4]{\quad T^4}$). The thermocouple temperatures did not appear as variable over the insulation surface. These thermocouple readings
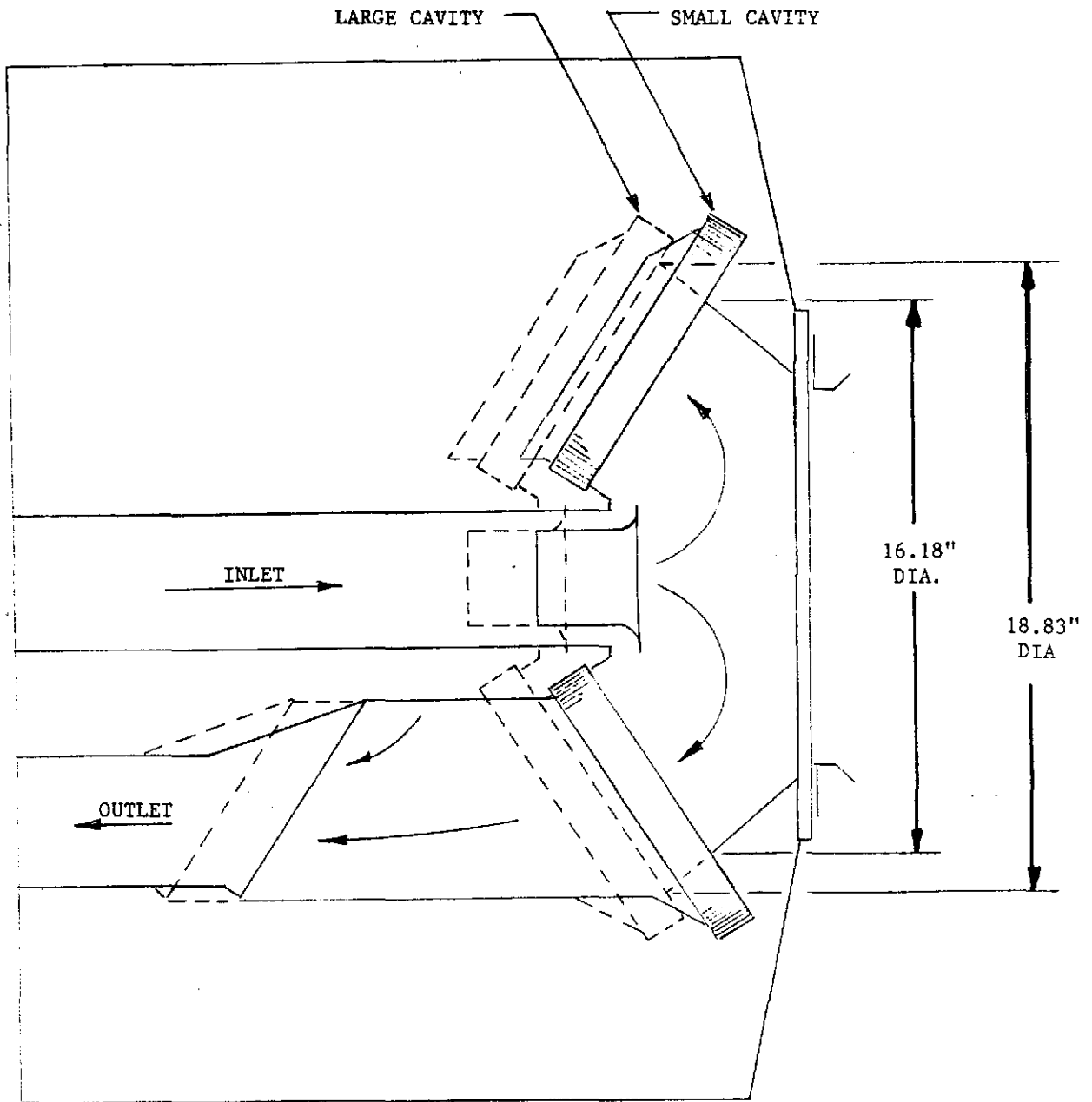
FIGURE 24. TWO CAVITY CONFIGURATIONS WERE TESTED UNDER SOLAR CONDITIONS. THIS RECEIVER WAS DESIGNED WITH THE CAPABILITY TO ALLOW REARRANGEMENT OF INTERNAL INSULATION SEGMENTS SO THAT THE ABSORBER COULD BE MOVED BACK TWO INCHES FROM ITS ORIGINAL POSITION.

Figure 22. Large and Small Cavity Configurations for DTM Receiver

were averaged for an inner and outer ring, as shown in Figure 20a.
Due to the demand for more data logger channels when the engine came
on line in June, these rings of four thermocouples were wired in
parallel to produce an average analog signal. Two thermocouples also
monitored the back side (opposite the incident solar) of the deflector
and these are also averaged in Table 4.

A direct account of the total energy losses in the absence of
solar input can be determined by measuring the temperatures at inlet
and exhaust, and the mass flow. A rake of three 1/16-inch diameter
thermocouples was positioned at both the entrance and exit of the
receiver. Each set of three thermocouples was logged and time
averaged over a two minute period. The temperature profile at the
exhaust duct was always good, displaying variances of generally $+ 2^O$F
between stations. On the inlet, radial variations of about $\pm 10^O$F
were observed with the preheater assembly. Inlet conditions with the
SABC power conversion assembly were on the order of those recorded at
the exit of the receiver. The temperature distribution at the
receiver exit during solar operation was also very good, exhibiting
variations of less than $\pm 5^O$F. Radiation corrections for these
thermocouples does not appear to be necessary. Both sets of
thermocouples have views only of the heavily insulated wall which is
very close to the air temperature. The thermodynamic characteristics
of air were used to estimate the working fluid enthalpy. Appendix F
addresses the potential variation which may exist due to the presence
of the other gaseous constituents.

In addition to the temperature measurements, the accuracy of this
analysis is contingent upon mass flow measurement. The accuracy of
the flow meter utilized in the preheater tests is such that an
uncertainty of about ± 5% is expected in those test conditions. The
method for predicting engine mass flow rates is outlined it Section
3.2.8.

Infiltration within the engine assembly and the receiver
increases the uncertainty of receiver flow enthalpy measurements. Air
entering the receiver upstream of the exhaust thermocouples reduces
the temperature and increases the mass flow rate at the statepoint.
Infiltration elsewhere in the system reduces the flow supplied to the
receiver. The results of the static leak tests (Section 3.2.4) have
allowed us to take into consideration these effects. However, the
exact contribution of these leaks is in some doubt since the leaks and
leak paths may vary from test to test and with temperature.
Fortunately, the magnitude of these energy terms, estimated in
Appendix B, is shown to be relatively small. Also, the leakage of hot
gas during positively pressurized non solar tests should not influence
the flow enthalpy prediction. In this case, the downstream
thermocouple would not be affected and the mass flow rate is based on

54

TABLE 4. SOLAR RECEIVER AND ABSORBER CAVITY WALL THERMOCOUPLE READINGS FOR 11 STEADY STATE TESTS

TEST DATE	3/26A	3/26P	4/12	4/13	5/3A	5/3P	6/8P	6/28	6/30A	7/10	7/13
ABSORBER OF											
Ta1 (North)	1042	245	930	930	477	1129	1358.8	1572	1529	1364	1461
Ta2	1292	859	1291	1375	1280	1570	1532.7	1825	1784	1642	1687
Ta3	1552	1665	1624	1777	828	1195	1439.3	1671	1557	1444	1599.5
Ta4	1337	1310	1277	1403	458	1038	1339.4	1606	1391	1239	1622.5
Ta5 (East)	1096	230	996	951	580	1267	1257.8	1558	1416	1349	1404
Ta6	1620	676	1675	1590	986	1551	1323.5	1618	1497	1424	1550
Ta7	1874	1107	1785	1753	897	1413	1312.7	1592	1466	1422	1594
Ta8	1364	812	1270	1287	434	1008	1275.5	1555	1396	1393	1591
Ta9 (South)	1050	245	891	885	282	922	1329.6	1428	1424	1559	1404
Ta10	1233	598	1108	1075	566	1158	1474.5	1519	1601	1644	1475
Ta11	1365	1148	1394	1318	801	1369	1587.2	1689	1775	1522	1611
Ta12	1192	1234	1193	1181	794	1187	1542.9	1733	1779	1358	1695
Ta13 (West)	1062	354	904	927	544	1106	1563.1	1472	1700	1526	1481
Ta14	1343	963	1205	1295	875	1323	–	1597	1679	1494	1590
Ta15	1518	1109	1391	1494	648	1193	–	1607	1644	1450	1553
Ta16	1297	574	1165	1218	330	996	–	1640	1576	1525	1484
$\sqrt[4]{\overline{T^4}}$	1369.8	997.4	1316.2	1342.4	760.2	1245.1	1421.7	1611.5	1589.3	1468.4	1555.8
Tave	1327.3	820.6	1256.2	1278.7	673.8	1214.1	1410.5	1605.1	1575.9	1459.7	1550.1
T std. dev.	228.9	430.4	270.5	283.5	266.1	191.2	117.2	96.62	139.4	109.2	90.1
CAVITY °F											
T17	1042.4	311.7	904	923.8	232.8	826.8	–				
T18	1035.7	318.7	891.5	919.9	257.3	857.5	–				
T19	1051.4	346.2	900.8	929.7	248.5	865.8	–				
T20	1066.3	387	913.2	954.2	314.0	915.0	–				
T21	1036.6	357.8	952.6	961.8	254.3	885.7	–				
T22	1054.4	405.4	984.8	996.8	322.8	920.4	–				
T23	1047.6	333.3	970.4	977.2	278.8	861.5	–				
T24	–	–	–	–	303.1	858.3	–				
TC Inner	1045.5	337.3	932.0	948.1	253.6	860.0	–	1250.5	1173.9	1105.3	1183.4
TC Outer	1051.5	370.4	929.8	957.0	298.0	887.8	–	1306.2	1239.4	1151.3	1251.0
Tc Ave	1048.0	353.8	930.9	952.5	275.8	873.9	–	1278.4	1207.7	1127.5	1217.1
Deflector	1554.1	1588.8	1536.1	1542.1	1186.2	1345.8	–	1807.6	1771.8	1563.1	1688.4

HYPHENS INDICATE INCIDENTS WHERE FAULTY INSTRUMENTATION PROHIBITED THE ACQUISITION OF DATA

the upstream measurement. The effect during solar operation is somewhat less clear since leaks upstream of the absorber would reduce its heat transfer effectiveness while raising the matrix temperature.

The prediction of the energy lost from the cavity is accomplished by summing the radiative effects of the 24 internal stations monitored by the thermocouples. Losses from the cavity are comprised of three general radiative components:

1) radiation from the absorber matrix transmitted directly through the quartz aperture,
2) the portion of this same radiation which is diffusely reflected by the cavity insulation through the aperture and,
3) radiation emanating from the cavity walls and transmitted by, as the quartz.

The general energy equations representing these terms are presented in Appendix A.

The wavelength dependent quariz absorption characteristics and reflection at the window surfaces are important factors in the prediction of cavity losses. The portion of infrared radiation deposited in the quartz by Beers' Law absorption may either radiate back to the cavity, conduct to the outside surface where it is lost, or be recovered by the impingement convection of the working fluid on the inside surface. To calculate the transmitted portion of energy directly lost from the cavity, the black body spectral characteristics of the three radiation components are integrated over the transmission spectrum of the GE 124 quartz.

An overall energy balance of the receiver has initally been conducted for test conditions in which no solar was added (tests 1/3/84). In these cases the summation of cavity emission losses, conduction through the insulated vessel, and window exterior surface losses should be equal to the intrinsic enthalpy drop of the air across the receiver. The general energy equations used in this modeling are presented in Appendix A. A prediction of the total heat loss from the receiver, in either solar or non solar conditions, can be derived by summing these individual quantities as outlined in Appendix A. The model introduces the thermocouple readings into these equations, with the temperature dependent material characteristics, to arrive at a solution.

Initial calculations based solely on thermocouple readings did not produce an adequate correlation. Heat loss estimations based on window thermocouple readings introduced the greatest uncertainty. In fact, leakage of the cavity gas was observed in the vicinity of the thermocouple stations on the window retaining mount. On both the pressurized and subatmospheric cavity tests, leakage was evident. The

magnitude of the leaks during preheater tests from 1/3/85 to 5/3/85 was somewhat greater than the measured values obtained at the conclusion of all testing (Table 5). Adjustments were often made during the course of testing by tightening the window retainer.

Thermocouples located on the edge of the window did not represent the true quartz temperatures since they were heated by leakage of the slightly pressurized gas during preheater tests. In tests with the SABC engine, these thermocouples were subjected to the opposite effect. Although leaks were less severe, data indicates some cooling of the sensors occurred as air leaked past them into the slightly subatmospheric cavity. Other errors in the exterior window surface temperature were introduced by reradiation of the graphite shield during all solar operation (illustrated in Figure 23). Very high shield temperatures at the aperture edge were recorded during the Solar tests. This data is presented in Table 4. These temperatures also provide an indication of the excessive quantity of spillage energy characteristic of the LEC460. Calculations show that thermocouple readings are not consistent with energy conservation about the window and therefore produce erroneous predictions of window related energy losses.

Correction of the thermocouple readings which monitored the window interior and exterior surfaces is necessary to provide a realistic estimate of the composite heat losses from the receiver. An analytical approach based on an energy balance about the quartz window was used. This method determines the heat load on the interior surfaces from the cavity thermocouple measurements to derive surface temperatures. Two major simplifying assumptions are made in this analysis. First, no radial temperature gradient exists in the window. Therefore, one dimensional conduction is assumed on the 12.2-inch diameter by 1/4-inch thick quartz disk. This assumption is supported by calculations which show the dominant heating effect on the inside surface to be a nearly uniform radiative (IR) load from the absorber elements. Even the smaller energy terms imposed by the impinging inlet air jet can be shown to exhibit only a slight dependance of heat transfer coefficient on window radius. Nusselt number correlations have been surveyed by Perry[5] for ratios of jet diameter to window distance and Reynolds numbers which are appropriate for this application.

During Solar operation the magnitude of the incoming flux vary widely across the window due to nonuniform mirror performance. However, absorption in the quartz is less than one half percent (0.005) and thus very small compared to the internal IR loading. This non-uniform absorption of the solar flux should be considered in a
****

5./Perry, K.P., "Heat Transfer by Convection from Hot Gas Jet to a Plane Surface", <u>Proc. Inst. Mech. Engineers</u>, Vol. 168, 1954.

TABLE 5. GRAPHITE SHIELD TEMPERATURES AND SUMMARY OF DATA FROM SOLAR PREHEATER TESTS

TEST DATE	3/26A	3/26P	4/12	4/13	5/3A	5/3P
RECEIVER INLET TEMP (°F)	956.0	76.4	776.9	768.7	74.2	759.7
RECEIVER EXHAUST TEMP (°F)	1062.0	298.5	1028.2	1031.6	348.6	981.2
MASSFLOW RATE LB/S	.297	.300	.288	.288	.288	.288
Δ ENTHALPY BTU/LBM	27.92	53.57	65.49	68.35	66.28	57.38
RECEIVER OUTPUT (KW)	8.757	16.97	19.92	20.79	20.16	17.45
TABS MAX °F	1874	1665	1785	1777	1280	1570
Tabs MIN	1042	230	841	885	282	922
Tabs AVG	1327.3	820.6	1256.2	1278.7	673.8	1214.1
WINDOW INSIDE	992.3	279.6	860.7	847.5	208.7	762.6
WINDOW OUTSIDE	680.0	372.8	439.8	833.3	429.4	538.6

GRAPHITE SHIELD STATIONS

	3/26A	3/26P	4/12	4/13	5/3A	5/3P
65	534	251	382.7	364.6	365.5	498.3
58	711.8	292.2	467.4	433.2	363.3	462.5
63	799.2	374.2	471.1	458.4	436.3	574.5
59	767.7	294.9	498.6	466	368.8	472.5
61	937.4	481.5	617	500.8	473.8	610.8
68	–	–	–	–	102.3	375.6
97	847.2	413.5	863.8	711.6	548.8	718.6
96	–	–	–	–	–	–
100	–	–	290.3	225.8	430.7	543.
T CAVITY AVG.	1053.0	355.4	937.6	958.5	305.0	958.7
TAMBIENT	46	40	62	60	60	60

THE RECEIVER SHIELD TEMPERATURES AT 9 STATIONS WERE MONITORED WITH THERMOCOUPLES JUST BELOW THE SURFACE OF THE GRAPHITE DURING THESE INITIAL SOLAR TESTS. THE STATION NUMBERS CORRESPOND WITH REFERENCES ON FIGURE 22B. A SUMMARY OF OTHER RECEIVER OPERATING CONDITIONS IS ALSO PRESENTED.

CAVITY

IR REFLECTION

RERADIATION

CAVITY
RADIATION

CERA FORM INSULATION

12.2" DIA.

FORCED
CONVECTION

QUARTZ

STEEL SHELL AND RINGS

11" DIA.

RADIATION   FREE
             CONVECTION

GRAPHITE SHIELD

SOLAR
ABSORPTION

CERAMIC ROPE GASKETS

INSIDE TO OUTSIDE
THERMOCOUPLE

AMBIENT
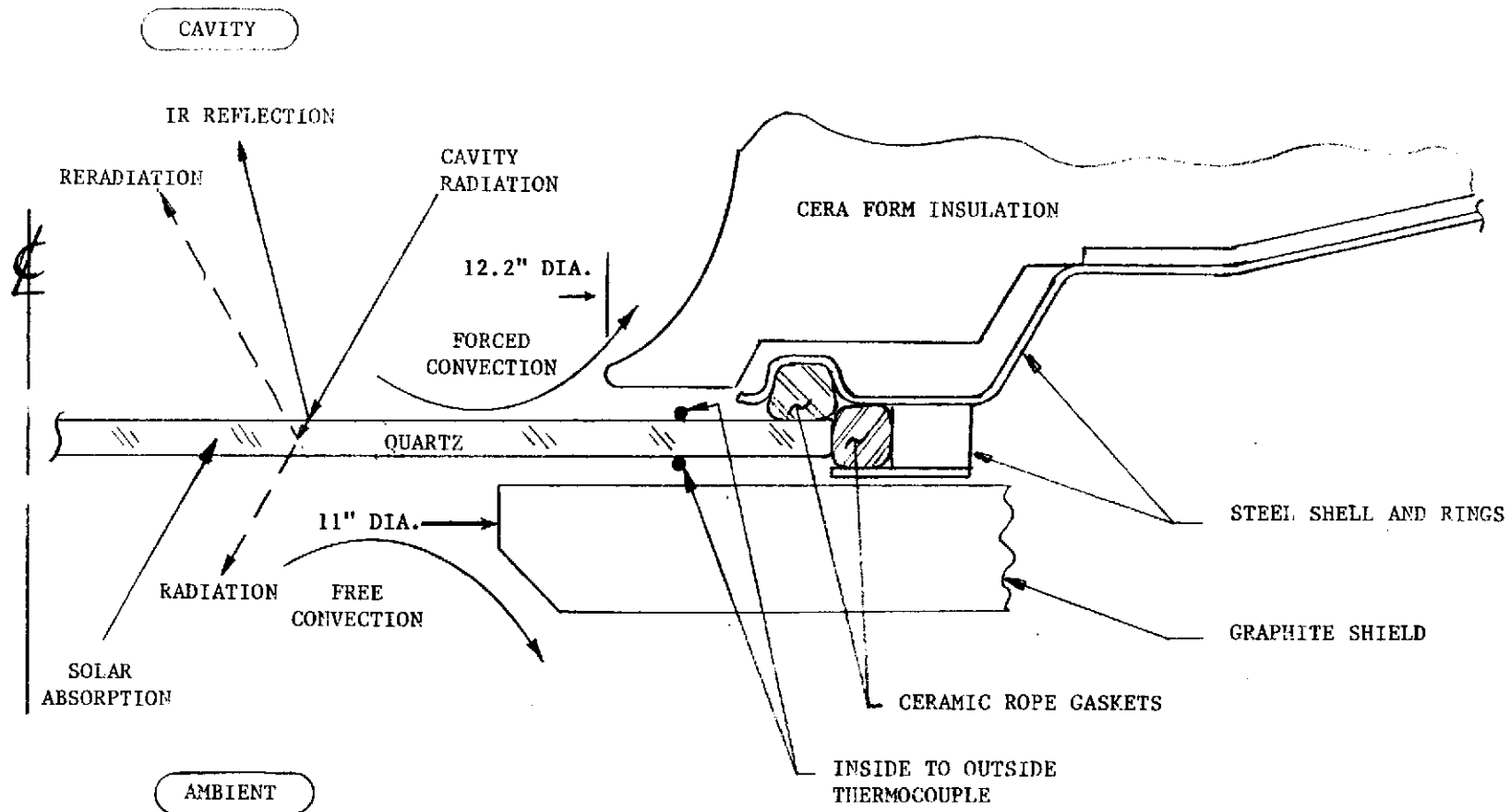
This illustration of the receiver window shows the energy terms used in the thermal
analysis. The location of the thermocouples is also shown. The internal TC is
shaded from the absorber radiation by the lip of the cavity cera-form insulation.
The exterior TC is influenced by the Graphite Shield Reradiation.

Figure 23.   Receiver Window Energy Balance As Used in Analytical
              Model

more rigorous thermal analysis of the window. To produce a conservative assessment of energy losses, at this time it will be assumed that this solar absorption component is neither absorbed nor transmitted, but essentially lost, as is the reflection component.

The second assumption is that the axial IR absorption gradient on the interior surfaces is negligible. This assumption is based on the large wavelength dependent absorption coefficient of the quartz. Essentially all blackbody radiation above 3.6 microns (except for the 4% dielectric reflection) is absorbed in the first few wavelengths.

The analysis implicitly calculates the radiative exchange between the hot cavity elements and interior window elements. Adding or subtracting from this load is the superimposed convective effect of the impinging receiver inlet gas. This quantity must then be conducted through the 1/4-inch thick window and then emitted from its outer surface. Through iteration, energy conservation is satisfied. The thermal conductivity and emissivity of the quartz as well as the convective film coefficients on both sides of the window are taken as functions of temperature. An illustration of the energy balance terms is presented in Figure 23.

The results of this analysis are encouraging. Upon comparing the adjusted composite heat loss sums with the enthalpy drop measured across the receiver in the absence of solar heat addition, a much better correlation is obtained. For tests with positive cavity pressure, the composite calculations showed lower heat losses which compensated for the artificially high window thermocouple readings. With subatmospheric pressure in the cavity, window temperature calculations were higher than thermocouple readings and thus an increased heat loss was calculated. In both situations, composite heat loss calculations moved to closer agreement with the measured air enthalpy drop. A more in-depth analysis of the window thermocouple readings and the effect of window leaks on receiver heat loss calculations is presented in Appendix B.

Table 6 displays the results of the window analysis. In this table a comparison is made between the original calculations of heat loss based solely on thermocouple data and the modified model which incorporates all of those same measurements except for the window temperature readings. In the columns entitled "Calculations based on window energy balance", the calculated window temperature replaces the thermocouple readings in the composite heat loss model. The "total heat loss" columns under each heading can then be compared directly to the drop in enthalpy of the air values listed in the far right hand column (negative values). The trend is, in general, towards better agreement of the energy balance predictions in column 11 with the enthalpy drop in column 12 than initially exhibited by column 6 thermocouple based predictions.

Justification for discarding window thermocouple data in favor of the calculated window temperatures is twofold. First, a consistent account of energy loss is achieved. That is, the sum of the individual loss contributions based on conduction, convection and radiation from the receiver approaches the enthalpy losses as indicated by inlet and exhaust gas thermocouple rakes. Secondly, energy conservation about the quartz window is satisfied based on a "first law" analysis utilizing cavity temperature measurements and flow conditions.

Correlation between the composite heat loss model and air enthalpy drop during non-solar tests is generally very good. Although the first two non-solar tests with the SABC assembly (6/8A and 6/30P in Table 6) indicate a good correlation, the three subsequent non solar tests display a divergence between loss prediction methods. This discrepancy is largely attributed to the uncertainty in mass flow rate arising from variations in the amount of bearing cooling bleed air (see Table 13). In the 7/9 tests, longer than usual operation at rated speed was required to make manometer pressure measurements at 12 taps and combustion make-up air measurements. In such situations of sustained operation at 75,000 RPM, an increase in bearing cooling air was required to prevent an over temperature condition on the turbine bearings. It was noted in the daily test log for 7/9 and 7/25 (also 75,000 RPM tests), that the air pressure feeding the bearings was increased to allow the tests to proceed. This added bearing bleed flow was not accurately measured. However, the following tests on 7/10 and 7/13 (Table 6) were conducted at engine idle speed and normal bearing bleed flow rate and show good correlation. Therefore the bearing bleed flow rates presented in Table 13 are believed to be accurate.

3.2.7.4 Energy Balance of all Receiver Heat Losses

Having defined and validated the method through which receiver heat losses are determined, a detailed inspection of specific losses under both solar and non-solar conditions can be conducted. The extension of the composite loss calculations to the solar conditions provides a means for determining the total solar energy input, and hence the receiver efficiency. Tables 7, 8, and 9 contain the receiver performance characteristics determined in the three major subtests.

Table 7 summarizes the results of the first receiver tests (1/3/84) conducted with the auxiliary preheater and blower located on the ground. The averaged (in space and time) air inlet and exhaust temperatures and the measured mass flow rate are listed for each consecutive test. The row entitled "total predicted power loss" contains the sum of the individual heat loss groups listed in the next

TABLE 6.

COMPARISONS OF WINDOW SURFACE TEMPERATURE READINGS AND PREDICTIONS BASED ON CAVITY MODEL ENERGY BALANCE

| DATE, TEST | CALCULATIONS BASED ON WINDOW THERMOCOUPLE READINGS | | | | | CALCULATIONS BASED ON WINDOW ENERGY BALANCE | | | | | ENTHALPY RISE IN AIR FROM RIT-RET |
	T in °F	T out °F	EXTERIOR RADIANT KW	EXTERIOR CONV KW	TOTAL PREDICT LOSS KW	T in °F	T out °F	EXTERIOR RADIANT (KW)	EXTERIOR CONV KW	TOTAL PREDICT LOSS KW	
1/3/84 A	1050.	860.	1.064	0.288	5.195	897.0	752.0	0.624	0.243	4.711	-4.579
B	1115.	905.	1.206	0.307	6.068	983.3	823.9	0.714	0.273	5.591	-5.623
C	1200.	960	1.402	0.330	7.113	1068.9	894.1	0.917	0.302	6.608	-5.847
D	1298.	1035	1.666	0.323	8.328	1149.7	961.0	1.079	0.331	7.709	-6.711
E	1330.	1099	1.821	0.391	9.447	1226.	1023.8	1.244	0.358	8.837	-8.977
3/26 A	992.3	680.	0.788	0.210	5.323	1017.3	851.6	0.821	0.280	5.426	8.757
3/26 B	279.6	372.8	0.114	0.096	1.163	362.6	301.4	0.099	0.071	1.123	16.970
4/12	860.7	439.8	0.451	0.110	4.149	922.2	774.6	0.662	0.239	4.547	19.917
4/13	847.5	433.3	0.436	0.109	4.241	942.7	790.9	0.694	0.247	4.700	20.789
5/3 A	208.7	429.4	0.106	0.107	0.951	209.8	177.8	0.035	0.026	0.800	20.158
5/3 P	762.6	538.6	0.451	0.148	3.841	856.1	720.4	0.564	0.218	4.024	17.45
6/8 A	-	222.4	0.047	0.030	2.769	730.3	617.6	0.398	0.163	3.254	-3.566
6/8 P	-	-	1.717	0.343	7.349	1093.2	918.9	0.966	0.280	6.536	11.675
6/28	1031.6	574.4	0.715	0.152	8.192	1273.1	1065.6	1.355	0.349	9.030	14.468
6/30 A	741.8	293.9	0.275	0.056	3.316	773.4	652.9	0.452	0.184	3.621	-3.585
6/30 P	980	641.2	0.731	0.180	7.500	1223.9	1024.2	1.240	0.335	8.164	19.346
7/9 A	813.8	264.6	0.299	0.046	3.991	878.1	739.2	0.594	0.218	4.458	-6.921
7/9 P	796.6	272.3	0.294	0.049	3.671	831.0	699.6	0.526	0.202	4.057	-5.244
7/10	995.7	800.1	0.921	0.243	6.516	1101.7	923.3	0.981	0.293	6.626	18.600
7/13	1104.4	739.3	0.976	0.214	7.650	1192.1	997.9			7.948	19.854
7/25	856.8	289.8	0.339	0.051	3.873	860.3	725.4	0.569	0.207	4.258	-5.628

Both thermocouple and energy balance calculations are used to evaluate the true interior and exterior window temperatures. A comparison of the window heat losses (by convection and radiation) are calculated from surface temperatures derived by these two methods. This exterior radiation and convection, plus the cavity transmission losses and the conduction through the vessel insulation (constant for both window cases), sum to the total predicted receiver losses (columns 6 and 11). These values may be compared directly to the enthalpy drop of the working fluid displayed in the last column for those tests conducted without solar input. The receiver mass flow rates used in these calculations are presented in Table 14.

*Receiver inlet temperature – Receiver outlet temperature

TABLE 7.

SOLAR RECEIVER PERFORMANCE CHARACTERISTICS FOR NON-SOLAR PREHEATER TESTS

TEST DATE 1/3/84

TEST LETTER	A	B	C	D	E
RECEIVER INLET TEMP. °F	1140.2	1242.0	1334.2	1426.2	1522.0
RECEIVER EXHAUST TEMP. °F	1083.1	1172.6	1262.7	1344.8	1413.9
RECEIVER MASS FLOW LB/S	0.285	0.285	0.285	0.285	0.285
AIR ENTHALPY RISE (KW)	-4.579	-5.623	-5.847	-6.711	-8.977
TOTAL PREDICTED POWER LOSS (KW)	-4.711	-5.591	-6.608	-7.709	-8.837
● CAVITY AND WINDOW LOSS	1.506	1.956	2.491	3.070	3.667
● FRONT HEADER CONDUCTION	1.589	1.772	1.942	2.117	2.305
● CYLINDER AND TOP WALL CONDUCTION	1.616	1.864	2.176	2.522	2.866
TOTAL SOLAR INTO CAVITY (KW)	0	0	0	0	0
AVERAGE ABSORBER INFLUX (KW/M^2)	0	0	0	0	0
POWER INCIDENT ON WINDOW (KW)	0	0	0	0	0
RECEIVER SOLAR EFFICIENCY	-	-	-	-	-

IN THE ABSENCE OF SOLAR HEAT ADDITION, CAVITY EMISSION AND VESSEL HEAT
LOSS PREDICTIONS CAN BE COMPARED TO THE ENTHALPY IN THE AIR MEASURED WITH
INLET AND EXIT THERMOCOUPLE RAKES. NEGATIVE VALUES OF ENTHALPY RISE
INDICATE A DROP OF ENTHALPY.

TABLE 8.

SOLAR RECEIVER PERFORMANCE CHARACTERISTICS FOR SOLAR PREHEATER TESTS

DATE, TEST	3/26 A	3/26 P	4/12	4/13	5/3A	5/3P
RECEIVER INLET TEMP. °F	956.0	76.4	776.4	768.7	74.2	759.7
RECEIVER EXHAUST TEMP. °F	1062.0	298.5	1028.2	1031.6	348.6	981.2
RECEIVER MASS FLOW LB/S	0.297	0.300	0.288	0.288	0.288	0.288
AIR ENTHALPY RISE (KW)	8.757	16.970	19.917	20.789	20.158	17.453
TOTAL PREDICTED POWER LOSS (KW)	-5.426	-1.123	-4.470	-4.618	-0.799	-4.024
● CAVITY AND WINDOW LOSS	2.615	0.500	2.077	2.224	0.157	1.739
● FRONT HEADER CONDUCTION	1.263	0.041	0.950	0.942	0.016	0.928
● CYLINDER AND TOP WALL CONDUCTION	1.549	0.581	1.442	1.453	0.626	1.357
TOTAL SOLAR INTO CAVITY (KW)	14.183	18.093	24.387	25.407	20.957	21.477
AVERAGE ABSORBER FLUX (KW/M^2)	93.3	119.0	126.8	132.1	108.9	111.6
POWER INCIDENT ON WINDOW (KW)	15.416	19.666	26.508	27.616	22.779	23.345
RECEIVER SOLAR EFFICIENCY	0.568	0.863	0.751	0.753	0.884	0.748

HAVING DEMONSTRATED AN AGREEMENT BETWEEN PREDICTICNS AND MEASUREMENTS
DURING TESTS WITHOUT SUN, THE TOTAL SOLAR ADDITION TO THE CAVITY AND
HENCE THE RECEIVER EFFICIENCY HAS BEEN CALCULATED. THE TRANSMISSIVITY
OF THE QUARTZ WINDOW IS ASSUMED TO BE 0.92.

TABLE 9.

SOLAR RECEIVER PERFORMANCE CHARACTERISTICS FOR DTM TESTS, WITH AND WITHOUT SOLAR

DATE, TEST	6/8A	6/8P	6/28	6/30A	6/30P	7/9A	7/9P	7/10	7/13	7/25
RECEIVER INLET TEMP. °F	982.8	1107.3	1202.6	1056.1	1032.9	1190.3	1114.4	979.3	1022.0	1152.8
RECEIVER EXHAUST TEMP. °F	903.1	1322.1	1464.8	1400.7	967.9	1062.2	1021.7	1302.5	1434.5	1048.5
RECEIVER MASS FLOW LBM/S	0.1621	0.1996	0.1917	0.1985	0.1971	0.1971	0.2020	0.2039	0.1690	0.1920
AIR ENTHALPY (KW)	-3.567	11.675	14.468	19.346	-3.585	-6.923	-5.244	18.600	19.854	-5.628
TOTAL PREDICTED POWER LOSS (KW)	-3.254	-6.536	-9.030	-8.164	-3.621	-4.458	-4.057	-6.626	-7.948	-4.258
● CAVITY AND WINDOW	0.829	2.942	4.484	4.167	0.973	1.362	1.175	3.177	3.887	1.291
● FRONT HEADER CONDUCTION	1.234	1.436	1,627	1.381	1.341	1.612	1.480	1.255	1.312	1.530
● CYLINDER AND TOP WALL CONDUCTION	1.191	2.158	2.919	2.616	1.308	1.483	1.402	2.194	2.749	1.437
TOTAL SOLAR INTO CAVITY (KW)	0	18.211	23.498	27.510	0	0	0	25.226	27.802	0
AVERAGE ABSORBER INFLUX (KW/m^2)	0	94.9	122.4	143.3	0	0	0	131.4	144.8	0
POWER INCIDENT ON WINDOW (KW)	0	19.79	25.54	29.90	0	0	0	27.42	30.22	0
RECEIVER SOLAR EFFICIENCY	–	0.590	0.566	0.647	–	–	–	0.678	0.657	–

DTM TESTS WERE CONDUCTED WITH THE COMPLETE SABC POWER CONVERSION ASSEMBLY. DATA WAS GATHERED UNDER BOTH SOLAR AND NON-SOLAR CONDITIONS.

three rows. The vessel conduction (radiation and convection off the exterior surfaces) losses are separated into the two zones discussed earlier in this section. As expected, cavity losses (containing transmission and window surface losses) display a stronger dependence on operating temperature than do losses attributed to conduction through the vessel insulation. In fact, a greater than fourth power relation exists because the blackbody emission spectrum shifts towards the high transmission band of the quartz.

Table 8 contains the results of the first solar tests conducted between 3/26/84 and 5/3/84. The same assembly used in the initial ground tests (1/3/84) was mounted on the LEC460 for solar characterization. The "Total Solar into the cavity" row is comprised of the sum of predicted heat loss terms and the enthalpy rise experienced by the working fluid. The efficiency for each test case is based on the concentrator power delivered to the receiver aperture. Therefore, the losses incurred by the transmission of solar spectrum through the quartz represents an additional loss. The transmissivity of the GE 124 quartz is available from product data presented in Appendix C. This data shows a transmissivity of between 92% and 93% over the solar spectrum. A working value of 0.92 will be assumed in this analysis.

The first four columns (tests 3/26 to 4/13) contain the test data for the smaller (16.62 inch diameter) silicon carbide absorber. Although air temperatures were well below engine design specifications, local absorber temperatures shown in Table 4 surpass our design point predictions. Also, a significant limitation to these initial characterization efforts was the excessive temperature attained by the stainless steel deflector. With the smaller cavity, temperatures in excess of $1700^{o}F$ on the deflector were common for inlet air temperatures of only 700° to $800^{o}F$. Some improvement in this situation was achieved by moving the absorber back two inches and therefore expanding its diameter to 18.82 inches. The resulting effect on the average radiating temperature, and hence efficiency, is important.

Data presented in Table 8 illustrates a relevant comparison between tests 3/26P and 5/3A and again for the 4/13 and 5/3P tests. On the 3/26P and 5/3A tests, in which no preheat was added to the inlet air, the larger absorber cavity of 5/3A yielded a substantially lower cavity loss (by 343 watts). Although the slightly lower inlet air temperature and flux levels accounted for some of the advantage of 5/3P over 4/13, the larger cavity operates at a lower absorber temperature and hence lower losses. Direct comparison of receiver efficiencies is somewhat misleading since most losses at these temperatures are attributed to conduction through the vessel insulation and are therefore dependent on ambient conditions. Also, insulation measurements were not obtained for these initial tests.

The emission characteristics of the two cavities evaluated are also influenced by the internal configuration of the absorber and cavity walls. The radiative exchange between the elemental areas within the cavity is taken into consideration through the geometrical view factors (FV) incorporated into the energy equations of Appendix A. The distance between the absorber and the window is therefore an important optimization parameter in the effort to minimize losses. Convection heat exchange between the absorber and the working fluid is also influenced by the position of the absorber matrix, and therefore must be considered in the optimization process. This relation is investigated in following sections.

An inspection of the air flow distribution across the back surface of the absorber was conducted for both the 16.62-inch and the 18.12-inch diameter cavities. Using the Euler number for similitude, flow distributions on the two surfaces appeared similar. However, a very pronounced effect was observed in the temperature distribution across the matrix during solar operation. An indication of the spatial variation of temperature readings is given by the standard deviation of the data shown in Table 4. The comparison of tests conducted under similar conditions, such as 3/26P and 5/3A and again for 4/12 and 5/3P, is significant. Data from the smaller cavity exhibits a much greater spatial variation of readings and a higher overall radiating temperature. This is mainly attributed to greater diffusion of the very irregular solar flux distribution, which results when the distance between the absorber and the focal plane is increased.

It is certainly evident from these tests that some reduction in the absorber temperature, and a consequent reduction in emission losses, results from the deeper cavity. Also, this modification lowered the temperature on the stainless steel deflector so that the DTM testing could proceed at the higher Brayton temperatures.

The extreme variations in the flux and flow distribution on the absorber does not permit a clear cut determination of the optimum cavity ratio. Given a homogenous flux and flow distribution in each case, the advantage of the larger absorber configuration might not be as pronounced and therefore may be out-weighed by losses incurred by reduced wall insulation or a larger overall cavity volume. In our test cases the modification of the cavity insulation did not significantly benefit one absorber position over the other. This receiver was designed to accommodate the modification without changing the insulation thickness on the cylindrical portion, on the rear cover or around the window. Figure 22 illustrates the design modification.

Table 9 contains the DTM information under the same headings as Tables 7 and 8. Results from both solar and non solar tests are

67

presented. The receiver mass flow rates are substantially lower than previous tests conducted with the auxiliary blower assembly. At the time the preheater assembly was designed and tested the anticipated receiver mass flow rate, based on baseline engine specifications, was 0.27 lb/S. Although in many cases the Brayton compressor pumped more flow than this due to choking, cycle leaks and excess combustion air injection reduced the flow supplied to the receiver.

3.2.7.5 Analysis of the Solar Absorber Matrix

The solar test results in Tables 7, 8 and 9 display the strong influence the absorber temperature has on receiver efficiency. Nonhomogeneity of the flux and flow distribution have given rise to wide variations in local absorber temperatures. Because of the high order temperature[6] relationship governing radiative losses, variations in local temperature increase the difference between the average radiating temperature and the mean temperature that might have been achieved under uniform conditions. In other words, the radiation temperature defined as the fourth root of the sum of the local temperatures to the fourth power will always be greater than the arithmetic mean temperature. Additionally, the arithmetic mean temperature of the absorber is likely to be greater than the homogeneous temperature achieved given ideal uniform flow and flux conditions.

To use this data to benefit future designs, we must be able to interpret the interrelationships between the absorber temperatures, the incident solar flux and the fluid flow conditions. To proceed in this direction a comprehensive finite difference model of the silicon carbide matrix has been developed. The model attempts to predict the axial temperature distribution in the silicon carbide and the fluid passing through it as a function of the entering mass flow rate, temperature and incident solar flux. Variation of these parameters through adjustments in the cavity geometry will ultimately lead to the optimization of the receiver design. A step in this direction has
****

6./The radiation emanating from a surface is related to the fourth
   power (T^4) of temperature by the Stefan-Boltzman constant. The
   actual losses from the receiver aperture occurs as a result of the
   superposition of the gray body radiation spectrum and the spectral
   transmission characteristics of the quartz window. Because the
   spectral distribution of a body of increasing temperature shifts
   towards the shorter wavelengths where quartz exhibits a higher
   transmissivity, the total percentage of the T^4 energy transmitted
   (lost) further increases with temperature. The net result is a
   greater than fourth power relation between the cavity temperature
   and receiver losses, Data from these tests (Tables 8, 9, and 10)
   exhibit roughly a $T^{4.4}$ correlation with temperature over the range
   investigated.

been taken by the development of this model and the correlation of the theory with test results. However, the immediate goals of this report are only to compare the data and the current theory and discuss the influence of these parameters on the present design.

The finite difference approach solves for the axial temperature distribution in both the air and the silicon carbide matrix. The generalized energy and continuity equations are set up for incremental axial elements of a single square tube. Figure 24 illustrates the control volume terms surrounding an individual element. The following list outlines the model characteristics:

o   Steady state
o   1 dimensional axial conduction in silicon carbide wall.
o   Adiabatic surface on each of four walls along centerline of wall thickness.
o   Absorption of solar flux symetrically in a prescribed manner on front edge and all four walls of exposed internal elements (nominally the first five diameters inward).
o   Inter-element radiation exchange as defined by element-to-element geometric view factors.
o   Nusselt number for fully developed laminar flow in a square tube calculated as function of temperature at each element.
o   Fluid taken as air with all characteristics functionally dependent on temperature.
o   Emissivity and thermal conductivity of SiC function of temperature.

The following terms have been neglected because of their relatively small magnitude.

o   Dissipation of energy by viscosity $(\mu(\delta u/\delta y)2 \cong 0)$
o   Work done by compression $(u\, \delta P/\delta X \sim 0)$
o   No axial conduction in air.

The limitations of the experimental set-up have made it difficult to accurately determine the local flow and flux conditions on an individual matrix cell. Cold air velocity measurements were taken from a geometrically similar wooden flow model at Euler numbers comparable to design specifications.

The Euler number was chosen as the critical similitude parameter, representing the ratio of inertial to static pressure forces within the cavity. The flow within the cavity is essentially inviscid and therefore the distribution of flow over the matrix is largely governed by the inertial forces in the turning flow. The viscous pressure drop across the matrix is small relative to the dynamic head at the discharge into the cavity and therefore is assumed to have only a small influence over the flow distribution. These assumptions will be reassessed following evaluation of the analysis results.

69

Figure 24. Solar Absorber Cell Model
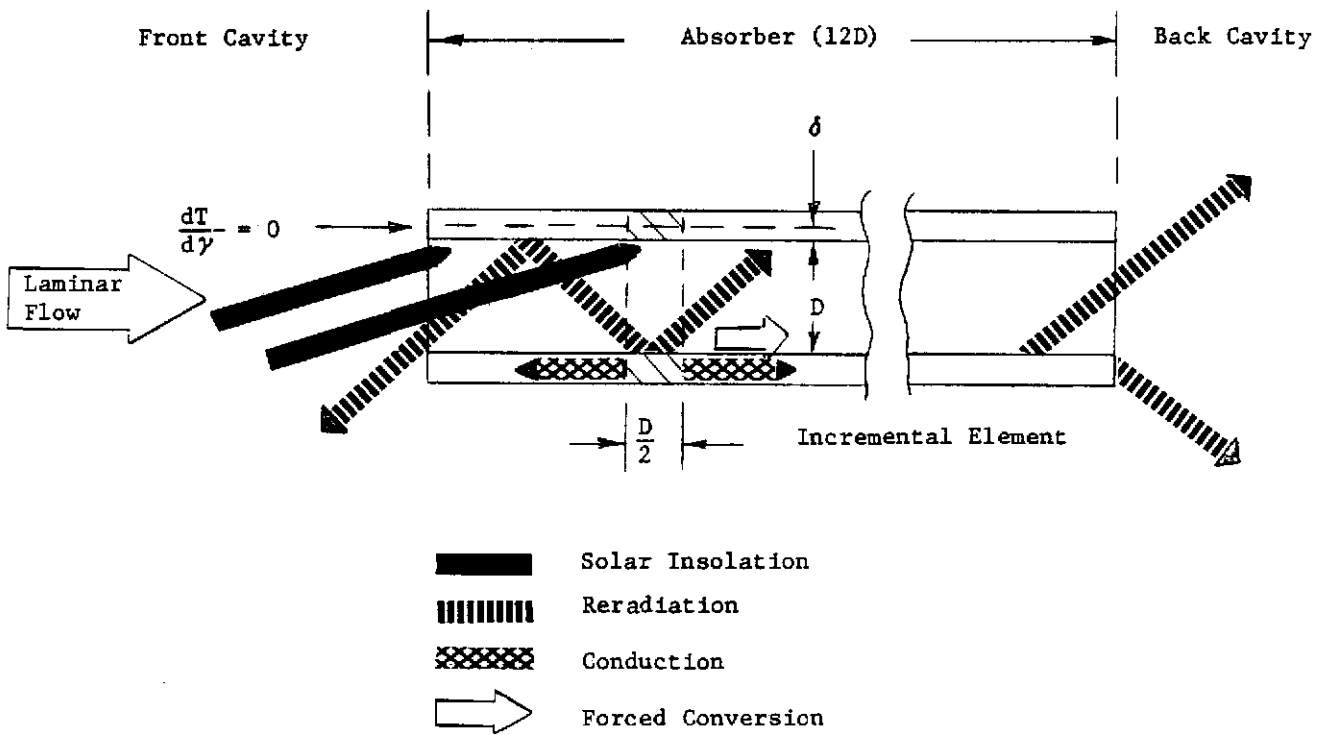
The approach to modeling the solar absorber characteristics is to conduct an energy balance of incremental elements along the length of an absorber cell

Both large and small cavity configuration were surveyed across the back surface of the honeycomb matrix with a hot wire anemometer. Air velocities measured on the cold flow model at the 16 thermocouple stations are shown in Appendix D. Velocity magnitudes varied by a factor of five in both cavity configurations. As a basis for analysis, the cold flow model readings were normalized against the average velocity over the total matrix surface. These scaling factors were then multiplied by the average velocities obtained for each of the solar test points to derive the local velocity at the 16 absorber stations.

The flux distribution at the absorber plane could not be measured in these experiments. A gross assumption that the solar power is distributed uniformly over the surface of the matrix has been used for the initial analysis. Previous arguments which compared the standard deviation of absorber temperature measurements for the small and large cavities suggest that the uniform flux assumption is certainly highly questionable for the large cavity as well, but proceeding with this simple case will allow us to test our assumption.

The local flow and flux conditions from each of the 10 solar tests have been assembled into the computer model. The model will then predict the absorber temperature distribution to which the thermocouple reading can be compared. One quadrant represented by the 4 thermocouple stations was evaluated. Stations one through four represent the north to south traverse along the axial plane of the exhaust duct. Stations five through eight are on the adjacent quadrant (symetrical with 13 to 16) along the east to west traverse (see Appendix D).

A comparison of the predicted absorber temperatures is cross plotted with the local thermocouple readings for the 40 data points in Figure 25. The open symbols are used for the DTM tests with the larger of the two cavities investigated. Each data point is labled with the station number. For comparison, the tests conducted with the smaller cavity are all symbolized with a point. These points exhibit poor correlation and no obvious trends. Explanations will be presented in the concluding discussions. For the DTM (large cavity) tests good correlation is demonstrated, especially for stations 7 and 8 which represent very nearly the mean flow. At station 6, which has been prescribed velocities of about one third of the mean, a significant over-estimation of the absorber temperature exists. Similarly, station 5 which has more than the average amount of flow, displays an underestimation of the temperature.

Judging from the consistency of the stations representing the exaggerated local velocities, additional inspection of these assumptions is warranted. Some misrepresentation of the flow field on
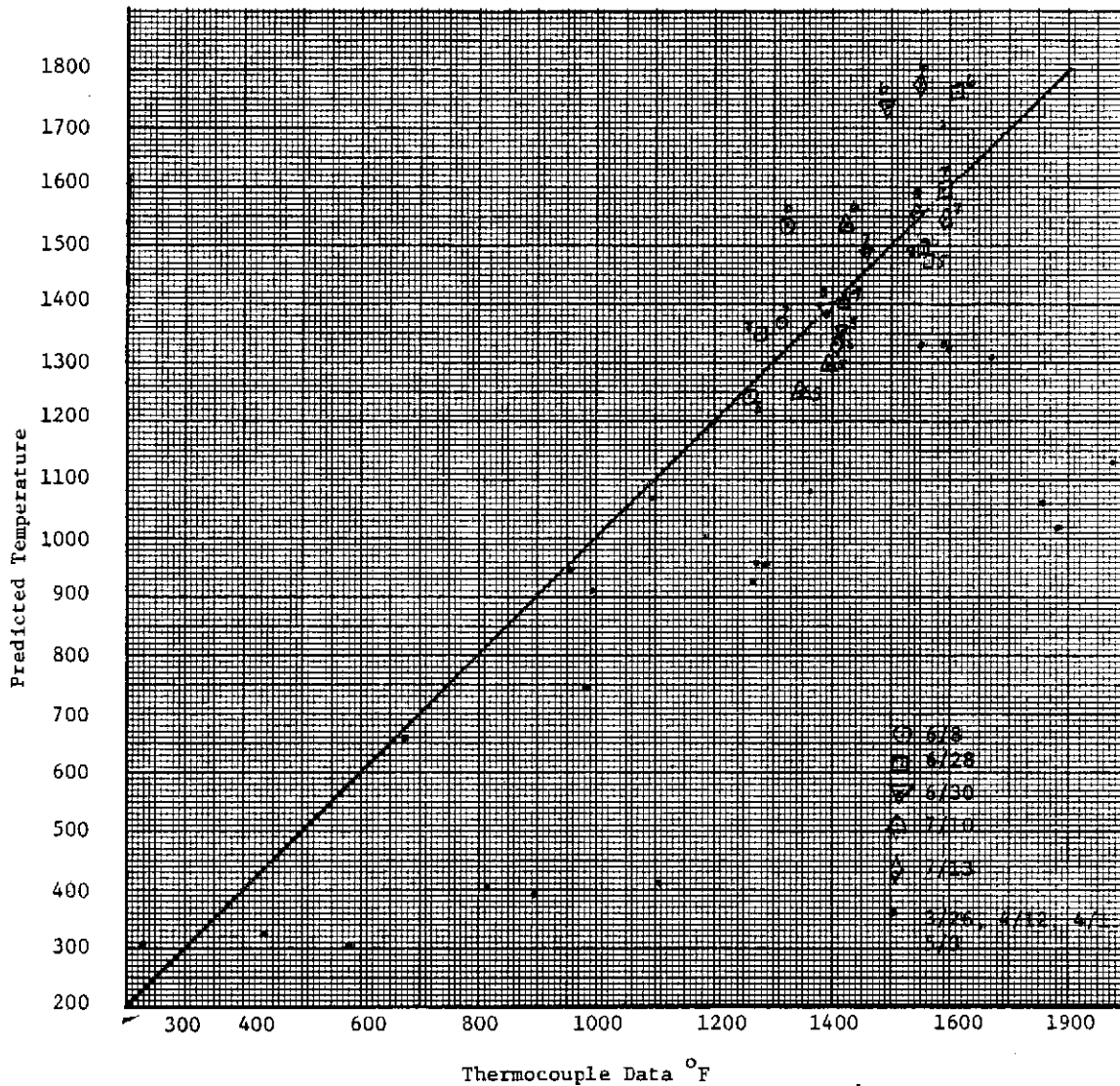
A computational finite difference approach has been used to predict the absorber
temperature as a function of the inlet temperature (RIT), local mass flow rate,
the actual geometry and material characteristics during solar operation.
Local data from stations 5, 6, 7, 8 (illustrated in fig. D1, appendix D) can be found
on Table 6. The open symbols represent data from tests conducted on the larger of
two absorbers (18.82 inches) where relatively good agreement exists. The points
are from tests on the small absorber. The poor correlation in attributed to our
inability to accurately determine the flow and flux distribution in the small cavity.

Figure 25.   Comparison Between Finite Difference Model and
             Thermocouples Located in the Solar Absorber

72

the back of the matrix must be attributed to the limitations of the cold flow tests. It is not possible to simultaneously simulate all the important dimensionless flow parameters. With minimal effort we were able to duplicate the Euler numbers in the inviscid cavity region. By accepting this, we were grossly misrepresenting the momentum parameters in the viscous dominated flow through the matrix. Applying the Poiseuille solution, the laminar pressure drop through the matrix is proportional to the product of the viscosity and velocity for both hot and cool simulations. From this standpoint, our cold flow test has underestimated the pressure drop through the matrix by a factor of approximately five. Alternatively, matching Poiseuille flow parameters will require the cold flow model to operate at more than 10 times the desired Euler numbers. To fully resolve this dilemma, either a more elaborate experimental set-up or a combined experimental/computational approach is required.

The purpose of this discussion is to suggest that some reallocation of the flow over the matrix may occur at the higher temperatures of the actual solar tests. The additional pressure drop over the absorber will produce some leveling of the velocity profile used as the basis of this preliminary analysis. Filling in the flow deficient stations with some of the high flow regions will move all predicted temperatures in Figure 25 into better agreement with thermocouple readings. Figure D4 of Appendix D illustrates this effect.

Another important factor not addressed in the analytical model is the radiative influence of the absorber stations on each other. Since the absorber is conically shaped, radiative exchange between elements on the absorber is significant. The analytical model has been set up to derive the solution for each station in radiative equilibrium with the cavity walls. The natural effect will be a redistribution of incident flux among elements. A leveling of temperatures on the absorber surface will therefore occur. This again will have a positive influence on the data correlation.

The results of this study allow us to reassess our underlying assumptions of the uniform solar flux distribution. It is significant that common stations from each of the five DTM tests (large absorber) appear nearly colinear and parallel, as well as demonstrating good agreement in Figure 25. This consistency suggests that there must be reproducibility of the flux distribution and the flow between tests. This is not to suggest that the flux distribution is uniform, but that it must have been quite consistent over the 2 month test period. It is very unlikely that the magnitude of variations indicated by the flux rake measurements at the focal plane could exist on the absorber plane in the DTM tests. The fact that the absorber is well behind the focal plane, and that radiative leveling occurs on the conical absorber, contribute to smoothing the distortions present at the

73

aperture. This argument therefore leads to the conclusion that the variations in temperature over the large absorber are attributed more to the distortions in the flow rather than the flux profile. By the same token, the inadequacy of the analytical model to predict the conditions on the small absorber suggests that flux distortions at the intermediate plane do exhibit some of the distortions indicated by the flux rake measurements. The small cavity tests, indicated by the points, do not illustrate the consistentcy between common stations at each test as does data from the large absorber tests.

3.2.7.6 Receiver Analysis Conclusions

In the previous section it was pointed out that variations in the temperature distribution on the absorber plane can significantly reduce the potential thermal efficiency of the receiver cavity. Both flux and flow distortions are present on the absorber plane, but it appears that most of the temperature variations on the larger cavity geometry are induced by poor air flow characteristics, while a combination of the two problems contributed to poorer performance on the small cavity design.

A great deal of effort was directed toward improving both the intercept factor and the flux distribution of the LEC460 by minor realignment and focusing. Little, if any, improvement was achieved. However, the study of the absorber temperature distribution and associated losses does suggest that flux distortions at the focal place need not cause serious problems on the absorber plane if its location is carefully optimized.

Temperature variations on the absorber caused by flow distribution problems can be resolved by additional modeling and testing. As with the flux distribution, these problems are reduced by enlarging the absorber area. Also, alternative cavity geometries have been proposed and tested. Analytic models developed on this program will provide the means to evaluate these cavity configurations to optimize performance.

The final step in the analysis of the receiver is to inspect the total energy balance of the solar collection system (concentrator and receiver). All factors which contribute to the loss of solar energy from the concentrator to the Brayton Cycle have been experimentally determined, except for the concentrator film reflectivity. The total reflectance integrated over air mass-2 solar spectrum is claimed to be approximately 86% by the manufacturer (product data in Appendix E). We recognize that this figure is highly susceptible to degradation from environmental factors.

Table 10 contains the pertinent performance factors for two of the tests previously discussed. These tests were chosen for this

TABLE 10. RECEIVER/CONCENTRATOR PERFORMANCE FOR TWO TEST POINTS AND DTM BASELINE CONDITIONS

| | ACTUAL OPERATING CONDITIONS | | DESIGN OPERATING CONDITIONS |
	6/28	7/13	
Insolation (KW/M^2)	.87	0.95	1.0
Effective Concentrator Area (M^2)	42.05	47.186	42.05
Reflectivity	0.83	0.86	0.86
Intercept Factor at 11 inches	0.84	0.78	1.00
Quartz Transmittance	0.92	0.92	.92
Exhaust Air Temp (°F)	1464.8	1434.5	1514.9
Inlet Air Temp. (°F)	1202.6	1022.0	1197
Mass Flow (LB/S)	0.1917	0.1690	0.24
Absorber Temp $\sqrt[4]{\Sigma T^4}$	1611.5	1555.8	1525.
Power at Focal Plane	30.05	38.74	33.27
Power into Receiver Cavity	23.50	27.80	30.61
Flux Absorber (KW/M^2)	122.4	144.8	140.3
Predicted Power Loss (KW)	−9.030	−7.948	−8.628
o Cavity Only Loss	−4.484	−3.887	−3.790
o Vessel Conduction Loss	−4.546	−4.061	−4.8381
Receiver Efficiency	0.566	0.657	0.661
Power to Engine (KW)	14.47	19.85	21.99
Comments on LEC 460 Quality	Original 24 facets with visible dirt and dust build up on reflective surface	3 addition. facets added and immediately following thorough cleaning	Assumed clean facets with 100% capture in 11 inch receiver aperture

Performance quantities relating to the collection of solar energy
and the conversion to a sensible heat rise in the engine work fluid
are presented for two tests and an extrapolation to design conditions.
The third column assumes the same receiver geometry as the two test
cases with the major difference being an improvement in concentrator
performance and on-design engine flow and temperatures. Uniform
flow and flux conditions on the absorber are assumed for the extrapolation.

analysis because they most nearly approach the original design point operating conditions for the receiver. Other solar tests did not achieve exhaust temperatures in a range appropriate for the Brayton cycle. The third column contains the baseline receiver input conditions. To calculate the receiver output for these conditions, the four analytical models developed in this section have been applied. The heat loss through the vessel was calculated empirically from the inlet and exit exhaust air temperatures. The absorber temperature was determined by assuming a homogenous flux and flow field over the actual absorber geometry. Window temperatures and cavity emission losses were calculated given the radiation characteristics of the cavity. The baseline analysis also assumes the modified concentrator size (24 facets as apposed to 27) but assumes an intercept factor of 100%. The intercepted factors for the two test points have been acquired through the flux rake measurements discussed in Section 3.2.1. The intercept measured for test 7/13 decreased from what was measured on 6/28 because of the addition of the three outboard facets.

The reflectivity values for each of the two experimental columns has been determined indirectly to achieve a consistent account of the available energy. The selections appear to be representative in light of the actual test environment. By 6/28, the concentrator had been exposed to about five months of winter and spring and was noticeably dirty. Prior to 7/13 the facets were washed with a portable power spray washer using a detergent solution and clear water rinse then several of the facets with deteriorated reflective surfaces were replaced. A rise of a few reflectivity percentage points was therefore anticipated.

In comparison to the 7/13 test point, upward extrapolations of inlet temperature, mass flow rate and solar input have been conducted to achieve the baseline conditions. With the exception of the solar input, the experimental test range has achieved or exceeded all of the other baseline operating requirements. The increase in inlet temperature and hence exhaust temperature will result in additional vessel conduction losses and cavity emission losses. The additional mass flow rate of the baseline engine will enhance the heat transfer characteristics of the absorber, and therefore, will act to keep down the absorber temperature. The increased solar input will produce a net increase in receiver efficiency, although the additional power on the absorber matrix will be accompanied by some elevation of cavity temperatures. This analysis concludes that the net effect of the positive and negative influences involved in the extrapolation to baseline conditions essentially cancel each other. Thus with this receiver geometry, and having simultaneously achieved the rated solar input, inlet air temperature and the mass flow rate (uniform over the absorber), a receiver efficiency of 65.4% was projected.

Virtually all of Sanders design and analysis since the start of the PDME program has predicated success of the Brayton system on obtaining a concentrator capable of providing a geometric concentration ratio of approximately 2000 or greater. Although previously uncharacterized, the LEC460 was chosen for PDME on the basis of its low production cost. At the preliminary design review (1/26/83) optimization studies were presented using LaJets' predicted concentrator characteristics which turned out to be very optimistic. A receiver aperture diameter of 6.8 inches (CR=1794) was selected on this basis. As the design proceeded, it became increasingly evident that, at least for preliminary tests, we would have to make do with much lower concentrator performance. Because of our concern to minimize the risk of overheating the receiver flange, and some reports of reduced optical performance from LaJet, the receiver aperture was expanded. The DTM receiver was thus designed and built with a 15-inch diameter quartz window lying behind an 11-inch diameter aperture in the graphite shield (CR=685).

Two factors have been identified as adversely affecting the performance of the DTM receiver. First, by using the graphite ring to define the 11" aperture, the diameter of the inside insulation next to the window had to be increased to 12.2 inch to avoid shading the absorber OD (see Figure 23). Reradiation losses from the cavity are therefore related to the 12.2-inch aperture. This is because radiation emitted from the cavity which intercepts this 0.6-inch wide outer ring is essentially lost, as it is either absorbed in the shield which has convective cooling or is absorbed in the quartz. Second, early-on in the testing it was determined through use of the flux rake that an intercept factor of only 80 to 85% was being achieved due to the reduced optical performance of the concentrator.

As the conclusion of this portion of the study, Table 11 lists the major contributers to the receiver's low thermal performance. An estimation of the significance of each area of improvement is possible through the application of the analytic models developed and tested on this program.

The potential vessel heat losses are obtained from a comparison of the SAGT-1A receiver operating at comparable temperatures. Detailed measurements on this receiver indicated that 0.89 KW were lost through the insulated vessel. Should the same design standards (no leaks, rigid insulation) been achieved, about 3KW would have been recovered in the DTM.

The second category is the losses attributed to the very large receiver window (low concentrated ratio). This potential loss value was obtained by first order approximation, by ratio of the baseline and existing window areas. In addition to this, other small gains could be realized by optimizing the cavity geometry.

TABLE 11.

POTENTIAL IMPROVEMENTS OF RECEIVER THERMAL EFFICIENCY AT BASELINE INPUT CONDITIONS

AREA OF IMPROVEMENT	Present Loss	Potential Loss	Non Cumulative Efficiency	COMMENTS
Vessel Heat Loss (Leaks, conduction)	4.84 KW	0.89 KW	0.765	Measured vessel conduction losses from SAGT-1A receiver at these same internal temperatures. The O.D. of the SAGT-1A is 29".
Cavity emission losses of 12.2 inch internal aperture	4.24 KW	1.32 KW	0.735	Increase geometric concentration ratio to 1794 (6.8 inch aperture) estimated by ratio $(6.8/12.2)^2$. The average radiating temperature of the absorber is expected to be 1586°F if flow non-uniformities are present.
Elimination of temperature variations on absorber attributed to flow field.	4.24 KW	3.79 KW	0.661	To achieve an exhaust temperature of 1515°F given uniform flow condition the absorber temperature is 1525°F. Under flow variations measured with the DTM receiver, an average radiating temperature of 1586°F was projected by the model.

THE CUMULATIVE EFFECT WILL BE AN INCREASE IN RECEIVER EFFICIENCY FROM 0.641 TO 0.858

The design operating conditions are stated in Table 11. However, the reference performance conditions for this table assume non-uniform flow conditions on the absorber. This is predicted to raise the average radiating temperature to 1586°F. The receiver efficiency will therefore be 0.641 with cavity losses of 4.24 KW. The maximum attainable receiver exhaust temperature at baseline inlet conditions is 1515°F with the LEC 460.

The third row in Table 11 contains an estimation of the potential improvement which can be obtained by attaining uniform flow over the solar absorber matrix. At these low flux levels, the analytical modeling indicates that an average radiating temperature of 1585°F did occur under non uniform flow conditions and that under uniform flow, the matrix temperature would drop to 1525°. Than with uniform flow over the absorber, losses would be reduced by about 1/2 kW over the existing non-uniform flow condition.

The cumulative result of all three categories is determined by summing the potential gains in rows 1 and 2 plus (6.8/12.2)2*(4.24-3.79) kW for the row 3 effect. Given the expected efficiency of 64.1% for the DTM configuration with existing non uniform flow in the cavity, these modifications will increase the efficiency to 85.8% for the exhaust temperature of 1515°F.

Appendix H describes and illustrates the DTM receiver and compares it with the projected 120 kWt ABC receiver design. Design changes for improved performance are also discussed.

3.2.8   ENGINE ANALYSIS

This section contains the data obtained by Sanders to PDM tests of the AirResearch Mark IIIa engine. Also included is a parametric sensitivity analysis of those factors which have been identified as the source of the dominant efficiency losses. The centrifugal compressor performance, system leaks and the low temperature ratio are sited as the major contributers to the poor PCA performance. Details and results of the leak tests are described in Section 3.2.3. The cycle temperature ratio, defined by the ratio of turbine inlet to compressor inlet temperatures, can be obtained from the state point temperature presented in Table 12. These state point number designations relate to Figure F1 in Appendix F. Compressor efficiency, measured under nonadiabatic conditions during these DTM tests, has also been derived from this tabulated data.

The compressor map supplied by AiResearch for this compressor is shown in Figure 26. This map represents the design performance characteristics for the Mark IIIA SABC and has been obtained by scaling the characteristics of their commercial F15 impeller. Some mass flow rate, pressure ratio, and speed data obtained from AiResearch has provided spot check verifications on the map. However, no data has been made available to verify the efficiency predictions. Also, the shape of the speed curves is subject to question since no characterization data is available with the actual inlet section and diffuser. Nonetheless, the steady state operating points attained from pressure ratio and speed measurements are located on the map (Figure 26).

Total Pressure Ratio

2.8

2.6

2.4

2.2

2.0

1.8

1.6

1.4

1.2

1.0

$\frac{N}{\sqrt{\theta}}$ = 85,000 RPM

Figure 31. The 10 DTM test points and their test dates have been located on this compressor map supplied by Airesearch

80,000

70,000

60,0000

50,000

40,000

7/9A

6/28

7/9P

6/8P

6/30

7/25

6/8A

7/13

7/10

8   12   16   20   24   28   32   36   40   44   48   52   56

Corrected Mass Flow Rate (lbs/min) $W(Pol/P\infty)/\sqrt{Tol/T\infty}$
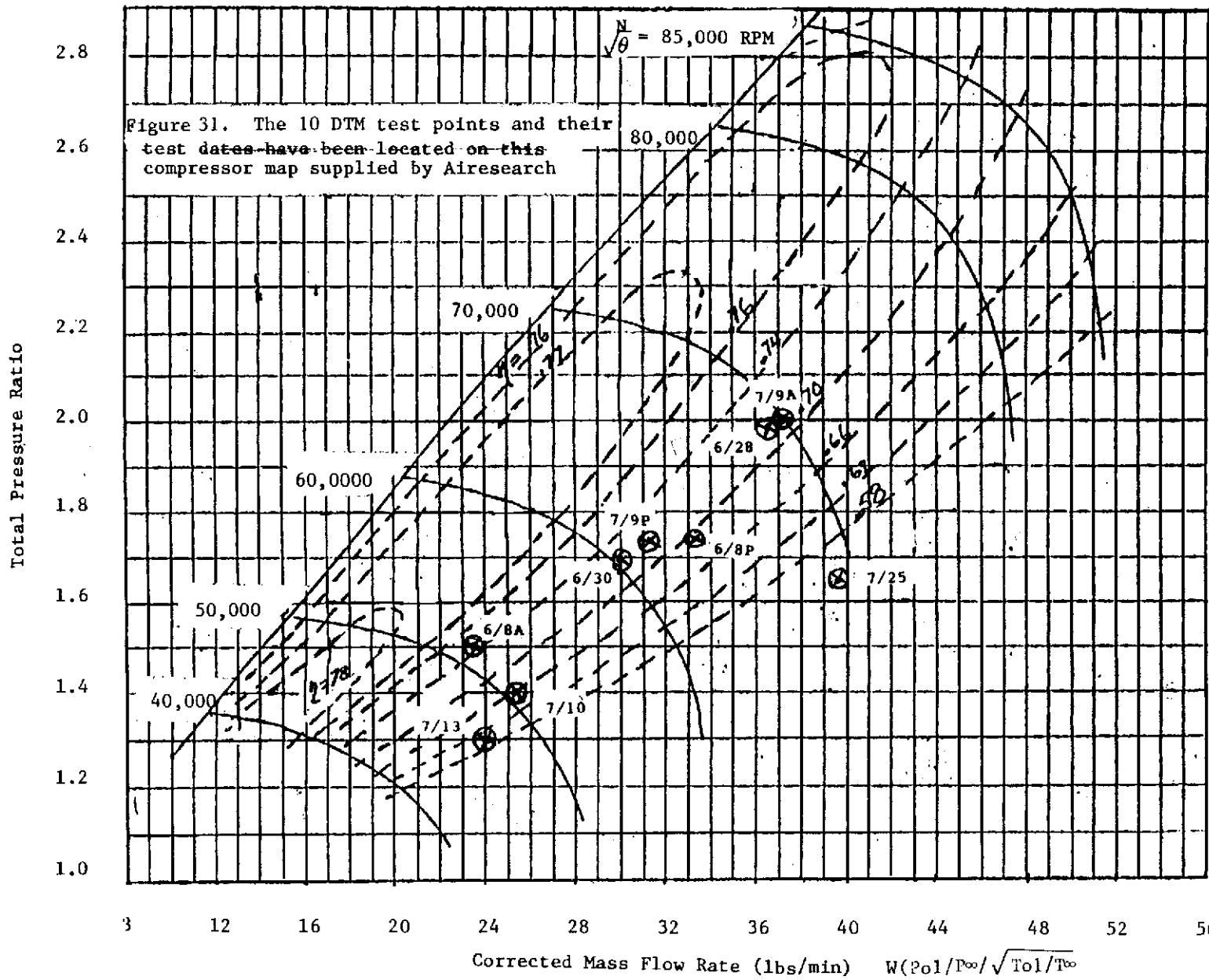
Figure 26. Estimated GRI Brayton Compressor Performance

TABLE 12. DTM DATA SETS FOR 11 STEADY STATE CONDITIONS

TABLE 12.

DTM DATA SETS FOR 11 STEADY STATE CONDITIONS

TEST DATE	6/8A	6/8P	6/28	6/30P	6/30P	7/9A	7/9P	7/10	7/13	7/25
ENGINE SPEED (KRPM)	54.9	69.7	75.0	65.0	64.9	74.7	66.7	53.0	50.9815	74.8
CORRECTED SPEED	51.11	63.8	68.9	60.6	60.3	68.6	62.3	50.2	47.9	59.3
TURBINE INLET TEMP ($^\circ$F)	1259.3	1451.8	1598.3	1353.2	1347.7	1607.8	1475.7	1236.6	1261.2	1562.2
Tamb ($^\circ$F)	90	94	80	75	76	76	76	74	82	85
TO1	138.8	158.7	138.9	137.4	141.6	144.4	135.8	118.9	128.1	144.0
TO2	252.6	329.6	339.7	291.7	292.7	335.5	292.6	226.7	235.2	339.5
TO3a	1010.7	1134.0	1224.1	1071.5	1060.5	1215.1	1142.4	999.7	1029.0	1184.2
RIT	982.8	1107.3	1202.6	1056.1	1032.9	1190.3	1114.4	979.3	1022.0	1152.8
RET	903.1	1313.0	1464.8	1400.7	967.9	1062.2	1021.7	1302.7	1434.5	1048.5
TO4b	903.1	1302.9	1440.5	1375.5	975.9	1067.1	1029.4	1274.8	1386.6	1057.0
TO6a	1101.1	1220.4	1313.1	1141.8	1141.0	1311.9	1236.0	1075.2	1114.4	1273.2
TO6b	1062.5	1172.2	1256.9	1095.4	1095.0	1257.6	1184.	1027.2	1062.6	1225.9
TO7a (BELLOWS)	477.7	581.3	609.4	546.3	532.4	592.8	540.2	470.1	501.9	576.1
TO7b	491.3	584.3	622.4	552.2	533.7	628.3	562.9	488.0	528.1	608.2
PO1 PSIA	10.2	8.45	7.79	8.60	8.65	7.34	8.44	9.73	11.39	9.09
PO5	14.35	14.16	14.19	14.24	14.22	14.48	14.52	14.63	14.64	14.17
ΔPrec (IN.H2O)	0.46	.859	1.80	1.74	1.38	1.85	1.59	1.57	2.28	1.61
P2/PO1	1.44	1.74	1.88	1.71	1.70	2.00	1.74	1.51	1.29	1.62
Tabs (MAX)	950.0	1627.	1839.	1855.	1003.	1124.	1064.	1656.	1733.	1109.
Tabs (MIN)	887.	1253.	1426.	1374.	956.	1046.	1005.	1258.	1388.	1029.
Tabs (AVG)	920.	1403.	1607.	1559.	975.	1085.	1030.	1461.	1548.6	1065.
Tcav (AVG)			1278.3	1207.9	908.8	992.3	964.6	1127.5	1217.1	985.5
TW (INSIDE T.C.)			1031.6	980.0	741.8	813.8	796.6	995.7	856.8	1104.4
TW (OUT T.C.)	222.4	765.0	574.4	641.0	293.9	264.6	272.3	800.1	739.3	289.8
DC VOLTS	215.5	249.1	230.27	244.06	243.09	243.10	236.90	211.30	203.50	245.45
DC AMPS	3.85	8.34	15.51	6.09	6.06	13.10	9.20	3.08	2.86	12.10
GRID AC (KWe)	0.16	1.70	2.89	1.46	1.138	2.56	1.73	0.457	.4079	2.410
FUEL FLOW (LB/HR)	3.67	4.57	5.87	3.93	5.93	4.23	3.96	4.24	<0.5	4.37
FUEL HEAT ADDITION KW	22.70	28.27	36.27	24.26	36.65	26.11	24.48	26.21	-	27.00
CONCENTRATOR AREA (M^2)	43.80	43.80	43.80	43.80	43.80	43.80	43.80	49.28	49.28	49.28
INSOLATION KW/M^2	0	.805	.871	.908	0	0	0	.877	.95	.90
NEW/OLD FOCUS	OLD	OLD	OLD	OLD	OLD	OLD	OLD	NEW	NEW	NEW

Temperature and pressure state point designation numbers are shown in Figure F of Appendix F. Average absorber cavity and window temperatures are also summarized. Alternator output voltage, and current and inverter integrated power output are tabulated. Fuel flow measurements and the direct solar insolation were also measured.

Mass flow rates through the receiver and at other state points have been determined by considering the system as a balanced flow circuit. The infiltration rates (measured where indicated on Table 13) are therefore contributions of the total mass flow derived from the compressor map.

The compressor and turbine inlet pressures and the receiver pressure drop were continuously monitored with transducers for the 10 DTM tests and are presented in Table 12. A more complete account of state point pressures (designated in Figure F) was gathered on test 7/9 and is shown in Table 14. In these tests, water manometers were used at each pressure tap supplied with the SABC assembly.

From the state point information in Table 11, the total compressor efficiency has been calculated. These values are compared to the efficiency predictions displayed on the compressor map. The discrepancy displayed in Table 15 is attributed primarily to two effects:

1. Aerodynamic design defects within the compressor section.
2. The nonadiabatic circumstances under which data was obtained.

The compressor consists of the inlet ducting, the impeller section, and the diffuser and scroll sections. The most significant aerodynamic inefficiencies are thought to relate to the poor inlet flow field propagating into the inducer section and the non-optimum diffuser design. The inlet flow field is caused by the constricted duct work joining the compressor to the heat sink. These issues are discussed further in this section. The tubular diffuser is acknowledged to be a problem by AiResearch but far more instrumentation would be required to quantify its performance.

The magnitude of the error introduced by heat flow between the back-to-back turbocompressor assembly is dependent upon the working temperature differential and the thermal impedance. Blueprints of this engine show a disk of insulation between the turbine and compressor which tapers from about 0.2 inches near the shaft to about 0.4 inches at the outer diameter. Having viewed the actual unit assembly, an estimate of 0.2 inches over the full surface appears to be a realistic assumption. In this case, the estimated effect at full temperature would produce an under-estimation of compressor efficiency by a maximum of two percentage points.

In addition to the lower than expected efficiencies across the compressor map, the operating points are shown in Figure 26 to be well outside the most efficient region. This problem is attributed to the high pressure drops and especially system leaks. The matching points between the compressor and the system at turbine inlet temperature of

82

TABLE 13.

DTM BRAYTON CYCLE MASS FLOW RATES (LBM/S)

TEST DATE	6/8A	6/8P	6/28	6/30A	6/30P	7/9A	7/9P	7/10	7/13	7/25*
COMPRESSOR MAP	.238	.282	.279	.279	.278	.272	.286	.282	.247	.272
LOW PRESSURE SIDE LEAKS	.0047	.0077	.0087	.0067	.0067	.0087*	.0067*	.0047	.0047	.0087
BEARING BLEED	.024	.024	.024	.024	.024	.024	.024	.024	.024	.024
RECEIVER UPSTREAM LEAK	.00095	.00195	.0022	.0017	.0017	.0022*	.0017*	.00095*	.00095	.0022
RECEIVER DOWN STREAM LEAK	.00255	.00505	.0058	.0043	.0043	.0058*	.0043*	.00255*	.00255	.0058
COMBUSTOR MAKE UP	.0446	.0457	.0488	.0455	.0455	.0417*	.0490*	.0469	.0469	.0466
TURBINE	.209	.2503	.2463	.2483	.247	.2392	.2454	.2533	.2184	.239
RECEIVER	.1621	.1996	.1917	.1985	.1971	.1917	.2020	.2039	.1690	.1920

83

The Brayton Compressor flow has been determined from the measured speed, pressure ratio, and inlet temperature using the modified FI5 compressor map. Make up flow is assumed to be 18.7% of turbine flow (measured average of two 7/9 data points).

* Indicates measured data points, all else calculated. Bearing bleed flow measured at AiResearch and modified for Sanders system.

TABLE 14.

PRESSURE TAP MEASUREMENTS ON TEST 7/9 AT
THREE OPERATING SPEEDS

STATE POINT	AIRESEARCH LOCATION	50,000 RPM	65,000 RPM	75,000 RPM
1	COMPRESSOR INLET (STATIC) (psia)	10.40	8.44	7.34
2	COMPRESSOR OUT, STATIC (inwc)	0.0	0.0	-0.1
3a	RECEIVER IN, STATIC (inwc)	-1.54	-0.71	-0.60
4a	RECEIVER OUT, STATIC, (inwc)	-1.65	-2.2	-1.85
4c	SERVICE HX OUT, STATIC (inwc)	-1.75	-2.30	-2.03
5	TURBINE INLET, ˜TOTAL (inwc)	-9.28	-14.5	-17.0
6a	TURBINE OUT, STATIC (psia)	13.59	13.31	13.24
6b	RECUP. HOT IN, STATIC (psia)	10.65	8.695	7.70
7b	SINK HX IN, STATIC (psia)	10.54	8.876	7.36

All of the pressure taps supplied with the SABC were read from water manometers on this test date only. These results are highly question-able since static taps were made from straight 1/8" tubing protruding into the flow, perpendicular to the stream lines. Also the only total tap, at the turbine inlet, was 1/8" tubing bent to 90° but was rotated about 37° and, therefore, was not parallel to the flow. Negative signs indicate the pressure referenced to the barometric pressure datum of 14.6 PSIA. The ambient temperature was 76°F.

TABLE 15. COMPARISON OF CALCULATED COMPRESSOR EFFICIENCIES
TO GRI MAP PREDICTIONS

DATE	To1	To2	Pr_c	ηtt	ηmap	Nc krpm
6/8A	138.8	256.6	1.50	0.606	.745	51.11
6/8P	158.7	329.6	1.74	0.602	.60	63.8
6/28	138.9	340	1.88	0.570	.71	68.9
6/30A	137.4	279.7	1.70	0.666	.72	60.6
6/30P	141.6	"	1.71	0.699	.72	60.3
7/9A	144	335	2.00	.693	.71	70.0
7/1P	135.8	292.6	1.74	.670	.715	62.3
7/10	119	226.7	1.4	.531	.66	50.2
7/13	128.1	235.2	1.3	.416	.62	47.9
7/25	144	339.5	1.62	.442	<55	69.3

THE TOTAL – TOTAL COMPRESSOR EFFICIENCY HAS BEEN
CALCULATED IN THE FIFTH COLUMN. NONADIABATIC
CONDITIONS WERE PRESENT AND THEREFORE MAY CAUSE
SOME MISREPRESENTATION. COLUMN 6 CONTAINS
VALUES TAKEN FROM FIGURE 28.

compressor and the system at turbine inlet temperature of nominally 1600°F (tests 6/28, 7/9A, 7/25) is shown on the map to be near the choked region. High compressor inlet temperatures experienced in all tests actually contributed to moving the operating points to the left (away from choke, towards the surge line) of where they otherwise may have occurred. However, this small benefit to the compressor efficiency resulting from the decrease in inlet Mach numbers was certainly outweighed by the detrimental effect of the low cycle temperature ratio.

SABC ADVANTAGES AND DESIGN LOGIC

The SABC concept is very different from other gas turbine systems and incorporates several unique features. The heat pump application for which it was designed demanded high efficiency and reliability to crack a very competitive market. Some of the economic attractiveness of this cycle lies in its ability to utilize relatively low cost natural gas fuel. Two key features which strongly influenced the cycle concept were:

1. The ability to utilize low pressure natural gas while avoiding the penalties associated with a fuel pump and

2. the potential commercial OEM market which could use units producing shaft power below the normal range of high efficiency turbocompressors.

To utilize commonly available low pressure natural gas, the combustor operates at nominal atmospheric pressure. This design feature allows the combustion section to resemble and operate within the limits of conventional gas heating systems. Avoidance of the gaseous fuel boost pump was motivated by the cost and reliability goals, as well as the desire for low parasitic power requirements.

The consequence of maintaining the heat addition side of the Brayton cycle at atmosphere is that the low pressure, heat rejection end must operate at a partial vacuum. Also, since the recuperator is connected to the compressor intake through a heat rejecting heat exchanger, the cycle is schematically closed. The cycle is vented at two points, to aspirate the combustor and to vent the system at the compressor discharge.

Several advantages of this subatmospheric configuration arise as a result of the low working fluid densities. From aerodynamic similitude relations it can be shown that scaling of the turbine and compressor is approximately inversely related to the gas density ratio. That is to say, a conventional compressor designed to intake at atmospheric pressure will pump only half its design mass flow at an inlet pressure of 1/2 atmosphere. This is of particular interest

86

since the power levels for this application require turbomachinery close to the generally accepted size limit for reasonable efficiency. To produce 10 HP from an open cycle would require 3 inch diameter or smaller rotors while in the SABC configuration the more commonly available 4 inch components are optimal. As well as improving the availability of fully characterized components, first order improvements in isentropic efficiency are realized with larger wheels.

When scaling down rotor sizes, as would be required for the 8 KW (10HPs) open cycle, several design factors will not readily scale in this size range. Frozen dimesions such as blade thicknesses fillet radii and blade-to-shroud clearances are serious limitations, for sub-3 inch compressors especially. Frictional effects would have a less severe performance penalty in the higher Reynolds number components and, therefore, would favor the smaller open cycle unit. All in all, the impact of these scaling effects on compressor and turbine efficiencies becomes increasingly adverse as the "wheel" diameter decreases. A survey of components, primarily those used in the turbocharger industry, suggests that the achievable efficiencies for the 3 inch families is about 4 to 6 points below that for the 4 inch turbocomponents.

3.2.8.2   Disadvantages of SABC and Comparisons to Open Cycle

The closed cycle SABC has several distinct disadvantages when compared to the more common recuperated open cycle. This discussion centers around those features which specifically distinguish the closed cycle from the open cycle. The most significant disadvantage inherent in the SABC engine is the necessity for a sink heat exchanger and the means by which the cycle must be altered to accept fresh air into the combustor. Other problem areas that are not necessarily inherent characteristics of the SABC concept are discussed in the next section.

To analyze the SABC loss mechanisms we have assembled the SABC engine parameters into a thermodynamic model of the Brayton system. This model is used to evaluate the sensitivity of PCA efficiency to variations in a selected parameter under a fixed set of baseline conditions. The assumed baseline conditions (listed on each curve) represent each component operating at or near its maximum potential. The operating temperatures reflect test point conditions for which data was obtained. These curves cannot be evaluated individually as none of the parameters of interest can actually be isolated from other parameters in the study. This is because secondary effects occur as a result of the interrelated influence of one parameter on another. In fact, losses resulting from secondary effects may in some cases be greater than the loss directly attributable to the primary effect. With respect to the sensivity curves presented in the sections to follew, generally, only the primary effects are illustrated.

87

HEAT SINK AND RELATED PROBLEMS

The requirement for a heat exchanger on the low temperature end of the cycle introduces several losses. In the SABC the recuperator exhaust gas must run through an external sink heat exchanger before it enters the compressor. A stainless steel heat exchanger and an electric blower are employed for this function. The blower provides approximately 1800 SCFM (a factor of 4 more than the engine flow) through a crossflow heat exchanger. The electric power consumed by the blower is approximately 500 watts.

The heat sink affects the cycle performance in three ways, and the penalties are the same as those incurred in external combustion engines such as the Stirling and Rankine cycles. Direct engine efficiency losses result from the rise in compressor inlet temperature (reduced temperature ratio), the additional pressure drop in the device and associated ducting, and the parasitic power consumption of a blower. Also important are the effects on overall system reliability and cost.

A low compressor inlet temperature resulting in a high temperature ratio improves thermodynamic cycle efficiency. Since the heat sink must be cooled by ambient air, the engine performance suffers due to the inefficiencies of this process. Furthermore, it is shown by the Carnot relation that the cycle is most sensitive to changes in the low temperature end. This is exemplified by noting that the effect of raising the compressor inlet temperature by 60°F over standard ambient conditions would require the elevation of the turbine inlet by 238°F to achieve the same temperature ratio. However, such an elevation of the hot section temperature is not feasible for most gas turbines because it would significantly reduce engine life. The design condition of a 40°F differential between compressor inlet and ambient temperature was not achieved during the DTM tests, Due primarily to a combination of lower than expected heat sink effectiveness and higher than expected recuperator exhaust temperatures, the compressor inlet operated in the range of 60°F to 80°F above ambient conditions. Some of the reduction in effectiveness of the heat sink has been attributed to the poor inlet flow distribution in the overly compact blower/heat sink manifold. Also corrosion within the heat exchanger core may have degraded the heat transfer effectiveness.

Figure 27 illustrates the influence of compressor inlet temperature on cycle efficiency. The baseline condition assumes that a compressor inlet temperature of 100°F will be achieved at an ambient temperature of 60°F. The baseline efficiency of 19.6% is shown to degrade two percentage points as a result of an actual rise in compressor inlet temperature of about 20°F.

FIGURE 27. SENSITIVITY OF PCA EFFICIENCY TO COMPRESSOR INLET TEMPERATURE

ALTERNATOR EFFICENCY   82 %
COMP INLET PRESS 6.125 PSIA
COMP PRESS RATIO   2.4'
MASS FLOW RATE   .23 LBM/S
TURBINE EFFICENCY   64 %
RCUP EFFECTIVENESS   90 %
COMB EFFICENCY   95 %
MECH EFFICENCY   94 %
THERMAL LOSSES   2 KW
PRESSURE DROP   8 %
SEAL LEAKAGE   10 %
COMP INLET TEMP 40 or 160 F
TURBINE INLET TEMP   1600 F'
COMP EFFICENCY   78%
AMBIENT TEMP   59 F

EXCLUDING RCVR THERMAL LOSSES
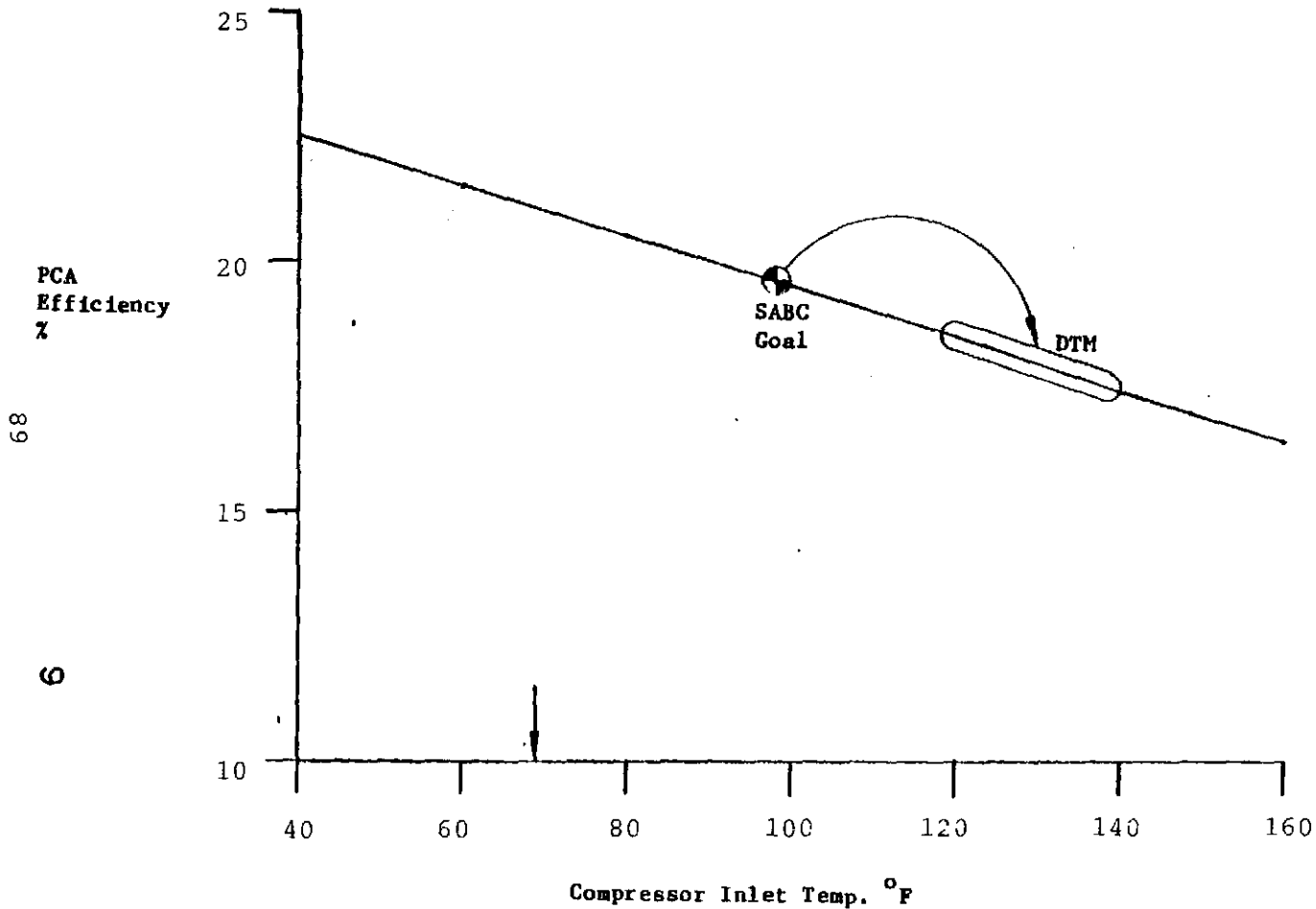
Higher than expected heat sink inlet temperatures (recuperator exhaust) occurred primarily due to the inefficiency and off design conditions within the recuperator and the low expansion ratio at the turbine. This illustration of the influence of the heat sink on the SABC cycle can be generalized as follows:

Closing the cycle causes the performance of each component in the cycle to be affected by the performance of every other component in the cycle. Thus, a change in the performance of any component (be it the recuperator, compressor or other) propogates reduced performance throughout the cycle by shifting the other design peaks. Furthermore, it can be demonstrated that the effect of any non-optimum component ultimately results in a rise in compressor inlet temperature.

In the open cycle, the compressor cannot be subjected to inlet temperature and pressure variations from other components within the cycle since there are no upstream components. This greatly simplifies the design and limits the risk in reaching performance goals. By adopting the open cycle Brayton, the potential for the cyclic propagation of negative effects is broken. Neither the highly influential compressor inlet temperature nor the inlet flow conditions can be altered by upstream component characteristics.

The manifolding between the compressor and the heat sink has complicated the design of the SABC compressor. Upstream flow conditions have a strong influence on the design of the inducer section of the compressor. Distortions in the entrance region of the impeller decrease efficiency and promote aeroelastic vibration.

In the absence of a requirement for variable inlet geometry (radial or axial inlet guide vanes), the preferred flow conditions consist of straight axial flow with thin shroud boundary layers. Any deviation from this simple case requires detailed calculations in order to ascertain the velocity distribution and hence the levels of incidence, along the radial extent of the blade's leading edge.

The Garrett SABC utilizes a cast volute to surround the angular space betwen the alternator and the impellor. This casting terminates with a rectangular flange. A transition duct with sharp 90° bends in two planes is required to mate to the heat sink manifold. The presence of these sharp 90° elbows at the mouth of the inlet volute suggests the need for a combination of experimental work and quasi-three dimensional analysis. Adding to this complexity is the varying temperature and pressure at the compressor inlet in this region which is characteristic of the heat sink discharge. Furthermore, as a consequence of three 90 flow redirections in a meridional distance of less than 18 inches, flow instabilities are likely. Also, imposing a

strong static pressure gradient on a complex velocity gradient will introduce secondary flows and hence vorticity. In acknowledgement of this situation AiResearch employed flow splitters in the vicinity of the impeller. However, due to the extremity of this situation, only limited success resulted.

These complications must certainly be considered as factors. in the disappointing performance of the SABC compressor. The impeller design was taken from a successful air cycle machine (ACM) used on the F-15. Apparently,only minor modifications were made in adapting it for the SABC. On the F-15/ACM, very good adiabatic efficiencies of 78% to 80% are reported. However, under controlled laboratory conditions at AiResearch in SABC test rigs, no more than 70% has been reported. As a result of other problems discussed later in this report, Sanders estimates from many measurements that the compressor operated with an adiabatic total-static efficiency of 60 to 64%.

SABC COMBUSTOR AND RECUPERATOR DESIGN

As a result of internal combustion, the bulk of the working fluid is composed of nitrogen and the products of methane combustion. To satisfy the stoichiometric requirements of combustion, a theoretical air:fuel ratio of 17.3:1 (by mass) is required. The air introduced upstream of the combustor must at the very minimum, satisfy this requirement. To take into consideration actual non-optimum mixing effects, some excess air should be designed into this process to ensure safe and efficient combustion. However, introduction of ambient temperature air at this point in the cycle represents a thermodynamic loss, so there is an incentive to minimize the excess.

The venting of exhaust gas from the actual MOD I SABC engine occurs in the recuperator entrance manifold. Atmospheric pressure is established at this point in the cycle by an exhaust port in this plenum. The subatmospheric pressure (-2 to -3 in. WC) in the combustor is therefore developed by the fluid pressure drop through the recuperator.

COMBUSTION AIR INTAKE

Schematically the make-up air for combustion is drawn through a dedicated portion of the recuperator. Two segregated flow paths must therefore be provided through the heat addition side of the recuperator. The major portion is allocated for the compressor discharge flow (minus that which is vented) while a smaller section is provided for the make-up combustion air. The proportioning of the make up flow is accomplished by partitioning the entrance region of the recuperator. Having first determined the quantity of fuel to be burned, we can readily determine the percentage of the total engine mass flow which must be exchanged for fresh air. A reasonable design

selection would be 120% of the ideal stoichiometric requirement. The proportioning of the entrance areas for the mainstream compressor discharge and the make-up air is not simply the same as the ratio of mass flow rates. Since the temperature of the compressor exhaust is approximately 260°F higher than that of the make-up air, a correction must be applied to balance the pressure drop for each flow path through the recuperator. This factor tends to increase the area allotment or the hotter passages by approximately the square root of the temperature ratio. Based on the expected conditions, this factor is about 1.2. From these design approaches, the partitioning of the recuperator to allow the proper quantity of make-air to enter the combustor can be determined.

The loss of enthalpy from the cycle occurs because a portion of the compressor exhaust is replaced by the ambient temperature make-up air. From an overall efficiency stand point, it is not quite as bad as simply the difference between the exhaust enthalpy and the intake. Since the temperature of the make-up air is lower than the vented gas, more heat will be transferred to it from the waste heat (turbine exhaust) than would otherwise be the case. In other words, due to the high effectiveness of the recuperator, the cooler make-up air will recover more of the waste heat than the same quantity of warmer gas when passing through the same portion of the recuperator. The net loss to the cycle is therefore the difference between the enthalpy exhausted on the heat addition side and the portion of this which is recovered by the make-up air from the heat rejection side.

Considering the ideal assumptions from which AiResearch likely based their initial calculations, the net impact of the combustion air on overall efficiency can be shown to be small. For instance, assuming that 8% of the design engine mass flow (0.23 lbm/s) is required for make-up combustion air, approximately 5% of the heat addition is vented but 80% to 90% of this should be recovered by the make-up air in the recuperator. The net effect is therefore theoretically 1% or less. In practice, however, the inefficiencies resulting from this situation were demonstrated to be far more significant.

It appears from inspection of the hardware that the partitioning of the recuperator was based on the assumption that the engine performance would meet its original high efficiency goals of about 30% (fuel to shaft). When the hardware was originally designed and fabricated, AiResearch's expectations of fuel flow were a factor of 2 or 3 below what was ultimately needed to deliver the rated shaft power. This erroneous premise lead to an improper allocation of make-up flow. The allocated portion of the recuperator was only capable of intaking less than half of what was required in the combustor. The proper solution would have been to move the partition to provide more flow area for the make-up air. The other option was to decrease the

92

resistance of the make-up air flow path to the combustor without changing the original design. AiResearch chose the latter fix. Over the course of testing a relatively large hole was put through the plenum wall to allow fresh air to directly enter the combustor without preheating.

Although plenty of air was now made available for the combustion process, this method was self-defeating. Since relatively large quantities of unpreheated air entered the combustor, efficiency decreased and the fuel requirement was further increased. One other design oversight further accentuated this problem: the make-up air was not plumbed through the solar receiver as it should have been. Only the mainstream gas was ducted through the receiver, thus raising the resistance of this circuit relative to the make-up air. Upon adding the solar receiver for the acceptance test, even greater ingestion of make-up air resulted. Measurements made toward the end of the DTM testing indicated that the make-up flow was approximately 20 to 25% of the total design engine flow rate. Since the makeup air portion of the recuperator could accommodate only about 6%, the bulk of the primary combustor air was at ambient temperature.Most of this air replacing the vented gas does not get preheated from the waste heat stream and thus less heat recovery occurs in the recuperator. The energy lost from the cycle is therefore approximately 9 kWt, and must be made up by an increased fuel flow to the combustor.

The mishandling of the makeup air impacts the cycle in an other way. Since the total flow through the heat addition side of the recuperator core is lower than expected, the exhaust temperature to the heat sink increases. This, in turn, contributes to the rise in compressor inlet temperature.

A degradation of receiver efficiency is the other direct consequence of allowing the large quantity of makeup air to enter the combustor directly. The effect of reducing the mass flow through the receiver raises the opererating temperature of the solar absorbing media and thus increases reradiation losses. This effect has not yet been quantified but will be addressed in detail in the DTM test report.

Late in the DTM testing, being only partially aware of this problem, Sanders added a throttling butterfly valve to shut off this cool air ingestion while in the "solar-only" mode of operation. At the time, the existence of the unrestricted flow path into the combustor was not known. The modification was made primarily to limit the ingestion of cool air while the combustor was not being used. It could not be used while in the fuel mode since the combustion requirements had to be satisfied. Moreover, during solar only operation, only part of the benefits of eliminating the intake were realizable. By starving the make-up air portion of recuperator

altogether, the recuperator continued to operate below specification. Also, the pressure drop was elevated because the total engine flow was forced through about 92% of the available heat exchanger core.

In summary, the mishandling of the make-up air was one of the primary contributers to the poor performance of the SABC. As pointed out in the initial discussions, if executed properly, make-up air intake for internal combustion could have been accomplished with only a minor penalty. However, in practice, the problems were magnified. Rigorous testing and some trial iterations were required to properly diagnose and solve these problems.

The open cycle recuperated Brayton configuration avoids all of these complications. Internal combustion is accomplished with commonly available hardware. Since all of the working fluid upstream of the combustor is air, the recuperator design and manifolding is simplified as well. The losses associated with venting enthalpy on the heat addition side of the cycle are avoided entirely.

From what has already been written it should be evident that the problems experienced with the DTM SA8C are a result of factors which inherently render the closed cycle particularly vulnerable to errors in hardware design or implementation. The open cycle avoids the many potential losses associated with the heat sink and the particular combustor arrangement.

AIR BEARINGS AND THEIR EFFECT ON THE SABC

Although gas or air bearings are not specifically required for the SABC concept, significant development has been dedicated toward their incorporation into this engine. The pros and cons of their use in this application should be reassessed, and certainly more developmental testing is required.

There is no doubt that gas bearings have gained widespreadacceptance in several areas of turbomachinery. The AiResearch Air Cycle Machines (ACM) and cooling turbines utilizing air bearings have demonstrated a significant life improvement over the earlier ball bearing units. Also, the rotating speed threshold has been increased. This technology was applied to the SABC engine.

Although the AiResearch line of ACMs operates with nominally the same bearing loads and shaft diameters as the SABC, they are clearly not gas turbine engines. These ACMs are utilized to supply pressurized air to the cabins of many commercial and military aircraft. In essence they are turbines and centrifugal compressor mounted on the same shaft,much like a turbocharger. They do not operate with a combustor nor do they operate near the temperatures characteristic of today's gas turbines. Typically the turbine drives

94

the compressor by extracting work from the auxiliary power unit (APU) exhaust. APUs are gas turbines since they provide stand-alone power to the aircraft. All of AiResearch's APUs utilize oil journal or ball bearings.

Because air bearings require a relatively large surface area to produce the journal effect needed to float the shaft, they are responsible for a large amount of windage and shaft work. The SABC engine requires a 1.4-inch diameter by 1.4-inch wide foil journal bearing plus a 2.8-inch outer diameter thrust bearing to perform the same function as one 3/8-inch diameter by 1/4-inch wide ball bearing in the WR34 engine. The aerodynamic friction and windage of the SABC air bearings is estimated to consume approximately 800 watts,or about 12% of the maximum shaft power. A functionally equivalent oil spray lubricated ball bearing unit uses only 2 to 3% of the available shaft power.

Large quantities of power dissipation within the bearings gives rise to additional cycle inefficiencies. More than 10% of the engine mass flow was required for cooling to maintain safe temperatures on the foil coatings. To avoid the use of a rather large electrical parasitic pump, the SABC design utilizes the suction created by the engine centrifugal compressor to draw ambient air through the bearings. In order to sustain this condition the compressor was required to pump 10% more mass flow than the turbine. Leaks on the low pressure side of the cycle compounded this same effect.

Two detrimental effects resulted which directly decreased the system efficiency. First, there is no way around the fact that the increase in the power consumption of the compressor reduces the net output shaft power available. In fact, since about 70% of the total turbine output power is normally required by the compressor, an increase of 10% in the compressor power requirement requires an additional 7% of the total turbine output power. This reduces the original 30% of the total turbine power available as net output shaft power by 7%, to 23% of the turbine output. The end result is that output shaft power to the alternator is reduced by 7/30 or 23%.

The second detrimental effect occurs because the actual magnitude of the flow imbalance was not correctly assessed in the design phase of the turbocompressor assembly. The additional mass flow caused the compressor to operate in a low pressure ratio, low efficiency, choked region. The consideration of the compatability of the compressor pumping characteristics with the turbine throttling characteristics is termed "matching." A properly matched system is designed such that both the turbine and compressor operate in high efficiency regions. This SABC system was not properly matched and a loss of as much as 10 percentage points of compressor efficiency is attributed to this condition.These leakage effects are treated in a more quantitative manner later in this report.

95

The large cooling air requirement for the SABC is certainly a severe design limitation. An additional reason for the large quantity of bearing cooling air is attributed by AiResearch to the close coupling of the back-to-back turbine and compressor. Also, heat soak from hot section parts to bearing foils after shutdown is a concern since the cooling flow is established only during operation. By comparison, the WR34 ball bearing configuration is able to accommodate a sufficiently large separation of the turbine and compressor for thermal isolation. Also, much less work is required to pump the small quantity of oil required for cooling and lubricating the ball bearings.

Although the open cycle 18 kw modification of the SABC would potentially have a lower percentage of bearing associated losses, other factors require consideration. The primary problem is that the SABC method of inducing ambient air for bearing cooling will be eliminated due to the pressurized configuration. Instead, the compressor discharge air, at approximately 300°F would have to be cooled to around 100°F before being be forced through the bearings for cooling. This would not only introduce a heat exchanger but additional electrical parasitics of the fan needed to cool it. A design trade-off would have to be conducted to arrive at the configuration which optimizes the fan power, the heat exchanger size, the discharge temperature and the bleed flow rate to minimize overall cycle losses. Nevertheless, between the increased bleed flow and the additional electrical parasitics, the air bearings would consume a large portion of the available cycle output power.

It is understandable that bleed requirements and bearing windage losses are less significant in the aircraft companies' ACM evaluation process. Since large quantities of very cool air are readily available for bearing requirements, design complications are greatly reduced. Finally the air foil bearing windage drop helps to load the cooling turbine and so it is a benefit to the environmental control system (ECS) function.

There is evidence that foil bearings exhibit a longer life than ball or roller bearings in a comparable application. Some of this advantage is lost when considering the sensitivity of air bearings to contamination. Gas turbine environments will differ from the typical ACM operating conditions. It was found during the DTM testing that condensed water vapor, oil residue (from the auxiliary air supply) or dust particles larger than about 0.1 mil may prohibit the engine from starting. This is because the contamination increases the starting torque on the foils such that the starter cannot achieve the shaft speeds necessary for air bearing lift-off. Upon inspection following one such incident, several small scrapes through the coatings, as well as a very thin oil film, were detected. Water condensate, which

produces the same effect as the oil, was suspected in other failed start attempts. We avoided repeat failures in the DTM test sequence by filtering and drying the auxiliary compressed air.

Although air bearing technology can achieve ultra high shaft speeds and long life, both the speed and life requirements of the WTS-34 can be met with ball bearings. Since the required ball bearing diameters are relatively small compared to those for air bearings, the bearing rim speed (DN), to which life is correlated, can be kept well within safe limits. In fact, the ball bearings specified for the WTS34 have a greater design life than the turbomachinery.

3.2.8.3 Cycle Packaging and Configuration Design Factors

The configuration of the basic components in a recuperative Brayton cycle is extremely important. The fundamental components of the Brayton PCA are the turbogenerator, the recuperator, the combustor and the solar receiver. The turbogenerator in this case is a radial turbine, a centrifugal compressor and an alternator on a common shaft. With the SABC there is additionally the heat sink heat exchanger. What remains is little more than transition ducts with hydraulic diameters of from 3 to 6 inches and controls.

Several factors which greatly influence system efficiency are governed by the PCA layout. These are the intercomponent pressure drops and the leakage of working fluid. Also of importance is the heat loss from the component package. Other factors such as velocity distributions entering the recuperator, receiver, combustor and the turbomachinery are more difficult to diagnose and may give the appearance of poorly performing primary components. Exit flow conditions from the turbine and compressor should be considered during the design of the downstream ducting to minimize kinetic energy losses which translate to pressure drop.

Along with system efficiency, the life, cost and maintainability of the components are influenced by the layout and packaging. One such life extending design goal is to attain a uniform temperature distribution at the turbine entrance. These and other factors relating to thermal stresses and vibratory isolation will be covered in the final DTM report.

PRESSURE DROP ON THE HEAT ADDITION SIDE

Since the AiResearch SABC requires more intercomponent connections than the open cycle Brayton, the significance of the ducting design details is increased. The SABC design utilizes large plenum boxes to replace ducts wherever possible. AiResearch adopted this strategy in an attempt to minimize pressure losses on the heat

addition side (near atmospheric pressure) of the cycle.The trade-off in this approach is that heat loss and the susceptibility for leaks is likely to be greater than in a duct configuration. Also, the large size of the ducts or boxes does not necessarily ensure low pressure losses without careful consideration of entrance and exit transitions. Pressure drops through the heat addition side of the cycle were approximately 20% to 30% higher than what is considered a reasonable design goal. Heat loss to the ambient and heat "soak" to other components has not yet been fully assessed.

Although it is anticipated that energy conduction through the large insulated plenums of the SABC is excessive relative to a mature packaging configuration, this does not appear to be a strong contributor to the performance problems. Leakage also appears to be a small energy loss factor since the pressure differential is low.

A detailed analysis of the individual component pressure and temperature losses throughout the engine was not undertaken.However, care was taken to determine an end-to-end pressure drop over the total heat addition (high pressure) and heat rejection (low pressure) sides of the cycle.

The heat addition side average stagnation pressure drop was measured to be between 5.5% and 6% at rated turbine inlet temperature and speed. This is considered reasonable since only preliminary steps were taken to integrate the solar receiver with the existing Mark IIIA hardware. The goal for this side of the cycle, for both the SABC and the open cycle,is from 4% to 5%. The relative effect of pressure drop on PCA efficiency is illustrated by the slope of Figure 28. From these assumptions the discrepancy of 1.5 percentage points of heat addition side pressure drop is expected to cause a cycle efficiency degradation of just slightly more than one percentage point.

PRESSURE DROP ON THE HEAT REJECTION SIDE

Pressure drop is most sensitive to velocity and therefore prime consideration must be given to those regions where the velocity of the working fluid is the greatest, For this reason the most critical transition section is between the turbine exhaust and the recuperator hot side entrance. On this side of the cycle the open cycle engine would have the option to utilize large, low pressure plenums where the SABC requires a pressure containment vessel. Sanders DTM experience indicates that high pressure drop and significant leakage occurred in this section. Most of the concern over pressure drop arises from the inability of the turbine exhaust diffuses to efficiently decelerate the turbine exhaust flow. The SABC design incorporates an axial mounted cone engaged at the exducer shroud of the turbine housing.Furthermore, the bayonet mounting arrangement utilizes a piston ring to seal against ambient air infiltration, Significant

FIGURE 28. SENSITIVITY OF PCA EFFICIENCY TO PRESSURE DROP

PCA
Efficiency
%

25

20

15

10

4   6   8   10   12   14   16

Total P/P % (Both sides)

SABC
Goal

DTM

ALuumATOR Err .CENCI   o.! %|
COMP INLET PRESS 6.125 PSIA'
COMP PRESS RATIO   2.4
MASS FLOW RATE   .23 LBM/S
TURBINE EFFICIENCY   84 %
RCUP EFFECTIVENESS   90 %
COMR EFFICENCY   ·   95 %
MECH EFFICENCY   94 %
THERMAL LOSSES   2 KW
PRESSURE DROP   4 TO 15%
SEAL LEAKAGE   10 %
COMP INLET TEMP   98 F
TURBINE INLET TEMP   1600 F
COMP EFFICENCY   78 %
AMBIENT TEMP   59 F

EXCLUDING RCVR THERMAL LOSSES

leaks, equal to about 1% of nominal engine mass flow, have been measured here in a post-DTM static inspection.

The kinetic energy of the fluid leaving the turbine can be an appreciable portion of the available enthalpy drop. In a radial flow turbine much of this exit kinetic energy is contained in the tangential swirl velocity component during off-design operation.Only under ideal conditions is the tangential velocity reduced to zero. Due to the mismatched turbine and compressor this can hardly be considered the case in the SABC engine. Inspection of the velocity triangles reveals that the swirl component was significant at operating points within the DTM test range.Because of this, the high exit kinetic energy is not likely to be recovered in this diffuser manifolding design. Again sufficient instrumentation was not provided to quantify this effect but indirect evidence is available which strongly suggests high stagnation pressure losses in this vicinity.

As stated, diffusion of the swirling turbine exhaust is not easily accomplished with an axial cone arrangement such as that employed in the SABC. Other practical constraints have also aggravated the situation in this design. A brief critique of three of these factors is presented below to substantiate Sanders' concern over this design.

1. A pronounced annular step of about 1/4 inch deep by 1/4 wide exists at the piston ring located at the entrance to the conical diffuser. This is certainly large enough to disturb the boundary layer and decrease the effective throat diameter of the diffuser. Losses in total pressure will result.

2. Any infiltration from this piston ring seal will feed the boundary layer and again decrease the throat. Since leakage from this point has long been a topic of discussion by AiResearch through several design iterations, it appears to Sanders that an acceptable seal cannot be obtained by this method. Preliminary measurements have been made at the conclusion of the DTM which indicate that 1 to 3% of design engine flow infiltrates through this point alone. (A more accurate means to determine the local static pressure is being investigated so that an accurate static test may be accomplished).

3. The piston ring at the exit end of the diffuser cone has been replaced (due to excessive leakage) by a bellows segment for our DTM assembly. This may have solved one problem while introducing another, The 7° (half angle) cone now discharges into the bellows section which is about 1 inch larger in diameter. The side of the recuperator cone, oriented 90° from this exhaust axis, partially obstructs the flow entering

100

the plenum 3 or 4 inches downstream of the core. These conditions will lead to a loss of total pressure, especially in light of poor upstream flow conditions.

Studies of radial flow turbine exhaust indicate that the "snail shell" volute design is better able to recover the dynamic head than the axially discharging conical diffuser in carefully executed designs. The Williams WTS34 does incorporate such a volute and thus is expected to improve turbine efficiency as well as enhance the entrance flow conditions at the recuperator core.Also, leakage in this region should be negligible since the static pressure at the mechanical connection is likely to be very close to ambient.

The overall pressure loss on the heat rejection side of the SABC cycle was also carefully measured on several occasions.Pitot static measurements in the compressor inlet transition duct from the heat sink and at the recuperator core entrance were adjusted to stagnation (total pressure) conditions. The normalized pressure drop between the turbine exhaust and the compressor inlet was found to be approximately 7.0%. This exceeds the SABC design goal by about 30%. By the same token, the open cycle configuration goal of 3% should be much easier to achieve by eliminating the heat sink and its manifolding, and improving the turbine exhaust diffuser. A larger, redesigned recuperator will also be utilized in the open cycle PCA.

Figure 28 shows pressure drop to be a very influential parameter. Again it is pointed out that this is a sensitivity curve for this one isolated effect. The resulting secondary effects on other upstream and downstream components are not illustrated. The overall degradation of the baseline cycle efficiency resulting from the additional pressure drop is about 10% (Figure 28 displays this as a drop of about 2 percentage points of PCA efficiency).

Secondary effects of pressure drop will be experienced most notably at the compressor. Unlike open cycle Braytons, a restriction in the heat rejection side will result in a decrease in compressor pressure ratio. A portion of the drop in design point pressure ratio of 2.4 to the 2.0 measured in the DTM SABC engine is attributed to this effect. This reduced pressure ratio is accompanied by a sharp decline in compressor efficiency.

LEAKAGE OF CYCLE WORKING FLUID

Infiltration of ambient air into the subatmospheric portions of the cycle is considered to be a major source of many of the SABC inefficiencies. Several specific leak points have been mentioned in previous discussions. With reference to the sensitivity curve in Figure 29 these leaks must be divided into two categories: those which occur on the low pressure side of the cycle, and those on the high pressure, heat addition side.

FIGURE 29.   SENSITIVITY OF PCA EFFICIENCY TO LEAKAGE

102

PCA
Efficiency
%

Low Pressure Side Leakage %

The treatment of high pressure side leaks follows the discussions presented for the combustor make-up air. Air that leaks in through the high pressure exhaust plenum, the solar receiver, or the combustor replaces approximately the same quantity of preheated gas at the particular point in the heat addition process. Infiltration downstream of the recuperator not only increases the venting of compressor exhaust by the amount of the leak,but it also reduces the heat recovery on the other side of the recuperator. Leaks in the receiver exhaust have this same effect while also displacing a portion of hot gas from the solar receiver. For this reason, receiver exhaust leaks during solar operation are more serious than receiver intake leaks. In the fuel only mode of operation, all leaks between the recuperator exhaust and the combustor affect the cycle in the same manner as the combustor make-up air which passes through the plenum hole. These inflow points, unlike those on the low pressure side of the cycle, do not affect the pressure ratio established by the compressor. To put the magnitude of these leaks in perspective, the total high pressure side leakage is about 15% of that which is allowed to directly enter the combustor through the hole provided by AiResearch. Moreover, if they were sealed, little gain would be realized since the rise in flow resistance through these components would be accompanied by greater ingestion through the relatively unimpeded combustor make-up hole.

The receiver operating pressure in the DTM tests was approximately 1" WC (below atmospheric) on the inlet and 2 or 3" WC at the exhaust duct. Leaks in the exhaust side of the receiver had the effect of slightly decreasing the mass flow through the absorber, thus reducing the heat transfer effectiveness. Leaks on the inlet side had the opposite effect by providing a slight increase in flow rate,accompanied by an improvement in effectiveness. The leaks on the two sides, divided by the solar absorber, were approximately equal and therefore had a negligible effect on solar absorption in the receiver. The leaks were significant in terms of displacing enthalpy and accounted for about 2.6% of the engine flow. This enthalpy loss to the cycle can be observed as the combined effect of the discharge of compressor exhaust gas and a reduction in the heat recovered by the recuperator. The total effect of the receiver leaks has been estimated to produce a thermal loss of 1.78 KW. This is 6.6% of the design point heat requirement (excluding receiver thermal losses).

Infiltration on the low pressure side of the cycle affects PCA efficiency in two ways. The penalties to the cycle are characterized by a rise in compressor work and a drop in compressor efficiency. Compressor work increases since in addition to the turbine mass flow, the bleed air must be pumped for no benefit to the cycle. Secondly, the compressor isentropic efficiency tends to drop because high speed turbomachinery compressors typically have a rather narrow high

efficiency operating range. With respect to this, the compressor could be "matched" to the system with the additional capacity to provide maximum efficiency while pumping the leak quantity. This is rarely done since most leaks are generally unexpected. For leaks of less than 2%, the decline in compressor efficiency is likely to be small, but low pressure side leaks approaching the magnitudes experienced in the DTM cause partially or fully choked conditions within the compressor stage. This situation is initially characterized by transonic shock waves at the diffuser and eventually at the inducer as well.

The primary contribution to the low side infiltration is the air flow requried for bearing cooling. This accounts for a minimum of 1.3 lb/min, about 9 to 12% of the compressor throughput. The DTM air consumption may have been 10 to 20% more than the 1.3 lb/min specified by AiResearch. This is because safe bearing operating temperatures could not be maintained for more than one hour at full speed without increasing the recommended cooling air flow.

Static leak tests of components on the heat rejection side were conducted at the conclusion of the DTM program. At a pressure of 6.9 psia, the total leak rate (excluding bearing cooling) was measured to be from 2.9 to 3.8% (.40 to 0.52 lb/min).By selectively sealing potential leak areas, three primary leak zones were identified: the turbine exhaust piston ring, all low pressure side gaskets, and the heat sink and manifold.

The heat sink was connected to the compressor intake duct with a fiberglass manifold. An individual static pressure test of this assembly exposed several serious leaks. Amoung these were a crack in the fiberglass at a point where AiResearch had machined a notch to allow access to a bolt head on the flange. Also, in this same manifold, leakage occurred around the tapped threads of an unused pipe plug imbedded in the fiberglass.

The composite total of all leaks measured on the low pressure side of the cycle exceeded the AiResearch design goal by a factor of 2 or 3. The reason for this discrepancy is not clear. Leaks at the gasketed flanges were not an appreciable portion of the total leakage (<0.1 lb/min) and therefore were consistent with AiResearch's specification. The leakage in the heat sink section appears to account for the difference between the figures provided by AiResearch and those measured at Sanders. A more complete description of the leak tests as well as photographs showing leak zones will be presented in the DTM final report.

The total quantity of air infiltrating the low pressure side of the cycle was therefore determined to be from 1" to 16% of turbine mass flow. This certainly had an overwhelming effect on the system

efficiency. Figure 29 illustrates the isolated effect of low pressure side leakage on the work of the compressor. As compressor work increases, less surplus is available from the work of the turbine and thus system efficiency decreases. Note that all other variables, including the compressor efficiency, have been maintained at the baseline conditions. For reasons previously stated, the actual increase in leakage was accompanied by a decline in compressor efficiency. It is not possible at this time to correlate compressor efficiency with the leakage and other critical parameters. The excess pressure drops, compressor inlet temperature, the intake ducting configuration and the non-optimum compressor diffuser are also contributors to the disappointing compresor performance. In the absence of these additional effects, Figure 29 demonstrates that each percentage point drop of leakage will result in slightly more than half of a percentage point drop in overall cycle efficiency. Inclusion of compressor degradation effects will yield a steeper slope.

INFLUENCE OF PACKAGING FACTORS ON TURBOCOMPRESSOR MATCHING

Leakage, pressure drops, and to some extent compressor inlet temperature have drastically influenced the operating point of the compressor. This is not to imply that any physical changes have occurred in the compressor section. It is the "throttling" characteristics of the system which the compressor must work against that have been altered.

As an example, consider a constant speed motor driven compressor with a throttling device on its intake. Throttle wide open, the compressor would deliver its maximum mass flow at a pressure ratio of only slightly greater than one. The pressure ratio is defined as the pressure at the exhaust divided by the intake pressure downstream of the throttle. As the valve is closed, the pressure at the intake drops, due to the pressure losses across the valve. This increase in pressure will be accompanied by a reduction of man flowing through the system. The procedure of closing the valve to decrease mass flow and increase pressure ratio can be continued until the physical limitation of the system is reached. In the case of a low pressure blower, the maximum pressure ratio might be achieved when the valve is practically closed. Due primarily to compressibility effects, the operating range of high pressure (Pr>1.8) gas turbine compressors is limited by aerodynamic instabilities, termed surge. Due to this phenomenon, the achievable pressure ratio will level off while continued throttling will result in a decrease in mass flow. Aerodynamic stall will occur in this region due to an increase in the angle of incidence of the velocity component at the leading edge of the inducer.

The previous example is presented to clarify the discussion of the SABC compressor characteristics shown in Figure 26. This "map"

displays the trends discussed. The line defined by the leftmost point of each speed line is the surge region. The right side of a given speed line, at low pressure ratios, is generally regarded as the choking region. This condition is characterized by high (relative blade) Mach numbers. This figure also clearly illustrates the trends for low efficiency at the two extreme ends of the speed line. The desired operating point for the compressor would therefore be in the high efficiency region near the maximum pressure ratio.

Just as the hypothetical throttle was able to dictate the mass flow, pressure, and consequently efficiency at the point of operation, so does the entire Brayton system ducting. The pressure drop over the throttle is analogous to resistance of the flow through the ducting and turbine, The throttling characteristics of the turbine are influenced by the turbine inlet temperature (TIT). In general an increase in TIT will result in an increased expansion ratio over the turbine along a constant speed line, For this reason an optimally matched turbocompressor assembly is one in which the throttling characteristics of the system are such that the compressor will operate in its high efficiency range while the turbine operates at its maximum TIT. This condition was not achieved in the DTM experiments.

Infiltration of air into the low pressure side of the SABC caused less mass to flow through the turbine than the compressor. This can be envisioned as a hole between the throttle valve and the compressor intake in the hypothetical model. In this case the ability of the turbine to "control" the operating point of the compressor is limited. In effect, there are two throttling devices in parallel, of which only the turbine extracts useful work.

Therefore, the available pressure ratio established by the compressor must be divided between that which occurs over the turbine, the leaks, and the pressure drop through the ducting. With reference to the compressor map in Figure 26 the combined effect of raising the pressure drop on the heat rejection side and increasing leakage will move the 1600°F matching point down the speed line towards choke. In fact, the elevated pressure drop and the air infiltration (bearing bleed air included) caused the SABC compressor to operate at a pressure ratio of 2.0 at rated TIT and speed (75,000 RPM). The drop in efficiency was extremely large. Before taking this map too literally, we must reemphasize that the efficiencies indicated here are for the best possible configuration utilizing the F-15 impeller. Based on inspection of the compressor inlet configuration and a questionable diffuser design, all efficiencies should be derated across the map until test data indicates otherwise. However, approximately 8 to 10 percentage points can be readily recovered without modification to the turbocompressor hardware. Figure 29b illustrates the sensitivity of cycle efficiency to the compressor efficiency.Assuming baseline conditions for all other pertinent

Figure 29b. Sensitivity of PCA Efficiency to Compressor Efficiency
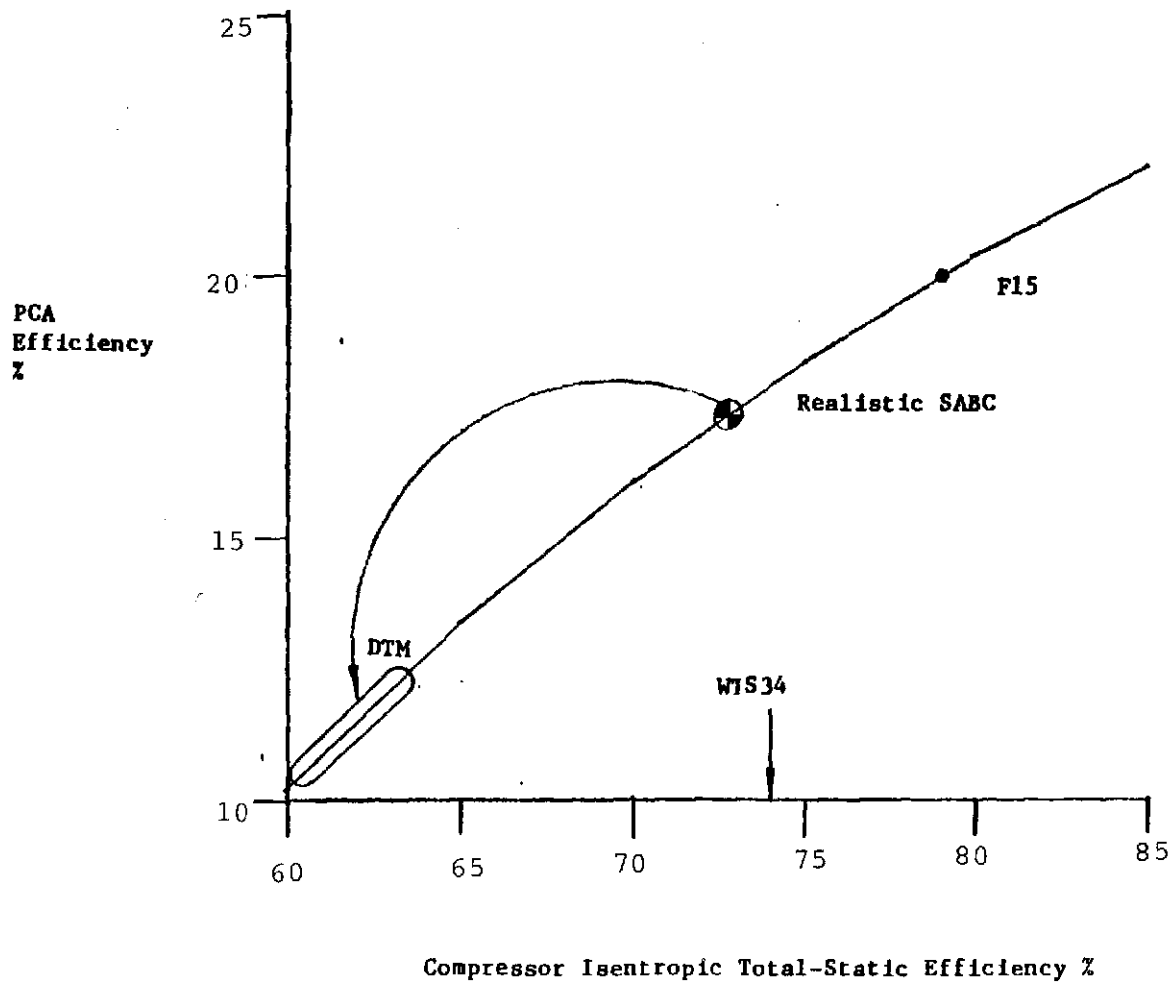
107

variables, a compressor efficiency drop from 78% to 62% will result in a cycle degradation of 8 percentage points.

This clearly demonstrates that those parameters such as pressure drop, leakage and compressor inlet temperature, which influence compressor efficiency, have a profound impact on cycle efficiency.

3.2.9 PMA/RECTIFIER LOSSES

Charactization of the PMA and rectifier performance was conducted at AiResearch prior to the acceptance tests (3/84). The PMA/rectifier unit was tested separately by measuring speed, torque, output ac and dc voltage, and current over a wide range of speed and load conditions. The data provided by AiResearch is provided in Appendix I.

As an example, the loss mechanisms from two test cases have been analyzed. Sample points from Figures H-4 and H-5 in Appendix H define PMA operating characteristics at 70,000 and 80,000 RPM respectively. The following list of data contains the breakdown of losses for these cases:

	70 KRPM	80 KRPM
ACTUAL SPEED (KRPM)	70	80
RECTIFIED VOLTAGE (VDC)	248	276
RECTIFIED CURRENT (AMPS)	12.5	13.5
RECTIFIED POWER (KWDC)	3.10	3.75
COMBINED EFFICIENCY	0.79	0.80
RECTIFIER EFFICIENCY	0.983	0.984
ALTERNATOR EFFICIENCY	0.80	0.81
ALTERNATOR LOSSES (WATTS)	790	890
ROTOR WINDAGE (WATTS)	59	98
COPPER LOSSES (WATTS)	10	12
BEARING FRICTION & WINDAGE (WATTS)	~535	~605
STARTER STACK CORE (WATTS)	~90	~90
STARTER STACK TEETH (WATTS)	~90	~90
ROTOR (WATTS)	~5	~5

The PMA and rectifier efficiencies have been interpolated from the AiResearch curves in Appendix H for each of the 10 DTM test conditions. This information can be found in Table 16.

3.2.10 TRANSMISSION LOSS

Given the alternator/rectifier characteristics, the maximum transmission current was never higher than 15 amps. The DC power cable was AWG 6-4 with two legs used for dc+ and dc-. One leg was used for with equipment ground and the fourth leg was not used. The one way

TEST DATE	6/8A	6/8P	6/28	6/30A	6/30P	7/9A	7/9P	7/10	7/13	7/25
SHAFT SPEED (KRPM)	54.9	70.0	75.0	65.0	64.9	74.7	66.7	53.0	50.9815	74.8
DC VOLTS	215.5	249.1	230.27	244.06	243.09	243.10	236.90	211.30	203.4986	245.43
DC AMPS	3.85	8.34	15.51	6.09	6.06	13.10	9.20	3.08	2.86	12.19
DC KW	0.8324	2.100	3.5717	1.4865	1.4733	3.1865	2.1823	0.6543	0.5829	2.9925
AC VOLTS	236.23	238.42	241.60	238.75	239.10	240.25	238.86	237.65	236.05	241.40
AC AMPS	2.6227	7.0370	12.1603	4.8816	4.8343	10.8436	7.4065	1.9545	1.7546	10.1388
AC KW (GRID)	0.610	1.700	2.890	1.146	1.138	2.560	1.730	0.457	0.4079	2.410
INV. EFF.	0.7330	0.7925	0.8100	0.7722	0.7726	0.8052	0.7984	0.6991	0.6997	0.8055
PMA EFF.	0.599	0.741	0.827	0.691	0.691	0.810	0.753	0.533	0.544	0.803
RECTIFIER EFF.	0.9760	0.9815	0.9835	0.9800	0.9800	0.9835	0.9823	0.9842	0.9740	0.9835

The rectified three-phase alternator, direct current (DC) characteristics are shown in rows 3, 4 and 5. The 60Hz alternating current (AC) inverter output characteristics are listed in the next three rows. The Permanent Magnet Alternator (PMA) and rectifier efficiencies were measured for this unit at AiResearch prior to delivery.

cable run was 250', 0.411 ohms/1,000 ft. at 30°C. The I^2R losses were thus 46 watts at maximum power.

3.2.11 INVERTER PERFORMANCE

The 8 kW ABACUS Controls, Inc. inverter is comprised of two 4 kW power inverters working in parallel uner one set of control electronics.

During the inverter acceptance tests, efficiency at maximum power was measured at 90% under the following conditions:

1. at 203 VDC and 8.184 KVA, efficiency was 0.902
2. at 250 VDC and 8.217 KVA, efficiency was 0.903

The minimum inverter input power required to maintain line tie was rated at 250W. In an actual test sequence we measured 345 to 351 watts of inverter loss when operating at 3.5 to 4.0 kw output.

The inverter efficiencies were substantially lower at the power levels achieved in these tests. Table 16 contains the inverter and alternator data from the first 7 DTM tests between the idle and rated speed.

3.2.12 PARASITIC POWER REQUIREMENTS

Parasitic power requirements for the DTM vary with the mode of operation. Figure 30 illustrates the three modes of operation and the parasitic power associated with each. Note that most of this power is required by the heat sink blower, which will not be used on the open cycle 20KW Brayton PCA. This will reduce the parasitic power to nominally 206 to 376 watts.

The 10W average power for the diurnal drive represents the 7.4% duty cycle of the 135W diurnal drive. The elevation drive only operates for a few seconds once each day and thus requires negligible energy.

The fuel shutoff valve is a normally closed device for fail-safe operation and consequently requires the constant power indicated during fuel fired operation. The throttle valve constantly "hunts" during operation and so was assigned a 100% duty cycle.

3.3 FIELD EXPERIENCE

In addition to demonstrating the technology and performance of the DTM, three other topics were addressed:

o   Application of field experience to Design-to-Cost considerations.

Figure 30. DTM Operating Parasitic Power Allocation

BASE PARASITICS

480W* HEAT SINK BLOWER
8W   ALTERNATOR OVER TEMP. SW
120W EXECUTIVE PROCESSOR
_____
608W
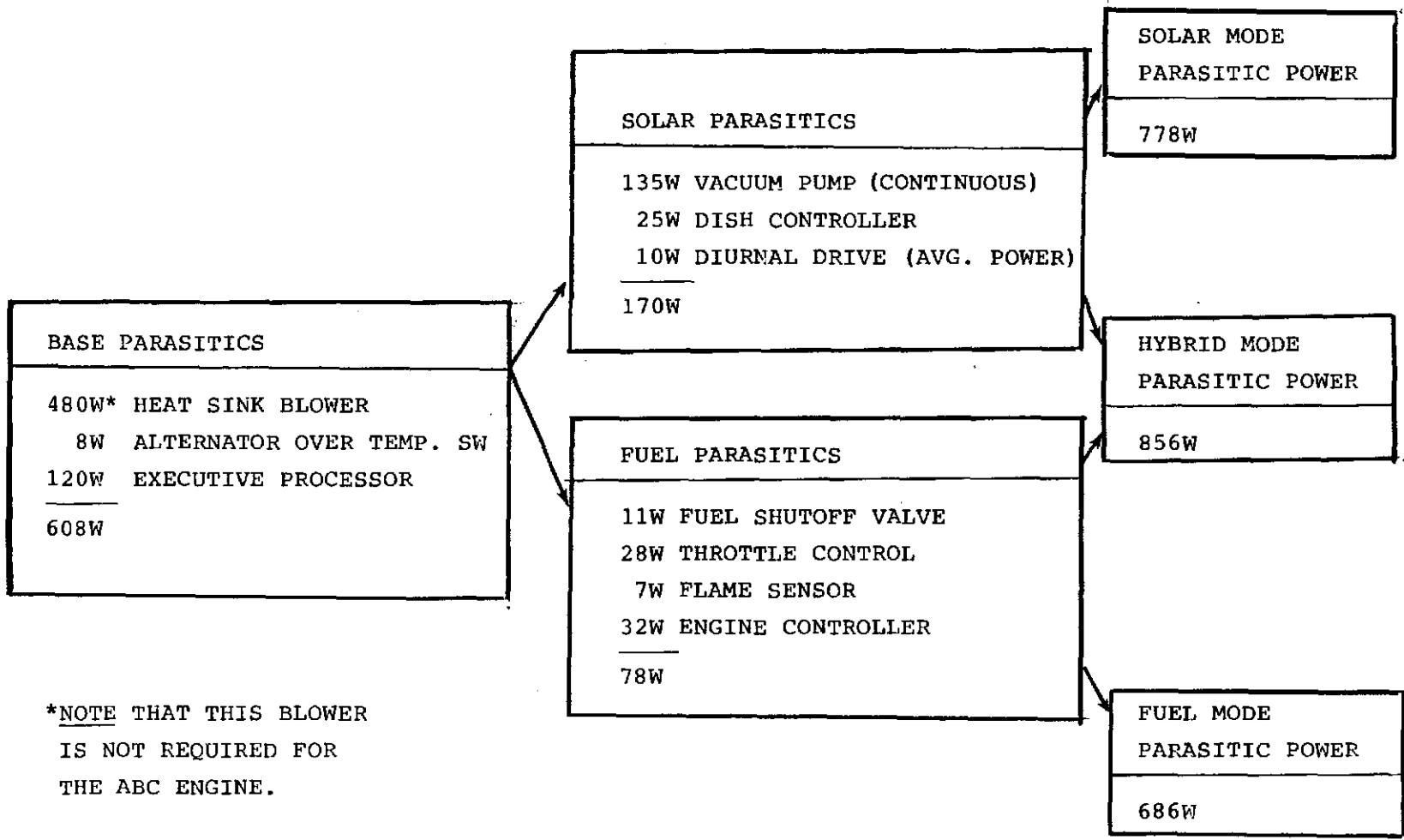
*NOTE THAT THIS BLOWER
IS NOT REQUIRED FOR
THE ABC ENGINE.

SOLAR PARASITICS

135W VACUUM PUMP (CONTINUOUS)
25W DISH CONTROLLER
10W DIURNAL DRIVE (AVG. POWER)
_____
170W

FUEL PARASITICS

11W FUEL SHUTOFF VALVE
28W THROTTLE CONTROL
7W FLAME SENSOR
32W ENGINE CONTROLLER
_____
78W

SOLAR MODE
PARASITIC POWER

778W

HYBRID MODE
PARASITIC POWER

856W

FUEL MODE
PARASITIC POWER

686W

111

o   The value of field operating experience

o   Field maintenance experience

These topics are described in this subsection.

3.3.1   APPLICATION OF FIELD EXPERIENCE TO DESIGN-TO-COST
         CONSIDERATIONS

One of the objectives of the PDME program was to improve our understanding of the cost drivers in the system and thus permit the development of a reliable cost model for a production Brayton module. Some useful insights into the cost drivers in the major components are described below.

3.3.1.1 Concentrator

The LaJet LEC 460 concentrator is admirably well designed for low production cost. The entire structure is efficiently designed to use a minimum amount of low cost structural steel, galvanized for long life, and designed for rapid field assembly with semi-skilled labor. Since the dish and engine assembly is supported at its center of gravity, low cost, low power drives an be used. The microprocessor control system provides all of the necessary operating and diagnostic functions in a simple, low cost package. Although we encountered the types of problems usually associated with a new product, these were being corrected, and the result should be a concentrator with low initial and O&M cost. However, cost per kilowatt is the bottom line, and we did find the optical performance to be below expectations. The reasons for this are described later in the test results section of this report. Our estimate of the installed cost per kilowatt of the LEC 460 in large quantities is as follows:

        Unit production cost (1984$) = $3500
        Unit production cost (installed) = $5000 = 150 $/kWt

        Measured power into aperture* = 34 kWt

        *1kW/m Insolation, 11" Aperture, 90% Acceptance

LaJet is working to improve the optical performance of these facets in their larger Innovative Concentrator[8] which will further reduce the cost per kilowatt. To the extent that the concentration ratio can be increased, it will permit smaller apertures, which will correspondingly increase the solar receiver efficiency.

----

8. DOE Contract # DE-FC04-85ET 30171.

3.3.1.2 Engine

When firm production cost estimates were sought, the Garrett AiResearch SABC engine assembly turned out to have a substantially increased initial cost per kilowatt. This resulted from a sharp increase in the estimated production cost of the engine (when Garrett was pressed to quote this number in March of 1984) coupled with a disappointing conversion efficiency as revealed by our testing. On the other hand, there is good reason to believe that its O&M costs would be quite low.

The reasons for the disappointing performance are discussed later in this report, but the conclusion reached was that we must look to an Atmospheric Brayton Cycle engine (ABC) to meet our production cost-performance goal. This is because a given turbocompressor will produce nominally 2.4 times the output power in the atmospheric pressure mode over what it did in the subatmospheric mode, due to the increased mass density of the air. Thus the cost per kilowatt of the turbocompressor is reduced by approximately 1/2.4. Furthermore, the heat sink exchanger required for the SABC mode is eliminated in the ABC mode for a further cost reduction.

It is now feasible to take advantage of this increased engine output as the Innovative Concentrator program is developing three low production cost concentrator designs in the 100-120 kilowatt thermal range that is required for a 20-25 kWe ABC engine.

Williams International has estimated the 1000 unit/year production cost of their WTS-34 turbocompressor and gear box assembly at $10,000 each, with a 20 kWe output in the ABC mode. With this engine and an innovative concentrator we project a very competitive $2.70/W for the Brayton solar module in 1000/year production.

The other insight gained from our experience with the SABC engine was that the packaging of the engine assembly and the design of the ducting are critical to the performance and efficiency of the engine assembly. The SABC engine was not well designed in this respect. It had excessively long ducts with many sharp bends and transitions, and many leaks. This had a very detrimental effect on the overall engine performance. We are using this experience to design the 20 kW engine assembly to minimize these losses, which will translate into higher efficiency and lower cost per kilowatt.

3.3.2 THE VALUE OF FIELD OPERATING EXPERIENCE

There is no substitute for living with the system in the field. We discovered the unexpected problems that are inevitably associated with the initial operation of a new system, and this experience has put us in an excellent position to specify and design the 20 kWe PCA.

113

We encountered a number of relatively small problems with the concentrator, ranging from such minor annoyances as failure of low cost connectors and wiring to more serious operating problems with the LaJet controller system. The mechanical structure and drives worked very well, although we did have a failure of one of the drive encoders.

Not too surprisingly, we found that in nearly all cases, LaJet had experienced the same problems in their Warner Springs installation and either had identified or were working on a solution, which they subsequently passed on to us.

The most significant problem was with the facets themselves. About half of the initial lot of facets experienced degradation of portions of the reflective film, or failure of the bond between the film and its mounting ring. These facets were replaced but the replacements had similar problems. Although we did not receive a consistently good batch of facets we believe that LaJet has subsequently improved their manufacturing process and are now producing "very good" facets.

The most costly problem with our concentrator was the lack of documentation for the controller, due to frequent design changes. This cost us a lot of extra effort in integrating the dish control system with our executive processor and subsequently modifying it to accommodate control circuit design improvements.

Our test program was successful, both in terms of integrating the concentrator with the remainder of the system and in terms of its operation after the bugs had been removed. However, the optical performance of the concentrator was less than the manufacturers prediction. The reason for this are discussed in the test results section of this report.

Another field related experience was adapting the concentrator to survive worst case combined wind and snow conditions. To achieve this required three modifications. First, to increase the load carrying capability of the concentrator, a finite element analysis[9] of the entire structure was undertaken to identify the necessary areas of reinforcement. This led to a simple and effective reinforcing scheme consisting of "tee" sections which were clamped between the welded frame sections of the cantilever assembly along the highest stress areas. Also, the foundations were supplemented with earth anchors.

To accommodate the engine assembly, we extended the tripod legs and constructed a rectangular interface frame to support the engine.

----

9. Appendix I, Worst case structural stress for the reinforced LEC 460.

A counterweight was added to the back side of the dish to balance the substantial engine weight. These modifications are illustrated in Figure 31.

Second, a new "snow stow" position was devised wherein the dish was stowed in an inverted position to avoid snow and ice accumulation on the mirror surfaces, and to facilitate snow removal. This also proved to be a useful position for servicing the engine at ground level (see Figure 32).

Third, a fabric snow cover was prepared which was attached to the back surface of the space frame holding the facets. Thus with the dish in its inverted "snow stow" position the snow cover prevented snow accumulation on the back side of most of the mirrors while its smooth, slippery surface facilitated snow removal. The overall arrangement worked very well and we experienced no difficulty with snow or ice.

The most illuminating field experience was operating the engine as part of the complete solar system. In the "getting acquainted" stage, with the engine on the ground, we started and operated the engine six times for a total of six and half hours while we refined our starting procedures and checked out the executive processor/engine control interface.

On the seventh start, the engine failed to turn over and we determined that there was excessive breakaway torque on the engine shaft. We removed the turbocompressor assembly and accompanied it back to Garrett where it was disassembled. It was determined that liquid contamination had entered the air bearings via the cooling air and caused a sticking condition. The bearings were solvent cleaned and the unit reassembled and returned to Sanders, where we reinstalled it along with water/oil filters in the bearing cooling air supply line. The engine was then mounted on the solar concentrator and operated for an additional 16 starts and 30 1/2 hours with no further engine problems.

Further refinements were made to the control algorithms to improve engine speed control while transitioning from hybrid to solar and under varying load conditions. Near the end of the testing we were achieving proper engine start up and automatic system operation in accordance with our design goals.

3.3.3   FIELD MAINTENANCE EXPERIENCE

3.3.3.1 Garrett AiResearch Engine Assembly

The only major maintenance problem experienced with the Garrett SABC engine occurred when the bearing cooling air supply became contaminated with oil as described above. Minor problems experienced

TUBULAR SLEEVE
EXTENSIONS FOR TRIPOD

COUNTERWEIGHT ARM

COUNTERWEIGHTS

NEW ENGINE/TRIPOD INTERFACE FRAME

"TEE" REINFORCEMENT
TO ALL BASE AND
CANTILEYER LEGS

101/06114-67
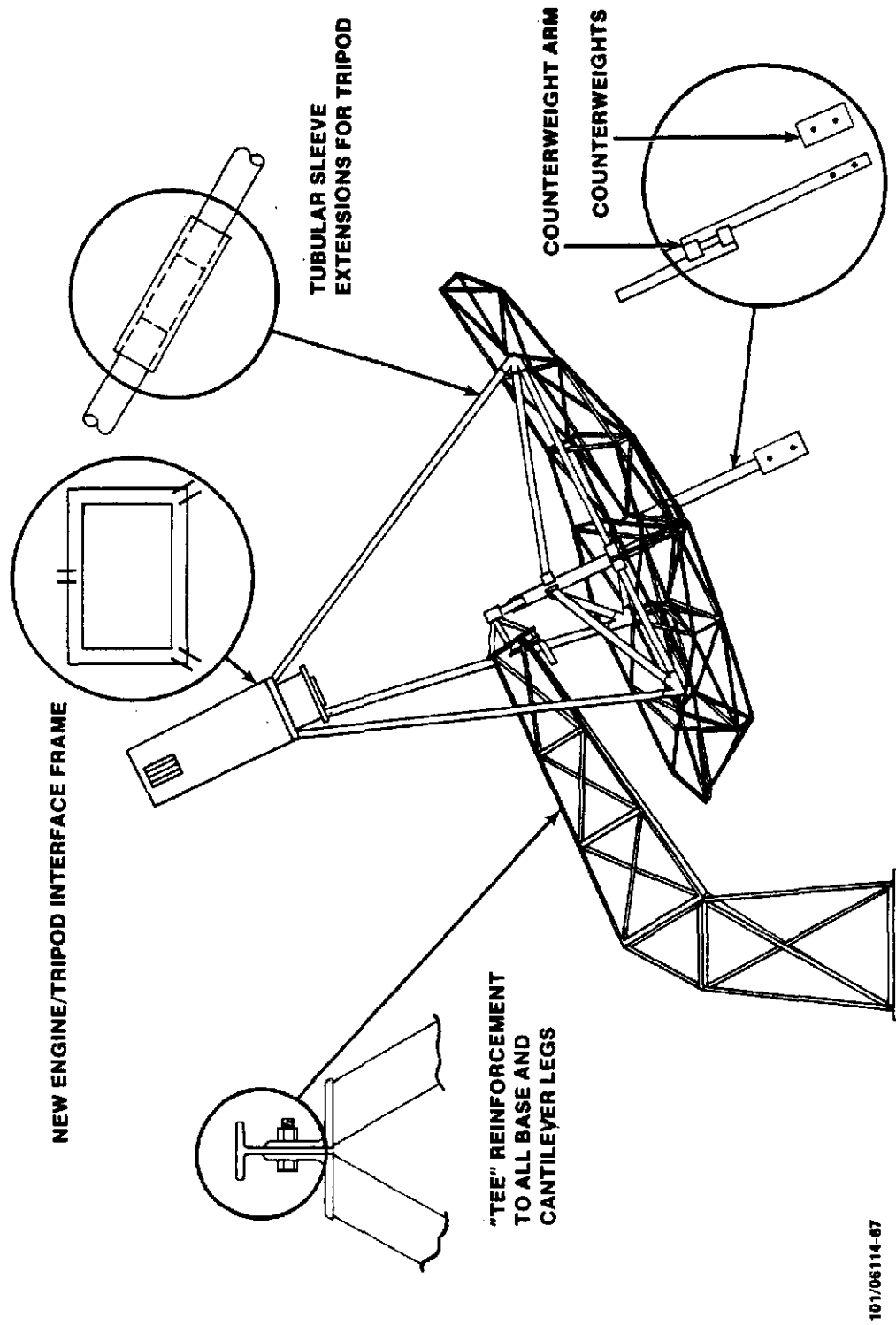
Figure 31.   Sanders Reinforcement of LEC 460 concentrator

116
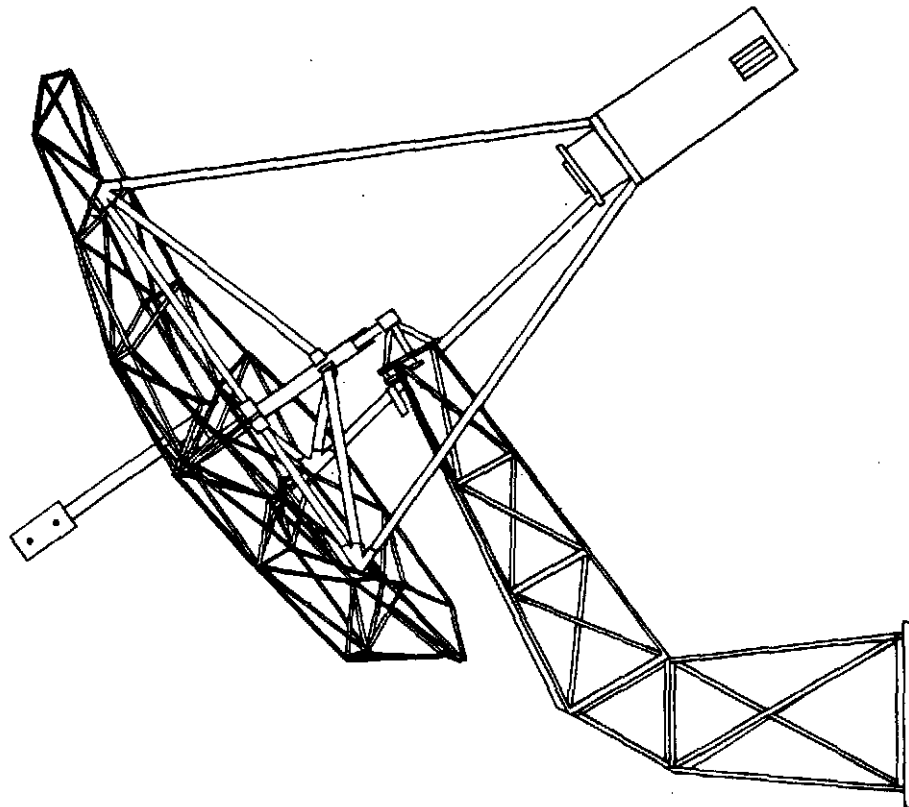
Figure 32. Inverted Stow Position

117

with the Garrett engine included failure of the alternator overtemperature relay and loosening of the throttle valve linkage and the methane supply line. The latter was probably caused by an assembly oversight.

The "start cart" used to vacuum start the engine experience two problems. One was a failed vacuum switch, and the other was a collapsed vacuum hose, which was apparently overheated by hot engine exhaust gas being drawn through it during an extended start cycle. This was repaired by submerging the hose in hot water and reforming it. Subsequently, the starting cycle purge times were more carefully controlled to prevent overheating of the hose.

The Gould processor which controlled the starting sequence and emergency shutdowns of the Garrett PCA required no maintenance.

3.3.3.2 LEC 460 Concentrator

The greatest maintenance problems associated with the LEC 460 were vacuum leaks in the stretched membrane facets and deterioration of the reflective surfaces. The vacuum leaks in all cases were caused by failure of the bond between the mylar reflective surface and the plastic rim to which it is attached. In some cases, the leaks could be stopped by repairing with electrical tape; in worse cases, the mirrors were replaced.

Not surprisingly, LaJet also encountered these problems and had solutions for both. The bond failure problem was corrected by improvements in the film bonding procedure at LaJet. The deteriorating reflective surface problem was caused by the protective coating over the aluminized film sticking to the mylar on the back side of the film when the material was rolled for shipping. When the film was unrolled, portions of the protective coating would peel off, exposing the aluminum to rain, which caused it to corrode away. This has been eliminated by changes in the manufacturing process at 3M, the film manufacturer.

Other lesser LEC 460 problems encountered by Sanders include the following:

o   A broken declination drive home-reference sensor. This was apparently caused by an ice build up during a winter storm. A rubber boot or shield could be added to prevent icing of this component.

o   The declination drive screw coating showed signs of deterioration. An inquiry to LaJet established that the coating process has been changed and that other vendors are being sought for this component.

118

o   A problem was encountered with the coupling between the
    diurnal drive motor and the gearbox input shaft. the
    coupling loosened and moved axially along the shaft, causing
    the encoder rotating blades to self destruct. LaJet has also
    encountered this problem an the immediate solution is to
    Locktite the set screw and tighten firmly in place. Their
    next generation concentrator will use a different type of
    encoder which will eliminate this problem.

o   The Molex connectors used on the LEC 460 have caused problems
    for both Sanders and LaJet, and we both have changed to a
    different type of connector with good results, Sanders to
    Winchester and LaJet to a telephone type connector.

o   Some of the wire insulation used on the concentrator control
    system showed signs of cracking. These cables were either
    replaced or repaired. The solution to this problem is to use
    a higher quality cable insulation.

o   Although electrical component failures in the LaJet
    controller were rare, we experienced a voltage regulator
    failure which appeared to be the result of thermal stresses
    brought on by a poor heat transfer through its mounting. An
    op amp also failed on the same circuit card for no apparent
    reason and was attributed to a normal MTBF.

3.3.3.3   Solar Receiver

The only maintenance required on the receiver was replacement of
the inner graphite solar shield, which is considered an expendable
item. The need for replacement after 16 hours of use was apparently
due to a misalignment of the solar flux to the receiver window. The
operating temperatures were measured at the stations shown in Figure
20b. Thermocouples imbedded just below the surface provided the data
for Table 17.

3.4   POST-TEST INSPECTIONS

3.4.1   HEAT SINK

GRI/Lennox had experienced corrosion problems with the heat sinks
on their SABC engines due to acidic condensate remaining in the heat
sinks for long periods of storage. To avoid this problem, the PDME
heat sink was painted internally with an aluminized paint, and
provisions were made for draining the condensate from the sink after
testing. Post-test inspection revealed only superficial corrosion of
the heat sink interior.

TABLE 17. SUMMARY OF CONCENTRATOR ANALYSIS ERRORS

RUN NO.	TOTAL POWER (W)	INTERCEPT FACTOR (%)	POWER INTO $\mathscr{U}''$ APERTURE (W)	MEASUREMENT SYSTEM ERRORS		
				± 2.53 OF % SIGNAL ERROR	±.54% OF FULL SCALE ERROR	TOTAL MEAS. ERROR
5/18/84 TESTS						
32	23412W	82.8%	19385W	±709W	±3484W	±4193W 17.9%
33	19872	80.6	16017	602	3484	4086 20.6
45	16797	86.3	14496	509	3484	3993 23.8
46	15946	87.6	13969	483	3484	3967 24.9
9/18/84 TESTS						
CON 01	24011	71.0	17048	728	2021	2749 11.4
CON 04	39491	77.8	30724	1197	2021	3218 8.4
CON 05	30474	79.5	24227	923	2021	2944 9.7

At the time when the turbocompressor was disassembled to clean the bearings it was noted that there were small "sparkle" like metallic particles in the compressor scroll. These were apparently from the aluminized coating of the heat sink.

The solution to both the corrosion and particle migration problems with the heat sink would be to fabricate it of stainless steel. The ABC engine offers the best solution by eliminating the heat sink and its associated cost and the 480W of parasitic power.

3.4.2   RECEIVER

After 68 hours of high temperature operation the Sanders ceramic solar receiver was carefully disassembled and inspected. It showed no evidence of coating or material deterioration. The Manville Corp. Ceraform 126 rigid insulation showed no evidence of deterioration. It had been coated with a Johns Manville Corp. product, #1130 colloidal silica, on all surfaces exposed to the hot gas flow. The joints or seams in the Johns Manville Corp. Ceraform 126 insulation had been sealed with a mixture of chopped ceraform and cerakote material. This sealant was not cracked or damaged. The absorber matrices showed no sign of deterioration, nor did the stainless steel inlet air deflector. The quartz window and its retainers and gasket were also in excellent condition.

Pressure drop across the receiver outlet filter was measured and it was determined that there was no measurable increase in pressure drop. A microscopic inspection revealed only a few very small particles of insulation, probably liberated during the assembly and burn-in process.

The graphite solar shield which serves as the aperture plate was the only receiver component which deteriorated. It was significantly eroded in one quadrant after 16 hours of solar operation. The shield is considered expendable, but clearly should have a much longer life to be cost effective. Examination of the eroded area indicated that the concentrated solar flux had not been properly aligned with the receiver aperture and consequently overheated a section of the shield, causing it to oxidize and erode.

Normally, the four temperature sensors surrounding the aperture would have detected this condition and corrected the tracking of the dish. However, these sensors were not operating during the solar tests due to a software problem with the dish controller.

3.4.3   LEC 460 CONCENTRATOR

As discussed in previous sections, a number of small mechanical and electrical problems have been repaired or corrected with upgraded

retrofits from LaJet. Thus at the conclusion of testing we find the concentrator to be in overall good health. Only two retrofits have not been implemented:

1. Replacement of the elevation drive lead screw and floating nut assembly. The original elevation drive screw shows evidence of deterioration of its protective coating. The coating process has been changed by LaJet and a new drive review provided. Also the drive nut assembly, which showed some signs of looseness, has been replaced with a stronger improved design by LaJet.

2. Many of the mirrors should be replaced to obtain optimum performance, but it was decided to leave about half of the original mirrors on the concentrator face-up for the winter to learn more about their weathering characteristics.

3.4.4 CONCENTRATOR ELECTRONICS

The concentrator electronics and electrical components were in good condition at the end of the test program.

The electrical components for the transport of electric power to and from the concentrator were installed by Sanders in accordance with the National Electrical code for weatherproof service and were fault-free.

The electronic components and concentrator control wiring were the source of numerous problems during early operation. In general, the problems stemmed from LaJet's very aggressive implementation of cost control in the selection of components and assembly methods. The problems were typical of an immature commercial design. Connectors, for example, that work well in static appliances in a controlled environment corroded or came loose in the concentrator, where weather and vibration were significant factors. Light gauge, solid conductor wires with low cost insulation parted at flex points or shorted when their insulation cracked. Both of these problems were probably exacerbated by the cold winter climate at Sanders, but they suggest that long-term reliability of the inexpensive wiring harnesses will be a problem.

3.4.5 INVERTER

The inverter worked well during the tests and showed no signs of degradation.

3.4.6 EXECUTIVE PROCESSOR

Similarly, the executive processor worked well and showed no signs of degradation. The executive processor generally employed

military or industrial grade components and was sturdily built, though it was not ruggedized. A commercial controller designed to run and manage the system would – without extensive operator interactive test capability and special test flexibility – be much simpler and less expensive. A commercial/industrial level of components and packaging should be used to combine low cost and high reliability.

3.5 ENGINE PERFORMANCE IMPROVEMENT

This section, excerpted from Sanders report, "A Response to Sandia Questions concerning PDM Brayton Cycle Engine Performance", January 15, 1985, discusses the factors that contributed to the reduced performance of the SABC and how they would be corrected in an optimized engine. The performance improvements that would result from using a 20kW open cycle engine are also presented.

SECTION 4
CONCLUSIONS AND RECOMMENDATIONS

4.1 DTM ACHIEVEMENTS

The DTM design effort and prototype hardware represents a important step forward in the application of small Brayton engines to distributed solar thermal electric systems. With the successful completion of the DTM tests, the fundamental question of Brayton system feasibility has been answered affirmatively and several technical milestones have been achieved.

The more significant technical milestones are;

1. Operation of a Brayton cycle engine with the in-series pressure drop and heat addition of an operating solar receiver. The low pressure drop characteristic of the Sanders ceramic matrix receiver design was essential to this achievement.

2. Operation of a solar thermal electric system powered by a hybrid combination of heat from fossil fuel (methane) combustion and solar energy - June 1984. This demonstrated the feasibility and controlability of hybrid operation, and represents an important capability not currently available in the organic Rankine and Stirling cycle engines.

3. Operation of a Brayton engine-based solar thermal electric system completely powered by solar thermal energy - July 1984. This was accomplished after Sanders modified the SABC MKIII's package to throttle the combustion air inlet.

4. Use of a lightweight, low-cost thin film concentrator to power a high temperature (1600 - 1700°F) thermo-dynamic engine cycle. The concentrator delivered an average flux concentration of about 550:1 over the receiver aperture.

5. The power conditioning equipment that converted high frequency ac output power from the engine alternator to grid-compatible 60 Hz, single-phase, 240 Vac was programmed to match engine performance for maximum efficiency and was run with a solar thermal electric system for the first time.

6. The power conditioning equipment was also the first to run with grid compatibility and stand-alone capability (no grid stabilization required to maintain 60 Hz) while powered by a solar thermal heat engine.

7. Actual system performance data was collected for the first time from a parablic disk module of a distributed Brayton

124

solar thermal electric system. From an engineering standpoint, this was a critical event that has subsequently allowed us to analyze engine performance in detail and identify equipment and design deficiencies that can now be corrected.

Major technical milestones were achieved and key performance characterization was accomplished to qualify the DTM test program as very successful. While engine performance was significantly below expectation the subsequent analysis of data has provided detailed insight and a clear definition of the steps necessary to complete the development of an efficient, reliable and cost-effective 20 kWe module.

4.2 DTM CONCLUSIONS

In-depth analysis of the DTM performance test data has led Sanders to the identification of several loss mechanisms that collectively contributed to the reduced system performance of the DTM equipment.

A comparison of the subsystem efficiency predictions (as presented in January 1983 at the Preliminary Design Review) and the observed efficiencies (as quantified after the DTM test) shows an across-the-board shortfall.

Analysis of the test data suggested the need for some component testing which was subsequently performed. Results of this component testing led us to a better understanding of the mechanisms so that the subsystems can be methodically improved.

Predicted and measured efficiencies of the DTM subsystems are given in Table 18. A qualitative review of the reduced subsystem efficiency factors is given in Tables 19a, b, c and d.

The PDME has demonstrated that a Brayton PDM is practical but additional hardware and technology development is required before a mature product design can be achieved.

The system comprises four main subsystems:

1. Concentrator

2. Power conversion assembly

    a. engine
    b. alternator
    c. receiver
    d. balance of PCA thermodynamic and structural package

126

	PRELIMINARY DESIGN REVIEW (1/83) PREDICTION		CRITICAL DESIGN REVIEW (7/84) MEASUREMENTS 6-28	
	POWER KW	EFFICIENCY	POWER KW	EFFICIENCY
EFFECTIVE AREA (m^2)	42.05		42.05	
		(.86x.99x.1.0)*		(.83x.84x.87)*
SOLAR TO FOCAL PLANE	35.8		25.5	
		0.837		0.566
SOLAR THERMAL TO ENGINE	30.0		14.43	
FOSSIL THERMAL TO ENGINE	0		36.29	
TOTAL THERMAL TO ENGINE	30.0		50.70	
		.256		0.086
ENGINE SHAFT POWER	7.7		4.39	
		(.96x.91)**		(.81 x.81)*
INVERTER OUTPUT POWER	6.7		2.89	

*Reflectivity x Intercept factor x Insolation

**Alternator x Rectifier x Inverter efficiencies

Test conditions: turbine inlet temp.=1598°F, T∞ = 80°F, 75,300 RPM (see tables 12, 13, 17)

The percentage of the solar radiation incident on the concentrator which is reflected into the receiver aperture was predicted at 0.85, but is now estimated at 0.69 based on intercept factor measurements and calculated power balances. This 19 percent reduction results fromthe combined effects of:

1. A working hemispherical reflectance of the film of about 0.83 for an AIRMASS 2 spectrum rather than the anticipated 0.86;

2. Dirt and dust reduced hemispherical reflectivity and worsened specularity.

3. Possible out of plane distortions of the facet hoops

4. Macroscopic slope errors (visible wrinkles or ripples of the film) that are caused:
   1. by uneven prestressing of the film at assembly; and 2. by uneven relaxation of the film due to its anisotropy.

5. Facets made with reflective film from a defective batch that suffered from protective film penetration. This subsequently led to corrosion and flaking of the aluminum.

TABLE 19a. CONTRIBUTORS TO DEPRESSED EFFICIENCY FACTORS

The baseline efficiency of the receiver with a 6.8 inch aperture was predicted at 0.84. Subsequent measurements of the DTM receiver with the 12.2 inch diameter window and reduced solar input and mass flow indicated 0.56 efficiency. Correcting the data to baseline inlet mass flow, temperature and solar power, gives an efficiency of 0.66. The remaining discrepancy of .18 is attributed to:

1. Ineffective sealing of the working fluid and low thermal impedance in the receiver front header region.

2. Very low geometric concentration ratio. The window area and hence the reradiation losses were approximately three times that of the PDR baseline aperture.

3. Higher than predicted radiating temperatures on the solar absorber due to nonuniform internal flux and flow distributions.

Efficiency at rated power was predicted to be 0.257 at PDR and later reassessed at 0.203 for the DTM. Experiments indicate an efficiency of 0.086. The shortfall resulted from the compounding effects of:

1. Excess compressor work and low isentropic compressor efficiency caused by:

   a. low pressure side infiltration leaks
   b. plumbing of air bearing coolant flow through compressor
   c. higher cycle pressure drops

2. Low cycle temperature ratio and Carnot efficiency potential due to an elevation of compressor inlet temperature by 20°F to 30°F caused by:

   a. low heat sink effectiveness
   b. cumulative effects of off-design components

3. Excess combustion make-up air flow which displaces high temperature working fluid, thereby resulting in an enthalpy loss in the cycle. Also, this short circuit decreased the flow through the receiver and reduced its thermal efficiency.

Predicted efficiency of 0.874 was not obtained. The measured value of 0.659
at 40% power would correct to 0.737 at rated power levels. The remaining 15% shortfall
was caused by:

1. an alternator/rectifier efficiency of 0.81 rather than the vendor predicted 0.96.

2. low inverter efficiency resulting from:

   a. fixed tare losses being subtracted from a lower than anticipated input power.
   b. inverter efficiency at rated power (0.89) and at 40% power (0.81) was about
      5% lower than predicted, and this was accentuated by running the unit at less
      than 50% of rated input power.

3. power conditioning equipment

4. controls

The following subsections summarize the conclusions reached for each of these subsystems or a result of the DTM tests.

4.2.1 CONCENTRATOR

The LEC 460 concentrator was selected for its low production cost and adequate predicted (but not demonstrated) performance. After carefully installing and tuning the concentrator our measurements showed its performance to be 19% below the predicted performance (see table 19a. This, in turn, hurt the performance of other components of the system, such as the receiver, which required an 11 inch diameter aperture instead of the predicted 6.8 inch diameter. DTM test results showed that the LEC 460 concentrator delivered only 550 kW/m^2 average to the receiver apertue, or about one third of the flux density required for optimum system performance.

This experience has demonstrated that to achieve overall system optimization and maximum system efficiency the performance of the concentrator must be rigorously established before the remainder of the PCA components can be finally designed. The most likely prospect for achieving the competing goals of low production cost and good performance will apparently come from the Innovative Concentrator program. However the performance of the four designs must be well established along with their production cost estimates before a selection can be made and the final design of a 20 ke Brayton PCA completed

4.2.2 POWER CONVERSION ASSEMBLY

4.2.2.1 Summary of SABC Engine Losses

To summarize the DTM SABC engine loss mechanisms, we will review the five most significant loss areas and compare their relative importance. Note that with the exception of number 1, each of these problems can be specifically related to the inherent characteristics of the SABC design and would not be a factor in an open cycle design. These are the conclusions from the engine analysis (section 3.2.8).

1. Leaks: The commitment of the SABC design to air bearing mandates that 9 to 12% of the working fluid must be bled into the compressor intake. An additional 3 to 4% infiltration occurred primarily at the heat sink and the turbine exhaust piston ring.

131

2. Compressor Efficiency: Leakage and excess pressure drop were the prime contributors to the mismatching of the compressor and turbine. Poor distribution of flow entering the compressor section due to heat sink transition ducting will always handicap the SABC engine. The compressor efficiency measurements, although somewhat inconclusive; indicate that adiabatic total static efficiencies are in the 60 to 68% range for rated speeds.

3. Elevated compressor inlet temperature: This cannot be attributed to a single cause. All off-design components in the cycle contribute to a rise in inlet temperature in the SABC closed cycle configuration. The measured increase of approximately $20^{\circ}F$ to $30^{\circ}F$ (60 to $80^{\circ}F$ above ambient) is the result of sub-optimum performance in all components. This cannot occur in the open cycle, which will always ingest ambient air.

4. Pressure drops: These were really not too far out of line. The SABC goal of 9.0% can be compared to the nominal measured value of 12.5%. Most of this deviation occurred on the heat rejection side. Elimination of the heat sink and improvement of the turbine exhaust diffuser would bring this in line with the 20 kWe open cycle goal (Figure 33).

5. Induction of ambient temperature combustion air: This was permitted in order to avoid a redesign of the recuperator high pressure side entrance partition. The AiResearch CDR presentation at Sanders made reference to this when stating that air was bypassing the recuperator enroute to the combustor. Additional fuel is consumed to make up for the enthalpy loss from the cycle. Receiver efficiency was also reduced as a result of the subsequent by-passing of flow around the receiver.

4.2.2.2 Alternator Performance Summary

The performance of the shaft speed permanent magnet alternator was substantially below that originally advertised by the manufacturer. Following a set of detailed characterization tests of the alternator driven by a calibrated dynometer, efficiency (shaft to DC electric) expectations dropped about 10 percentage points to about 82%. The discrepancy between these measurements and earlier calculations is primarily attributed to aerodynamic frictional effects in the rotor passage and the integral air bearings. Electrical losses in the rectifier (voltage drop) and copper losses appear to be in line with original predictions but represent roughly only 10% of the power lost. Viscous losses in the two journal and

132

Open Cycle 20KW Eliminates SABC Inherent Problems
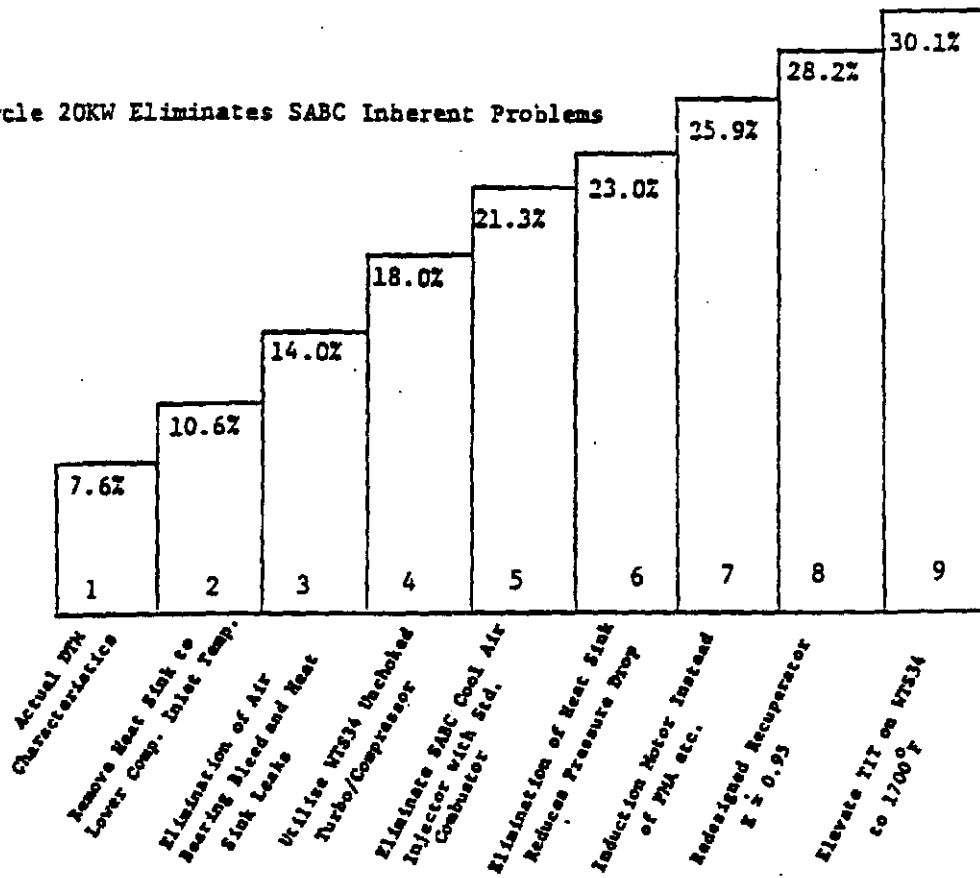
Figure 33. Thermal to Electric PCA Efficiency
Excluding Thermal Loss in Receiver

two thrust bearings proved to be very difficult to predict. Later measurements of air bearings from other test rigs implied that losses on the order of 350 to 400 watts should be expected. This factor accounts for about half of the discrepancy. At this point in the study, the remaining shorfall is assumed to be associated with the drag between the rotor and staor. Analytical inspection of the flow in the rotor gap reveals a friction factor many times greater than that predicted for conventional Couette flow conditions. At rotor peripheral speeds of approximately 550 ft/s, the Renolds number in the gap is in the transition region between turbulent and laminar. The preence of secondary flow vorticies as observed by Taylor and Pai (ref. 3) are thought to be responsible for a portion of the excess shaft torque lost. Also the uncertainties introduced by the slotted rotor and the superposition of substantial cooling flow in the gap contributed to the difficulty in deriving analyticaly based performance prediction.

4.2.2.3 Receiver

The receiver is now quite well understood. DTM test data has provided a valuable opportunity to correlate the receiver performance data and the receiver predictive model. It is clear that a low cost, $1600^{\circ}F$ receiver can be built to operate at near 80% efficiency with a suitable high performance concentrator.

4.2.2.4 Balance of PCA

The balance of PCA thermodynamic and structural package represents a straightforward engineering design problem. Abandoning the subatmospheric cycle simplifies the hardware requirement and assures that high performance efficiency (over 0.30) is achievable.

4.2.3 POWER CONDITIONING EQUIPMENT

Power conditioning equipment is that equipment that takes PCA electrical output and delivers it to the grid.

Equipment that accepts uncontrolled frequency AC power from an alternator or rectified DC power provides maximum stand-alone remote capability. This equipment adds $250/KW to the system capital cost and exacts an efficiency (0.8-0.9) penalty. Equipment that only connects or disconnects 60 Hz power to the grid is obviously low cost and high efficiency, but it sacrifices grid independence.

For applications that do not require tight frequency control, AC generators operating at 1,800 or 3,600 RPM offer a combination of moderate efficiency and low cost.

The issue here is to determine the application requirement and design accordingly.

134

4.2.4 CONTROLS

The DTM controls effort was highly successful. Sanders developed a control system that reliably and safely controlled the engine, communicated with the concentrator, interacted with the operator, provided remote modem capability, and provided fail-safe monitoring of system condition.

The DTM controller was designed to be used in the test environment and to provide flexibility for operating the engine at points throughout its envelope to provide the the performance data not provided by the engine sub-contractor.

The next step is to design a production oriented low cost, minimum function controller, which provides speed control and allows direct generation of (near) 60 Hz power without an inverter.

This does not represent a significant technical risk.

4.3 EFFICIENCY PREDICTIONS FOR THE 20kWe RECOMMENDED OPEN CYCLE ENGINE

Now that the reasons for the performance shortfall of the SA8C engine have been identified,the next issue is how to achieve the design performance goals with the 20 kWe open cycle engine. To do this, the previously presented results will be used to show what is required to build the system efficiency back up to a level of performance typical of larger Brayton systems. The argument is based primarily on the fact that the SABC is a research model and is far more complicated and untested than a larger system in the 20 kW range. Incompletely tested SABC concepts such as the combustor, the heat sink-to-compressor inlet transition,and the air bearings had not been previously developed for gas turbine applications. The actual turbomachinery and the recuperator do not require further research. Alhtough they operated in a predictible,trouble free manner with potentially good efficiencies, their performance was impaired by the ineffective manner in which they were installed in the system.

To provide specific demonstrated engine performance data for our 20 kWe PCA performance projection, we have used the Williams International WTS 34 as our model. However, it should be recognized that a better optimized Brayton engine can be specifically designed for this application. The baseline operating conditions which determine the near term efficiency goals for the open cycle, ball bearing, 20 kW system are essentially the same as those for the turbocompressor and recuperator portion of the existing SABC. However, the potential efficiency is much higher for the 20 kW system. The turbine and compressor in the WTS34 are conservatively designed,

135

consistent with Williams' approach to successful design. State-of-the-art compressor and turbine performance in this size and duty range would yield efficiencies of 82% and 87% respectively. Most importantly, to achieve the new baseline efficiency, no new component development is required.

The greatest improvements over the SABC are realized simply by eliminating the heat sink and the air bearings. Eliminating the heat sink avoids the 60 to 80°F rise in compressor inlet, the difficulties with the combustor, the air leaks and pressure drop. Eliminating the air bearings avoids 70% of the air leakage and the relatively high friction and windage compared to ball bearings. These factors will allow the turbocompressor assembly to operate out of the choked region.

Figure 33 illustrates the performance gains which will be realized by adopting the open cycle concept. The numbers at the base of the columns reference the explanatory paragraphs below:

1. The closed cycle SABC was forced to operate with the compressor inlet at 60° to 80°F above ambient temperature. The open cycle inhales ambient air.

2. All of the measurable leakage on the heat rejection side is directly attributable to the cooling air of the air bearings, the leaks in the heat sink, and the turbine exhaust piston ring. These three features will be eliminated in the 20 kW system. The total remaining low pressure side leakage in the SABC was less than 1%. Sanders has previously built a 20kWe regenerative Brayton system with a much longer gas path and more component interfaces which had no measurable leakage. One percent total leakage is assumed for the new baseline. Sanders has also built three solar receivers which operated at the pressures required for this application without appreciable leakage.

3. Aerodynamic design of the SABC turbomachinery is acceptable. The poor efficiency of the SABC compressor was exacerbated by the system design. Pressure drops and leakage were responsible for a drop in compressor isentropic efficiency of ten percentage points. Absolutely no technical development is required to design the open cycle system such that the WTS34 compressor will operate at its previously demonstrated efficiency of 74%. The WTS34 baseline turbine efficiency is 81%. We have achieved these efficiencies in our earlier program using the original WR34 designed in 1980.

4. The open cycle Brayton avoids entirely the combustor complications which.plagued the SABC. Since the working

fluid will be fresh air on the heat addition side of the cycle, no cool air ingestion will be required at the combustor. The recuperator will not need to be partitioned because stoichiometric requirements will be met as they are in any industrial combustor.

5. Sanders engineers are fully cognizant of the factors which govern system pressure drops. This baseline design assumes no improvement over the pressure drop measured on the heat addition side of the SABC (5.5%). A reduction of four percentage points (P/P) will be realized in the low pressure, heat rejection side of the cycle. This position is strongly supported by the DTM data already gathered. Removal of the heat sink and its awkward transition requirements will account for the bulk of this improvement. Also, the WTS34 turbine exhaust volute will surpass the SABC conical diffuser efficiency for reasons previously stated. An upscaling of the recuperator is already through the design phase. Substantial improvements in pressure drop are expected, especially in the entrance and exit flow conditions.

6. Commercial test data for induction motors clearly supports efficiencies above the 92% used for the baseline; 94.5% is not uncommon. The requirement for a gearbox (98%) does not offset this advantage over the shaft speed alternator. Also, the elimination of the costly inverter will save at least 8 to 18% of the electrical output. Finally, windage and friction losses in the large air journal and thrust bearings of the SABC alternator are 2 or 3 times greater than the losses of the spray lube ball bearing assemblies.

7. Sanders has found the plate and fin recuperator to be a commercially available component. Numerous cost-effective responses to our RFQ by heat exchanger manufacturers support this position. Heat transfer and pressure drop data from the DTM experiments has provided valuable redesign information. Based on this, no changes other than a slight increase in overall size and modifications to the manifolds are required. From an economic standpoint, we believe that the additional plate-fin stacks required to achieve an effectiveness of 95% will add no risk and will enhance the life cycle cost of the unit.

8. Elevation of the turbine inlet temperature (TIT) is not a necessary step in this phase of the program. However, Williams supports this upgrade based on extensive testing of this engine at TITs ranging from 1900°F (short life applications) to 1600°F (greater than 60,000 hour industrial applications). Figure 34 illustrates the relative magnitude of this improvement with respect to the SABC sensitivity studies.

137

Figure 34. Sensitivity of PCA Efficienty to Turbine Inlet Temperature

138

PCA
Efficiency
%

25

20

SABC

15

WTS34

10

1400   1500   1600   1700   1800   1900   2000

Turbine Inlet Temperature °F

4.4 ADDITIONAL TESTING REQUIREMENTS

The PDME program test was a successful effort with solid engineering achievements. The PDM subsystems were characterized and integrated into the Development Test Model. The DTM was characterized and the performance of sub-systems as they interact was analyzed. The DTM was extensively instrumented and reams of raw test data were collected.

Test data and run descriptions were reviewed to select meaningful data sequences where specific test parameters and quasi-steady state conditions were met.

As the data was analyzed and correlated with (partially) validated models, an understanding and quantification of sub-system performance evolved. Many of the initial discrepancies between model predictions and test data were explained by post-test inspections of the test hardware. Numerous leaks in the engine ducting were found. High bearing coolant air flow and low heat sink exchanger effectiveness were identified. Once these off-design engine characteristics were known, better model-to-data correlation was possible. Energy balance calculations based on test data have improved the accuracy of the predictive models.

Beyond the context of the DTM test, additional testing is needed to assure that the 20 kWe Brayton PDM design is well understood and to ensure that the product, in fact, performs up to its potential.

Concentrator characterization will be required to assure that the receiver achieves maximum net energy conversion.

Receiver material and performance tests must be run to further validate and upgrade the predictive model, so that maximum system efficiency consistent with life cycle cost goals can be realized.

Engine tests must be conducted to validate and optimize performance in constant speed and variable speed modes. Accelerated life tests to verify steady-state and transient effects on engine life must be conducted.

Numerous control components must be tested to prove their suitability to the application and environment.

Finally, a full up 20kWe Brayton PDM must be built to demonstrate performance, and reliability and to showcase its cost advantages over competing systems.

APPENDIX A

ANALYTICAL RELATIONS USED IN RECEIVER MODELS

RELATIONS USED IN RECEIVER CAVITY ANALYTIC MODEL

Absorber radiation transmitted through Quartz

$$\dot{Q}_{ARAD} = \sigma * \varepsilon_a (T) * T_Q (\lambda) * \sum_{n=1}^{16 \text{ Elements}} Fva_n * A_n * (Ta_n^4 - T\infty^4)$$

Absorber radiation diffusely reflected off cavity walls through Quartz aperture

$$\dot{Q}_{AR} = [\sigma * \varepsilon_a (T) * T_Q (\lambda) * \sum_{n=1}^{16 \text{ Elements}} - (1 - Fva_n) * A * (Ta_n^4 - T\infty^4)] * R * FV_c$$

Cavity wall radiation through quartz aperture

$$Qc_{RAD} = \sigma * \varepsilon_c * T\sigma (\lambda) * Ac * F_{vc} * (\overline{T}_c^4 - T\infty^4)$$

Emperical equation for estimating conduction/convection through receive front header (KW)

$$QF_h (RIT) = (.440 \times 10^{-3} * \theta_1 + 2.911 \times 10^{-7} * \theta_1 * (\theta_1 - 1093)$$

Where $\theta_1 = (RIT - T\infty)$ °R

Emperical equation for estimating conduction/convection through receiver vessel walls and top (KW)

$$Q_{NT} (RET) = 1.453 \times 10^{-3} * \theta_2 + \theta_2 * (\theta_2 - 566.5) * (\theta_2 - 1132) * 2.253 \times 10^{-9}$$

$$\theta_2 = (RET - T\infty)$$

RELATIONS USED IN ANALYTIC WINDOW MODEL

Absorber radiation absorbed in Quartz first surface

$$\dot{Q}_{A-W} = \sigma * \varepsilon_a * \alpha_Q \ (\lambda) * \sum_{n=1}^{16 \ elements} Fva_n * A_n \ (Ta_n^4 - Tw_i^4)$$

Absorber radiation diffusely reflected off cavity walls, absorbed in Quartz
first surface

$$\dot{Q}_{ARW} = [\sigma * \varepsilon a * \alpha_Q \ (\lambda) * \sum_{h=1} (1 - Fva_n) * A_n * (Ta_n^4 - Tw_i^4)] * R * Fv$$

Cavity wall radiation absorbed in Quartz first surface

$$\dot{Q}_{cw} = \sigma * \varepsilon_c * \alpha_Q \ (\lambda) * Ac * Fv_c \ (\overline{T}_c^4 - T_{wi})$$

Forced convection on Quartz aperture by in pinging inlet air

$$\dot{Q}_F = \overline{h} * Aw * (T_{RI} - T_{WI})$$

Where $\quad h = 0.44 * \dfrac{K}{DW/2} * Pr^{.36} * Re_r^{.5}$

From Perry (Ref. 2)

RELATIONS USED IN ANALYTIC WINDOW MODEL - CONTINUED

Free Convection off Quartz aperture exterior

$$\dot{Q}_E = h * Aw * (T_{wo} - T\infty)$$

Where $h = 0.54 * (Pr * Gr)^{\frac{1}{4}}$

   (Downward facing flat plate from Ref. 1)

Radiation from quartz aperture to ambient

$$\dot{Q}_{RW} = \sigma * \epsilon_Q (T) * Aw * (T_{wo}^4 - T\infty^4)$$

APPENDIX B

AN ESTIMATION OF THE POTENTIAL ERRORS

INTRODUCED BY RECEIVER LEAKAGE

The receiver performance is discussed in Secton IV.2.
Receiver losses were calculated by two methods based on
thermocouple data taken during tests. The two methods differed in
their quantification of receiver losses from the window. Wall
losses from the balance of the receiver were calculated
indentically in the two methods.

In one method the outside window thermocouple reading was
used to calculate window losses. In the second method, window
temperatures and losses were calculated based on energy heating
from the cavity, internal convection, solar absorption and
external free (or light wind driven) correction.

The result of both these methods were compared to entalpy
change in cycle air as determined by inlet and exhaust air
temperature measurements as the air passed through the receiver.

Figure B1 shows that the receiver losses calculated by the
energy balance method agree more closely with the measured
enthalpy changes.

This correlation then raises the spectre of erroneous
readings from the outside window thermocouple, though there seems
to be a ready explanation for the discrepancy.

On figure B1 the first set of data run with no engine (receiver at slight positive pressure) and no solar (so air temperature drop - or enthalpy loss) results only from receiver losses shows the generally close agreement between enthalpy loss and energy balance loss estimates.

In the third set of data (with the receiver plumbed to the engine - it was therefore operating at a slight negative pressure) energy balance and enthalpy loss points still provide a better agreement, though the discrepancy is greater than in the pressurized receiver case mentioned above.

Post test inspection showed that leakage occured around the window.

During tests with the engine (receiver at negative pressure) cold air infiltration and dilution effect of the cycle air would cause an apparent (based temperatures) enthalpy loss of nearly .5 kw.

During preheat tests with the receiver slightly pressurized the combustion blower, a mass transport loss would occur around the window but the receiver exhaust is not diluted, so the

enthalpy loss due to leakage would not be detected by a difference in inlet/exhaust temperatures.

The window thermocouple data was reviewed to determine whether or not a correlation between operating conditions and temperature readings supported the window leak hypothesis. Such a correlation was found and it indicates that the outside thermocouple was heated by hot air leaks during preheat tests (with a pressurized receiver) and cooled by infiltrating cold air during engine tests (when receiver pressure was negative).

There was not apparent correlation between window thermocouple errors and the presence or absence of solar input to the receiver.

COMPARISON OF LOSS ESTIMATES BY VARIOUS METHODS
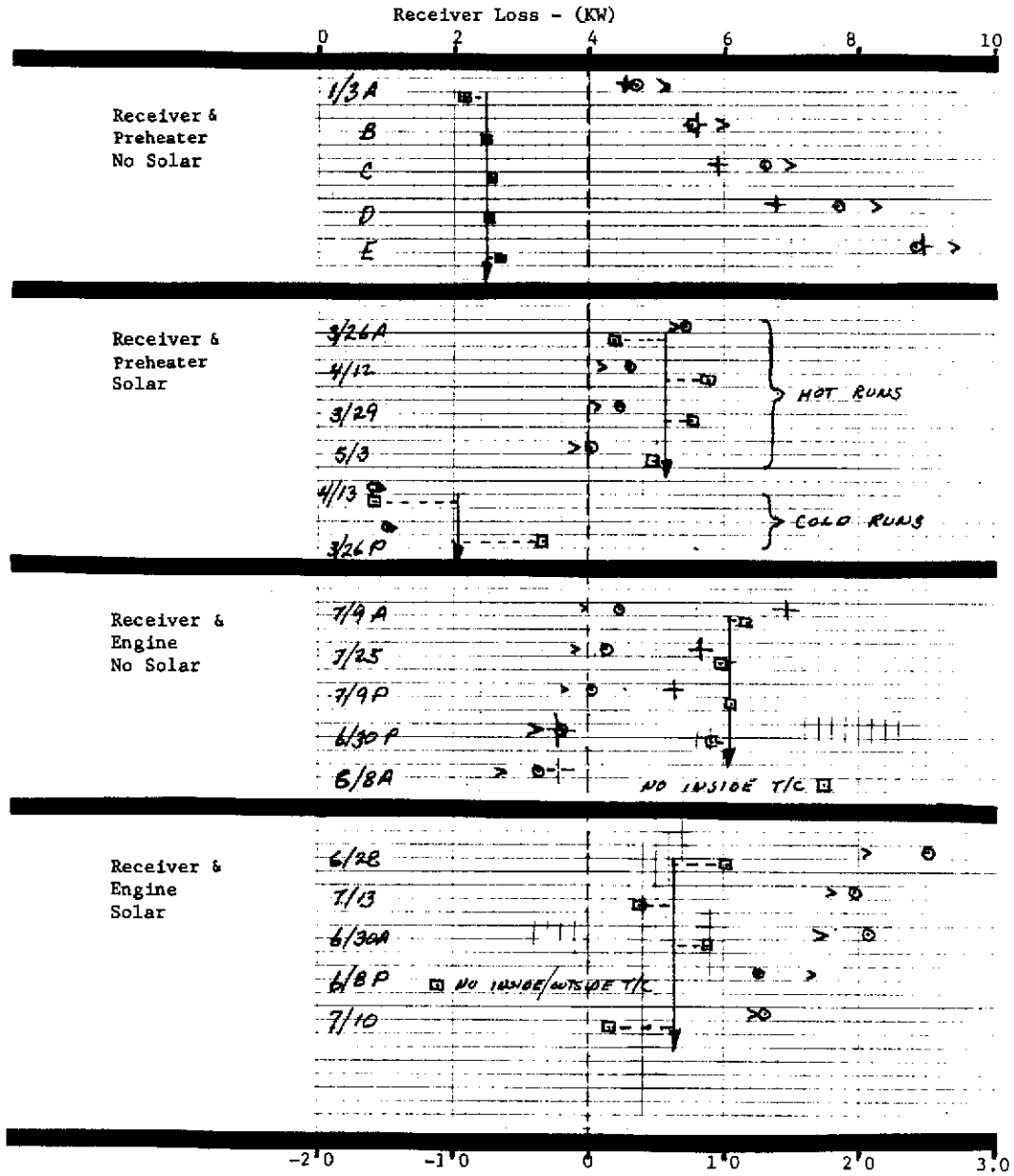
$$\% \text{ Difference} \left[100 \times \left(\frac{\text{Energy Balance} - \text{TC Loss}}{\text{TC Loss}} \right) \right]$$

LEGEND

Upper Scale > Losses Calculated From TC Data
Upper Scale ⊙ Losses Calculated From Energy Balance
Upper Scale + Losses Calculated From Enthalpy Change
Lower Scale ⊡ % Difference Between TC & Energy Balance

NOTE that losses, ⊙ , calculated by energy balances agree more closely than losses,
>, calculated by TC (thermocouple) data do with losses, +, calculated from air
enthalpy changes as measured in non-solar tests.

Page B-5

FIGURE B1

PARAMETERS USED IN QUARTZ WINDOW ENERGY CONSERVATION ANALYSIS

DATE, TEST	IN IR LOAD (KW)	IN CONV. (KW)	SOLAR LOAD (KW)	$\sqrt[4]{Ta^4}$ (°F)	RIT (°F)	RET (°F)	H in BTU/HR/FT^2/R	H out BTU/HR/FT^2/R	K BTU/HR/FT^2/R
1/13/84 A	0.578	0.332	0	1099.0	1140.2	1083.1	5.682	1.418	0.521
B	0.726	0.360	0	1187.3	1242.0	1172.6	5.794	1.446	0.360
C	0.908	0.376	0	1278.9	1334.2	1262.7	5.895	1.472	0.609
D	1.084	0.400	0	1361.7	1426.2	1344.8	5.988	1.494	0.651
E	1.252	0.432	0	1434.0	1522.0	1413.9	6.078	1.513	0.690
3/26 A	1.244	0.085	1.185	1369.9	956.0	1062.0	5.760	1.448	0.583
3/26 B	0.486	−0.306	0.203	997.4	76.4	298.5	4.455	1.131	0.245
4/12	1.138	−0.192	0.291	1316.2	776.4	1028.2	5.493	1.395	0.535
4/13	1.221	−0.230	0.302	1342.4	768.7	1031.6	5.501	1.404	0.545
5/3A	0.200	−0.136	0.235	760.2	74.2	348.6	4.167	0.922	0.168
5/3P	0.957	−0.126	0.258	1245.1	759.7	981.2	5.435	1.378	0.501
6/8 A	0.355	0.250	0	914.5	982.8	903.1	4.128	1.290	0.437
6/8 P	1.320	0.016	0.237	1415.1	1107.3	1313.0	4.837	1.414	0.623
6/28	1.914	−0.083	0.305	1611.5	1202.6	1464.8	4.867	1.477	0.715
6/30 A	1.892	0.288	0.343	1589.3	1056.1	1400.7	4.845	1.470	0.689
6/30 P	0.393	−0.195	0	977.5	1032.9	967.9	4.62	1.326	0.459
7/9 A	0.526	0.351	0	1088.5	1190.3	1062.2	4.676	1.366	0.512
7/9 P	0.467	0.322	0	1039.3	1114.4	1021.7	4.736	1.348	0.488
7/10	1.515	−0.142	0.312	1468.4	979.3	1302.5	4.290	1.439	0.627
7/13	1.792	−0.182	0.346	1555.8	1022.0	1434.5	4.451	1.454	0.673
7/25	0.509	0.327	0	1072.6	1152.8	1048.5	4.652	1.349	0.503

APPENDIX C

QUARTZ MATERIAL DATA

OPTICAL PROPERTIES

Types 125 and 126 fused quartz are high on the list of the most efficient materials commercially available for transmission of ultraviolet and visible radiation. In addition, it has low infrared absorption, out to about 4.0 micrometers, and has a small water absorption band at 2.72 micrometers. Type 124 fused quartz is not generally considered where optical clarity is desired because its appearance is hampered somewhat by the presence of small bubbles. It too has a small water absorption band at 2.72 micrometers.

Fused quartz will darken with the absorption of atomic radiation, and this effect is normally measured by transmittance specimens

TRANSMITTANCE CURVE - 124 FUSED QUARTZ TUBING FOR ONE CM THICKNESS *(INCLUDING SURFACE REFLECTION LOSSES)

TRANSMITTANCE CURVE - 125 & 126 FUSED QUARTZ TUBING FOR ONE CM THICKNESS *(INCLUDING SURFACE REFLECTION LOSSES)
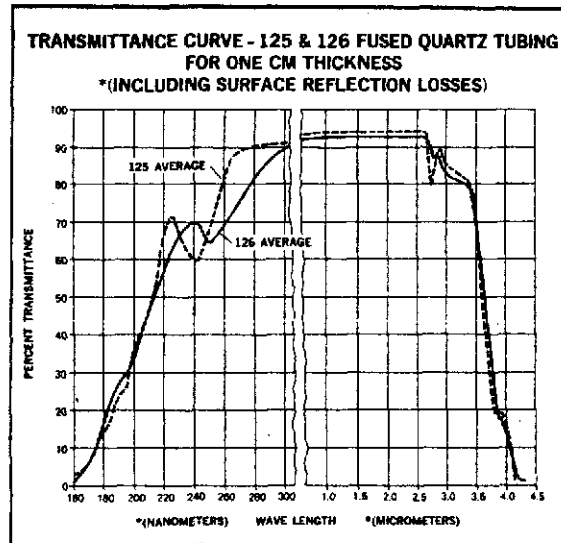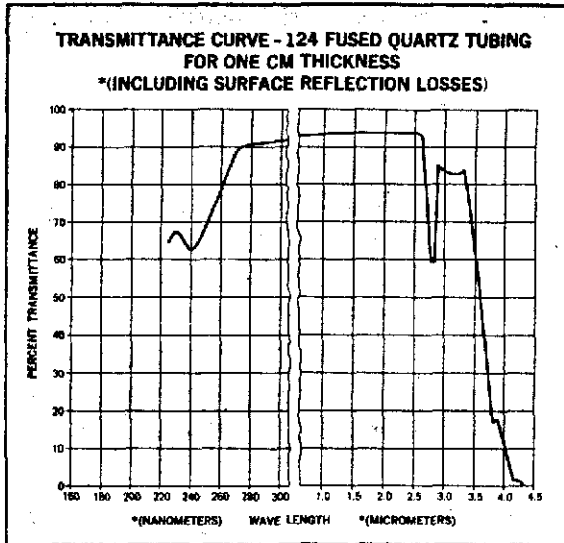
TABLE III — TRANSMITTANCE OF TYPE 124

Wavelength in Nanometers	Average Transmittance in Percent	Average Absorption Coefficient (CM⁻¹)
225	65.0	.342
230	67.4	.308
240	62.6	.383
250	69.5	.280
270	89.0	.035
300	91.2	.014
350	91.9	.009
450	92.5	.005
550	92.3	.004
650	92.9	.003
750	92.8	.005

Wavelength in Micrometers	Average Transmittance in Percent	Average Absorption Coefficient (CM⁻¹)
1.00	93.2	.002
1.50	93.4	.001
2.00	93.6	.001
2.50	93.2	.007
2.60	92.9	.011
2.73	59.3	.460
2.90	85.2	.099
3.00	83.3	.122
3.17	82.5	.132
3.32	83.6	.120
3.60	48.3	.671
3.80	17.2	1.704
3.88	17.5	1.687
4.14	1.7	4.017
4.27	1.5	4.135
4.31	0	∞

TABLE IV — TRANSMITTANCE OF TYPE 125

Wavelength in Nanometers	Transmittance in Percent Average	Minimum	Absorption Coefficient (CM⁻¹) Average	Minimum
160	2.79	0	3.46	
170	6.53	0	2.62	
180	14.4	0	1.83	
190	24.3	0	1.32	
194	27.00	0	1.21	
200	36.0	0	.926	
210	45.4	0	.697	
220	66.3	11.6	.322	2.06
225	71.2	25.7	.251	1.27
230	67.7	35.5	.302	.949
240	59.9	38.4	.428	.872
250	69.3	52.1	.284	.569
267	88.7	88.7	.039	.039
300	90.9	90.9	.017	.017

Wavelength in Micrometers	Transmittance in Percent Average	Minimum	Absorption Coefficient (CM⁻¹) Average	Minimum
2.5	93.8	92.5	0	.014
2.6	93.9	93.0	0	.010
2.7	93.8	92.1	.002	.020
2.72	79.7	73.1	.165	.251
2.8	82.5	77.4	.130	.190
2.9	88.1	86.0	.065	.089
3.0	84.7	83.6	.105	.119
3.2	82.9	82.4	.128	134
3.4	80.0	79.5	.132	.139
3.5	68.6	64.5	.319	.381
3.6	48.5	48.3	.667	.671
3.8	18.6	18.3	1.624	1.645
3.9	18.8	18.4	1.614	1.640
4.0	15.0	15.0	1.845	1.845
4.15	2.0	2.0	3.863	3.863

Fig. 3
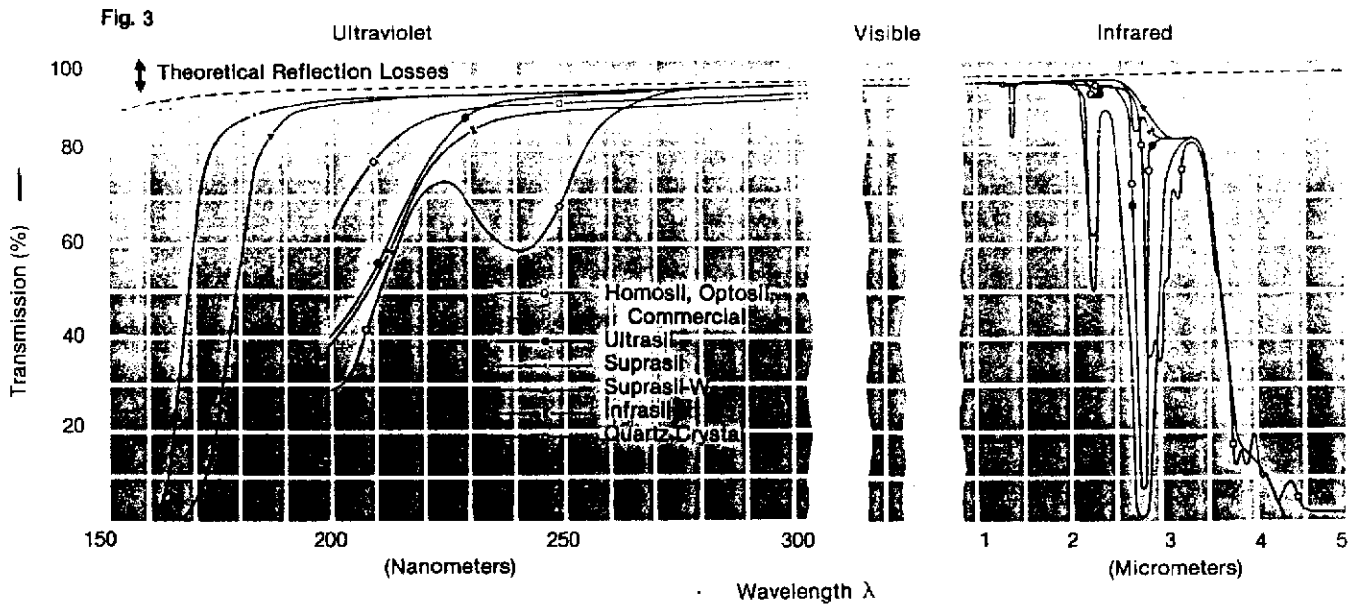
Transmission

Careful use of the above transmission curves will be of great assistance in selecting the proper quality for a specific application and is generally a more reliable method than depending on specific trade names. The curves shown above indicate the transmission characteristics of all of our quality groups, together with that of natural quartz crystal. The sample thickness is 10mm and maximum deviation from the indicated figure is normally 5% for stock materials. However, on special orders the indicated transmissions can be held more uniformly. Therefore a comparision can be made of our various qualities at specific wavelengths from 160 nm in the short UV, through the visible region and out to 5 μm in the IR region. More specific curves for each grade showing the transmission at several sample thicknesses will be found on later pages describing each specific quality.

Please note that all curves indicate external "Transmission." To convert to internal "Transmittance" it is only necessary to add the reflective loss as indicated.

Transmission: D is the measurable or measured optical transmission including the reflection losses at the outside surfaces:

$$D = (1-R)^2 \times 10^{-kd} \qquad R = \frac{(n-1)^2}{(n+1)}$$

Because of these reflection losses, these transmission curves never reach a transmission of D=100%

Transmittance: T is defined as the "internal transmission" called transmittance and does not consider the conditions of the surfaces.

$$T = 10^{-kd}$$

R = Reflection losses at one surface
k = Coefficient absorption
d = Path length
n = Refractive index

Fig. 4 ## Absorption Coefficient

Wavelength (nm)
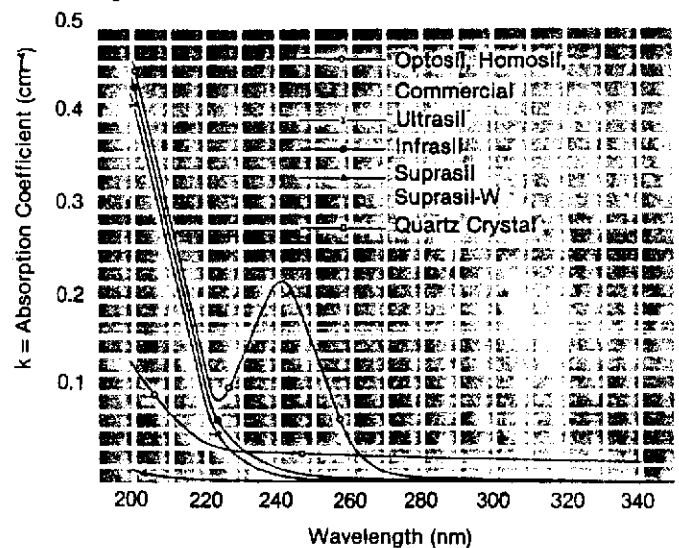
Fused Quartz—Fused Silica

Typical Properties
at 293K unless otherwise noted

	Natural*	Synthetic*
Softening Point(K)	2000	1870
Annealing Point(K)	1450	1390
Strain Point(K)	1350	1300
Max. Temp.—Continuous(K)	1270	1225
Limited Life(K)	1570	1470
Density (kg/m³)	2.203×10^3	2.201×10^3
Moh Hardness	5.5-6.5	5.5-6.5
Micro-Hardness (N/m²)	$8.6\text{-}9.8 \times 10^9$	$8.6\text{-}9 \times 10^9$
Knoop Hardness		
(.1kg load, N/m²)	6×10^{-3}	6.1×10^{-3}
Avg. Coef. of Thermal Expansion (m/mK)		
273-373K	5.1×10^{-7}	5.1×10^{-7}
273-473K	5.8×10^{-7}	5.8×10^{-7}
273-573K	5.9×10^{-7}	5.9×10^{-7}
273-873K	5.4×10^{-7}	5.4×10^{-7}
273-1173K	4.8×10^{-7}	4.8×10^{-7}
223-273K	2.7×10^{-7}	2.7×10^{-7}
Thermal Conductivity (W/mK)		
@ 293K	1.38	1.38
@ 373K	1.46	1.46
@ 473K	1.55	1.55
@ 573K	1.67	1.67
@ 673K	1.84	1.84
@ 1223K	2.68	2.68
Specific Heat (J/kgK)		
293-373K	750	750
293-773K	960	960
293-1173K	1045	1045
Dielectric Strength (V/m)		
@ 293K	$2.5\text{-}4 \times 10^7$	$2.5\text{-}4 \times 10^7$
@ 773K	$1.5\text{-}2 \times 10^7$	$1.5\text{-}2 \times 10^7$
Dielectric Constant		
0 to 1MHz	3.70	3.70
9×10^3MHz	3.77	3.77
3×10^4MHz	3.81	3.81
Dielectric Loss Angle Tangent		
10^{-3}MHz	<.0005	<.0005
1MHz	<.0001	<.0001
10MHz	<.0001	<.0001
10^2MHz	<.0001	<.0001
10^3MHz	<.0001	<.0001
3×10^4MHz	.0004	.0004

	Natural*	Synthetic*
Resistivity (ohm m)		
@ 293K	1×10^{18}	1×10^{18}
@ 373K	1×10^{14}	1×10^{14}
@ 473K	4×10^{11}	4×10^{11}
@ 573K	1×10^9	1×10^9
@ 873K	8×10^6	8×10^6
@ 1073K	6.3×10^4	6.3×10^4
@ 1273K	1×10^4	1×10^4
@ 1473K	1.3×10^3	1.3×10^3
Compressive Strength (N/m²)	1.17×10^9	1.17×10^9
Tensile Strength (N/m²)		
@ 293K	5.0×10^7	5.0×10^7
@ 573K	6.6×10^7	6.6×10^7
@ 873K	7.4×10^7	7.4×10^7
@ 1173K	8.1×10^7	8.1×10^7
Torsional Strength (N/m²)	3.0×10^7	3.0×10^7
Bending Strength (N/m²)	6.7×10^7	6.7×10^7
Young's Modulus (N/m²)		
@ 293K	7.0×10^{10}	7.0×10^{10}
@ 1173K	8.1×10^{10}	8.1×10^{10}
Torsional Modulus (N/m²)		
@ 293K	3.1×10^{10}	3.1×10^{10}
@ 1173K	3.4×10^{10}	3.4×10^{10}
Poisson's Ratio		
@ 293K	0.17	0.17
@ 1173K	0.19	0.19
Velocity of Sound for		
Compressional Wave (m/s)	5720	5720
Shear Wave (m/sec)	3750	3750
Ultrasonic Velocity for		
Compressional Wave (m/sec)		
@ 323K	5968	5944
Shear Wave (m/sec)@323K	3774	3769
Temp. Coef. of Ultrasonic Velocity		
for Compressional Wave (K⁻¹)	$71. \times 10^{-4}$	81.4×10
Sonic Attenuation (db/m MHz max)	0.1	0.1
Internal Damping	1×10^{-4}	1×10^{-4}

*Source of Raw Material

The above properties are stated as typical values and may not necessarily be the maximum or minimum values unless specifically defined as such. Deviations in properties may occur from lot to lot. Strength values are highly dependent upon the surface finish of the material and generally a 10:1 safety factor is recommended in strength designs.

APPENDIX D

SIMILITUDE TESTS OF RECEIVER MATIRIX FLOW

DISTRIBUTION

LARGE CAVITY AIR FLOW DISTRIBUTION

At Stations 1 through 16 from wooden cold flow model tests

Stations

Conical Absorber Matrix

$$\frac{9}{73}$$

$$\frac{10}{18}$$

$$\frac{11}{25}$$

$$\frac{12}{37}$$

Insulation

Inlet Duct

$$\frac{13}{58} \qquad \frac{14}{20} \qquad \frac{15}{43} \quad \frac{16}{52} \qquad\qquad \frac{8}{80} \quad \frac{7}{30} \qquad \frac{6}{18} \qquad \frac{5}{92}$$

$$\frac{4}{65}$$

$$\frac{3}{53}$$

$$\frac{2}{20}$$

$$\frac{1}{87}$$

Air Velocity
(ft/min)

Exhaust Duct Location
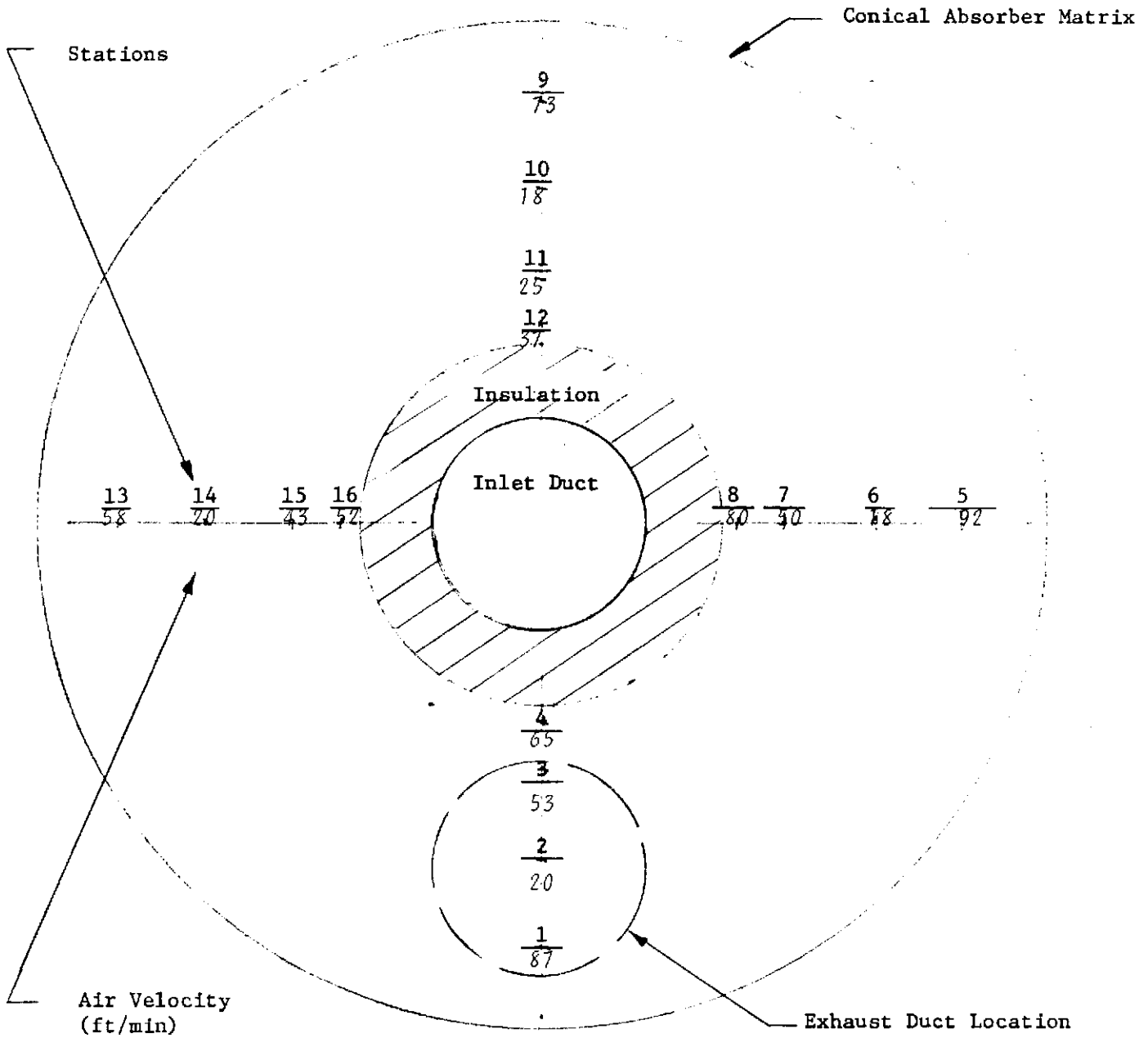
Front View of Receiver Model

Test # 3

Meriam DP = .63 $\implies$ $\dot{m}$ = 0.0943 $\ell b/\delta$

Meriam Inlet Temp $115^{o}F$

LARGE CAVITY AIR FLOW DISTRIBUTION

At Stations 1 through 16 from wooden cold flow model tests

Conical Absorber Matrix

Stations

$\dfrac{9}{125}$

$\dfrac{10}{47}$

$\dfrac{11}{42}$

$\dfrac{12}{42}$

Insulation

Inlet Duct

$\dfrac{13}{120}$ $\dfrac{14}{37}$ $\dfrac{15}{43}$ $\dfrac{16}{55}$ $\dfrac{8}{110}$ $\dfrac{7}{90}$ $\dfrac{6}{45}$ $\dfrac{5}{175}$

$\dfrac{4}{110}$

$\dfrac{3}{70}$

$\dfrac{2}{40}$

$\dfrac{1}{120}$

Air Velocity
(ft/min)

Exhaust Duct Location
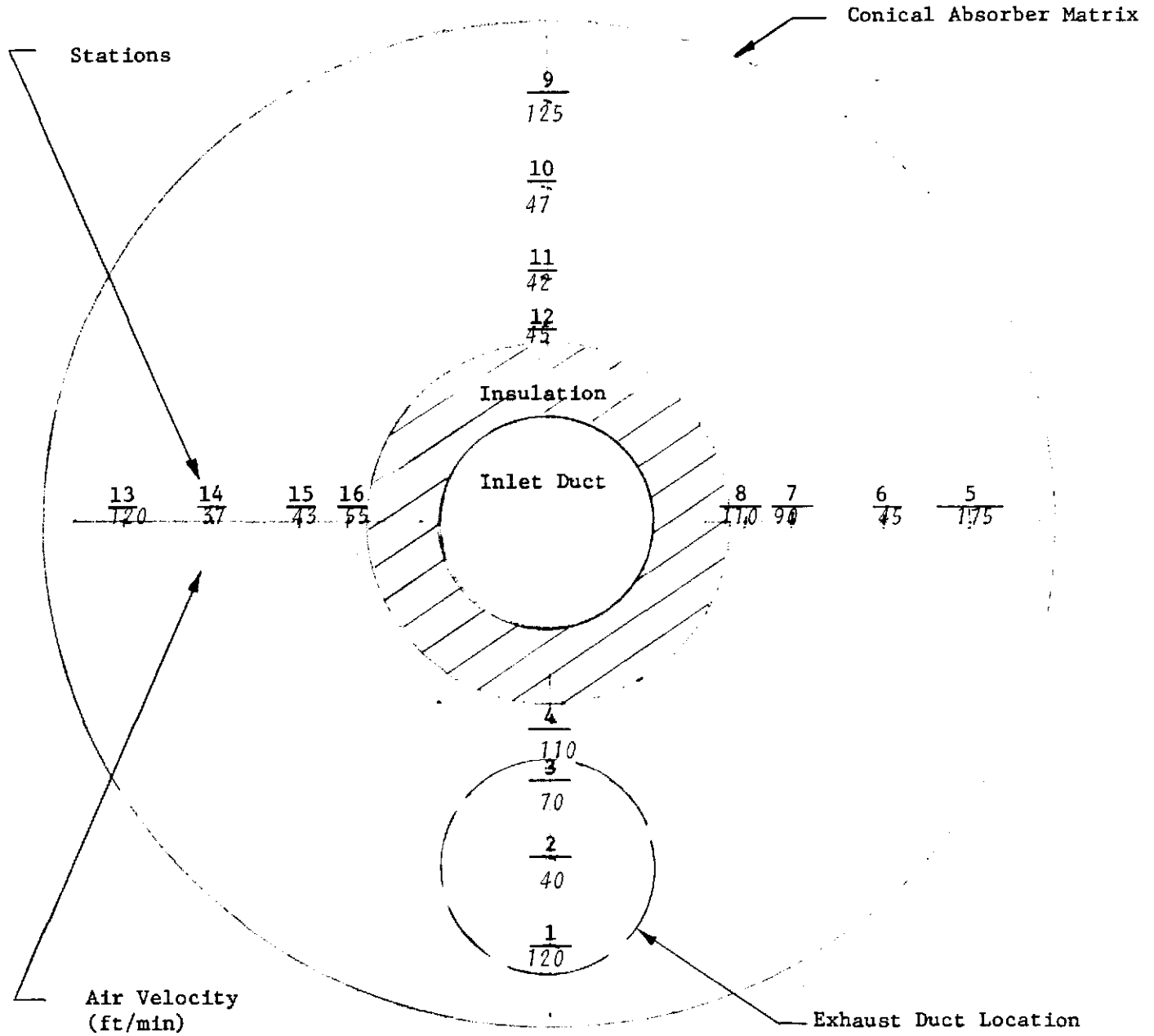
Front View of Receiver Model

Test # 1

Meriam DP   = 1.65" ➡ $\dot{m}$ = 0.254 ℓb/ʒ
Meriam Inlet Temp $99^{\circ}F$

FIGURE D2
Page D-3

LARGE CAVITY AIR FLOW DISTRIBUTION

At Stations 1 through 16 from wooden cold flow model tests

Conical Absorber Matrix

Stations

$$\frac{9}{650}$$

$$\frac{10}{200}$$

$$\frac{11}{170}$$

$$\frac{12}{210}$$

Insulation

Inlet Duct

$$\frac{13}{550} \quad \frac{14}{250} \quad \frac{15}{500} \quad \frac{16}{360} \qquad \frac{8}{300} \quad \frac{7}{445} \qquad \frac{6}{470} \qquad \frac{5}{550}$$

$$\frac{4}{700}$$

$$\frac{3}{120}$$

$$\frac{2}{130}$$

$$\frac{1}{380}$$

Air Velocity
(ft/min)

Exhaust Duct Location

Front View of Receiver Model

Test #2

Meriam DP = $5.55''$ $\Longrightarrow$ $\dot{m} = 0.862$ lb/s

Meriam Inlet Temp $94^{O}F$

FIGURE D3

Page D-4

APPENDIX

Velocity Profile assumed for stations 5, 6, 7, 8 in
the finite difference model of the abosorber

$$\frac{V}{V_m}$$

Velocity distribution
measured in cold model
experiments simulating
Euler number.

Hypothetical "leveled"
flow field required to
improve agreement between
predictions and theromo-
coupler readings

8
(center)

7

6

5
(East)

Absorber Stations
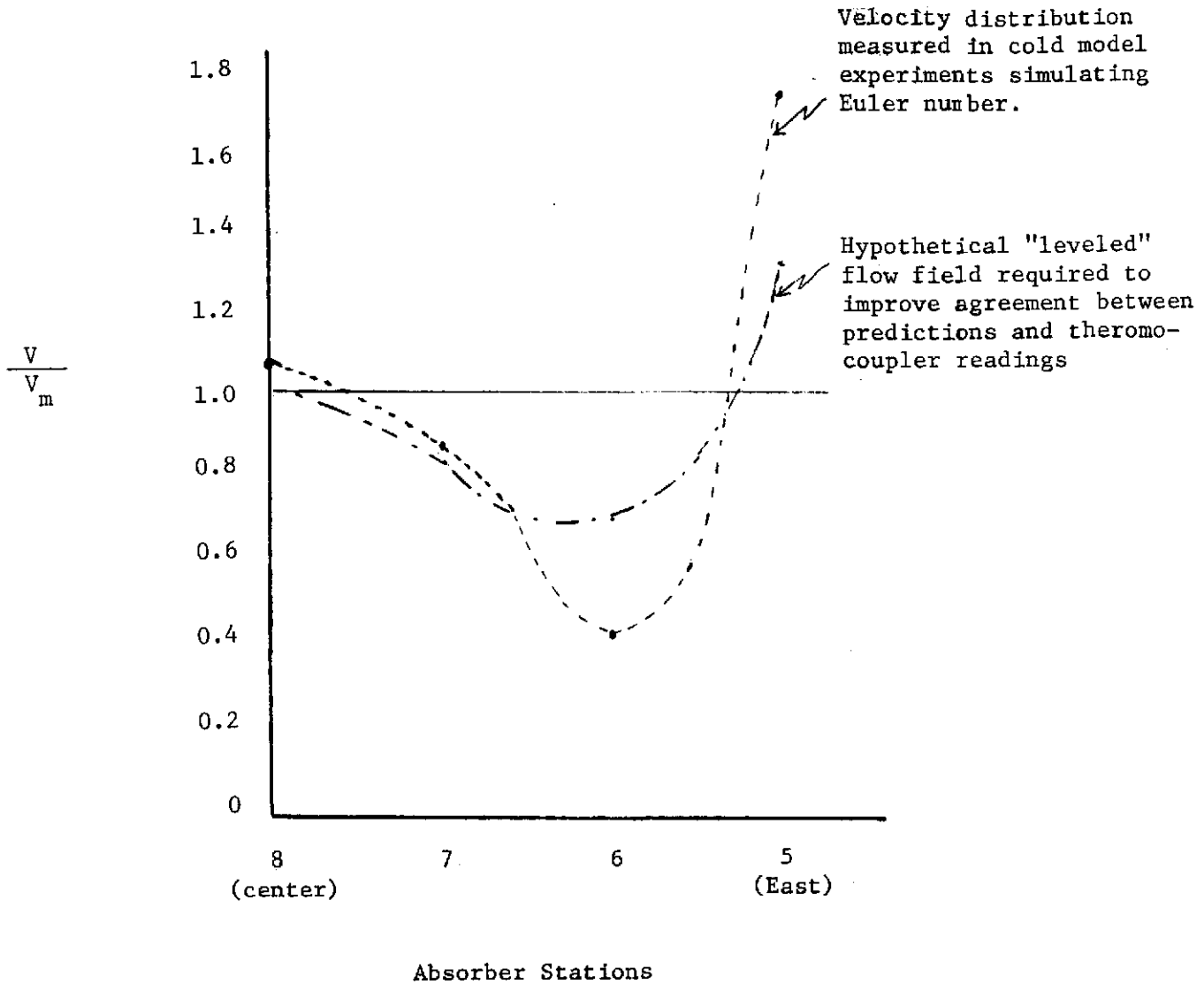
FIGURE D4

APPENDIX E

REFLECTIVITY DATA FOR 3M ECP-91

Energy Control Products

3M

Design Guide

ECP-91 Solar Energy Collection Film

Description
ECP-91 is an energy collecting film being offered as a cost effective, highly reflective, high strength film with superior outdoor weathering properties.

Construction
Opaque, highly reflective metallized layer on a special smooth surface, high strength, 3M Polyester. A protective overcoating on the metallized surface provides low loss specular optics with durable, long lived outdoor weathering properties.

Physical Properties
Tensile Strength: 45 lbs/in. of width
Nominal Thickness: .002"
Stretch a Break: 100%

Optical Properties
Solar Reflectance: Minimum of 85% total reflectance integrated over air mass-2 solar spectrum.

Terms and Conditions of Sale
The following is made in lieu of all warranties, express or implied: Seller's and manufacturer's only obligation shall be to replace such quantity of the product proved to be defective. Neither seller nor manufacturer shall be liable for any injury, loss or damage, direct or consequential, arising out of the use of or the inability to use the product. Before using, user shall determine the suitability of the product for his intended use, and user assumes all risk and liability whatsoever in connection therewith.

Statements or recommendations not contained herein shall have no force or effect unless in an agreement signed by officers of seller and manufacturer.

Spectral Reflectance of ECP-91 Solar Energy Collection Film
(Measured using a Beckman DK2A Ratio Recording Spectrophotometer and an Edwards-Type Integrating Sphere Reflectometer)
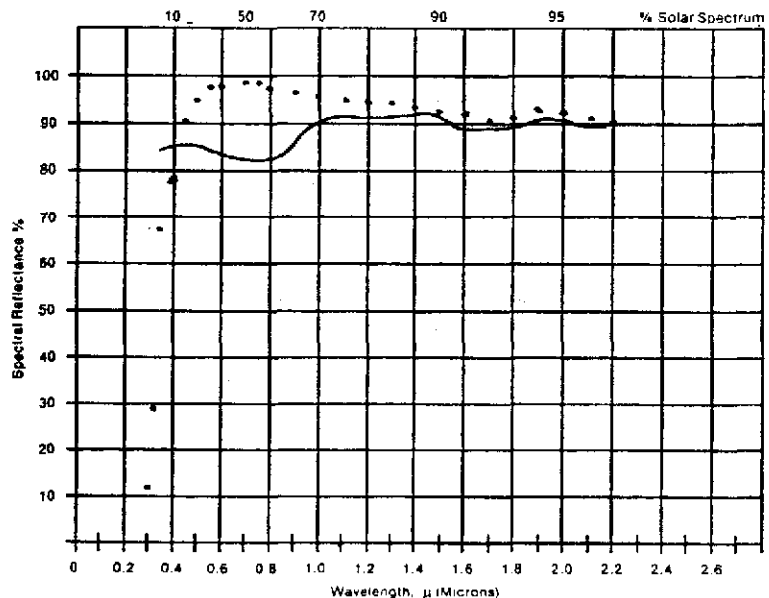
APPENDIX F

EFFECT OF AIR EXCHANGE RATE ON

CYCLE SPECIFIC HEAT

EFFECT OF AIR EXCHANGE RATE ON
CYCLE FLUID SPECIFIC HEAT
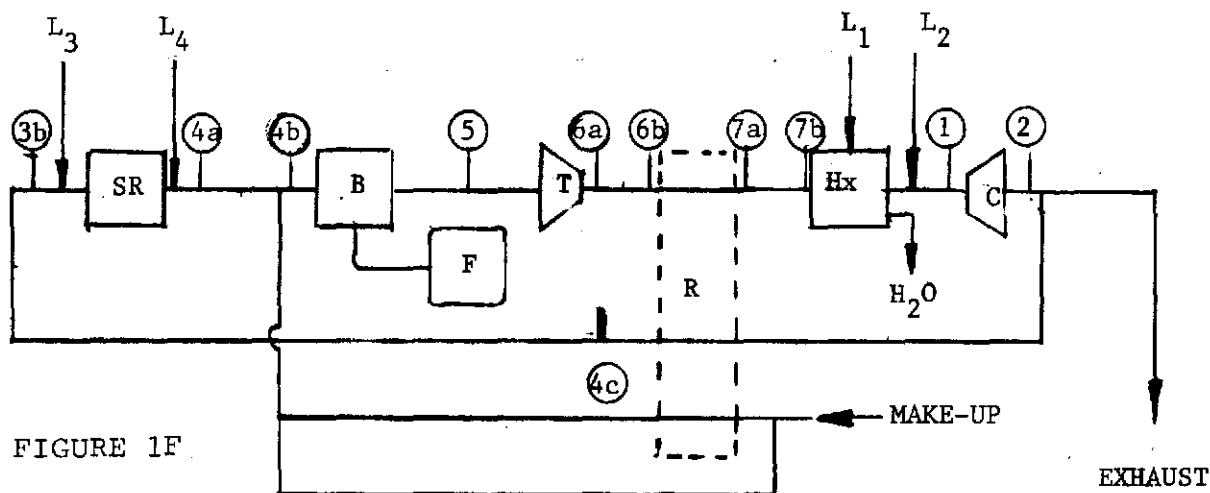
FIGURE 1F

DATA FROM TEST 6/28

LOCATION	EXCHANGE FLOW lb_m/sec	CYCLE FLOW lb_m/sec
① ② Compressor		.279
Condensate Extraction	(.0006)	
L_1 Low Pressure Side Leak	.0087	
L_2 Bearing Coolant Air Bleed	.024	
⑤ ⑥a ⑥b ⑦a ⑦b Low Side		.2469
F→B Fuel Flow	.0016	
④b		.2453
Make Up Air	.0488	
④a		.1965
L_4 Receiver Downstream Leak	.0058	
SR Solar Receiver		.1907
L_3 Receiver Upstream Leak	.0022	
③a ③b		.1885
Exhaust	(.0905)	

CALCULATE STEADY STATE MASS MIXTURE

$$CH_4 + 2O_2 \rightarrow CO_2 + 2 (H_2O)$$
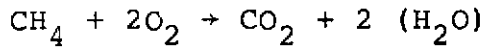
$$(12.011 + 4*1.008) + 2*(2*(15.9994)$$

$$= (12.011 + 2* 15.9994) + 2 (2*1.008 + 15.9994)$$

$$16.043 + 63.998 = 44.010 + 36.031$$

$$80.041 = 80.041$$

$\dot{f}$ = Fuel flow rate

$\dot{w}$ = Water flow rate

$\dot{c}$ = Carbon dioxide flow rate

$\dot{O}_2$= Oxygen flow rate

$\dot{N}_2$= Nitrogen flow rate

Approximate air composition by mass is:

N_2 = .768 and O_2 = .232

O_2 molecular weight = 31.9988

N_2 molecular weight = 28.0134

F fuel mass flow fraction at ②

W water   "

C carbon dioxide "

O oxygen   "

N nitrogen

∴ F + W + C + O + N = 1.0

Recirculating mixture at $\boxed{3a}$, $\boxed{3b}$ is .676 of mix at $\boxed{1}$, $\boxed{2}$.

$\therefore$ Exhaust is .324 M_2

$$M_2 = -.324\, M_2 + \sum_{n=1}^{4} L_n + \text{Make Up} + F$$

$$-F - (3.989F\,(O_2) + 2.743F\,(CO_2) + 2.246F\,(H_2O)) * .95$$

$$- .0006\, H_2O$$

$F = .005735\, M_2$, by comparing fuel flow to compressor flow

	$\dot{f}$	$\dot{w}$	$\dot{c}$	$\dot{O}_2$	$\dot{N}_2$	
INITIAL CONDITIONS				.0647 [1]	.2143	
$\sum_{n=1}^{4} L_n$				.0094	.0313	
Make Up				.0113	.0375	
Fuel	.0016					
Combustion	-.0015	.0034	.0041	-.0060		
Condensate		-.0006				
$\dot{m}$	.0001	.0028	.0041	.0147	.0687	w/leaks
%	.11	3.10	4.54	16.26	76.00	$\sum$= .0904
$\dot{m}$	.0001	.0028	.0041	.0053	.0374	w/o leaks, but w/excess make up
%	0.20	5.63	8.25	10.66	75.25	$\sum$= .0497
$\dot{m}$	.0001	.0028	.0041	.0004	.0210	w/o leaks w/o excess
%	0.35	9.86	14.44	1.41	73.94	$\sum$= .0284

[1] Flow rates in lb_m/sec

Comparison of Cp of Air vs Cp of three different gas mixtures that are representative of characteristic engine air exchange rates.

Constituent specific heats at 900°F, from marks, Standard Handbook for Mechanical Engineers, McGraw-Hill, 7th Edition.

4-12 THERMAL PROPERTIES OF SUBSTANCES AND THERMODYNAMICS

Table 18. Specific Heats of Gases at 1 Atm

Gas	Symbol	Equation for C_p in Btu per mol	Temp range, deg R	Source
Oxygen	O_2	$11.515 - \left(\frac{172}{\sqrt{T}}\right) + \left(\frac{1530}{T}\right)$	540–5000	a
		$11.515 - \left(\frac{172}{\sqrt{T}}\right) + \left(\frac{1530}{T}\right)$ $+ \left(\frac{0.05(T - 4000)}{1000}\right)$	5000–9000	a
Nitrogen	N_2	$9.47 - \left(\frac{3.47 \times 10^3}{T}\right) + \left(\frac{1.16 \times 10^6}{T^2}\right)$	540–5000	a
Carbon monoxide	CO	$9.46 - \left(\frac{3.29 \times 10^3}{T}\right) + \left(\frac{1.07 \times 10^6}{T^2}\right)$	540–5000	a
Hydrogen	H_2	$5.76 + \left(\frac{0.578T}{1000}\right) + \left(\frac{20}{\sqrt{T}}\right)$	540–4000	a
		$5.76 + \left(\frac{0.578T}{1000}\right) + \left(\frac{20}{\sqrt{T}}\right)$ $- \left(\frac{0.33(T - 4000)}{1000}\right)$	4000–9000	a
Water	H_2O	$19.86 - \left(\frac{597}{\sqrt{T}}\right) + \left(\frac{7500}{T}\right)$	540–5000	a*
Carbon dioxide	CO_2	$16.2 - \left(\frac{6.53 \times 10^3}{T}\right) + \left(\frac{1.41 \times 10^6}{T^2}\right)$	540–6300	a
Methane	CH_4	$4.22 + 8.211 \times 10^{-3}T$	492–1800	b
		$27.0 - \frac{14,400}{T}$	1800–5940	b
Ethylene	C_2H_4	$6.0 + 8.33 \times 10^{-3}T$	720–1400	c
Ethane	C_2H_6	$6.6 + 13.33 \times 10^{-3}T$	720–1440	c
Ethyl alcohol	C_2H_6O	$4.5 + 21.1 \times 10^{-3}T$	680–1120	c
Methyl alcohol	CH_4O	$2.0 + 16.67 \times 10^{-3}T$	680–1100	c
Benzene	C_6H_6	$6.5 + 28.9 \times 10^{-3}T$	520–1120	c
Octane	C_8H_{18}	$14.4 + 53.3 \times 10^{-3}T$	720–1440	c
Dodecane	$C_{12}H_{26}$	$19.6 + 80.0 \times 10^{-3}T$	720–1440	c

a Sweigert and Beardsley, Empirical Specific Heat Equations Based upon Spectroscopic Data, *Ga. Sch. Tech., State Eng. Expt. Sta. Bull.* 2, 1938.

b Schwarz, Die Spezifischen Wärmen der Gase als Hilfswerte zur Berechnung von Gleichgewichten, *Arch. Eisenhüttenw.*, 9, 1936, p. 389.

c Parks and Huffman, *ACS, Mon.* 60, 1932.

* Approximate. An equation based on the most recent data is given by Keyes in *J. Chem. Phys.*, 15, Aug. 1947, p. 602.

FIGURE 2F

T = 1360°R

	LB/Mol	BTU/LB°R
$O_2 = 11.515 - \dfrac{172}{\sqrt{1360}} + \dfrac{1530}{1360}$	31.9988	.2493
$= 7.976$ BTU/Mol °R		
$N_2 = 9.47 - \dfrac{3.47E3}{1360} + \dfrac{1.16E6}{1360^2}$	28.0134	.2694
$= 7.546$ BTU/Mol °R		
$CO_2 = 16.2 - \dfrac{6.53E3}{1360} + \dfrac{1.41E6}{1360^2}$	44.010	.2763
$= 12.161$ BTU/Mol °R		
$H_2O = 19.86 - \dfrac{597}{\sqrt{1360}} + \dfrac{7500}{1360}$	18.0154	.5099
$= 9.186$ BTU/Mol °R		
$CH_4 = 4.22 + 8.211\ E\text{-}3\ (1360)$	16.0430	.9591
$= 15.387$ BTU/Mol °R		

CONSTITUENT CP BTU/LB°R	AIR	CYCLE AS MEASURED	CYCLE W/O LEAKS W/EXCESS AIR	CYCLE W/O LEAKS W/O EXCESS AIR	
FUEL	-0-	.0011	.0020	.0035	%
.9591		.0011	.0019	.0034	Cp
WATER	-0-	.0310	.0563	.0986	%
.5099		.0158	.0287	.0503	Cp
CARBON DIOXIDE	-0-	.0454	.0825	.1444	%
.2763		.0125	.0228	.0399	Cp
MOLECULAR NITROGEN	.768	.7600	.7525	.7394	%
.2694	.2069	.2047	.2027	.1992	Cp
MOLECULAR OXYGEN	.232	.1626	.1066	.0141	%
.2493	.0578	.0405	.0266	.0035	Cp
MIXTURE Cp	.2647	.2746	.2827	.2963	
RATIO: Cp/Cp AIR	1	1.037	1.068	1.119	

APPENDIX G

SOLAR RECEIVER DESIGN IMPROVEMENTS

FIGURE I1

DTM RECEIVER ASSEMBLY

SHOWN WITH
GRAPHITE PLUGS REMOVED

REF

.437-.444 DIA
12 HOLES EQ SPACED
ON A 31.680 DIA B.C.

7.00
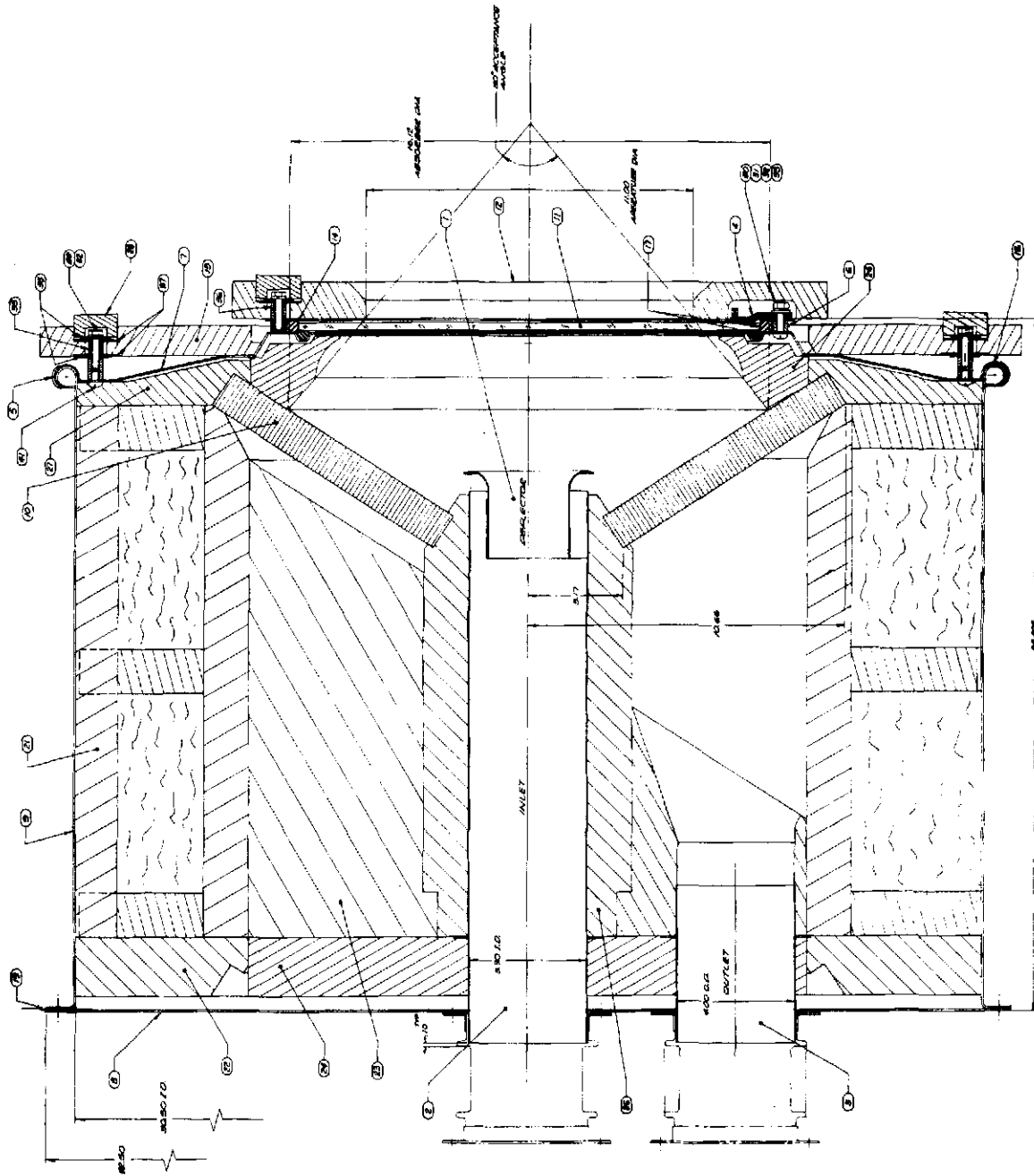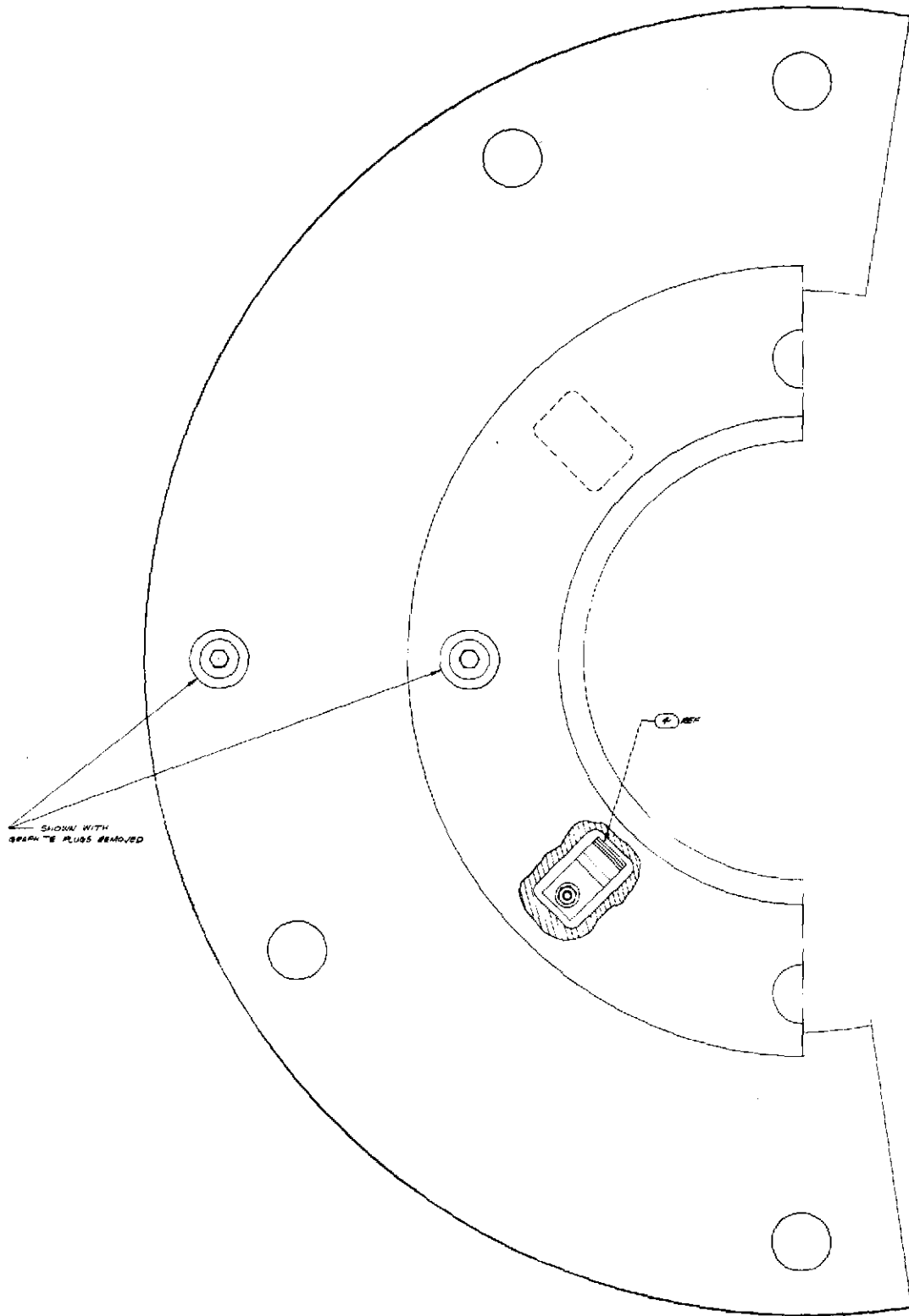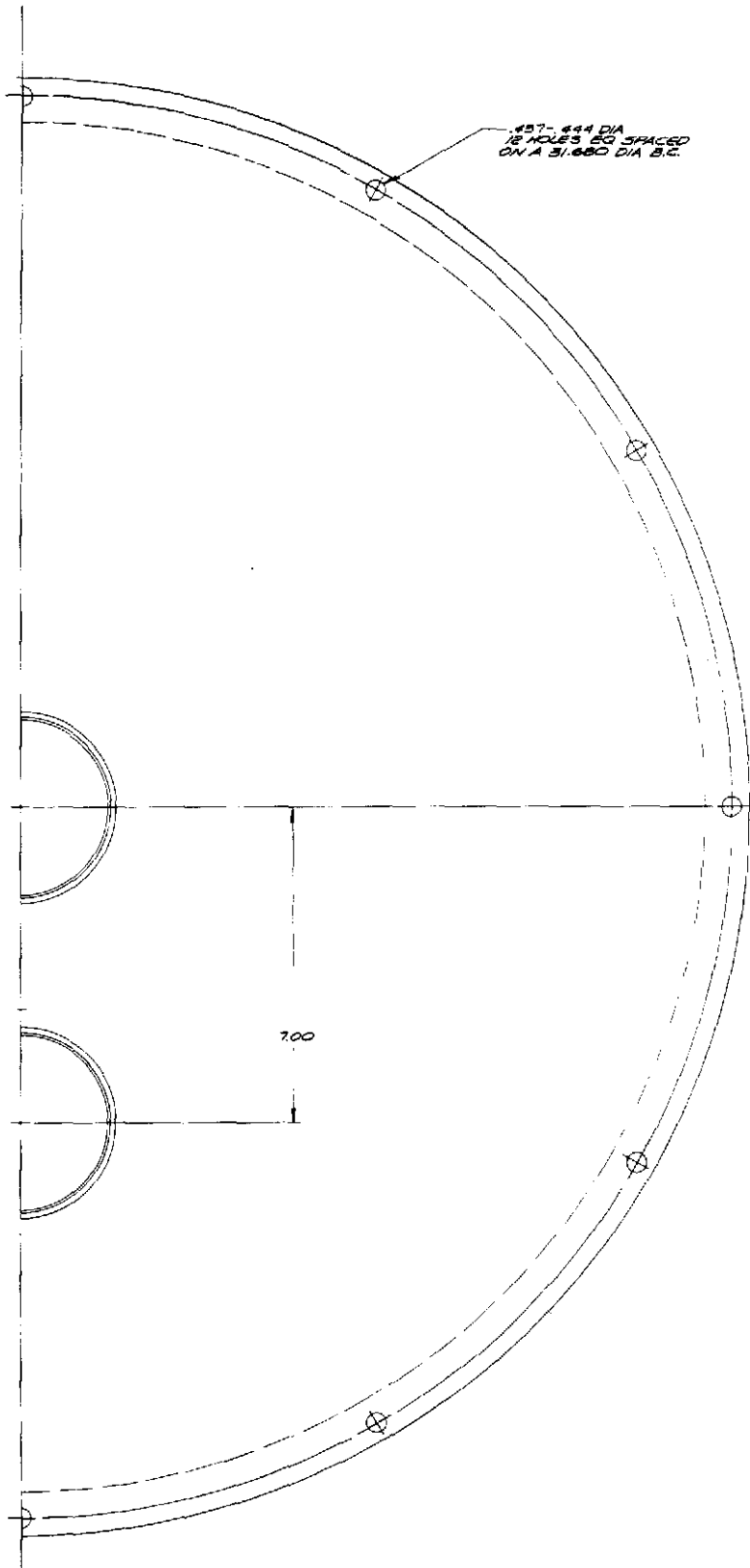
REVISION STATUS														REVISIONS			
	SH	1	2	3	4	5	6	7	8	9	10	11	12	LTR	DESCRIPTION	DATE	APPROVED
PARTS	REV	—	—	—														
	SH	13	14	15	16	17	18	19	20	21	22	23	24				
LIST	REV																

DWG REV	—
WL REV	

2. PARTS LIST SHEET ONE IS THE CONTROLLING REVISION
   FOR THE COMBINED PARTS LIST, DRAWING AND WIRE LIST.

1. SHOP PRACTICE TOLERANCES AND DRAWING INTERPRETATION
   WITHIN 815002 SUPPLEMENT THIS DRAWING.
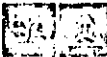
CONT NO.		SANDERS ASSOCIATES, INC	NASHUA, NEW HAMPSHIRE
DR	DATE		
APPD		*RECEIVER ASSY,*	
CHK		*BRAYTON PWR MODULE*	
DEV			
E/M		SIZE: A CODE IDENT NO. 94117 PL 4029102	
PROJ			

PCM

MFG	NEXT ASSY	USED ON	SHEET 1 OF 1
	APPLICATION		

PARTS LIST

ITEM NO.	QTY PER ASSY			DWG SIZE	CODE IDENT	PART OR IDENTIFYING NO.	DESCRIPTION	SYM
	G1	G	G					
1	1			C		4029103 G1	DEFLECTOR ASSY, AIR INLET	
2	1			C		4029104 G1	TUBE ASSY, INLET	
3	1			C		4029105 G1	TUBE ASSY, OUTLET	
4	4			C		4029106 G1	RETAINER ASSY, WINDOW	
5	1			D		4029107 G1	BAND CLAMP ASSY	
6	1			D		4029108 P1	RING, WINDOW SUPPORT	
7	1			D		4029109 P1	COVER, FRONT	
8	1			C		4029110 P1	COVER, BACK	
9	1			D		4029111 P1	HOUSING, RCVR	
10	12			C		4029136 P1	PANEL, MATRIX	
11	1			D		4029112 P1	WINDOW	
12	1			D		4029113 P1	INNER SHIELD, GRAPHITE	
13	1			C		4029114 P1	OUTER SHIELD, GRAPHITE	
14	1			C		4029115 P1	RING, CUSHION RETAINING	
15	1			C		4029116 P1	GASKET, FRONT COVER	
16								
17	AR			C		4029118 P1	GASKET, WINDOW SEAL	
18	12			C		4029119 P2	PLUG, GRAPHITE, LONG	
19	1			C		4029120 P1	GASKET, BACK COVER	
20								
21	1			C		4029121 P1	INSULATOR, OUTER CYLINDER	
22	1			C		4029122 P1	INSULATOR, OUTER RING	
23	1			D		4029123 P1	INSULATOR, INNER CYLINDER	
24	1			C		4029124 P1	INSULATOR, INNER RING	

SHEET ONE REVISION LETTER IS THE IDENTIFYING
 REVISION FOR THIS MULTISHEET DWG
SEE SHEET ONE FOR REVISION DESCRIPTIONS
SYMBOLS ‡ INDICATES VENDOR ITEM - SEE
 SPEC/SOURCE CONTROL DWG.

SIZE	CODE IDENT NO.	
A	94117	PL 4029102

REV — SHEET 2 OF 3

PARTS LIST

ITEM NO.	QTY PER ASSY			DWG SIZE	CODE IDENT	PART OR IDENTIFYING NO.	DESCRIPTION	SIM
	G1	G	G					
25	1			C		4029125 P1	INSULATOR, INLET TUBE	
26	1			C		4029126 P1	INSULATOR, AIR DEFLECTOR	
27	1			C		4029127 P1	INSULATOR, FRONT COVER	
28								
29								
30	4			–		MS51958-83	SCR, MACH, PNH .250-28UNF X 1.00LG.	
31	4			–		MS15795-810	WASHER, FLAT-METAL NO. 1/4	
32	12			–		MS35338-139	WASHER, SPLIT-LOCK NO. 1/4	
33	4			–		MS51972-1	NUT, PLAIN HEX .250-28	
34								
35	8			B			SLEEVE, SHORT (AMATOM)	
36	4			B			SLEEVE, LONG (AMATOM)	
37	8			B			WASHER, SPECIAL (.75 I.D. X 1.5000)	
38							WASHER, FLAT METAL .28 ID 1.000C	
39	8			–		MS35308-310	SCREW, CAP, HEX HD .250-28 X 1.25LG.	
40								
41	8					MS51958-77	SCREW, MACH, PNH .250-28 X .38LG.	
42	REF			D		4029137	FOUNDATION DESIGN – PDTS	
43	REF					4029133	INSULATION ASSY	
44	1			C		4029138	FILTER ASSY, OUTLET	
45								

SHEET ONE REVISION LETTER IS THE IDENTIFYING
REVISION FOR THIS MULTISHEET DWG
SEE SHEET ONE FOR REVISION DESCRIPTIONS
SYMBOLS : INDICATES VENDOR ITEM – SEE
SPEC/SOURCE CONTROL DWG.

SIZE	CODE IDENT NO.		
A	94117	PL	4029102
		REV —	SHEET 3 OF 3

SOLAR RECEIVER DESIGN IMPROVEMENTS

DESIGN COMPONENT	DTM SABC RECEIVER (FIGURE ⚓)	PROJECTED ABC RECEIVER DESIGN

SPECIFICATIONS

THERMAL INPUT	34 KW	120 KW
APERTURE DIAMETER	11.0IN	
ABSORBER DIAMETER	19.0IN	
MASS FLOW	0.2 LB/SEC	0.6 LB/SEC
INTERNAL PRESSURE	-2" WATER	35 PSIG
EXHAUST TEMPERATURE	<1600^F	<1700 F

1. PRESSURE SHELL

DESCRIPTION

DESCRIPTION

- 16 GA (.60) TYPE 321 CRES ROLLED CYLINDRICAL BODY AND SLIGHTLY CONICAL FRONT HEAD WITH FLAT GASKET SEAL.

- 14 GA (.075) CRES BACK COVER DISK WITH REENFORCING BARS AND FLAT GASKET SEAL.

- DESIGNED TO MEET ASME   PRESSURE CODE.

- CONSISTS OF TWO 1/4" CRS, ELIPTICAL, 2:1 RATIO ASME CODE TYPE F&D HEADS WITH WELDED FLANGES, BOLTED TOGETHER WITH AN O RING SEAL. PAINTED WITH SILICONE BASE, HIGH TEMP., HIGH REFLECTANCE PAINT.

● INLET AND OUTLET DUCTS ARE GASKET SEALED TO BACK COVER.

● DESIGNED FOR LIGHT WEIGHT AND LOW PRODUCTION COST
WITH NO REQUIREMENT FOR HIGH TEMP. PAINT FINISH

KEY ISSUES

● EXPERIENCED AIR LEAKS AT GASKETED JOINTS DUE TO
METAL DISTORTION AT HIGH TEMPERATURE.

2. WINDOW ASSEMBLY   DESCRIPTION

● TO ACCOMODATE SLIGHT NEGATIVE PRESSURE IN RECEIVER
THE WINDOW IS SEALED ON A 3/8 X 3/8 INCH CERAMIC ROPE
GASKET LOCATED IN A GROOVE ON THE FRONT HEAD AND
HELD AGAINST THE GASKET BY 4 SPRING FINGERS AND THE
INTERNAL VACUUM.

● INLET AND OUTLET DUCTS ARE WELDED TO
REAR HEAD

● PRESSURE SHELL IS AT LOW TEMP. DUE TO
HEAVY INSULATION. THEREFORE, STANDARD
CRS HEADS CAN BE USED ALONG WITH A
VITON O RING AT THE EQUATOR FLANGE
SEAL.

SOLUTION

● THE ONLY HOUSING SEAL REQUIRED IS THE
RELIABLE "O" RING EQUATOR SEAL.
● INLET AND OUTLET DUCTS ARE WELDED
TO REAR HEAD.
● THE WINDOW MOUNT IS WELDED TO FRONT
HEAD.

DESCRIPTION

● TO ACCOMODATE A NOMINAL 35 PSIG
INTERNAL PRESSURE THE WINDOW SEAT
WILL BE WELDED TO THE FRONT HEAD.

● THE WINDOW IS A 1/4" THICK 15.5" DIA. QUARTZ DISK.

● THE WINDOW WILL BE A QUARTZ DISK, APPROXIMATELY 0.5 TO 1 IN THICK, DEPENDING ON THE APERTURE DIAMETER DIAMETER AS DETERMINED BY THE SELECTED CONCENTRATOR.

KEY ISSUE

SOLUTION

● LIGHT SEALING FORCES (FINGERS + VACUUM) PERMIT SOME AIR LEAKAGE AROUND THE WINDOW.

● THE HIGH SEALING FORCES PROVIDED BY THE INTERNAL PRESSURE ASSURE GOOD SEALING TO THE GASKET.

3. INTERNAL AIR DUCT MATERIAL AND INSULATION

DESCRIPTION

DESCRIPTION

● INLET AND OUTLET DUCTS ARE .049 WALL TYPE 321 CRES TUBE. THE REMAINING INTERNAL DUCT SURFACES ARE CARVED FROM CERAFORM J.M. TYPE 126 RIGID CERAMIC INSULATION, WITH SURFACE IMPREGNATION OF A 30% MIX OF COLLODIAL SILICA. THIS SURFACE TREATMENT PERFORMED VERY WELL, WITH NO EVIDENCE OF CHIPPING OR FLAKING AS PREVIOUSLY EXPERIENCED WITH SURFACE COATINGS.

● CRES AND/OR FORMED CERAMIC WILL BE USED FOR ALL INTERNAL DUCT SURFACES. THIS WILL AVOID POSSIBLE LONG TERM SURFACE EROSION AND PERMIT THE USE OF LESS EXPENSIVE AND MORE EFFECTIVE BATT TYPE INSULATION:

● CURRENT INSULATION:
  JM TYPE 126 CERAFORM BOARD, K = 1.2,
  INSTALLED COST = $60/80 PER CU. FT.

● PROPOSED INSULTATION:
  JM CERABLANKET, K = 2 TO 3
  INSTALLED COST = $24/36 PER CU. FT.

KEY ISSUES

SOLUTION

- NO PROBLEM WITH THE DUCTS. HOWEVER, LONG TERM
  TESTING IS REQUIRED TO ASSURE THAT THERE IS NO
  SURFACE EROSION.

- CRES AND/OR CERAMIC DUCTING WILL
  PREVENT LONG TERM EROSION.

- SOME INTERNAL AIR LEAKAGE OCCURED BETWEEN THE INLET
  AND OUTLET DUCTS, APPARENTLY PASSING BETWEEN PIECES
  OF RIGID INSULATION.

- THE ABOVE DUCTING WILL HAVE FEWER
  JOINTS AND THUS SHOULD SEAL BETTER.

- ABOUT 50% OF THE HEAT LOSS THROUGH THE SHELL PASSED
  THROUGH THE FRONT FACE.

- MORE INSULATION OF HIGHER R VALUE
  WILL BE USED BEHIND THE FRONT FACE.
  ADDITIONAL INSULATION MAY BE APPLIED
  BETWEEN THE FLUX SHIELD AND THE FRONT
  FACE TO FURTHER REDUCE HEAT LOSS.

4. RECEIVER EXHAUST
   AIR FILTER

DESCRIPTION

DESCRIPTION

- A 4" DIA. BY 12" LONG 50 MICRON, CRES WIRE MESH
  FILTER IS MOUNTED IN THE RECEIVER EXHAUST DUCT TO
  REMOVE PARTICLES LARGE ENOUGH TO ERODE THE TURBINE
  WHEEL. ITS PRESSURE DROP IS <0.8 INCHES OF WATER
  FOR 12 CUBIC FT/SEC OF AIR @ 1600 F AND 1 ATM.
  PRESSURE.

- WITH AN OPEN CYCLE ENGINE, AIR (AND
  DIRT) ARE NOT RECIRCULATED.
  THEREFORE, AN INLET AIR FILTER SHOULD
  BE SUFFICIENT.

● FILTER WORKED WELL, BUT ONLY A FEW INSULATION
PARTICLES WERE COLLECTED.

KEY ISSUE   SOLUTION

● FILTER ADDS A LITTLE COST AND PRESSURE DROP TO THE   ● DELETE RECEIVER EXHAUST FILTER. ADD
SYSTEM.   A LOWER PRESSURE DROP INLET AIR
                                                          FILTER.

5. ABSORBER MATERIAL

AND CONFIGURATION   DESCRIPTION   DESCRIPTION

● 12 TRIANGULAR PANELS OF SILICON CARBIDE HONEYCOMB   ● A COMPUTER MODEL TO OPTIMIZE
MATRIX ARE STACKED TOGETHER TO FORM A CONE OF 115 DEG.   CERAMIC HOLE SIZE, WALL THICKNESS
INCLUDED ANGLE FACING THE APERTURE. BOTH ENDS OF   AND PANEL THICKNESS AS A FUNCTION
THE PANELS ARE SUPPORTED IN GROOVES FORMED IN THE   OF MATERIAL CHARACTERISTICS AND FLUX
SURROUNDING RIGID INSULATION. AIR ENTERS THROUGH   DENSITY HAS BEEN CREATED AND
A 4" DUCT IN THE APEX OF THE MATRIX CONE AND EXITS   VERIFIED WITH PDM TEST DATA.
THROUGH THE MATRIX.

● A STAINLESS STEEL DEFLECTOR IS MOUNTED IN THE INLET   ● FINAL ABSORBER CONFIGURATION REQUIRES
DUCT TO IMPROVE AIR DISTRIBUTION TO THE APEX OF THE   FURTHER STUDY AND ANALYSIS, BUT WILL
MATRIX CONE.   PROBABLY BE A FLAT DISK WITH
                                                          PERIPHERAL AIR INLET.

KEY ISSUES   SOLUTION

● AIR DISTRIBUTION ACROSS THE MATRIX IS HARD TO   PERIPHERAL INLET AND EXPANDED
  OPTIMIZE.   ABSORBER AREA WILL PROVIDE BETTER

                                                               FLOW DISTRIBUTION. ADDITIONAL

                                                               EXPERIMENTAL AND COMPUTATIONAL

                                                               MODELING WILL VERIFY IMPROVEMENTS

● THE SILICON CARBIDE PANELS ARE QUITE EXPENSIVE.   ● ALTERNATE CERAMICS SUCH AS

                                                                 CORDIERITE WILL BE ANALIZED AND

                                                                 TESTED. GOAL IS LOWER COST, LONG

                                                                 LIFE, HIGH SOLAR ABSORBTIVITY, GOOD

                                                                 THERMAL CONDUCTIVITY.

6. SOLAR SHIELD   DESCRIPTION   DESCRIPTION

                       ● APERTURE PLATE, 20" OD BY 11" ID BY 1.25" THICK.   ● SEVERAL ALTERNATE MATERIALS ARE TO
                       ● OUTER SHIELD, 33" OD BY 18.7" ID BY 1.0" THICK.   BE EVALUATED, INCLUDING CORNING
                       ● BOTH OF THE ABOVE ARE FABRICATED OF UCAR GRADE   PYROCERAM, CRS PAINTED WITH HIGH
                         ATL GRAPHITE.   TEMP, HIGH REFLECTANCE PAINT,

                                                                              CERAMIC INSULATION BOARD, AND THE

                                                                              USE OF AN EXPENDABLE "WALKOFF STRIP"

                                                                              OVER THE WALKOFF PATH.

KEY ISSUES   SOLUTION

● PROLONGED EXPOSURE OF A PORTION OF THE APERTURE   ●   ONE OF THE ABOVE MATERIALS IS
  ID TO CONCENTRATED FLUX CAUSED SERIOUS ABLASION   EXPECTED TO PROVIDE IMPROVED

● FABRICATED GRAPHITE IS RELATIVELY EXPENSIVE.   PERFORMANCE AND LOWER FABRICATED

                                                        COST.

APPENDIX H

PERMANENT MAGNET ALTERNATOR AND RECTIFIER

DATA TAKEN AT AIRESEARCH, TORRENCE, CA (3/84)

RETIFIER EFFILIENLY (CALCULATED)

$\eta - \%$

100

99

98

97

96

95

80 KRPM — A

60 KRPM — B

40 KRPM — C

	V_{LL}	F
A	250	2870
B	187	2002
C	125	1335

DC CURRENT - AMP

0   5   10   15   20

FIG 2

AIRESEARCH MANUFACTURING COMPANY
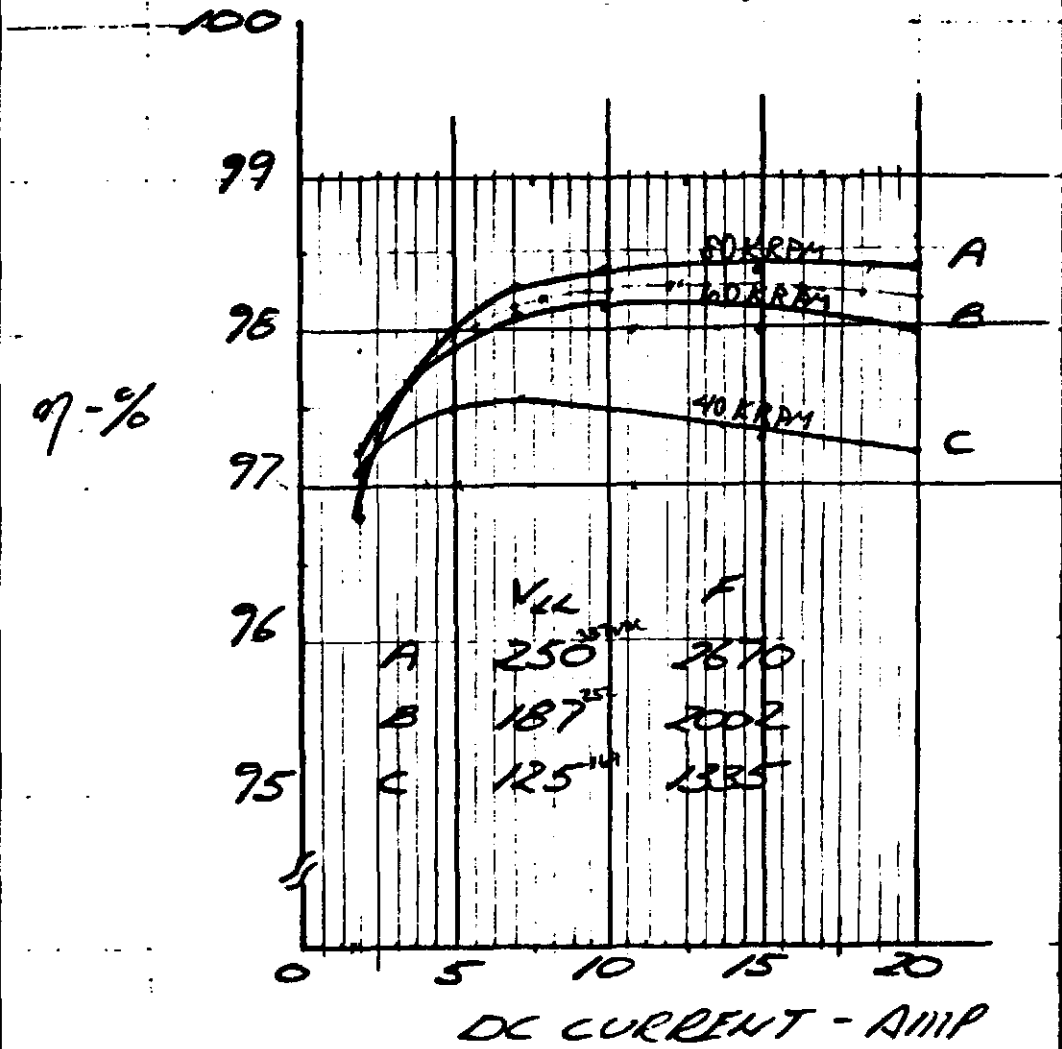
SANDERS 5-KW GENERATOR/RECTIFIER
PERFORMANCE @ 40,000 R.P.M.

COIL COOLING FLOW ≅ 3.0 #/min
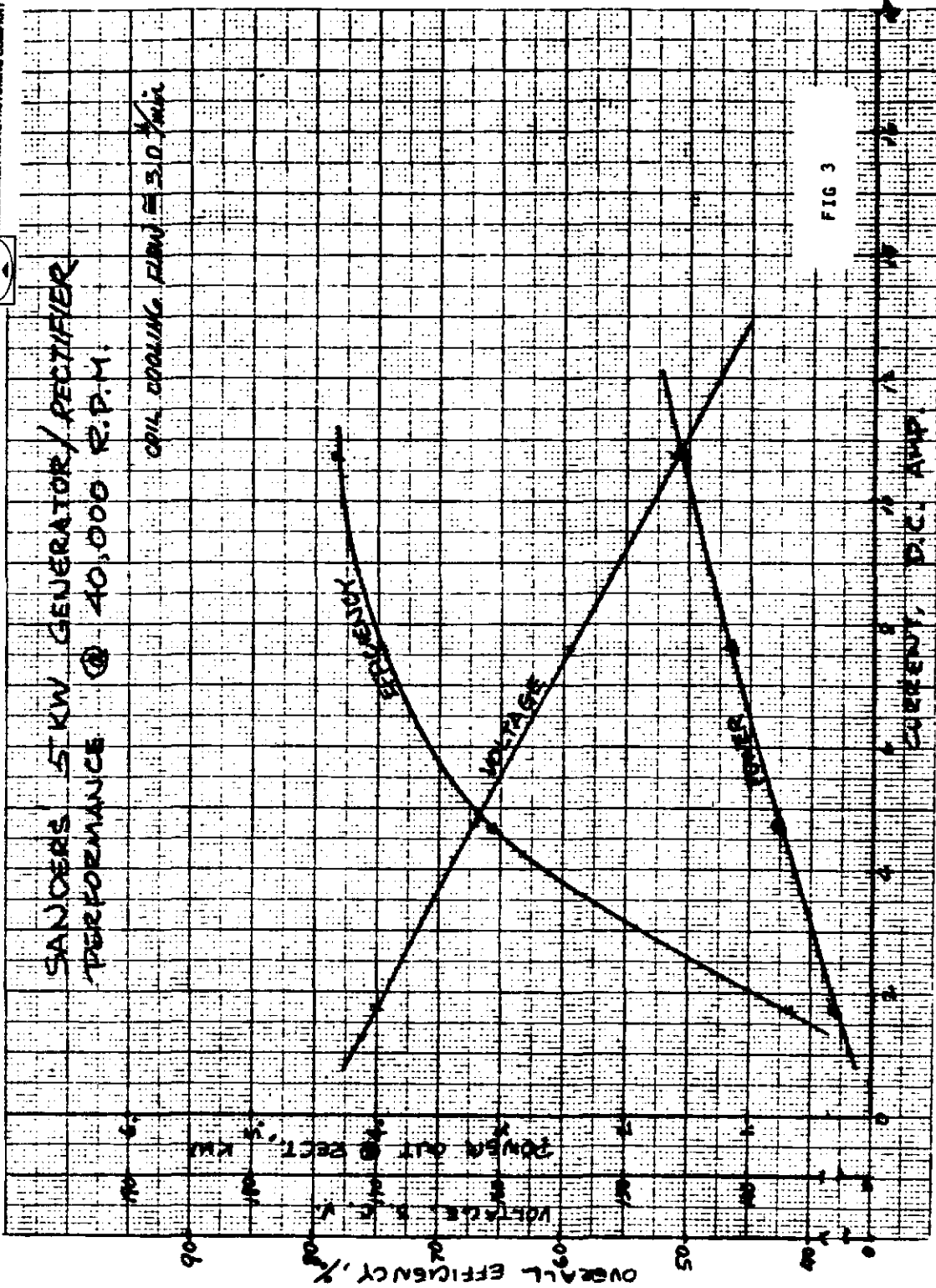
FIG 3

AIRESEARCH MANUFACTURING COMPANY

CONDAIRE 5 KW GENERATOR/RECTIFIER
PERFORMANCE @ 60,000 R.P.M.

OIL COOLING 172 in.³ @ 50 °F/sec

FIG 4

Garrett's 5KW Generator/Rectifier Performance @ 40,000 R.P.M.
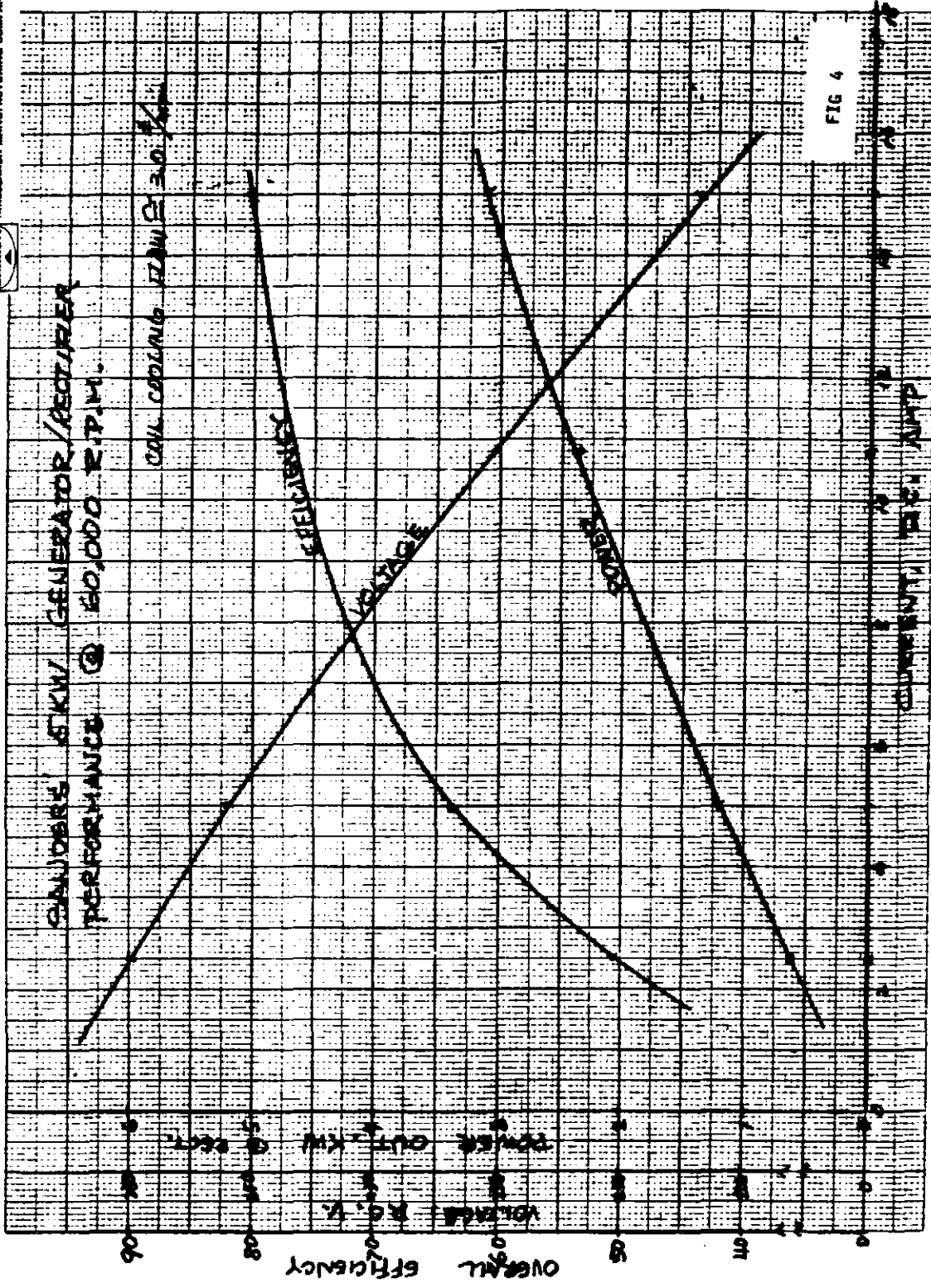
FIG 5

GARRETT AIRESEARCH MANUFACTURING COMPANY

GARRETT'S 5 KW GENERATOR
OVERALL PERFORMANCE @
50,000 ft, 77°F.
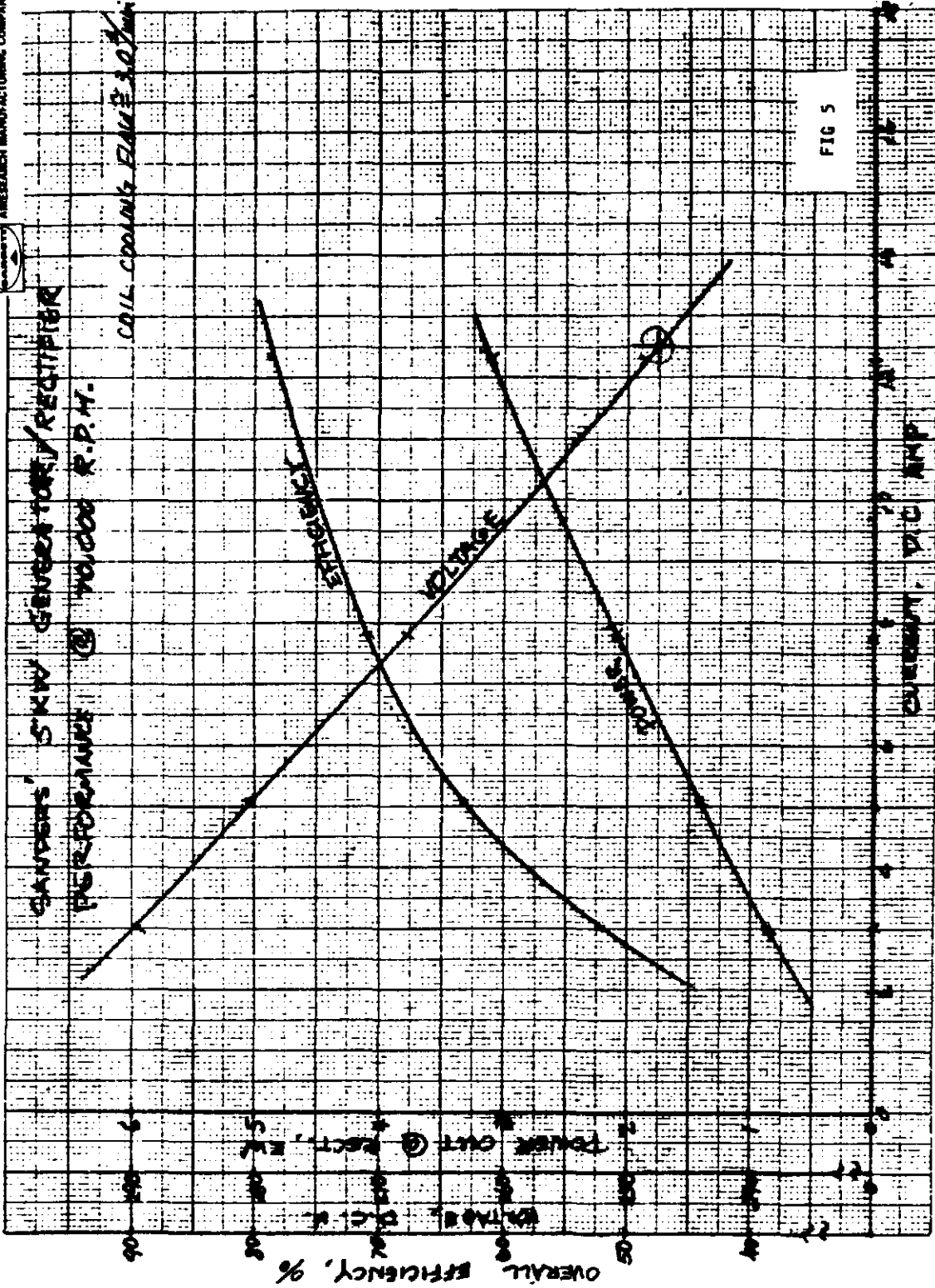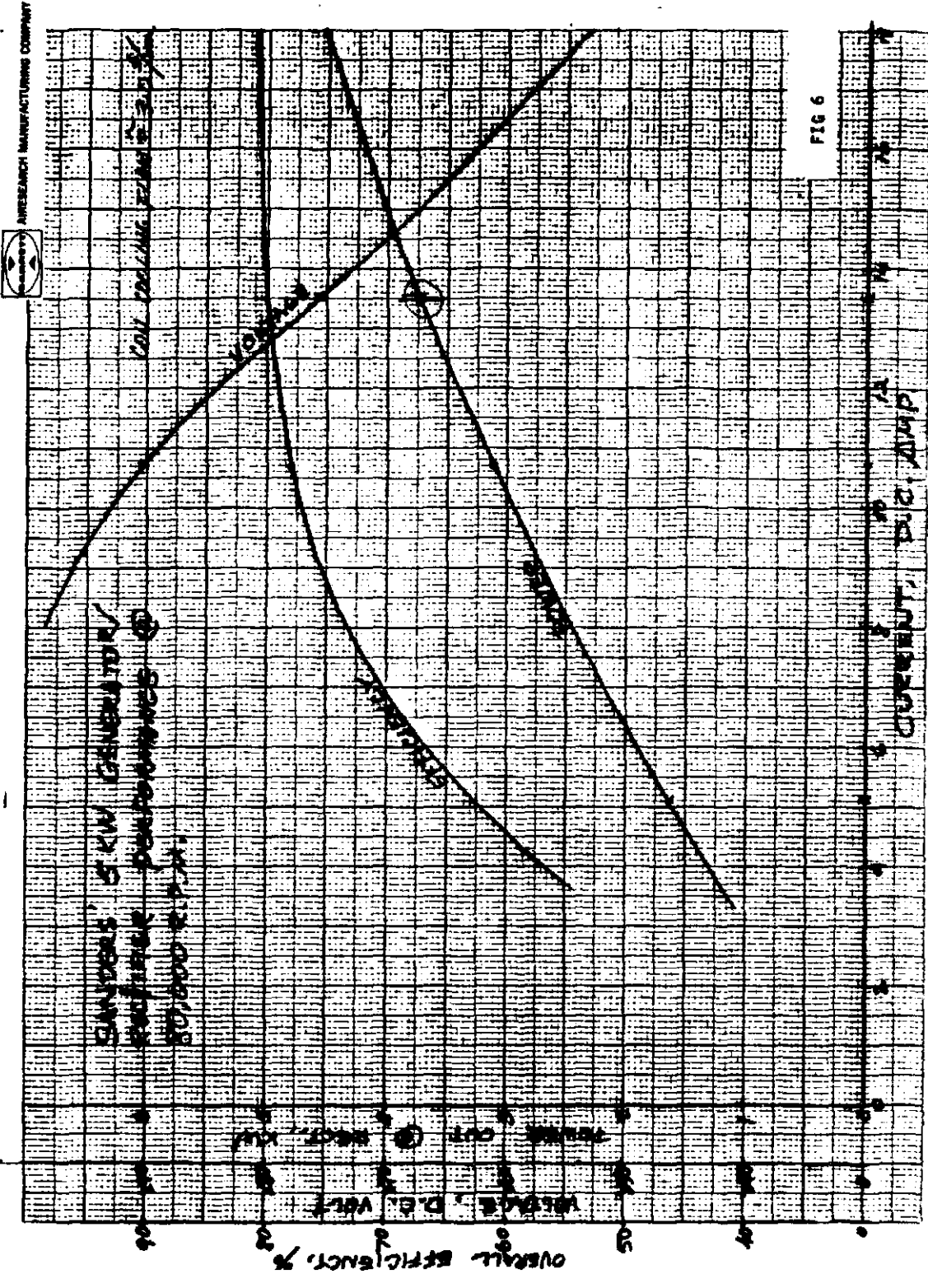
FIG 6

APPENDIX I

WORST CASE STRUCTURAL STRESS
FOR THE REINFORCED LEC 460

WORST CASE STRUCTURAL STRESS
FOR THE REINFORCED LEC 460

Maximum Stresses Occur In:

Case IVA + C + D where: IV = Stowed, 90 MPH Wind

A = Gravity forces (inc. 1290 lb eng. & 595 lb cw)

C = Wind from south

D = 3360 lb snow load (7 PSF)

Highest Stress Members	Case IVA, C, D	CASE IVA, C (No Snow)
#30	23K PSI	18.3
#33	19	15
#72	24	15
*#76	29.4	13.6

Highest stress Member is #76 (Diurnal Beam)

29.4K   (gravity and wind and snow)
-13.6   (without 3360 lb snow)
_____

Approximately   15.8K PSI is due to 3360 lb snow

Due to overweight engine (1620 lb) and counterweight (800 lb) for a total increase of 530 lb case approximation of the added stress of #76 is:

$$\frac{15.8K \ PSI}{3366 \ lb} = \frac{\Delta S}{530 \ lb} \qquad \underline{\Delta S \cong 2500 \ PSI \ for \ 530 \ lb \ \Delta W}$$

Therefore, stress in the Diurnal Beam with dish stowed and 90 MPH wind from south is approximately 13.6K + 2.5K ≅ 16K PSI

Same as above plus 3360 lb of snow = 32K PSI

ASTM A36 spec for tubing is 36K PSI yield.

Conclusions

The lowest structural safety factor occurs in the Diurnal Beam with the heavy engine and counterweight:

o SF_y = 2.25 without snow

o SF_y = 1.125 with 7 PSF (3360 lb) of snow

WORST CASE LOADS ON LEC 460 DRIVES

DIURNAL DRIVE

Maximum torque load on Diurnal drive occurs in case IV A + B (stowed, 90 MPH wind from east).

$$T_{Max} = 87,577 \text{ in lb*}$$

Rated load on diurnal drive is 60,000 in lb with a factor of 1.5+.

CONCLUSION

Is the worst case condition the diurnal drive has a SF = 1.02+.

ELEVATION DRIVE

Maximum axial load on elevation drive occurs in case IVA + C + D (Stowed, 90 MPH wind from south, 3360 lb snow load).

$$L_{Max} = 6560 \text{ lb*}$$

For case IVA and C (no snow) L = 1176 lb*

Rated load for elevation drive is 3,000 lb with a safety factor of 2.0.

CONCLUSION

In the worst case condition the elevation drive can be over stressed by 10% but without snow it has a SF = 5.1.

---

*Finite Element Analysis

I3

AN INDEX TO THE JANUARY 1984 FINITE ELEMENT ANALYSIS OF THE REENFORCED LEC 460

Nashua	Wind Vel.	Latitude	(FROM 1 JAN.) Day No.	(FROM LOCAL MIDNIGHT 24 HR. DAY) Time of Day	Notes
Case I	45 MPH	42.81°	80.8125	6	
Case II	45	42.81	46.0863	12	Noon
Case III	45	42.81	172.125	9	Looking East
Case IV	90	42.81	350.0	20	Unit Stowed

Osage City - Ground support for eng./dish to handle snow

Case V	80MPH	38.5°	-	-	Inverted stow - 1 leg, eng. to ground
Case VI	80	38.5°	-	-	Inverted stow - 2 leg, dish & eng. to ground

Sub Case A = Gravity loads (member mass and concentrator loads of):

    Node 23   500lb (Tripod Assembly)

    " 49   595lb (Counterweight)

    " 51   572lb (Dish)

    " 57   1290lb (Engine)

Sub Case B = Wind from East - Applied to Node 50

Sub Case C = Wind from South - "   "   "   "

Sub Case D = Snow load, 3360 lb Mass Applied to Node 51

Sub Case E = Snow load, 9600 lb Mass

1290 lb (PCA)

#72

(Diurnal Beam)#76

(Elevation drive)#313

500lb

Node 51

Node 50

752 lb (structure)
3360 lb (snow)

#33

#30

595lb (counterweight)

SBSS STUDIES
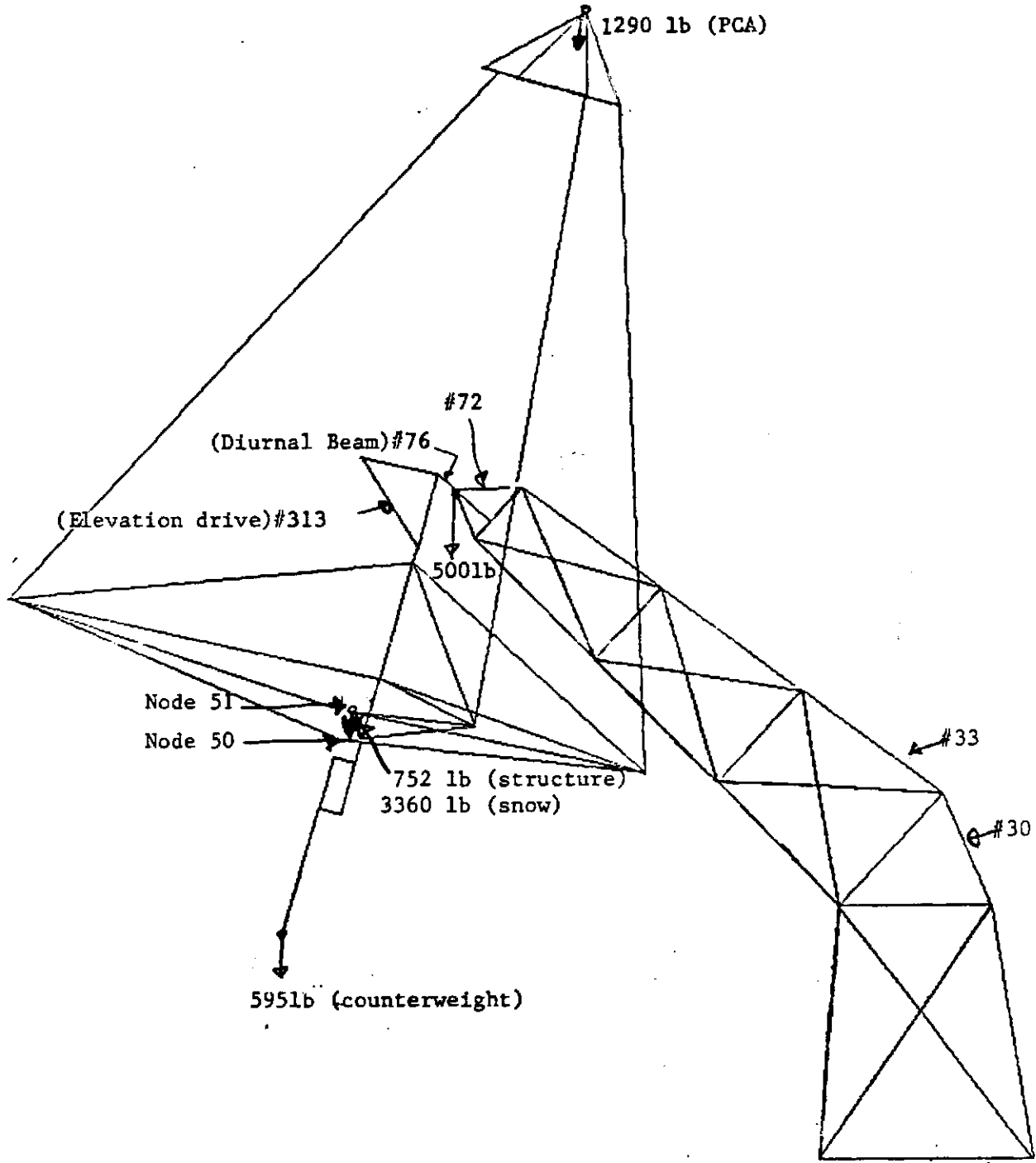
UNDEFORMED SHAPE

STANDARD DISTRIBUTION FOR SAND REPORTS (2/86)

TIC-4500-R70-UC-62 (156)

AAI Corporation
P.O. Box 6787
Baltimore, MD 21204

Acurex Aerotherm(2)
555 Clyde Avenue
Mountain View, CA 94039
Attn: J. Schaefer
      H. Morse

Alabama A&M University (2)
Department of Physics
P.O. Box 271
Normal, AL 35762
Attn: M. D. Aggarwal
      A. Tan

Alpha Solarco
1014 Vine Street
Suite 2530
Cincinnati, OH 45202

Applied Concepts
109K N. Main St.
Woodstock, VA 22664
Attn: J. S. Hauger

Applied Concepts
2501 S. Larimer County Rd. 21
Berthound, CO 80513
Attn: S. Pond

Australian National University
Department of Engineering Physics
P.O. Box 4
Canberra ACT 2600, AUSTRALIA
Attn: Prof. Stephen Kaneff

Barber-Nichols Engineering
6325 West 55th Ave.
Arvada, CO 80002
Attn: R. Barber

BDM Corporation
1801 Randolph Street
Albuquerque, NM 87106
Attn: W. E. Schwinkendorf

Battelle Memorial Institute
Pacific Northwest Laboratory
4000 NE 41st St.
Seattle, WA 98105
Attn: K. Drumheller

Battelle Memorial Institute
Pacific Northwest Laboratory
P.O. Box 999
Richland, WA 99352
Attn: T. Williams

Bechtel Group, Inc.
P.O. Box 3965
50 Beale Street
San Francisco, CA 94119
Attn: P. De Laquil

Black & Veatch
P.O. Box 8405
Kansas City, MO 64114
Attn: J. C. Grosskreutz

Boeing
   Engineering & Construction
P.O. Box 3999
Seattle, WA 98124
Attn: R. Gillette

Budd Company (The)
Fort Washington, PA 19034
Attn: W. W. Dickhart

Budd Company (The)
Plastic R&D Center
356 Executive Drive
Troy, MI 48084
Attn: K. A. Iseler

Burns & Roe   (2)
800 Kinderkamack Road
Oradell, NJ 07649
Attn: G. Fontana
      R. Cherdack

Cal Poly State University
San Luis Obisbo, CA 93407
Attn: E. J. Carnegie

California Institute of Technology
Aeronautics Library
MS 205-45
Pasadena, CA 91125
Attn: Jean Anderson

California Polytechnic University
Dept. of Mechanical Engineering
Pamona, CA 91768
Attn: W. B. Stine

Caterpillar Tractor Co.
San Leandro, CA 94577
Attn: Don Lucas

Chicago Bridge and Iron
800 Jorie Blvd.
Oak Brook, IL 60521
Attn: J. M. Shah

Colorado State University
Ft. Collins, CO 80523
Attn: T. G. Lenz

Columbia Gas System Service Corp.
1600 Dublin Road
Columbus, OH 43215
Attn: J. Philip Dechow

Custom Engineering, Inc.
2805 South Tejon Street
Englewood, CO 80110
Attn: C. Demoraes

Datron Systems, Inc.
200 West Los Angeles Ave.
Simi Valley, CA 93065-1650

DSET
Box 1850
Black Canyon Stage I
Phoenix, AZ 85029
Attn: G. A. Zerlaut

Donnelly Corporation
49 West Third Street
Holland, MI 49423
Attn: M. DeVries

Dow Chemical Company
  Contract Research,
  Development, and Engr.
Building 566
Midland, MI 48640
Attn: J. F. Mulloy

Dow Corning Corporation
Midland, MI 48640
Attn: G. A. Lane

Electric Power Research
  Institute
3412 Hillview Avenue
Palo Alto, CA 94303
Attn: E. A. Demeo
       J. E. Cummings

Energy Technology Engr. Ctr.
Rockwell International Corp.
P.O. Box 1449
Canoga Park, CA 91304
Attn: W. L. Bigelow

ENTECH, Inc.
P.O. Box 612246
DFW Airport, TX 75261
Attn: R. R. Walters

Eurodrive, Inc.
30599 San Antonio Rd.
Hayward, CA 94544

Florida Solar Energy Center
300 State Road 401
Cape Canaveral, FL 32920
Attn: Library

Ford Aerospace
Ford Road
Newport Beach, CA 92663
Attn: R. H. Babbe

Ford Motor Company
Glass Div., Technical Center
25500 West Outer Drive
Lincoln Park, MI 48246
Attn: V. L. Lindberg

Foster Wheeler Solar Dev. Corp.
12 Peach Tree Hill Road
Livingston, NJ 07039
Attn: M. D. Garber

Georgia Power Co.
7 Solar Circle
Shenandoah, GA 30264
Attn: E. Ney

Heery Energy Consultants, Inc.
Project Energy Manager
880 West Peachtree St. NW
Atlanta, GA   30309
Attn: Glenn Bellamy

Highland Plating
10001 N. Orange Drive
Los Angeles, CA   90038
Attn: D. May

Institute of Gas Technology
Attn: Library
34245 State Street
Chicago, IL   60616

Jet Propulsion Laboratory (3)
4800 Oak Grove Drive
Pasadena, CA 91109
Attn: W. A. Owen
       P. M. McElroy
       M. Alper

Kearney & Associates
14022 Condessa Drive
Del Mar, CA 92014
Attn: David W. Kearney

LaCour Kiln Service
P.O. Box 247
Canton, MS   39046
Attn: J. A. LaCour

LaJet Energy Co.
P.O. Box 3599
Abilene, TX 79604
Attn: Monte McGlaun
       Carl Williams

L'Garde, Inc.
1555 Placentia Avenue
Newport Beach, CA   92663
Attn: Mitchell Thomas

John Lucas
865 Canterbury Road
San Marino, CA   91108

Martin Marietta Corp. (2)
P.O. Box 179
Denver, CO   80201
Attn: T. Tracy

McCarter Corporation
200 E. Washington St.
P.O. Box 351
Norristown, PA   19404
Attn: R. A. Powell

McDonnell-Douglas Astronautics
    Company (3)
5301 Bolsa Avenue
Huntington Beach, CA 92647
Attn: J. B. Blackmon
        J. Rogan
        D. Steinmeyer

Mechanical Technology, Inc. (2)
968 Albany Shaker Road
Latham, NY 12110
Attn: H. M. Leibowitz
        G. R. Dochat

Meridian Corporation
5113 Leesburg Pike
Suite 700
Falls Church, VA   22041
Attn: D. Kumar

Midwest Research Institute (2)
425 Volker Blvd.
Kansas City, MO   64110
Attn: R. L. Martin
       J. Williamson

NASA Lewis Research Center (2)
21000 Brook Park Road
Cleveland, OH   44135
Attn: R. Beremand   500-215
       R. C. Evans   500-210

Naval Civil Engr. Laboratory
Port Hueneme Naval Station
Port Hueneme, CA 93043
Attn: Louis Huang

New Mexico Solar Energy Institute
New Mexico State University
Box 3SOL
Las Cruces, NM 88003

Parsons of California
3437 S. Airport Way
Stockton, CA 95206
Attn: D. R. Biddle

PG&E
3400 Crow Canyon Rd.
San Ramon, CA 94583
Attn: J. Iannucci
       G. Braun

Power Kinetics, Inc.
1223 Peoples Avenue
Troy, NY 12180
Attn: W. E. Rogers

Riegel Textile Corp.
La France, SC 29656
Attn: Mike Drummond

Reinhold Industries
Division of Keene Corp.
1287 E. Imperial Highway
Santa Fe Springs, CA 90670
Attn: J. Flynt

Research Systems, Inc.
Suburban Trust Bldg.,
     Suite 203
5410 Indian Head Hwy.
Oxon Hill, MD 20745
Attn: T. A. Chubb

Rockwell International
Energy Systems Group
8900 De Soto Avenue
Canoga Park, Ca 91304
Attn: T. Springer

Rockwell International
Space Station Systems Division
12214 Lakewood Blvd.
Downey, CA 90241
Attn: I. M. Chen

Sanders Associates
MER 15-2350
C.S. 2035
Nashua, NH 03061-2035
Attn: B. Davis

Solar Energy Information Center
1536 Cole Blvd.
Golden, CO 80401
Attn: R. Ortiz

Solar Energy Research Inst. (5)
1617 Cole Blvd.
Golden, CO. 80401
Attn: G. Gross
       B. P. Gupta
       J. Thornton
       D. Johnson
       A. Lewandowski

Solar Kinetics, Inc.
P.O. Box 47045
Dallas, TX 75247
Attn: J. A. Hutchison

Solar Steam
Suite 400
Old City Hall
625 Commerce Street
Tacoma, WA 98402
Attn: D. E. Wood

Southwest Research Institute
P.O. Box 28510
San Antonio, TX 78284
Attn: D. M. Deffenbaugh

SLEMCO
19655 Redberry Dr.
Los Gatos, CA 95030
Attn: A. J. Slemmons

Stearns-Catalytic Corp.
Box 5888
Denver, CO 80217
Attn: W. R. Lang

Sun Exploration and Production Co
P.O. Box 2880
Dallas, TX 75221-2880
Attn: R. I. Benner

Sun Power, Inc.
6 Byard St.
Athens, OH 45701
Attn: Mac Thayer

Sundstrand ATG (2)
P.O. Box 7002
Rockford, IL 61125
Attn: A. W. Adam
       B. G. Johnson

```
Suntec Systems, Inc.              University of Houston
P.O. Box 315                      Energy Laboratory; SPA
Savage, MN  55378                 Houston, TX  77004
Attn:  Harrison Randolph          Attn:  Lorin Vant-Hull
       J. H. Davison
                                  University of Kansas
Swedlow, Inc.                     Center for Research
12122 Western Avenue              2291 Irving Hill Dr.
Garden Grove, CA 92645            Lawrence, KA  66045
Attn:  E. Nixon                   Attn:  David Martin

3M-Energy Control Products (2)    University of New Mexico (2)
207-1W 3M Center                  Department of Mechanical Engr.
St. Paul, MN 55144                Albuquerque, NM 87131
Attn:  B. Benson                  Attn:  M. W. Wilden
       J. L. Roche                       W. A. Gross

Texas Tech University             USS Chemicals
Dept. of Electrical Engineering   P.O. Box 127
P.O. Box 4439                     Ironton, OH  45638
Lubbock, TX  79409                Attn:  E. H. Weber
Attn:  E. A. O'Hair
                                  Viking Solar Systems, Inc.
TRW (3)                           3223 N. Verdugo Rd.
Space & Technology Group          Glendale, CA  91208
One Space Park                    Attn:  George Goranson
Redondo Beach, CA  90278
Attn:  G. M. Reppucci
       A. D. Schoenfeld           0400  R. P. Stromberg
       J. S. Archer               1510  J. W. Nunziato
                                  1513  D. W. Larson
US Department of Energy (3)       1520  D. McCloskey
Albuquerque Operations Office     1524  A. K. Miller
P.O. Box 5400                     1810  R. G. Kepler
Albuquerque, NM 87185             1820  R. E. Whan
Attn:  D. Graves                  1824  J. N. Sweet
       R. Y. Lowrey               1830  M. J. Davis
       J. Weisiger                1832  W. B. Jones
                                  1840  R. J. Eagan
US Department of Energy (8)       1841  R. B. Diegle
Division of Solar Thermal Tech.   1846  R. K. Quinn
Washington, DC 20585              2520  N. J. Magnani
Attn:  Howard S. Coleman          2525  R. P. Clark
       R. Shivers                 2540  G. N. Beeler
       S. Gronich                 2541  J. P. Abbin
       C. Mangold                 3141  S. A. Landenberger (5)
       M. Scheve                  3151  W. L. Garner (3)
       F. Wilkins                 3154  C. H. Dalin (28) for DOE/OSTI
                                  3160  J. E. Mitchell
US Department of Energy           6200  V. L. Dugan
San Francisco Operations Ofc.     6220  D. G. Schueler
1333 Broadway                     6221  E. C. Boes
Oakland, CA 94612                 6222  J. V. Otts
Attn:  R. W. Hughey               6223  G. J. Jones
```

```
6224    D. E. Arvizu
6225    H. M. Dodd
6226    D. G. Schueler, Actg.
6227    J. A. Leonard (50)
6228    P. J. Eicker
6250    B. W. Marshall
6254    B. Granoff
8000A   C  Selvage
8024    P. W. Dean
8470    R. L. Rinne
8471    A. C. Skinrood
8473    J. C. Swearengen
8475    J. J. Iannucci
```